

# Studies in Phase Contrast X-ray Imaging of Biological Interfaces

---

Kaye Susannah Morgan  
BSc, BE(Hons)

Supervisors:  
Karen K. W. Siu and David M. Paganin



School of Physics, Monash University

## **Copyright Notices**

### **Notice 1**

Under the Copyright Act 1968, this thesis must be used only under the normal conditions of scholarly fair dealing. In particular no results or conclusions should be extracted from it, nor should it be copied or closely paraphrased in whole or in part without the written consent of the author. Proper written acknowledgement should be made for any assistance obtained from this thesis.

### **Notice 2**

I certify that I have made all reasonable efforts to secure copyright permissions for third-party content included in this thesis and have not knowingly added copyright content to my work without the owner's permission.

---

# Contents

<b>Contents</b>	<b>i</b>
<b>Abstract</b>	<b>iii</b>
<b>General Declaration</b>	<b>v</b>
<b>Acknowledgements</b>	<b>vii</b>
<b>1 Introduction</b>	<b>1</b>
1.1 Phase Contrast X-ray Imaging . . . . .	2
1.1.1 Propagation-Based Phase Contrast Imaging . . . . .	2
1.1.2 Analyser-Based Phase Contrast Imaging . . . . .	11
1.1.3 Interferometric Phase Contrast Imaging . . . . .	13
1.1.4 Grating-Based Phase Contrast Imaging . . . . .	14
1.1.5 Hybrid and Other Phase Imaging Methods . . . . .	15
1.2 Applications of PCXI . . . . .	16
1.2.1 Biomedical and Biological Applications . . . . .	16
1.2.2 Other Applications of PCXI . . . . .	18
1.3 Coherence considerations for PCXI . . . . .	19
1.3.1 Introduction . . . . .	19
1.3.2 Coherence Theory . . . . .	20
1.3.3 Means of Measuring Coherence . . . . .	23
1.4 Thesis Overview . . . . .	24
<b>2 Numerical Modelling of Propagation-Based PCXI of Interfaces</b>	<b>27</b>
<b>3 Exact Modelling of Propagation-Based PCXI of Cylindrical Interfaces</b>	<b>43</b>
<b>4 X-ray Coherence when using a Spinning Phase Diffuser</b>	<b>53</b>
<b>5 Propagation-Based PCXI using a Spinning Phase Diffuser</b>	<b>65</b>
<b>6 Propagation-Based PCXI for the Study of Airway Interfaces</b>	<b>81</b>
6.1 Introduction . . . . .	81
6.2 Cystic Fibrosis . . . . .	82
6.2.1 The Condition . . . . .	82
6.2.2 Long-term Treatments . . . . .	83
6.2.3 Assessing Treatments . . . . .	83
6.3 Airway Imaging Methods . . . . .	84

6.3.1	Introductory . . . . .	84
6.3.2	Gene Therapy Delivery Site Observation by CT . . . . .	85
6.3.3	ASL Monitoring by Live Imaging . . . . .	86
6.4	Approaches to Measuring ASL depth . . . . .	94
6.4.1	Obtaining an Interface Intensity Profile . . . . .	94
6.4.2	Tracking Airway Width over Time . . . . .	95
6.4.3	Interface Fringe Visibility . . . . .	96
6.4.4	Fringe Visibility as a Function of ASL Depth . . . . .	97
6.5	Enhancing Interface Fringe Visibility . . . . .	100
6.5.1	Enhancing Fringe Visibility by Experimental Set-up . . . . .	100
6.5.2	Enhancing Fringe Visibility by Image Analysis . . . . .	104
6.6	Mucociliary Clearance Monitoring . . . . .	106
6.7	Conclusion . . . . .	108
<b>7</b>	<b>PCXI for Live Imaging by a New Grating Method</b>	<b>111</b>
<b>8</b>	<b>Conclusion</b>	<b>117</b>
	<b>References</b>	<b>121</b>
	<b>Appendices: Supplementary Papers on PCXI of the Airways</b>	<b>135</b>
	<b>Appendix A</b>	<b>137</b>
	<b>Appendix B</b>	<b>143</b>
	<b>Appendix C</b>	<b>151</b>
	<b>Appendix D</b>	<b>165</b>
	<b>Appendix E</b>	<b>177</b>
	<b>Appendix F</b>	<b>191</b>
	<b>Supplementary Media</b>	<b>199</b>

---

# Abstract

This thesis studies the imaging of interfaces using phase contrast x-ray imaging (PCXI) with a synchrotron source, in theory, practice and application. An emphasis on biological interfaces means that the focus is on single-exposure methods of imaging, as desired when imaging a live sample. Firstly, we look at modelling the formation of propagation-based phase contrast fringes from a curved interface, studying the validity of the projection approximation, often used in this process. The emphasis then moves to how such fringes may be best realised in a non-ideal imaging set-up, looking at the coherence provided by the synchrotron source, notably in the presence and absence of a spinning phase diffuser. The effect that the set-up and associated coherence will have on the visibility and detail of phase contrast fringes from an interface is considered. These findings are then related to the detection of subtle biological interfaces, progressing towards the application of phase contrast imaging to the observation of changes in airway health in response to new treatments for cystic fibrosis. The difficulty in resolving these subtle airway interfaces motivates the final section of work; a new single-exposure sensitive method of phase imaging for live samples using a reference grating.

The first section of this work looks at a method of simulating the propagation of an x-ray wavefield through a sample and subsequently through free space in order to produce propagation-based phase contrast fringes. This approach uses the projection approximation to describe the effect of the sample on the incident wavefield, an approximation which does not describe the interference or diffraction of rays within the sample volume. It is seen, through comparison with experiment, that for a curved biological interface, diffraction within the sample volume becomes significant for propagation distances comparable to the sample volume dimension. Hence phase contrast fringes from a rounded interface (a good model for many biological interfaces) are underestimated for very short propagation distances. The intensity fringes seen from a curved edge are studied both in the complex Argand plane and through intensity profiles. At longer propagation distances, such as those typically used in biomedical imaging applications, where free-space propagation within the sample volume is a small percentage of the total propagation, the simulation model is found to match experiment.

This assertion is verified when the simulation model is compared to an exact solution to the inhomogeneous Helmholtz equation, both in the Argand plane and through intensity profiles. It is also seen that this exact solution for a plane wave incident on a cylinder will simplify to the projection approximation at the centre of the cylinder, where diffraction effects are negligible. This work demonstrates the value of the projection approximation simulation model, which is sufficiently accurate for the propagation distances commonly utilised for phase contrast images, with computational overheads many orders of magnitude less than the exact solution.

The effect of a limited transverse coherence width upon these ideal fringes is then considered. Transverse coherence measurements are taken at beamline 20XU of the SPring-8 synchrotron using a prism interferometer set-up. Measurements are taken at both the upstream and downstream

hutches for three sizes of beam-defining aperture. More particularly, measurements are taken with and without a spinning diffuser, an apparatus used to create a more uniform field of incident x-rays and remove unwanted phase effects introduced by upstream optics. It is found that while the presence of a diffuser did not decrease the transverse coherence width, the observed magnitude of the complex degree of coherence is decreased. Computer simulations of the imaging set-up show this same decrease in interference fringe visibility from a diffused beam.

The simulation model is then extended to look at the effect of a decreased degree of coherence, due to a diffuser, upon phase contrast fringes from an interface. The suppression of detail and visibility of the interface fringe in the presence of a diffuser is observed in both simulation and in experiment. However, both sets of results also show that simply moving the diffuser closer to the source is sufficient to significantly decrease this effect.

This is one of several modifications made to the experimental set-up while aiming to resolve subtle airway interfaces in the application work. This application seeks to measure changes in the airway health in response to new treatments for cystic fibrosis, which are tested (and hence imaged) in mouse models of the disease. One such measure of health is the depth of the airway surface liquid (ASL), which lines the inside of the airways and enables inhaled debris to be cleared from the lungs. While the interface between the ASL and the air-filled inside of the airway produces a strong propagation-based PCXI fringe set, the interface between the ASL and surrounding tissue provides a much weaker phase gradient which is not so easily detected. We detail experimental and analytical methods for increasing the visibility of fringes from this interface and ways to extract information about the ASL depth.

Finally, we describe and demonstrate a new single-exposure, large-grating method for detecting both high and low phase gradients. This is achieved by looking at the downstream distortion of a high visibility reference pattern that is incident upon the sample. The resulting quantitative phase maps from images of a phantom suggest this method may be of value in detecting the weak phase gradient at the ASL/tissue interface.

---

# General Declaration

**Monash University**

**Monash Research Graduate School**

**Declaration for thesis based or partially based on conjointly published or unpublished work**

## General Declaration

In accordance with Monash University Doctorate Regulation 17 / Doctor of Philosophy and Master of Philosophy (MPhil) regulations the following declarations are made:

I hereby declare that this thesis contains no material which has been accepted for the award of any other degree or diploma at any university or equivalent institution and that, to the best of my knowledge and belief, this thesis contains no material previously published or written by another person, except where due reference is made in the text of the thesis.

This thesis includes 11 original papers published in peer reviewed journals. The core theme of the thesis is phase contrast x-ray imaging of biological interfaces. The ideas, development and writing up of all the papers in body of the thesis were the principal responsibility of myself, the candidate, working within the School of Physics under the supervision of Karen K. W. Siu and David M. Paganin.

The inclusion of co-authors reflects the fact that the work came from active collaboration between researchers and acknowledges input into team-based research. The contribution of the PhD Candidate to each of the papers arising from the thesis is declared overleaf.

Signed:

---

Kaye Susannah Morgan

Thesis chapter	Paper Title	Status	Contribution
2	The projection approximation and edge contrast for x-ray propagation-based phase contrast imaging of a cylindrical edge	Published	Led the original experiments, analysed the PCXI images, wrote the code for and analysed the numerical simulations, developed the theoretical aspects, worked through the mathematics of the appendix and wrote up the paper
3	The projection approximation versus an exact solution for x-ray phase contrast imaging with a plane wave scattered by a dielectric cylinder	Published	Solved for and evaluated the exact solution detailed in the paper, wrote the code for and analysed results from the numerical simulations, developed the theoretical aspects, worked through the mathematics of the asymptotic approximations to the exact solution and wrote up the paper
4	Measurement of hard X-ray coherence in the presence of a rotating random-phase-screen diffuser	Published	Contributed to the original experiments, the data analysis, numerical simulations and the write-up
5	Assessment of the use of a diffuser in propagation-based x-ray phase contrast imaging	Published	Contributed to the original experiments, the data analysis, numerical simulations and the write-up
7	Quantitative x-ray phase contrast imaging using a single grating of comparable pitch to sample feature size	Published	Led the original experiments and developed the theoretical basis, performed the data analysis, and wrote up the paper
Appx A	Optimising coherence properties for phase contrast x-ray imaging (PCXI) to reveal airway surface liquid (ASL) as an airway health measure	Published	Contributed to the original live imaging experiments, led the phantom imaging and diffuser placement imaging, the numerical simulations, image analysis, and wrote up the paper
Appx B	Phase contrast x-ray imaging for the non-invasive detection of airway surfaces and lumen characteristics in mouse models of airway disease	Published	Contributed to the original live imaging experiments, image processing, numerical simulations and proofreading
Appx C	High-resolution visualization of airspace structures in intact mice via synchrotron phase-contrast x-ray imaging (PCXI)	Published	Contributed to the original CT and live imaging experiments, image processing and 3D render movie visualisation and proofreading
Appx D	Real-time non-invasive detection of inhalable particulates delivered into live mouse airways	Published	Contributed to the original live imaging experiments, image processing and proofreading
Appx E	A new technique to examine individual pollutant particles and fibre deposition and transit behaviour in live mouse trachea	Published	Contributed to the original live imaging experiments, image processing and proofreading
Appx F	Animals in synchrotrons: Overcoming challenges for high-resolution, live, small-animal imaging	Published	Contributed to the planning, original experiments and proofreading

---

# Acknowledgements

I am indebted to my two supervisors, Karen Siu and David Paganin for their support, enthusiasm and generosity in guiding me through my PhD. It has been an honour to have been able to work closely with two such intelligent and kind people. Their commitment to my supervision has been exceptional. Karen has ensured that I am afforded every opportunity to learn and develop as a researcher, and I am so appreciative to have benefited from her wealth of experience in synchrotron imaging during the many enjoyable trips to Japan together. David's positivity and his excellent grip on theory have been invaluable in our work together.

David Parsons' leadership in the animal work and his enthusiasm for the project have been so important and I would like to thank him for the time given in assisting me with the biomedical aspects of the work. I would also like to express my gratitude to Martin Donnelley for his input and support both while imaging in Japan and between experiments.

It is a pleasure to have worked with Sally Irvine on two papers, and I thank her for the enjoyable discussions which have led to a much deeper understanding of several of the concepts in this thesis.

The beamline scientists at the biomedical beamlines of the SPring-8 synchrotron have been so helpful in the many weeks spent doing experiments, and I am honoured to have learned from Yoshio Suzuki, Akihisa Takeuchi, Kentaro Uesugi and Naoto Yagi. Experiments in Japan have also been shared with a large group of researchers including the Monash MuBeta group; Andreas Fouras, Steve Dubsy, Aidan Jamison and Simon Higgins, Monash physicists David Vine and Konstantin Pavlov, the Monash lung imaging group including Marcus Kitchen, and many other excellent scientists. Their assistance with our experiments, the privilege of assisting with and learning from their work and the good times shared together are greatly appreciated. I would also like to thank Marcus for his help, particularly in the early months of my PhD. I enjoyed the opportunity to use the Australian Synchrotron earlier this year, and thank Chris Hall for making this happen.

I am grateful for the financial support of an Australian Postgraduate Award and a J. L. William Bequest Scholarship from the School of Physics, Monash University. The support from Cystic Fibrosis Australia in the form of a studentship is also greatly appreciated. Travel to SPring-8, Japan for the experimental components of this project has been largely supported by the Access to Major Research Facilities Program (AMRFP), managed by the Australian Nuclear Science and Technology Organisation (ANSTO) and the International Synchrotron Access Program (ISAP), managed by the Australian Synchrotron. I thank the Japan Synchrotron Radiation Research Institute (JASRI) for privilege of using the SPring-8 facility.

I would like to thank the organisers of the Cheiron Synchrotron School Japan 2007, for covering my travel expenses and place at the school. The support of the Monash Research Graduate School (MRGS), the Faculty of Science and the School of Physics in attending the X-ray Micro and Nano Probes Workshop (XMNP) 2010 is greatly appreciated, and the organisers of the workshop are thanked for their generosity in covering registration costs. I also acknowledge the National

Health and Medical Research Council (NHMRC) and the Australian Research Council (ARC) for supporting this project and my supervisors. The opportunity to attend the Medical Applications of Synchrotron Radiation (MASR) conference 2010, the Synchrotron Radiation Instrumentation (SRI) conference 2009, the Australian Synchrotron User meetings 2007-2010, the Australian Institute of Physics (AIP) workshop 2008 and several other meetings has been greatly appreciated.

The staff of the School of Physics have always been so helpful and supportive, including Jean Pettigrew, Tracey Lawrence, Julia Barnes and James Gibbons, as well as Michael Morgan. I have enjoyed the opportunity to teach in the undergraduate physics and radiography laboratories and to take lectures, and must thank Susan Feteris, Jenny McCabe, David Mills, Ruth Druva, Imants Svalbe, Lincoln Turner, Theo Hughes and Andrei Nikulin.

I consider myself most fortunate to have enjoyed the company of my colleagues in the School of Physics at Monash University, including those who were there at the start; Toby Beveridge, Guido Cadenazzi, Jeff Crosbie, Evan Curwood, John Gillam, Anowarul Habib, Sabeena Sidhu, David Vine and Ivan Williams, along the way; Alexis Bishop, Shekhar Chandra, Sally Irvine, Shane Kennedy, Marcus Kitchen, Gary Ruben, Naomi Schofield, Kathryn Spiers and Nadia Zatsepin, and at the end; Katie Auchetl, Richard Beare, Mario Beltran, Jeremy Brown, Daniel Carter, Ben Farmer, Shane Farnsworth, Elliot Hutchison, Martijn Jasperse, Brad Murnane, Jay Newstead, David Palamara, Rohini Shankar, Changxi Zheng and Zhenyu Zhou. The coffees, ice-creams, quizzes, triathlons, travels and your friendship have been very much enjoyed and appreciated.

Outside of the world of physics, I have valued the support of “The Girls”; Rachael Junor, Kathryn Lorimer, Fiona Maullin, Michelle Meyers, Lisa Snare and Kate Stone and their boys; Adam Farrelly, Julian Stone and Pete Yeoman, all the “Monday nighters”; particularly Scott Bailey, Nat Blizzard, Helen and Dave Boucher, Belinda Clear, Hannah Dungan, Al and Joel Hearnshaw, Sarah Lorimer and Kat, Jas and Nikki Mann. Also all the GWUC family, the “Mighty GWUCs” players, Nicole and Lyn Boyer, Bec and Pete Cornall, and the members of “Free Spirit”; particularly Philippa Hillman, Deb Pope, Lise Hales, Lyn Maslen and Tim Laub. And all those friends who I could not fit in!

Finally, this thesis would not have been possible without the backing and encouragement of my wonderful family; in particular my grandparents, Rose, Laura, Mum and Dad. Thank you for both the diverting holidays and for the continual support along the way, this thesis is dedicated to you.

---

# Introduction

The application of x-rays to medical imaging dates to Röntgen's first work in 1896 (Röntgen, 1896). He discovered that this new kind of rays were able to pass through materials opaque to visible light, revealing information about the internal structure of samples by creating a "shadow" image of denser structures. One of his first x-ray images was that of his wife's hand, demonstrating that the penetrating power of x-rays makes them ideal for differentiating between soft tissue and bone. Alongside this type of projection imaging, computed tomography (CT) methods (Kak and Slaney, 2001) developed for clinical use in the 1970s have enabled medical professionals to image three-dimensional volumes, and are now standard in most hospitals. X-ray sources have also increased in power and coherence, enabling high-resolution images which can differentiate between different types of tissue. Detector technology has been critical in this achievement and continues to be of great importance in developing new methods of imaging (Beutel et al., 2000). The advent of bright, highly coherent synchrotron sources (Margaritondo, 2002) has not only enabled high resolution absorption imaging, but has also prompted a breadth of imaging techniques which use phase contrast (Nugent, 2010).

Phase contrast imaging provides contrast not only due to absorption, as utilised by conventional x-ray imaging, but also due to phase gradients incurred across different materials. While a raindrop on the windscreen of a car at night will not produce a strong shadow on the dashboard, it may produce an image due to phase effects. The visible light rays will change direction as they pass through the drop, and this refraction will result in high-contrast intensity variations. The greater the distance between the drop and the dashboard, the stronger the contrast of the resulting image will be, until at even greater distances the image becomes defocused. It is this ability to image and differentiate between similarly-absorbing materials (air/water in the above example) which makes phase contrast imaging so powerful. This thesis looks towards the application of this ability to the imaging of airways, with the longer term goal of providing a non-invasive method of assessing new treatments for cystic fibrosis.

In this first chapter, we describe the main forms of phase contrast x-ray imaging (PCXI), with an emphasis on propagation-based techniques, the method predominantly used in this project. This includes looking at a mathematical description which may be used to model the creation of propagation-based phase contrast (§§1.1.1.2-1.1.1.3, in preparation for Chapters 2 and 3) and at algorithms used to retrieve additional information about the sample from such an image (§1.1.1.4). A brief qualitative description is then given of the remaining phase contrast methods to elucidate the ways in which phase effects may be visualised (§§1.1.2-1.1.5). We then move onto a short summary

of research areas to which PCXI has been applied, with a focus on biomedical applications (§1.2, relevant to the airway imaging described in Chapter 6). Finally we consider the effects of imaging with an x-ray beam which is not fully coherent (§1.3). This provides extra background to Chapters 4 and 5, and is key in some of the results observed in the application work of Chapter 6. Chapter 1 closes with an overview of the thesis itself (§1.4).

## 1.1 Phase Contrast X-ray Imaging

Conventional x-ray images use the absorption properties of materials to produce an image. Phase contrast imaging also visualises the phase changes introduced by the refractive properties of materials (Zernike, 1942; Gabor, 1948). This means that features of a sample with similar attenuation properties (but different refractive properties) may be differentiated, due to the phase gradients introduced across the different features.

As an incident wave passes through a material, the amplitude decreases according to the attenuation coefficient of the material. The intensity of the transmitted wave will be observed as the squared magnitude of the complex amplitude, so different materials or thicknesses will transmit different intensities. The intensity may then be observed and recorded using a position sensitive detector, such as a charge coupled device (CCD) or an image plate. The phase of the wave cannot be directly determined using a position-sensitive detector (Born and Wolf, 1999). Although features with different refractive indices will incur different phase changes, these will not be directly observable. In order to use the extra information provided in the phase of the wave, phase contrast imaging converts these phase variations into intensity variations, which may be achieved using a number of phase contrast techniques. We will now describe several of these techniques, with the most space given to propagation-based phase contrast, the method predominantly used in the work of this thesis.

### 1.1.1 Propagation-Based Phase Contrast Imaging

#### 1.1.1.1 Background on Propagation-Based PCXI

Propagation-based phase contrast is perhaps the most easily realised of the methods (Gureyev et al., 2009), since it requires no optical elements between either the source and the sample, or the sample and the detector. The only requirement is that the source has sufficiently high spatial coherence (Snigirev et al., 1995; Cloetens et al., 1996; Wilkins et al., 1996). In this technique, a distance is introduced between the sample and the detector (typically of the order of 1 metre for hard x-rays scattered by millimetre-sized sample features). This allows the modified waves to interfere during propagation (Keller, 1962), causing a fringe pattern in the image where the boundary occurs between two materials of different refractive indices, shaped as in Fig. 1.1. Contrast is also seen not only from edge features, but also from any variations in projected optical thickness across the sample, where transverse phase variations are introduced in the wave exiting the sample.

The width and magnitude of these fringes will initially increase as the propagation distance increases. This enables the high contrast between the central light and dark fringes to make an edge or interface sharp and clearly visible, as illustrated in Fig. 1.2.

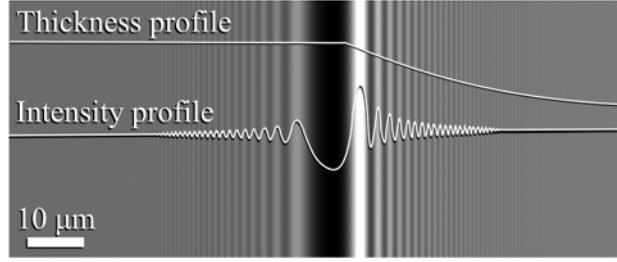


Figure 1.1: A simulated propagation-based phase contrast image of the edge of a 1 mm diameter cylindrical hole in perspex, created using the simulation model detailed in section 1.1.1.2, shows the fringe pattern for 25 keV x-rays propagating 50 cm.

The regime of phase contrast, relating to propagation distance, may be described by the Fresnel number (Saleh and Teich, 1991);

$$N_F = \frac{d^2}{\lambda z} \quad (1.1)$$

where  $d$  is the characteristic transverse length scale of the sample,  $\lambda$  is the wavelength and  $z$  is the propagation distance. If  $N_F$  is significantly greater than 1, the image is said to be in the near-field, where narrow phase contrast fringes may be observed, enhancing edge visibility (Fig. 1.2 b) and c)). In the intermediate field, the Fresnel number is close to 1 and a multiple-fringe pattern is observed at edges (Fig. 1.2 d)). Increasing propagation further to reach the far field, where  $N_F$  is much smaller than 1, the image then approaches the absolute value squared of the Fourier transform of the sample's exit-surface wavefield (Fig. 1.2 e)). In this thesis, imaging is predominantly conducted in the near-field, as seen in Fig. 1.2 c).

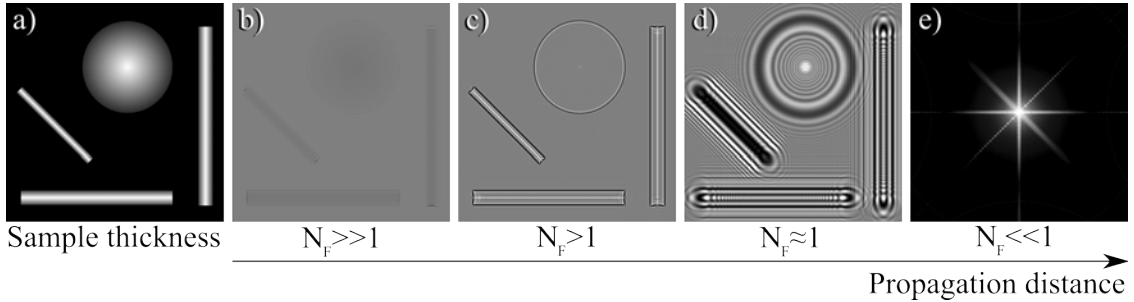


Figure 1.2: Phase contrast effects increasing with sample-to-detector propagation distance for projected sample thickness as shown in a), b) in the near field, c) in the near field with greater propagation, d) in the intermediate field and e) in the far field.

Propagation-based phase contrast x-ray imaging (PB-PCXI) using hard synchrotron x-rays was first demonstrated at the European Synchrotron Radiation Facility (Snigirev et al., 1995; Cloetens et al., 1996), with suggestions for biological and materials applications. The small source size and significant propagation from the source to sample found at the synchrotron provides high spatial coherence and the monochromator ensures high chromatic coherence (§1.3), so that all incident rays will interfere maximally, enabling sharp phase contrast fringes. Imaging by Wilkins *et al.* (Wilkins et al., 1996), using a microfocus source, showed that polychromatic x-rays will still produce high quality phase contrast images, provided the source size is sufficiently small.

Phase contrast images produced by propagation have been shown not only to improve the observable detail in images, but also to provide adequate information for quantitative measures of sample thickness and distribution to be made for single-material specimens of known composition (Nugent et al., 1996; Paganin and Nugent, 1998). This body of work, known as phase retrieval, is explored in section 1.1.1.4. The techniques of phase retrieval address an inverse problem, requiring reconstruction of the specimen given one or more measured images (§1.1.1.4). As a necessary pre-requisite for the inverse problem of phase retrieval, we will also examine the forward problem, namely the determination of the image that will be measured from a specimen given certain specified imaging conditions (§1.1.1.2).

Given that propagation-based phase contrast is easily realised in experiment, without the need for any specialised optical elements in addition to the source and detector, the technique is particularly suited to *in vivo*<sup>1</sup> biological imaging (Westneat et al., 2003).

### 1.1.1.2 Modelling Propagation-Based PCXI

It is important to have a mathematical basis which can describe the creation of propagation-based phase contrast images, in order to optimise imaging conditions and to correctly interpret images. An example of a typical set-up, which we wish to mathematically model, is shown in Fig. 1.3.

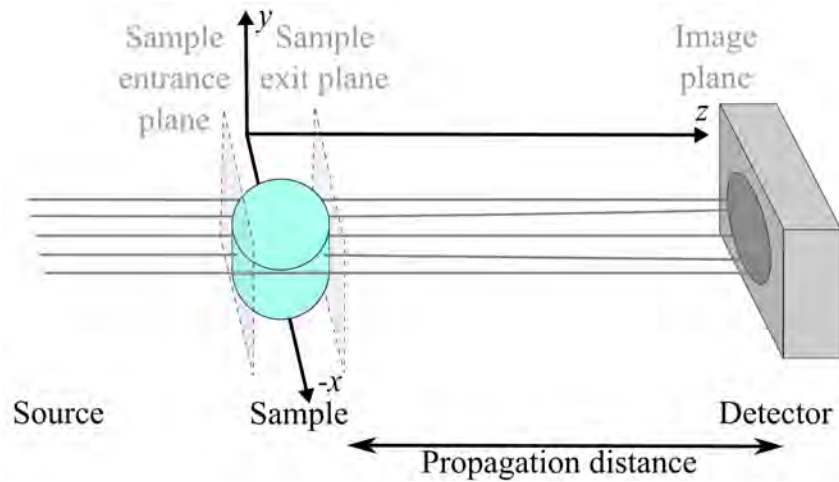


Figure 1.3: A typical propagation-based phase contrast imaging set-up, with waves propagating in the positive  $z$  direction, where the system may be separated into the propagation through the sample (between the sample entrance and exit planes) and the propagation from the sample exit plane to the image plane.

The propagating wavefield is governed by Maxwell's equations (Jackson, 1999). For the cases studied here, we can neglect magnetic effects and polarisation and can assume the scattering medium to be isotropic<sup>2</sup> at each point in space. For a static, isotropic, non-magnetic scatterer (sample), Maxwell's equations reduce to the inhomogeneous Helmholtz equation for each Cartesian component with monochromatic radiation (Born and Wolf, 1999):

$$\left[ \nabla^2 + k^2 n^2(x, y, z) \right] \psi(x, y, z) = 0. \quad (1.2)$$

<sup>1</sup>*In vivo* studies are done when the subject is alive and intact.

<sup>2</sup>A medium is isotropic at a given point in space, if its electromagnetic properties are independent of the direction of the electromagnetic field at that point in space.

Here  $\nabla^2 = \frac{\partial^2}{\partial x^2} + \frac{\partial^2}{\partial y^2} + \frac{\partial^2}{\partial z^2}$  denotes the Laplacian operator,  $k = 2\pi/\lambda$  is the vacuum wavenumber for wavelength  $\lambda$  and  $n$  the position dependent complex refractive index for a static scatterer, all operating on a wavefield  $\Psi(x, y, z, t) = \psi(x, y, z) \exp(-i\omega t)$ . The intensity of such a wave will be given by  $I = |\psi|^2$ , and the phase by  $\phi = \arg(\psi)$ .

Each material upon which a wavefield is incident may be characterised by the complex refractive index  $n$ ,

$$n = 1 - \delta + i\beta, \quad (1.3)$$

where  $\delta$  describes the refractive properties of the material and attenuation is determined by  $\beta = \mu/2k$ , where  $\mu$  is the linear attenuation coefficient. It is important to note that  $\delta$  is typically at least two orders of magnitude greater than  $\beta$  for hard x-rays and biological samples, providing the potential for significant contrast, even with high energy x-rays for which a material may be weakly absorbing (Fitzgerald, 2000). Both  $\delta$  and  $\beta$  vary with wavelength, hence if a polychromatic source is used, either an effective value of  $n$  may be used or a sum of images constructed covering the wavelengths present (Wilkins et al., 1996). In considering a real static sample, the sum of many composite materials will mean  $n$  will also change with position within the sample, hence become a function of  $(x, y, z)$ .

An exact solution to Eqn. 1.2 will then fully describe the behaviour of the wavefield, including absorption, refraction, diffraction and interference.

For x-ray wave propagation through tissue or a similar sample, some approximations may be made to enable a complex ray approach, which may be more easily applied to a range of samples. Provided that scattering within the sample will not be sufficiently strong to significantly change the direction of incident rays, paraxiality<sup>3</sup> along the  $z$  axis may be assumed, and the inhomogeneous paraxial equation used;

$$\left[ 2ik \frac{\partial}{\partial z} + \nabla_{\perp}^2 + k^2(n^2(x, y, z) - 1) \right] \psi(x, y, z) = 0. \quad (1.4)$$

Here  $\nabla_{\perp}^2$  refers to the transverse Laplacian,  $\nabla_{\perp}^2 = \frac{\partial^2}{\partial x^2} + \frac{\partial^2}{\partial y^2}$ . If the material in which the wave is propagating is taken to be vacuum, this gives the homogenous paraxial equation;

$$\left[ 2ik \frac{\partial}{\partial z} + \nabla_{\perp}^2 \right] \psi(x, y, z) = 0. \quad (1.5)$$

In the inhomogeneous paraxial equation (Eqn. 1.4), if the term  $\nabla_{\perp}^2 \psi$  is taken as small relative to the other terms (*i.e.* there are only slowly changing variations in the wavefield in the plane perpendicular to propagation), then adjacent complex rays become uncoupled and we arrive at the projection approximation. The projection approximation predicts the change in phase and intensity of a wavefield having passed through a sample volume of materials of refractive index  $n(x, y, z) = 1 - \delta(x, y, z) + i\beta(x, y, z)$ , as below (see, *e.g.*, (Paganin, 2006)),

---

<sup>3</sup>An optical system is paraxial if the rays are parallel to or close to parallel to the optical axis, *i.e.* the magnitude of the local wavevector in the direction of propagation is significantly greater than the magnitude of the component of the wavevector in the plane perpendicular to propagation.

$$\begin{aligned} \psi(x, y, z = z_{\text{exit}}) &= \psi(x, y, z = z_{\text{entrance}}) \times \exp\left(-ik \int_{z=\text{entrance}}^{z=\text{exit}} \delta(x, y, z) dz\right) \\ &\times \exp\left(-k \int_{z=\text{entrance}}^{z=\text{exit}} \beta(x, y, z) dz\right). \end{aligned} \quad (1.6)$$

The second term on the right side describes the phase change effected upon the incident wave and the third term the attenuation of the incident wave. Looking at attenuation only, substituting  $\beta = \mu/2k$ , and squaring the absolute value of both sides (to give the intensity at the exit surface), gives:

$$|\psi(x, y, z = z_{\text{exit}})|^2 = |\psi(x, y, z = z_{\text{entrance}})|^2 \times \exp\left(-\int_{z=\text{entrance}}^{z=\text{exit}} \mu(x, y, z) dz\right). \quad (1.7)$$

For a uniform material of total projected thickness  $T$ , this reduces to Beer's Law;

$$|\psi(x, y, z = z_{\text{exit}})|^2 = |\psi(x, y, z = z_{\text{entrance}})|^2 \times \exp(-\mu T). \quad (1.8)$$

A numerical model of an imaging set-up may safely apply the projection approximation to describe the propagation of an incident field through the sample, provided (i) the incident field is itself paraxial, and (ii) the complex refractive index of the sample is sufficiently slowly varying in space. However, since this approach does not describe diffraction, an alternative approach must be used to propagate the sample exit plane wavefield to the detector and observe propagation-based phase contrast.

Propagation of a wavefield through free space should satisfy the homogeneous Helmholtz equation (taking Eqn. 1.2 where  $n = 1$ ),

$$(\nabla^2 + k^2)\psi(x, y, z) = 0, \quad (1.9)$$

describing not only the propagation of complex rays, but also diffraction and interference between initially adjacent rays. An exact solution to the boundary-value problem for the above equation is given by the angular spectrum formalism (Mandel and Wolf, 1995). The boundary value  $\psi(x, y, z = z_{\text{exit}})$  can be written as a two-dimensional Fourier integral,

$$\psi(x, y, z = z_{\text{exit}}) = \frac{1}{2\pi} \iint \mathcal{F}(\psi(x, y, z = z_{\text{exit}})) \exp[i(k_x x + k_y y)] dk_x dk_y, \quad (1.10)$$

where  $k_x$  and  $k_y$  are the Fourier-space co-ordinates corresponding to  $x$  and  $y$  in the plane of the image and  $\mathcal{F}$  is the forward Fourier transform with respect to  $x$  and  $y$ . Multiplying each Fourier component by the propagator  $\exp(i\Delta k_z) = \exp\left(i\Delta \sqrt{k^2 - k_x^2 - k_y^2}\right)$  will then propagate the sum of plane waves forward by distance  $\Delta$  (*i.e.* the propagation distance in Fig. 1.3), as seen in Eqn. 1.11 (Delen and Hooker, 1998; Goodman, 2005; Nieto-Vesperinas, 2006):

$$\begin{aligned} \psi(x, y, z = z_{\text{exit}} + \Delta) &= \frac{1}{2\pi} \iint \mathcal{F}(\psi(x, y, z = z_{\text{exit}})) \exp[i(k_x x + k_y y)] \\ &\times \exp\left[i\Delta \sqrt{k^2 - k_x^2 - k_y^2}\right] dk_x dk_y. \end{aligned} \quad (1.11)$$

Numerical implementation using the Fast Fourier Transform makes this formalism particularly fast to implement in simulation (Press et al., 1992). This means that the process of propagation-based phase contrast may be simulated using the projection approximation (Eqn. 1.6) to describe the propagation of the wave through the sample, then this exit-surface wave may be propagated to the detector using the angular-spectrum diffraction integral (Eqn. 1.11). This method of modelling has been used in simulation work described in Chapters 2-6. The validity of applying the projection approximation in this way, *i.e.* neglecting diffraction within the sample volume, is explored in Chapters 2 and 3 (Morgan et al., 2010b,c).

If we utilise the convolution theorem<sup>4</sup> (Sherman, 1967), and substitute the Weyl expansion (Weyl, 1919; Nieto-Vesperinas, 2006) for a spherical wave into the resulting expression, we arrive at the Rayleigh–Sommerfeld diffraction integral of the first kind (Winthrop and Worthington, 1966), where  $R$  is the distance between each point on the plane  $z = z_{exit}$  and each point on the plane  $z = z_{exit} + \Delta$ :

$$\psi(x, y, z_{exit} + \Delta) = \frac{1}{2\pi} \int_{-\infty}^{\infty} \psi(x, y, z = z_{exit}) \frac{\partial}{\partial z} \frac{\exp(ikR)}{R} dx dy. \quad (1.12)$$

### 1.1.1.3 PB-PCXI Wavefield in the Argand plane

This thesis looks particularly at the application of propagation based phase contrast to the imaging of interfaces or edges. For PCXI, it is informative to look at both the phase and intensity of the propagated wave, which may be conveniently plotted in the Argand plane. For the case of a sharp square edge with a monochromatic plane wave incident, as shown in Fig. 1.4, the resulting wavefield may be described using the Fresnel integrals (Margaritondo and Tromba, 1999). This formalism is briefly reviewed below:

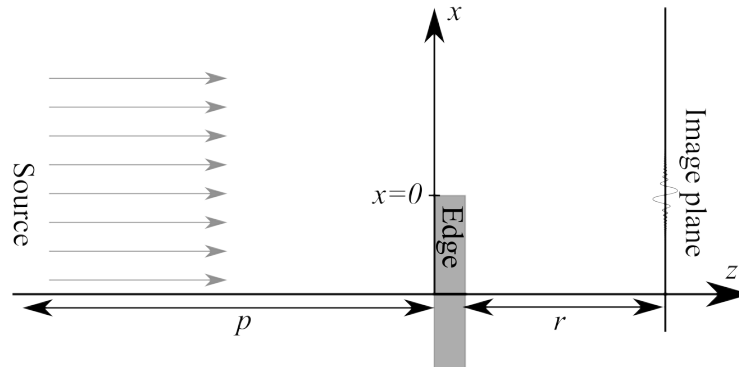


Figure 1.4: Geometrical set-up of a sharp edge ending at  $a$  with plane wave incident, which is then propagated  $r$  metres to the image plane.

For an incident wave  $\psi(x, z = 0)$ , diffracted by a sharp opaque edge at  $x = 0$ , the intensity  $I$  of wavefield  $\psi(x, z)$  at the image plane  $z = r$  can be obtained from Eqn. 1.12 by applying the paraxial approximation, to give the convolution formulation of Fresnel diffraction;

$$I(x, z) \propto \left| \int_{x'=0}^{x'=\infty} \Psi(x, z = 0) \exp(ik/2z(x - x')^2) dx' \right|^2. \quad (1.13)$$

<sup>4</sup> $A * B = \mathcal{F}^{-1} [\mathcal{F}(A) \times \mathcal{F}(B)]$ .

Expressing the complex exponential in terms of sine and cosine, and assuming a normally incident plane wave, this becomes;

$$I(x, z) \propto \left| \int_{x'=0}^{x'=\infty} \cos(k/2z(x-x')^2) - i \sin(k/2z(x-x')^2) dx' \right|^2. \quad (1.14)$$

In terms of the Fresnel integrals;

$$C(u) = \int_0^u \cos(\pi x'^2/2) dx', \quad (1.15)$$

$$S(u) = \int_0^u \sin(\pi x'^2/2) dx', \quad (1.16)$$

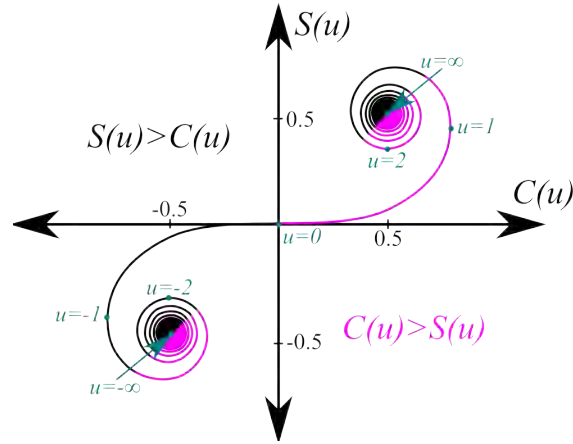


Figure 1.5: The Fresnel Integrals plotted in the complex plane, parameterised by their argument  $u$ , to form the Cornu Spiral (Born and Wolf, 1999).

(which are plotted as Fig. 1.5, parameterised by argument  $u$  in the Argand plane), the observed intensity of the complex wavefield may be expressed as:

$$I(x, z) \propto |[\mathcal{C}(\infty) - C(u)] + i[S(\infty) - S(u)]|^2, \quad (1.17)$$

where  $u = x \sqrt{\frac{2(p+r)}{pr\lambda}}$  is the scaled edge coordinate and  $p$  and  $r$  are source-to-sample and sample-to-detector distances respectively (see Fig. 1.4). The complex wavefield may therefore now be described using the Cornu spiral seen in Fig. 1.5, but shifted by  $1/2$  (given  $\mathcal{C}(\infty) = S(\infty) = 1/2$ ) in each of the real and imaginary components, as seen in Fig. 1.6 a). The intensity at a given propagation,  $z = r$ , is parameterised along the spiral by transverse position  $x$  in the image plane, and is now proportional to the distance from that point on the spiral to the origin, with the phase given by the angle from the real axis. Therefore the wavefield intensity is equal to the incident intensity  $I_0$  far from the edge, and 0 far behind the edge, as seen in Fig. 1.6 c).

If the edge is no longer fully opaque, but has complex refractive index such that the exit wave is multiplied by the factor  $\exp(-d + i\phi)$  in the region  $x = -\infty$  to  $x = 0$ , the complex wavefield intensity will now be (Margaritondo and Tromba, 1999):

$$I(x, z) \propto |[\mathcal{C}(\infty) - C(u)] + i[S(\infty) - S(u)] + \exp(-d + i\phi) ([C(u) - \mathcal{C}(-\infty)] + i[S(u) - S(-\infty)])|^2. \quad (1.18)$$

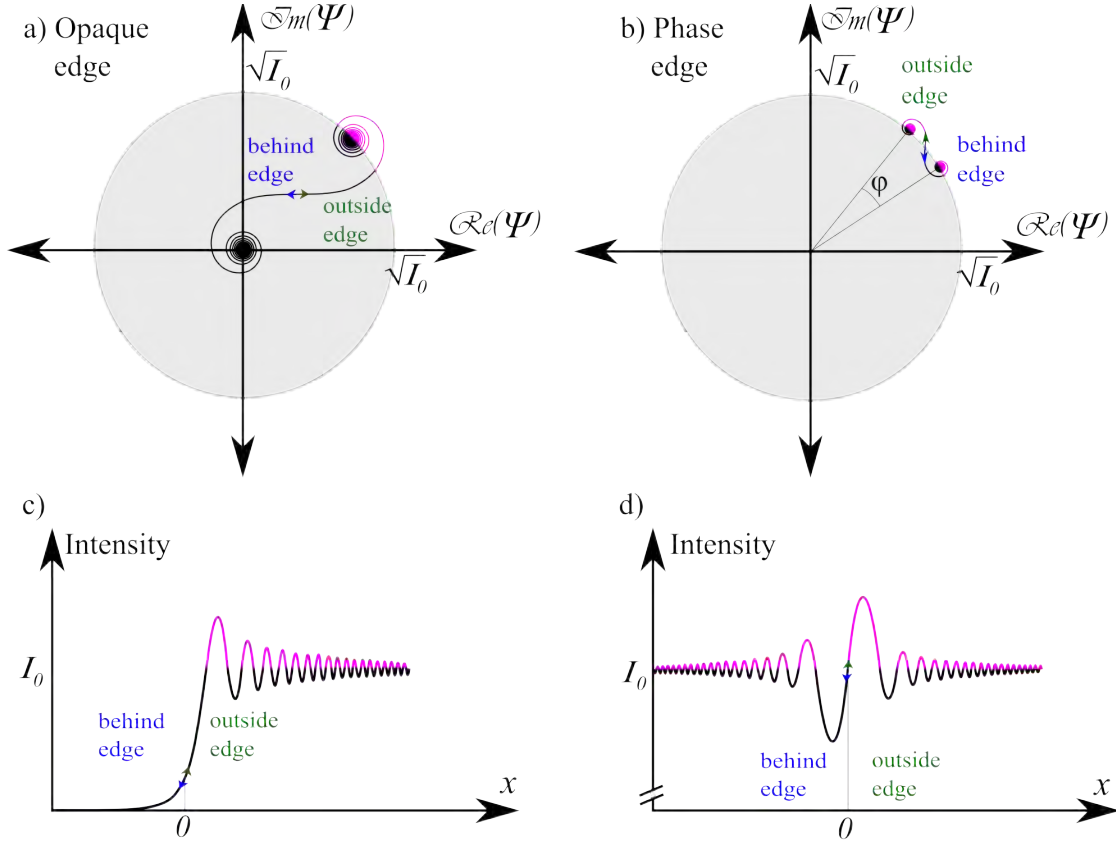


Figure 1.6: The Cornu spiral is transformed to describe the complex wavefield downstream of a) an opaque edge and b) a phase edge. Note that the “starting” phase (the centre of the spiral outside the edge) will rotate around the origin with each  $\lambda$  of propagation. The resulting intensity is then shown for c) an opaque edge and d) a phase edge.

Assuming that both  $\phi$  and  $d$  are small in magnitude compared to 1, so  $\exp(-d + i\phi) \approx 1 - d + i\phi$ , and looking at phase effects only, Eqn. 1.18 becomes  $I(x, z) \propto [ -\phi S(u) + 1 - \phi/2 ] + i[\phi C(u) + 1 + \phi/2]^2$ . This corresponds to rotating the Cornu spiral of Fig. 1.5 by  $\pi/2$ , scaling by  $\phi$  and shifting by  $(1 - \phi/2)$  along the real axis and  $(1 + \phi/2)$  along the imaginary axis, producing the complex field plot shown in Fig. 1.6 b). Using the same approximation ( $|\phi|, |d| \ll 1$ ), and looking at both phase effects and attenuation, the evaluated intensity will simplify to (Margaritondo and Tromba, 1999):

$$I(x, z) \propto 1 - d + \phi[C(u) - S(u)] - d[C(u) + S(u)]. \quad (1.19)$$

Again, if attenuation by the sample may be neglected (taking  $d = 0$ ), this means the intensity at a given point in the image plane will be greater or less than  $I_0$  depending on  $C(u)$  and  $S(u)$ . The intensity will therefore be greater than  $I_0$  where the spiral is pink in Fig. 1.6 b), which corresponds to the pink region  $C(u) > S(u)$  in Fig. 1.5, and the intensity will be less than  $I_0$  where each spiral is black ( $S(u) > C(u)$ ). This results in the intensity profile seen in Fig. 1.6 d).

If attenuation ( $d$ ) is significant, this will simply decrease the intensity behind the edge, hence pull the corresponding part of the Argand plot in towards the origin.

In Chapters 2 and 3, this Argand plane visualisation of the wavefield downstream of an edge is considered for a cylindrical or rounded edge. This effectively means that the phase shift incurred

behind the edge,  $\phi$ , will now be an increasing function of  $x$  across the imaging plane, hence will draw out that half of the Cornu spiral around the unit circle (Morgan et al., 2010b,c).

#### 1.1.1.4 Phase Retrieval from Propagation-Based PCXI

This understanding of how a wavefield evolves with propagation may then be used to attempt the associated “inverse” problem; reconstructing the complex wavefield at the sample exit surface using intensity images taken after propagation (see Fig. 1.3). Specifically, reconstruction of the phase variations incurred by the sample using only the diffraction pattern(s) is desired. Given that only the intensity of the wave may be recorded by the detector and not the phase, this means that in general, if both phase and intensity images are to be reconstructed at the sample exit surface, two intensity images are required as a necessary condition to provide a well-posed problem. Alternatively, constraints such as the refractive index and position of the sample may be sufficient to reduce the number of unknowns. Methods of phase retrieval have a longer history than x-ray phase contrast imaging, and fall into several categories.

Firstly, an iterative method may be applied, such as the Gerchberg–Saxton algorithm (Gerchberg and Saxton, 1972), which repeatedly applies known constraints until convergence is reached. This method uses two images to reconstruct the complex wavefunction; the Fraunhofer diffraction pattern (given by squaring the absolute value of the Fourier transform of the wavefunction) and the exit surface wave intensity. The method begins with an estimate of the sample exit plane wavefunction, then calculates what the resulting Fourier transform would be given this estimate for the wave-function. The amplitude of this is then corrected using the square root of the known intensity in Fourier space (*i.e.* the measured Fraunhofer diffraction pattern) and the resulting exit plane wavefunction calculated via inverse Fourier transform. This process is repeated until the solution ceases to change significantly upon further iteration, providing an image of the phase of the exit surface wavefunction as well as the known intensity image. The inability of the algorithm to converge for all cases has required adjustments to the method (Fienup, 1982). Similarly, Misell’s method (Misell, 1973) iterates between two planes separated by a given distance where each is “defocused”, rather than using the far field image. Although these methods may have demanding requirements in terms of known constraints and computation time, the numerical simplicity and stability is advantageous. The field of coherent diffractive imaging (CDI) uses a similar idea for phase-amplitude retrieval from far-field data, as first experimentally achieved by Miao *et al.* (Miao et al., 1999; Williams et al., 2006). The technique has since pushed far beyond the phase retrieval methods described above and there is a wealth of literature on this area of research. For a recent review see Quiney (Quiney, 2010).

A second group of phase retrieval methods are non-iterative and come from the transport-of-intensity equation (TIE). This results from substituting  $\psi = \sqrt{I(x, y, z)} \exp(i\phi(x, y, z))$  into Eqn. 1.5, the homogeneous paraxial equation, before separating out the imaginary part to give (Teague, 1983):

$$\nabla_{\perp} \bullet (I(x, y, z) \nabla_{\perp} \phi(x, y, z)) = -k \frac{\partial I(x, y, z)}{\partial z}. \quad (1.20)$$

A numerical solution to the TIE equation may be found (Gureyev et al., 1995) by solving the differential equation for unknown  $\phi$  using images taken at two propagation distances. Several ways

in which to do this, with various constraints, have been described in the literature. These include papers by Gureyev, Paganin *et al.* (Gureyev *et al.*, 1999; Paganin and Nugent, 1998), where again in order to retrieve both an intensity image and a phase image, at least two measured intensity images are required at differing propagation distances, so that the derivative of the field intensity with respect to the propagation distance may be calculated (Cloetens *et al.*, 1999). This type of phase retrieval algorithm has also been extended to include non-idealised imaging conditions, including partially coherent x-rays and an imaging system with a finite point-spread function (Gureyev, 1999; Gureyev *et al.*, 2004b, 2005). Alternatively two different energies may be used instead of two propagation distances, since the propagation distance is multiplied by the wavelength in TIE-based retrieval calculations (Gureyev *et al.*, 2001).

Gureyev has also investigated a combination of the above two phase-retrieval approaches, using a multi-scale algorithm where a TIE approach is used for large scale features and the Gerchberg–Saxton approach resolves small scale features (Gureyev, 2003). Approaches to the inverse problem using each of the first Born and Rytov approximations have also been presented (Gureyev *et al.*, 2004a).

The need for two intensity images may be relaxed if sufficient assumptions can be made regarding the sample. For example, if a single-material object is imaged, with both  $\beta$  and  $\delta$  known, a single defocused image is sufficient to produce both a phase and intensity image at the sample exit surface (Paganin *et al.*, 2002). Similarly, if the sample is known to change only the phase of the wave, one image is sufficient (Nugent *et al.*, 1996; Gureyev and Nugent, 1997).

Weak phase objects, where the phase changes are much less than 1 radian in magnitude, allow other methods of phase retrieval, such as those which use the contrast transfer function, which may also be combined with a TIE approach (Turner *et al.*, 2004; Gureyev *et al.*, 2004c; Guigay *et al.*, 2007). This  $|\phi| \ll 1$  restriction on the phase change, due to a sample of thickness  $T$ , using the projection approximation for a single material, then dictates  $k\delta T \ll 1$ , which in the case of hard x-rays on tissues (*i.e.*  $k \approx 10^{11} \text{m}^{-1}$  and  $\delta \approx 10^{-7}$ ) requires  $T \ll 0.1$  millimetre. This is not true in the case of centimetre-sized animals, hence these methods are not applicable to our studies.

Propagation-based phase contrast is used in this project, given the suitability to a live-imaging experimental set-up and the ability to enhance edges in all orientations. The remaining methods of phase contrast imaging are given a qualitative overview in sections 1.1.2-1.1.5, attempting to convey the essence of the techniques without taking on the mathematics of the theoretical basis or detailing the methods of analysis.

### 1.1.2 Analyser-Based Phase Contrast Imaging

Another method of phase contrast imaging is analyser-based phase contrast (AB-PCXI), also known as diffraction enhanced imaging (DEI). This method was initially shown with a conventional source by Förster *et al.* in 1980 (Förster *et al.*, 1980), then demonstrated with synchrotron radiation around the same time as propagation-based PCXI (Ingal and Beliaevskaya, 1995; Davis *et al.*, 1995a,b; Cloetens *et al.*, 1996; Chapman *et al.*, 1997).

The imaging set-up is typically as shown in Fig. 1.7, where a silicon crystal is now introduced after the sample, which will only maximally diffract rays incident at a particular angle (according to Bragg's law), to then be recorded by the detector. This means that if the sample introduces any

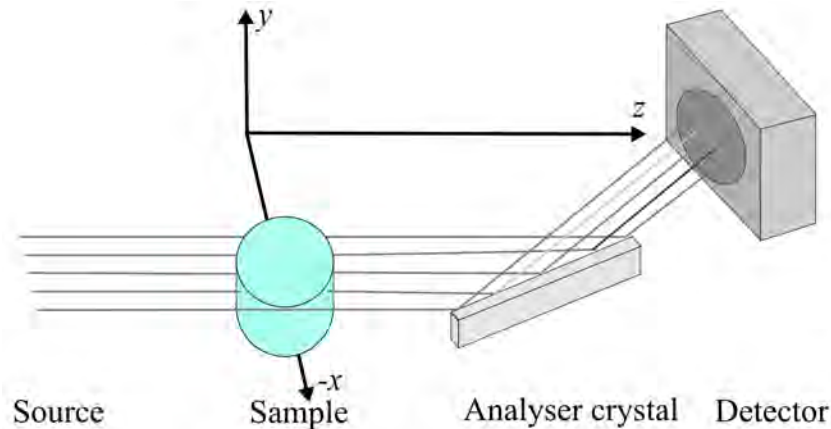


Figure 1.7: A typical analyser-based phase contrast imaging set-up, with waves propagating in the positive  $z$  direction.

deviation in the direction of the incident beam, more or less intensity will be diffracted from the analyser crystal, leading to transverse intensity modulations in the final image. The reflectivity of the analyser crystal, as a function of incident angle, is known as the “rocking curve”, with an idealised example shown in Fig. 1.8 (where the width is the order of tens of micro-radians). The “bandpass” (or “Darwin width”) of the rocking curve can be selected by using different diffraction planes and/or crystal cuts.

The crystal may be positioned so that the ray angle incident on the crystal occupies the point of highest gradient on the curve to maximise contrast (*e.g.*  $\theta_L$  in Fig. 1.8). For the sample projected thickness shown in Fig. 1.8 *a*), it can be seen in Fig. 1.8 *b*) that the resulting diffracted intensity is lower on the right of each feature in the sample, where the sample has refracted the rays to an angle further below the rocking curve peak, which is not as efficiently reflected by the analyser crystal. The left part of each sample shows an increase in the observed intensity, where the rays are refracted by the sample such that the angle of incidence sits further up the rocking curve, where they reflect more efficiently from the analyser crystal. If the analyser crystal is instead positioned such that unrefracted rays are incident at an angle greater than the rocking curve peak (*e.g.*  $\theta_H$ , Fig. 1.8 *c*)), the reverse is true, and the direction of contrast reversed.

There is a direction bias in the imaging method, since the analyser crystal predominantly diffracts in one plane only. Therefore the edges of samples will be more or less enhanced, depending on their orientation (Cloetens et al., 1996), as seen in Fig. 1.8. Here the features of the sample which sit at 45 degrees shows less contrast than vertical components, and the horizontal feature below the sphere is only visible at the right and left edges, where a horizontal phase gradient exists (*cf.* Fig. 1.2). However, this method of phase contrast is advantageous compared to propagation based PCXI in terms of sensitivity to very small variations in the refractive index of a sample.

Knowledge of the rocking curve of the analyser crystal will also enable quantitative reconstruction of the complex wave at the exit plane of the sample. This was first done by Chapman *et al.* (Chapman et al., 1997), taking an image from each side of the rocking curve and using a geometrical optics approach. The retrieved exit intensity  $I_{exit}$  and refraction angle  $\Delta\theta$  will then be given by (Chapman et al., 1997):

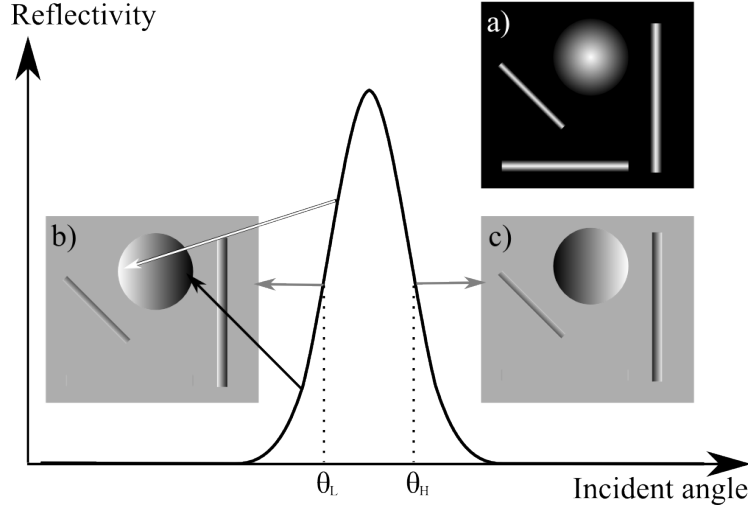


Figure 1.8: An idealised rocking curve for an analyser crystal as used in AB-PCXI, with *a*) sample projected thickness producing example images taken *b*) on the left and *c*) on the right of the rocking curve peak.

$$I_{exit} = \frac{I_L \frac{dR(\theta_H)}{d\theta} - I_H \frac{dR(\theta_L)}{d\theta}}{R(\theta_L) \frac{dR(\theta_H)}{d\theta} - R(\theta_H) \frac{dR(\theta_L)}{d\theta}}, \quad (1.21)$$

$$\Delta\theta = \frac{I_H R(\theta_L) - I_L R(\theta_H)}{I_L \frac{dR(\theta_H)}{d\theta} - I_H \frac{dR(\theta_L)}{d\theta}}. \quad (1.22)$$

Here  $I$  indicates intensity,  $R$  the rocking curve relative diffracted intensity, and  $\theta$  the incident angle, where subscripts  $L$  and  $H$  refer to the positions sitting lower and higher than the peak angle on the rocking curve (see Fig. 1.8).

The set-up initially described is known as using the crystal in a Bragg configuration, where the crystal is used to reflect the beam. Alternatively, the analyser crystal may be placed in a Laue configuration, where the beam is instead diffracted through the crystal, as well as transmitted, in order to create phase contrast.

### 1.1.3 Interferometric Phase Contrast Imaging

The third method described here, interferometry, is the earliest used method of achieving x-ray phase contrast. Contrast is achieved by looking at the interference pattern between a reference wavefield and a wavefield which passes through the sample, from the same source. This can be achieved using a Bonse–Hart interferometer (Bonse and Hart, 1965), as seen in Fig. 1.9. Three crystal blades from the same monolithic block are used to first split the beam into two (Crystal 1), secondly to reflect the two beams back towards each other (Crystal 2) and thirdly to analyse the resulting interference pattern (Crystal 3). The beam that has passed through the sample (the sample wave) will have incurred phase shifts which will then be visible in the final interference pattern (the coherent sum of the sample wave and the reference wave).

The phase map immediately after the sample may be retrieved from the resulting interference image, using the method described by Takeda (Takeda et al., 1982). This method works by shifting the spatial Fourier spectrum so that the frequency of the interference fringes is centred on the

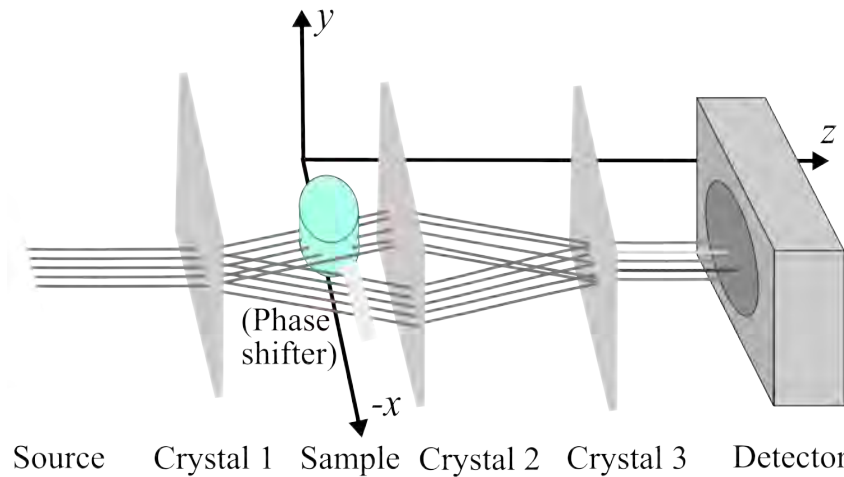


Figure 1.9: A typical interferometric-based phase contrast imaging set-up, with waves propagating in the positive  $z$  direction.

origin. A phase shifter may also be placed in the reference beam in order to avoid the difficulty of unwrapping the phase post-experiment (Momose, 2002). This phase shifter introduces a set phase lag to the reference wave, so that the bright/dark interference fringes may be shifted across the image to determine the sample exit-wave phase map.

Interferometry set-ups typically require highly stable crystals, making this method more difficult experimentally, and the size of the crystals used may impose restrictions in terms of the field of view (Takeda et al., 2000).

Alternative less-expensive interferometry set-ups have been shown, using a prism to refract half the beam and create two interfering beams downstream (Suzuki et al., 2002, 2010). This experimental arrangement is similar to that used in the coherence measurements of Chapter 4.

#### 1.1.4 Grating-Based Phase Contrast Imaging

Differential phase contrast may also be implemented using a series of gratings. As with analyser-based imaging, the grating set-up seeks to visualise the change in the direction of a ray as it refracts through the sample. As seen in Fig. 1.10, three gratings are typically used, with the sample placed between the first and second. The first grating serves to form a series of individually, but not mutually, coherent sources. The beam is then slightly refracted by the sample, before passing through the second grating. The configuration of the second and third gratings then analyses the change in ray angle to produce an intensity at the detector which is proportional to the sample phase gradient (Pfeiffer et al., 2006). This configuration is also known as a Talbot interferometer and the images may also be known as projection Moire images. The method requires scanning of the third grating over several exposures to obtain several differential phase maps that can then be used for phase retrieval.

This idea was demonstrated by Momose *et al.* (Momose et al., 2003), while David *et al.* showed a configuration with an analyser crystal in the place of the third grating (David et al., 2002). The technique was then applied at the Swiss Light Source and the European Synchrotron Radiation Facility in 2005 (Weitkamp et al., 2005; Pfeiffer et al., 2006), with quantitative reconstructions. The excellent sensitivity to phase gradients, particularly valuable in biological imaging, was shown by

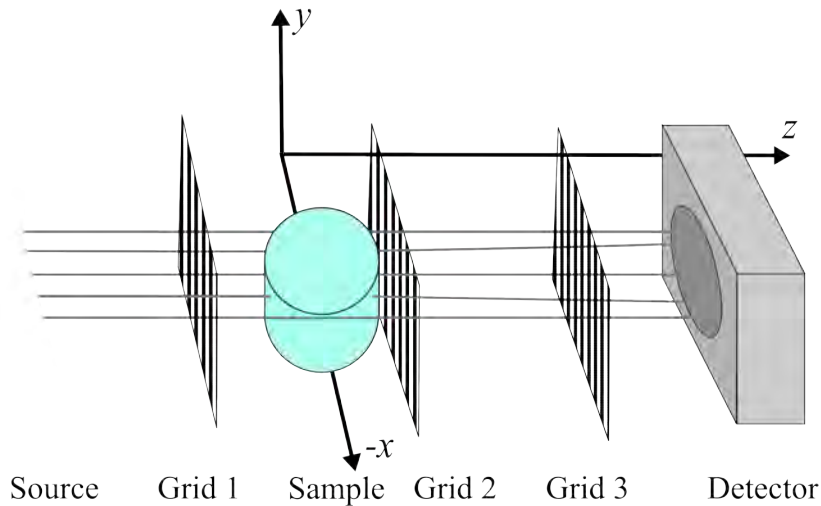


Figure 1.10: A typical grating-based phase contrast imaging set-up, with waves propagating in the positive  $z$  direction.

both groups (Momose et al., 2006; Pfeiffer et al., 2007; McDonald et al., 2009), including examples of tomographic imaging. The approach has since been extended in several different ways, such as taking measurements in two directions (Kottler et al., 2007) or using a multiline source in place of the first grating (Momose et al., 2009). Work has also been done using a conical beam to enlarge the image (Takeda et al., 2008; Yashiro et al., 2009). An approach using a single grating, scanned through 5 positions has been shown (Takeda et al., 2007), assuming a sinusoidal fringe profile. This requirement for multiple exposures may be an obstacle in live imaging, however the sensitivity to weak phase gradients makes this one of the most promising methods for imaging stationary samples.

### 1.1.5 Hybrid and Other Phase Imaging Methods

Combinations of several of these modalities, or variations on such ideas, have also been attempted, either to combine the advantages of multiple approaches or to take advantage of the characteristics of a particular sample.

The direction specificity of analyser based techniques may be lessened by combining analyser-based phase contrast imaging with propagation-based phase contrast imaging, realised by simply introducing a significant propagation between the sample and the crystal analyser (Pavlov et al., 2004; Coan et al., 2005).

Another method of visualising phase variations is that of Zernike phase contrast (Zernike, 1938, 1942). This works by effectively placing a phase-shifting, non-absorbing element near the origin of the Fourier space to introduce a phase bias upon the average component of a complex field (Schmahl et al., 1994; Neuhäusler et al., 2003). This is implemented in the x-ray region using a Fresnel zone plate before the sample and a micro zone plate and a nickel ring after the sample.

Some less-complex set-ups have been used to analyse the change in incident ray direction incurred by a sample. The distortion of a high contrast reference pattern by a phase sample has been studied first with visible light (Massig, 1999; Perciante and Ferrari, 2000) and then with x-rays

(Mayo and Sexton, 2004; Liu et al., 2008; Wen et al., 2010). It is upon this idea that the work of Chapter 7 is based.

A similar concept has been used in high-resolution phase contrast imaging using a scanning transmission x-ray microscope with steps (hence pixels) less than 100nm. The change in incident ray direction was measured using a multi-segment detector to determine the shift in the imaged intensity for a beam focused at each point within the sample (Feser et al., 2003; de Jonge et al., 2008).

Many of the aforementioned methods of producing phase contrast (Sections 1.1.1-1.1.4) have been used to enhance the contrast in computed tomography (CT) datasets (Kak and Slaney, 2001; Momose et al., 1995; Cloetens et al., 1996). The application of phase retrieval algorithms has proven valuable as a preliminary step to quantitative phase contrast CT slice reconstruction (Bronnikov, 2002; Beltran et al., 2010). There have also been developments using phase information to decrease the number of required projections for a CT slice reconstruction (Myers et al., 2007, 2008b,a).

## 1.2 Applications of PCXI

The penetrating power of x-rays and the sensitivity of phase contrast imaging to phase gradients incurred by similarly attenuating features of a sample has proven valuable in a number of different areas (Menk, 1999). As with conventional forms of x-ray imaging, there are many biomedical and biological applications, as well as materials and manufacturing uses. In this section, examples of recent work are described.

### 1.2.1 Biomedical and Biological Applications

The ability to image the internal structure of the body non-invasively has been of great value in medical practice and the transferral of phase contrast x-ray imaging into the clinic offers great potential (Thomlinson, 1992). Medical research has already benefited greatly from the ability provided by PCXI to examine anatomy and physiology in detail (Lewis, 2004) and to observe biological function *in vivo* (Fouras et al., 2009b). In this section we look first at PCXI as a tool to gain anatomical information and for enhanced disease detection, before describing new applications in functional physiology research.

Early biological phase contrast imaging applications predominantly looked at morphology, studying the structure of both bone and soft tissue. High resolution imaging and CT of bone and cartilage structure have been the focus of several experiments (Salomé et al., 1999; Mollenhauer et al., 2002; Coan et al., 2008). PCXI has proven particularly beneficial in soft tissue differentiation (Ingal and Beliaevskaya, 1997; Hwu et al., 2002; Lewis, 2004). This is directly applicable to cancer detection and monitoring, where the tissue density is altered by the presence of cancerous lesions. All the afore-mentioned methods of phase contrast imaging have been applied to the imaging of cancerous tissue, often combined with computed tomography (Momose et al., 1995; Bronnikov, 2002). Interferometry techniques have been tested by Momose *et al.* (Momose et al., 1998, 2001; Momose, 2002) on animal and human samples of cancerous tissues, and Takeda *et al.* used a triple Laue-case interferometer to successfully image carcinomas (Takeda et al., 2000, 2001). Lewis *et al.* demonstrated the biology visible in a range of organs, including the liver and kidneys, using analyser-based phase contrast (Lewis et al., 2002, 2003).

Analysar-based imaging was applied to mammography by Arfelli *et al.* and Ingal *et al.* (Arfelli *et al.*, 1998; Ingal *et al.*, 1998; Arfelli *et al.*, 2000), showing enhanced contrast of structure and calcifications, without increasing the radiation dose. Interferometric imaging of breast samples in a CT set-up has also shown increased visibility of features (Momose *et al.*, 1998; Takeda *et al.*, 1998). Research into PCXI mammography is continuing (Olivo *et al.*, 2009) and clinical trials using synchrotron radiation for *in vivo* patient imaging are underway (Castelli *et al.*, 2007; Tromba *et al.*, 2010).

Recent work using a grating interferometer set-up has shown very sensitive differentiation of soft tissue, with examples such as the detection of brain tumours (Pfeiffer *et al.*, 2007). The imaging of single cells and their structure is also now attracting attention (Hwu *et al.*, 2004), including their tomographic reconstruction and segmentation (Parkinson *et al.*, 2008).

Measures of dynamic biological function are now becoming possible, and offer great potential in medical research and the development of new treatment regimes (Fouras *et al.*, 2009b).

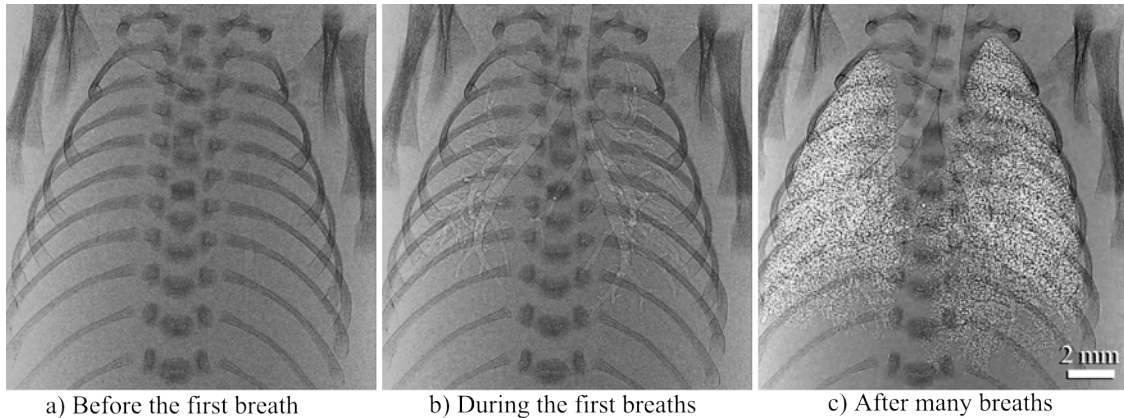


Figure 1.11: PB-PCXI of the lungs of a rabbit pup visualises the lungs when filled with air, seen here as a neonate rabbit *a*) first has lungs filled with liquid, then *b*) clears liquid from the lungs until *c*) the lungs fill with air. 24 keV x-rays are used with 3 metres propagation, imaged with 16.2  $\mu\text{m}$  pixels. Images courtesy of Marcus Kitchen, whose work is described and cited below.

Strong contrast has been observed from air to tissue interfaces, across which the real part of the refractive index differs significantly. Westneat *et al.* (Westneat *et al.*, 2003) utilised this to image the airways and observe the breathing cycle of insects. In vertebrates, this enables high-visibility images of the lungs when filled with air (Yagi *et al.*, 1999; Sera *et al.*, 2005; Lewis *et al.*, 2005), see Fig. 1.11. This ability has proven particularly valuable in visualising the intricate structure of the lungs when filled with air in 3 dimensions (Kono *et al.*, 2001; Schuster *et al.*, 2004). In particular this is of use in imaging the first breaths of infants, for the study of lung problems commonly associated with pre-term birth. Hooper, Kitchen, Lewis *et al.* have imaged mouse and rabbit pups in the minutes after birth, looking at ventilation strategies and successfully measuring lung volume through phase retrieval (Kitchen *et al.*, 2005b, 2007; Hooper *et al.*, 2007; Kitchen *et al.*, 2008; Hooper *et al.*, 2009; Kitchen *et al.*, 2010). The speckle pattern produced by the superposition of the many alveoli (air sacs) in the lungs, has also been a topic of interest (Kitchen *et al.*, 2004, 2005a). The position of this unique characteristic speckle pattern may be tracked during a breath cycle to study the dynamic movement of each region of the lungs, in studying lung function and injury (Fouras *et al.*, 2009a), by using particle image velocimetry (PIV).

The airways leading down to the lungs are also made visible through phase contrast imaging, and it is this application that is studied in this thesis. Both the nasal airways and the trachea may be observed, in projection and in CT (Siu et al., 2008; Parsons et al., 2008) (Appendices B and C). The *in vivo* imaging of an airway site over time (as described in Chapter 6) provides the ability to observe changes in an airway in response to treatments, and our work seeks particularly to enable immediate feedback on the effectiveness of therapies for the airway disease associated with cystic fibrosis. This may be either by tracking the ability of the airway to clear introduced debris (Donnelley et al., 2009, 2010b) (Appendices D and E) or by measuring the depth of the liquid lining of the airways (Morgan et al., 2009) (see Chapter 6 and Appendix 8).

Another application of live dynamic imaging is blood flow. While blood does not produce the same phase contrast with tissue as air does, the visibility of vessels is much improved over attenuation imaging alone. Most blood imaging methods require introduction of a contrast agent, such as iodine, which can give impressive visualisation, particularly when using subtraction imaging around the K-edge of the agent. Furthermore, Momose showed that phase information was sufficient to visualise blood vessels in an excised rat liver without contrast agent (Momose et al., 2000), and research has now advanced to imaging blood flow (Fouras et al., 2007; Irvine et al., 2008; Dubsky et al., 2010; Irvine et al., 2010). The superposition of many red blood cells produces a speckle pattern (see Fig. 1.12) to which PIV may be applied in order to map the speed and direction of blood flow.

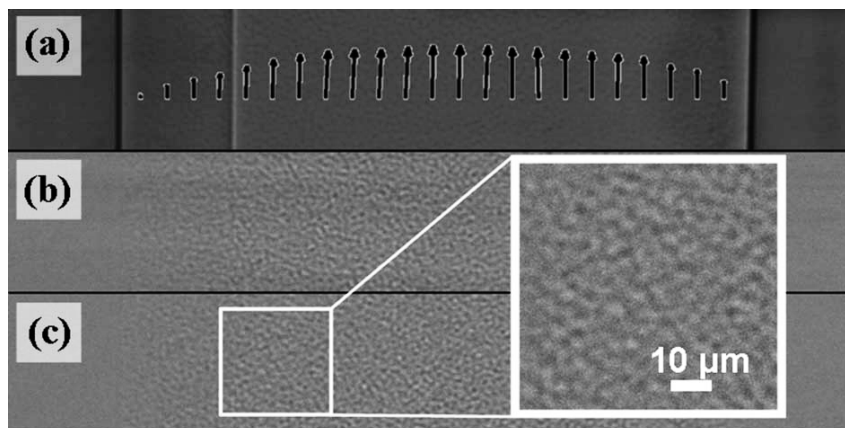


Figure 1.12: PB-PCXI of blood flowing in a tube enables retrieval of *a*) the velocity profile, given *b*) the speckle pattern produced by overlaid red blood cells, *c*) which is filtered to removed background beam and detector characteristics. Reprinted with permission from (Irvine et al., 2008). Copyright 2008, American Institute of Physics.

### 1.2.2 Other Applications of PCXI

While it is on biomedical applications that this thesis is focused, areas in materials and manufacturing can also benefit greatly from the advantages of phase contrast imaging (Menk, 1999; Hwu et al., 2002; Stevenson et al., 2003). The edge sensitivity of propagation based PCXI is valuable in detecting strain cracks (Cloetens et al., 1997) and microscopic damage (Cloetens et al., 1997; Buffière et al., 1999). Phase contrast has also been used to look at the results of manufacturing processes, such as the evenness of coatings (Kashyap et al., 2007) or fuel capsule wall thicknesses

(Kozioziemski et al., 2005). Similarly, tomographic imaging means that three dimensional studies of manufactured materials are possible, for example, imaging a polymer fleece with  $4.9 \mu\text{m}$  voxels in order to look at density, structure and connectedness (Cloetens et al., 2002).

## 1.3 Coherence considerations for PCXI

### 1.3.1 Introduction

Most forms of phase contrast imaging require a wavefield with a high degree of spatial or temporal coherence (Zernike, 1938). Specifically, examining complex biological interfaces using propagation-based PCXI requires a high degree of spatial coherence in order to produce high-contrast phase contrast fringes and achieve quantitative PCXI. Multiple fringes will otherwise be blurred or perhaps not even resolved.

The coherence of a wavefield describes the degree of statistical similarity or correlation within the wavefield. The descriptions of phase imaging up until this point in the thesis have assumed a fully monochromatic, coherent wavefield, and although synchrotron sources generally provide a very high degree of spatial and temporal coherence, in experiment this assumption will not always hold. Quantitative measures of coherence are therefore important in the design of coherent x-ray experiments (Kohn et al., 2000).

A high temporal/longitudinal coherence, or a long coherence time, corresponds to a narrow band of wavelengths, as stated in Eqn. 1.23 (Wolf, 2007);

$$\Delta l = \frac{2\pi c}{\Delta\omega} = \frac{\bar{\lambda}}{\Delta\lambda} \bar{\lambda}, \quad (1.23)$$

where  $\Delta l$  is the coherence length,  $\bar{\lambda}$  is the mean wavelength and  $\Delta\lambda$  is the range of wavelengths. In the second term of Eqn. 1.23,  $c$  is the speed of light and  $\Delta\omega$  is the spread in  $\omega = ck$  (the frequency of oscillation), converting the time delay ( $= 2\pi/\Delta\omega$ ), introduced by the spread of wavelengths, into a distance (Wolf, 2007).

When imaging with hard x-rays from a synchrotron source, high temporal coherence is usually obtained using a crystal monochromator. Propagation-based phase contrast has less stringent requirements on temporal coherence than spatial coherence, so may be realised with a laboratory microfocus source that produces a greater spread of wavelengths (Wilkins et al., 1996). When the wavelength is altered the point of steepest intensity gradient, between the central bright and dark fringes, will not move in position, hence a range of wavelengths will only smear out the narrow fringes further from the centre of the interface fringe set.

For propagation-based PCXI, the spatial coherence of the incident field will have a much greater effect on the quality of phase contrast x-ray images. Measures of transverse spatial coherence typically are made by looking at the interference pattern created using two transversely separated points across the wavefield (see Fig. 1.13). A measure of the distance across which the points are no longer sufficiently correlated to produce interference fringes is then known as the coherence width. In general, the transverse coherence width from a delta-correlated source will be taken as (Mandel and Wolf, 1995);

$$C \propto L\Delta\theta = \frac{\lambda L}{S}, \quad (1.24)$$

where  $C$  is the transverse distance defining the coherent width,  $L$  is the distance from the source,  $\Delta\theta$  is the angle across which the source is considered and  $S$  is the source dimension, as shown in Fig. 1.13. This means that in practice a greater coherence length may be obtained by either moving further from the source (in accordance with the Van Cittert-Zernike theorem, Eqn. 1.35 (van Cittert, 1934, 1939; Knox et al., 2010)) or by inserting an aperture to decrease the observed source size (Born and Wolf, 1999).

### 1.3.2 Coherence Theory

In order to measure this transverse coherence width, a set-up as shown in Fig. 1.13 is considered, where two pinholes,  $P_1$  and  $P_2$ , allow light from source  $S$  through, interfering at point  $P$  in the image plane (Born and Wolf, 1999). At the image plane bright/dark interference fringes will be observed, provided the distance between  $P_1$  and  $P_2$  is less than the coherence width (Eqn. 1.24).

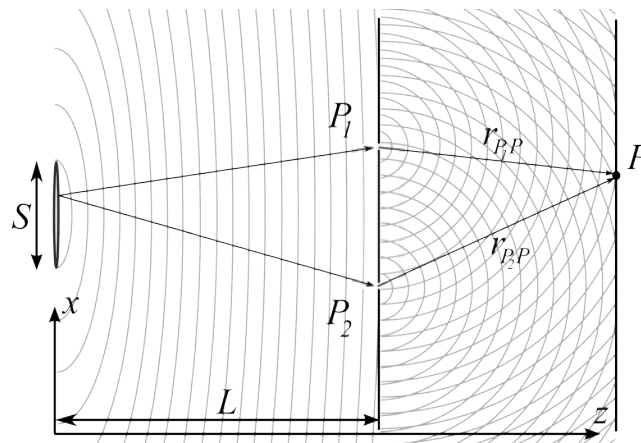


Figure 1.13: A Young's double pinhole set-up, used to measure the coherence  $L$  metres from source  $S$ , at the pair of pinholes  $P_1$  and  $P_2$ , by looking at the interference pattern observed for all points  $P$  across the image plane.

How visible these fringes are may be quantified by Michelson's measure of visibility,  $\mathcal{V}$ , using the maximum ( $I_{max}$ ) and minimum ( $I_{min}$ ) intensities (Michelson, 1995);

$$\mathcal{V} = \frac{I_{max} - I_{min}}{I_{max} + I_{min}}. \quad (1.25)$$

The magnitude of the degree of coherence between the points  $P_1$  and  $P_2$  is defined by this visibility,  $\mathcal{V}$ , of the interference fringes created by the field passing through  $P_1$  and  $P_2$  (Zernike, 1938). As shown in Fig. 1.14, visibility will be equal to 1 for maximum visibility fringes (created by fully coherent light) and 0 for no visible fringes (created by fully incoherent light). If the light is partially coherent, fringes will be observed, but with a non-zero visibility less than 1.

This experimental observation may then be linked to the relationship between the statistical similarity of the x-ray disturbances at the two points,  $P_1$  and  $P_2$ . Such an analysis is called second-order coherence theory, in that the relationship between two points is being studied. A given realisation of the incident complex wavefield will show random fluctuations in time and space, due to the nature of the source. The associated stochastic process is taken to be statistically stationary, in that changing the origin of time will not change the outcome. It is further considered to be ergodic, in that all ensemble averages may be replaced by the corresponding time averages.

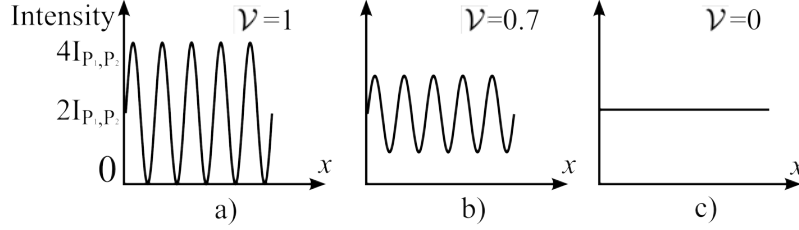


Figure 1.14: Interference fringes from the set-up shown in Fig. 1.13 range in visibility from 0 to 1, depending on the absolute value of the complex degree of coherence. This assumes the intensity incident at each pinhole is the same.

Given monochromatic light illuminating two pinholes  $P_1$  and  $P_2$  (as in Fig. 1.13), with wavefields  $\Psi(P_1, t)$  and  $\Psi(P_2, t)$  respectively, a cross correlation may be performed to calculate the statistical similarity of the two (note that angular brackets correspond to an ensemble average, which is a time average in this case, since ergodicity is assumed);

$$\Gamma(P_1, P_2, \tau) = \langle \Psi^*(P_1, t) \Psi(P_2, t + \tau) \rangle. \quad (1.26)$$

This measure,  $\Gamma(P_1, P_2, \tau)$  is called the mutual coherence function, where  $\tau$  is the difference in time taken to traverse the path from  $S$  to  $P$ , through  $P_1$  or  $P_2$ . If the light from the two points then interferes, the resulting intensity, averaged over time and assuming the field is statistically stationary, is:

$$I(P) = I_{P_1}(P) + I_{P_2}(P) + 2\mathcal{R}e \left( \sqrt{I_{P_1}(P)} \sqrt{I_{P_2}(P)} \gamma(P_1, P_2, r_{P_1P}/c - r_{P_2P}/c) \right), \quad (1.27)$$

where  $\mathcal{R}e$  indicates taking the real part and  $\gamma$  is the complex degree of coherence,

$$\gamma(P_1, P_2, \tau) = \frac{\Gamma(P_1, P_2, \tau)}{\sqrt{\Gamma(P_1, P_1, 0)} \sqrt{\Gamma(P_2, P_2, 0)}} = \frac{\Gamma(P_1, P_2, \tau)}{\sqrt{I(P_1)} \sqrt{I(P_2)}}. \quad (1.28)$$

This forms the link back to Eqn. 1.26, the mutual coherence function, describing the similarity of the wavefields at  $P_1, P_2$ . From Eqn. 1.27, moving the point  $P$  transversely across the imaging plane, one will therefore observe an average intensity equal to the sum of intensities from each of  $P_1$  and  $P_2$ , with sinusoidal intensity fringes superimposed. If the small angle approximation is taken and it is assumed that the average intensity is the same at each of the pinholes, the magnitude of these fringes around the average intensity will be proportional to  $|\gamma(P_1, P_2, \tau)|$  and may be described in terms of visibility, since;

$$\mathcal{V} = |\gamma(P_1, P_2, \tau)|. \quad (1.29)$$

As described earlier, the measure of visibility of interference fringes,  $\mathcal{V}$ , expresses the degree of coherence (Zernike, 1938). Therefore if the wavefields from each of the points are strictly monochromatic and therefore perfectly correlated, the ensemble average  $\Gamma(P_1, P_2, \tau)$  (Eqn. 1.26) will become  $\psi^*(P_1)\psi(P_2)\exp(-i\omega\tau)$ , hence the absolute value of the complex degree of coherence,  $|\gamma(P_1, P_2, \tau)|$ , will equal 1, producing intensity fringes reaching from zero intensity to four times the intensity seen from each of  $P_1, P_2$  (Eqn. 1.27), as seen in Fig. 1.14 a). If the two wavefields are completely uncorrelated,  $\gamma$  will equal zero and fringes will not be observed, leaving an intensity

equal to the incoherent sum of the intensities from each of  $P_1, P_2$ , Fig. 1.14 c). Again, in the case of partial coherence, fringes will be seen (Fig. 1.14 b)), with non-zero visibility less than 1.

A study of the visibility,  $\mathcal{V}$ , as the two points  $P_1$  and  $P_2$  are slowly separated, will therefore determine a measure of the transverse coherence width, the limit to the distance between two points for which the field can be considered coherent.

The shape of this curve, visibility as a function of transverse distance between two points in the wavefield, will be determined by the shape of the source, although a larger synchrotron x-ray effective source size will correspond to a shorter coherence width. As seen in Fig. 1.15, a square source (*e.g.* defined by an aperture) will produce a sinc visibility curve, where the coherence width may be defined as the minimum distance at which fringes disappear (zero visibility). A narrow Gaussian source (*e.g.* the size of the electron beam at a synchrotron source) will produce a wide Gaussian visibility curve, for which the coherence width is defined as the distance at which the fringe visibility falls to a certain percentage of the maximum (*e.g.*  $e^{-1}$ ). Ways of measuring this fringe visibility curve are described in section 1.3.3.

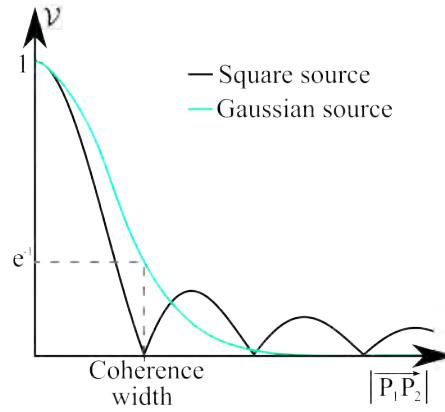


Figure 1.15: Visibility characteristic for a Gaussian and a square source, of the same coherence width  $C$ , as the points  $P_1$  and  $P_2$  are moved apart.

It is also important to look at how the degree of coherence changes with propagation. The mutual coherence function,  $\Gamma$ , for quasi-monochromatic light, may be expressed in terms of a mutual intensity,  $J(P_1, P_2)$ , as below, where  $\bar{\omega}$  is the average angular frequency:

$$\Gamma(P_1, P_2, \tau) = J(P_1, P_2)e^{-i\bar{\omega}\tau}. \quad (1.30)$$

The Fourier transform of the mutual coherence function ( $\Gamma$ ), with respect to time lag  $\tau$ , will describe the cross spectral density and will be given by

$$W(P_1, P_2, \omega) = \mathcal{F}(\Gamma) = \frac{1}{2\pi} \int_{-\infty}^{\infty} \Gamma(P_1, P_2, \tau) \exp(i\omega\tau) d\tau = \langle \psi^*(P_1, \omega), \psi(P_2, \omega) \rangle. \quad (1.31)$$

For a wavefield,  $\Psi(x, y, z, t)$ , which satisfies the wave equation ( $\nabla^2\Psi(x, y, z, t) = \frac{1}{c^2} \frac{\partial^2\Psi(x, y, z, t)}{\partial t^2}$ ), the associated mutual coherence function,  $\Gamma$ , will also satisfy the homogeneous Helmholtz equation (Eqn. 1.9), with the Laplacian now with respect to each of  $P_1$  or  $P_2$  (written as  $\nabla_1^2$  and  $\nabla_2^2$  respectively) for a statistically stationary field, resulting in the two Wolf equations, Eqn. 1.32 and Eqn. 1.33 (Wolf, 1954),

$$\left(\frac{1}{c^2} \frac{\partial^2}{\partial \tau^2} - \nabla_1^2\right) \Gamma(x_1, x_2, \tau) = 0, \quad (1.32)$$

$$\left(\frac{1}{c^2} \frac{\partial^2}{\partial \tau^2} - \nabla_2^2\right) \Gamma(x_1, x_2, \tau) = 0. \quad (1.33)$$

As a consequence, the cross spectral density ( $W$ ) and the mutual intensity ( $J$ ) will also both obey the homogeneous Helmholtz equation (Eqn. 1.9).

In order to propagate the cross spectral density,  $W$ , each realisation  $\psi$  must be propagated as below, where  $A_1$  and  $A_2$  are points in the  $z = 0$  plane, as are  $x'_1$  and  $x'_2$  (with source points at  $z < 0$ ), and  $r$  indicates the distance between the subscripted points. This leads to (Mandel and Wolf, 1995),

$$W(P_1, P_2, \omega) = \frac{1}{(2\pi)^2} \iiint W(x'_1, x'_2, \omega) \left[ \frac{\partial}{\partial z_1} \frac{\exp(ikr_{A_1 P_1})}{r_{A_1 P_1}} \right] \times \left[ \frac{\partial}{\partial z_2} \frac{\exp(ikr_{A_2 P_2})}{r_{A_2 P_2}} \right] dx'_1 dx'_2. \quad (1.34)$$

If the incident field is a monochromatic plane wave, so may be taken to be paraxial, originating at  $z = 0$  from a delta correlated source<sup>5</sup>, we then arrive at the van Cittert–Zernike theorem (van Cittert, 1934; Zernike, 1938; van Cittert, 1939):

$$J(P_1, P_2) = \frac{k^2}{(2\pi)^2} \iint I(x'_1) \frac{\exp(ik(r_{A_1 P_1} - r_{A_1 P_2}))}{r_{A_1 P_1} r_{A_1 P_2}} dx'_1 \quad (1.35)$$

Here,  $I(x'_1) = J(x'_1, x'_1)$  indicates the intensity at each point  $x'_1$  in the plane  $z = 0$ . Note that the van Cittert–Zernike theorem (Eqn. 1.35) describes the propagation of the mutual intensity function satisfying the Wolf Equations (Eqn. 1.32, 1.33) in a similar way as the Rayleigh–Sommerfeld equation (Eqn. 1.12) describes the propagation of the wavefield satisfying the inhomogeneous Helmholtz equation (Eqn. 1.2). Just as diffraction from a small feature results in a large scale feature with significant propagation, a small source will result in a large coherent width with propagation. This links back to Eqn. 1.24, where the transverse coherence length is proportional to propagation distance  $L$ .

### 1.3.3 Means of Measuring Coherence

Transverse coherence has traditionally been measured using a two-pinhole (or two-slit) interferometer as described in the previous section (Fig. 1.13), and was first realised with visible light by Young (Young, 1804). An experimental set-up, which directly implements this means of measuring coherence, must therefore provide variable separation of two precise slits. This method has successfully been used to measure the coherence of undulator x-rays (Paterson et al., 2001; Leitenberger et al., 2004), observing a transverse coherence distance slightly less than expected, due to speckle introduced by optical elements along the beamline.

A Hanbury Brown-Twiss intensity interferometer has also been used for precise measures of transverse coherence at SPring-8 (Yabashi et al., 2001), but does require a high precision diffractometer and high resolution monochromator. The analysis of the Fresnel diffraction patterns of fibres or slits (as interferograms) (Kohn et al., 2000; Gureyev et al., 2001) has recently been

<sup>5</sup>A delta correlated source has the radiation uncorrelated, at any pair of distinct points on the source.

used to measure the coherence width at the Australian Synchrotron Imaging and Medical Beamline (Stevenson *et al.*, 2009). Lin *et al.* have shown measurements with a uniformly redundant array (URA) acting as a complex phase mask to diffract the incident beam equivalently to the parallelized superposition of multiple Young's experiments (Lin *et al.*, 2003).

Alternatively, the incident beam may be divided into two using a prism to refract half the beam to interfere with the other half (Suzuki, 2004). This is the method used in Chapter 4 (Morgan *et al.*, 2010a). This paper specifically looks at the decrease in the absolute value of the complex degree of coherence observed when a spinning random-phase-screen diffuser is introduced (used to create a more even wavefield (White *et al.*, 1994)). While this decrease is seen due to time averaging, decoherence may also be observed as a result of imperfections in optical elements such as mirrors and windows (Vartanyants and Robinson, 2003; Robinson *et al.*, 2003). This is often seen as a result of spatial averaging where the detector pixels are larger than the wavefield features (Nugent *et al.*, 2003). This will have an effect on the ability of analyser and propagation based phase contrast imaging to resolve small features (Nesterets, 2008).

## 1.4 Thesis Overview

Chapters 2 and 3 are comprised of two papers published in *Optics Express* and *Optics Communications*, looking at the modelling of edge contrast created using PB-PCXI (Morgan *et al.*, 2010b,c). A cylindrical edge model is taken, which may be used to describe an ideal airway, or may be adapted (by selection of radius or by using several cylinders) to describe many different edges. Soft biological interfaces may therefore be well-described, as well as manufactured materials. In the first paper, included as Chapter 2, results from the commonly-used projection approximation (§1.1.1.2) in modelling PB-PCXI fringes are compared to experimental images to illustrate the inability of the projection approximation to describe diffraction within the sample volume. However, it is seen with propagations sufficiently larger than the sample volume that the projection approximation model accurately predicts phase contrast. Furthermore, the paper studies the Argand-plane signature (§1.1.1.3) of a propagation-based phase contrast fringe from a rounded edge.

Chapter 3 looks further at the Argand-plane signature, comparing plots given by the projection approximation model to those given by an exact solution to a plane wave incident on a cylinder. The results confirm the accuracy of the projection approximation for propagations that are large compared to the sample volume. It is then shown mathematically that the exact solution becomes the projection approximation at the centre of the cylinder. A discussion on the hierarchy of complexity of optics models follows. These two papers verify the computational model used for the remainder of the thesis and establish an understanding for the shape and behaviour of phase contrast fringes created by an interface of given curvature.

Work then moves on to experimental observation of these interface phase contrast fringes, and how such fringes may be optimised for visibility in order to reveal interfaces between similar media. Chapters 4 and 5 are the result of a joint investigation with Sarah Irvine<sup>6</sup> published in *Optics Communications* and *Optics Express*, looking at the fringe-dampening effect of a spinning random-phase-screen diffuser in propagation-based phase contrast imaging (Morgan *et al.*, 2010a;

---

<sup>6</sup>At the time of writing, Sarah Irvine was a post-graduate student at the School of Physics, Monash University, studying for her PhD in studies on speckle x-ray imaging. Both papers were published as joint-first-author publications.

Irvine et al., 2010). Given that the visibility of a phase contrast fringe will depend upon the transverse coherence of the x-ray source used, the image of an interface may be enhanced through optimisation of the experimental coherence. As seen in equation 1.24, this may be done by increasing the distance from the source or by decreasing the observed source size (§1.3). Chapter 4 looks at how the complex degree of second-order coherence of the beam (Eqn. 1.28) may also be affected by the choice and positioning of a spinning phase diffuser, commonly used to diffuse the x-ray field and create a more uniform, broader beam intensity. The paper reports on a set of measurements taken at two positions on beamline BL20XU at the SPring-8 synchrotron, the x-ray source used for most experimental components of this thesis. Numerical simulations of the prism interferometer, while varying the source size and shape, and while moving the diffuser in or out, are also detailed and compared with experimental results.

Chapter 5 then looks at the implications of reduced coherence due to a diffuser for propagation-based phase contrast imaging. Simulation and experiment show the fringe-dampening effect of a diffuser, with less of an effect for greater propagation between the diffuser and the sample. Further modelling of the diffuser material describes how the characteristic phase depth and length of the material will affect visibility of the entire fringe set as well as individual fringes from an interface. Finally, repositioning of the diffuser to immediately after the source is theoretically and experimentally shown to have minimal effect on the transverse coherence, hence PB-PCXI fringe visibility, while still diffusing the x-ray beam.

These conclusions from Chapters 4 and 5 describe how to increase the visibility of interface fringes studied in Chapters 2 and 3; imaging with the diffuser close to the source, the sample far from the source, and the smallest practical aperture after the source, while maintaining sufficient counting statistics.

Chapter 6 applies these optimisations to the observation of the liquid layer inside biological airways using PB-PCXI. The ability to non-invasively assess the depth of this layer would be key in the assessment of new treatments for the airway disease associated with cystic fibrosis, where a shallower depth is typically observed. While the air-to-liquid interface is easily visible, the liquid-to-tissue interface does not create a strong fringe, particularly in a live animal. Several approaches to this problem, all using PB-PCXI, are detailed. This includes approaches to maximising the visibility of interfaces in experiment (following on from Chapters 4 and 5) and in image analysis. The results motivate an even more sensitive method of measuring the phase gradient across the airway interface. Sections of the material in this chapter have been presented in talks by the author at the X-ray Micro and Nano Probes (XMNP) Meeting 2009 (Palinuro, Italy) and the Medical Applications of Synchrotron Radiation (MASR) Meeting 2010 (Melbourne, Australia).

Given the high sensitivity required to resolve these airway interfaces, Chapter 7 proposes a new method of x-ray phase imaging and analysis as accepted for publication (with revisions) by Optics Letters (Morgan et al., 2011). Aimed specifically at tracking a specific sample feature in live imaging, this method requires only a single exposure to retrieve phase information about the sample. Through the analysis of the shift of a high visibility reference pattern (designed for the sample feature in question), the method reveals weak phase gradients in high resolution. Experimental results using known phantoms validate the quantitative retrieval technique. The sensitivity of this new method is promising in terms of detecting the weak phase gradient at the liquid/tissue boundary investigated in Chapter 6.

The final section, Chapter 8, looks at possible areas of future research and draws together conclusions from this body of work.

---

## Numerical Modelling of Propagation-Based PCXI of Interfaces

---

*The projection approximation and edge contrast for x-ray propagation-based phase contrast imaging of a cylindrical edge.*

by K. S. Morgan, K. K. W. Siu and D. M. Paganin.

Published in Optics Express **18**, pp. 9865-9878, 2010.

Selected for the Virtual Journal for Biomedical Optics **5(9)**, 2010.

---

This chapter looks at modelling propagation-based x-ray phase contrast x-ray imaging (PB-PCXI) from a rounded edge. A curved interface is not only a good model for cylindrical objects (such as an airway, as described in Chapter 6), but also a good local model for many interfaces which are not perfectly square, *i.e.* various biological interfaces.

Results from the simulation model described in section 1.1.1.2 (where a wavefield was propagated through the sample using the projection approximation, then propagated to the image plane using the angular spectrum formalism) are compared to experimental PB-PCXI edges, taken at beamline 20XU of the SPring-8 synchrotron, to look at the validity of using the projection approximation to propagate the wavefield through the sample volume. It is seen that the simulation underestimates the width and intensity of phase contrast fringes at small propagation lengths, because the projection approximation does not describe diffraction and interference of initially adjacent rays. The complex wavefield in the Argand plane downstream of a curved edge is studied, following on from section 1.1.1.3, to illustrate this finding. Nevertheless, the simulation model is observed to correctly and efficiently predict the fringes observed in experimental images at significant propagation distances, as used in biomedical imaging (*e.g.* Chapters 5 and 6).

This verifies use of the simulation model (section 1.1.1.2) used in modelling the effect of a diffuser (Chapters 4 and 5) and in the application work of Chapter 6.

The modified Cornu spirals shown in this paper are not only of mathematical beauty, but may also be of use in the analysis of complex wavefields, for example using phase retrieval algorithms.

## Declaration for Thesis Chapter 2

In the case of Chapter 2, contributions to the work involved the following:

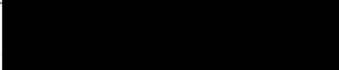
Name	% contribution	Nature of contribution
Kaye Morgan	90%	Led the original experiments, analysed the PCXI images, wrote the code for and analysed the numerical simulations, developed the theoretical aspects, worked through the mathematics of the appendix and wrote up the paper
Karen Siu		Contributed to the original experiments and theoretical discussions, provided supervisory advice, aided proofreading and drafting
David Paganin		Contributed to the theoretical discussions, provided supervisory advice, aided proofreading and drafting

### Declaration by co-authors

The undersigned hereby certify that:

1. the above declaration correctly reflects the nature and extent of the candidate's contribution to this work, and the nature of the contribution of each of the co-authors.
2. they meet the criteria for authorship in that they have participated in the conception, execution, or interpretation, of at least that part of the publication in their field of expertise;
3. they take public responsibility for their part of the publication, except for the responsible author who accepts overall responsibility for the publication;
4. there are no other authors of the publication according to these criteria;
5. potential conflicts of interest have been disclosed to (a) granting bodies, (b) the editor or publisher of journals or other publications, and (c) the head of the responsible academic unit; and
6. the original data are stored at the following location(s) and will be held for at least five years from the date indicated below: School of Physics and Monash Centre for Synchrotron Science, Clayton Campus, Monash University, Australia.

### Signatures:

Kaye Morgan:		Date: 19/10/10
Karen Siu:		Date: 19.10.2010
David Paganin:		Date: 18/10/10

---

This paper was published in Optics Express and is made available as an electronic reprint with the permission of OSA. The paper can be found at the following URL on the OSA website: <http://www.opticsinfobase.org/abstract.cfm?uri=oe-18-10-9865>. Systematic or multiple reproduction or distribution to multiple locations via electronic or other means is prohibited and is subject to penalties under law.

---

# The projection approximation and edge contrast for x-ray propagation-based phase contrast imaging of a cylindrical edge

K. S. Morgan<sup>1,\*</sup>, K. K. W. Siu<sup>1,2</sup> and D. M. Paganin<sup>1</sup>

<sup>1</sup>*School of Physics, Monash University, Victoria 3800, Australia*

<sup>2</sup>*Monash Centre for Synchrotron Science, Victoria 3800, Australia*

\**Kaye.Morgan@sci.monash.edu.au*

**Abstract:** We examine the projection approximation in the context of propagation-based phase contrast imaging using hard x-rays. Specifically, we consider the case of a cylinder or a rounded edge, as a simple model for the edges of many biological samples. The Argand-plane signature of a propagation-based phase contrast fringe from the edge of a cylinder is studied, and the evolution of this signature with propagation. This, along with experimental images obtained using a synchrotron source, reveals how propagation within the scattering volume is not fully described in the projection approximation's ray-based approach. This means that phase contrast fringes are underestimated by the projection approximation at a short object-to-detector propagation distance, namely a distance comparable to the free-space propagation within the volume. This failure of the projection approximation may become non-negligible in the detailed study of small anatomical features deep within a large body. Nevertheless, the projection approximation matches the exact solution for a larger propagation distance typical of those used in biomedical phase contrast imaging.

©2010 Optical Society of America

**OCIS codes:** (110.7440) X-ray imaging; (340.7440) X-ray imaging; (050.5080) Phase shift; (170.3880) Medical and biological imaging; (260.0260) Physical optics; (340.0340) X-ray optics.

---

## References and links

1. W. C. Röntgen, "On a new kind of rays," *Nature* **53**(1369), 274–276 (1896).
2. P. Cloetens, R. Barrett, J. Baruchel, J. P. Guigay, and M. Schlenker, "Phase objects in synchrotron radiation hard x-ray imaging," *J. Phys. D Appl. Phys.* **29**(1), 133–146 (1996).
3. A. Snigirev, I. Snigireva, V. Kohn, S. Kuznetsov, and I. Schelokov, "On the possibilities of x-ray phase contrast microimaging by coherent high-energy synchrotron radiation," *J. Phys. D Appl. Phys.* **29**, 133–146 (1995).
4. S. W. Wilkins, T. E. Gureyev, D. Gao, A. Pogany, and A. W. Stevenson, "Phase-contrast imaging using polychromatic hard x-rays," *Nature* **384**(6607), 335–338 (1996).
5. M. J. Kitchen, R. A. Lewis, M. J. Morgan, M. J. Wallace, M. L. Siew, K. K. W. Siu, A. Habib, A. Fouras, N. Yagi, K. Uesugi, and S. B. Hooper, "Dynamic measures of regional lung air volume using phase contrast x-ray imaging," *Phys. Med. Biol.* **53**(21), 6065–6077 (2008).
6. D. W. Parsons, K. S. Morgan, M. Donnelley, A. Fouras, J. Crosbie, I. Williams, R. C. Boucher, K. Uesugi, N. Yagi, and K. K. W. Siu, "High-resolution visualization of airspace structures in intact mice via synchrotron phase-contrast X-ray imaging (PCXI)," *J. Anat.* **213**(2), 217–227 (2008).
7. D. M. Paganin, *Coherent X-ray Optics*, Oxford University Press, New York, 2006.
8. D. M. Paganin, S. C. Mayo, T. E. Gureyev, P. R. Miller, and S. W. Wilkins, "Simultaneous phase and amplitude extraction from a single defocused image of a homogeneous object," *J. Microsc.* **206**(1), 33–40 (2002).
9. N. Yagi, Y. Suzuki, K. Umetani, Y. Kohmura, and K. Yamasaki, "Refraction-enhanced x-ray imaging of mouse lung using synchrotron radiation source," *Med. Phys.* **26**(10), 2190–2193 (1999).
10. P. Cloetens, W. Ludwig, J. Baruchel, J.-P. Guigay, P. Pernot-Rejmánková, M. Salomé-Pateyron, M. Schlenker, J.-Y. Buffière, E. Maire, and G. Peix, "Hard x-ray phase imaging using simple propagation of a coherent synchrotron radiation beam," *J. Phys. D Appl. Phys.* **32**(10A), 330–336 (1999).
11. J. B. Keller, "Geometrical theory of diffraction," *J. Opt. Soc. Am. A* **52**(2), 116–130 (1962).

12. D. F. Lynch, M. A. O'Keefe, and A. F. Moodie, "n-beam lattice images. V. "The use of the charge-density approximation in the interpretation of lattice images," *Acta Crystallogr.* **31**, 300–307 (1974).
13. N. Delen, and B. Hooker, "Free-space beam propagation between arbitrarily oriented planes based on full diffraction theory: a fast Fourier transform approach," *J. Opt. Soc. Am. A* **15**(4), 857–867 (1998).
14. M. Nieto-Vesperinas, *Scattering and Diffraction in Physical Optics*, 2nd ed. (World Scientific Publishing, New Jersey, 2006).
15. T. E. Gureyev, C. Raven, A. Snigirev, I. Snigireva, and S. W. Wilkins, "Hard x-ray quantitative non-interferometric phase-contrast microscopy," *J. Phys. D Appl. Phys.* **32**(5), 563–567 (1999).
16. M. J. Kitchen, D. M. Paganin, R. A. Lewis, N. Yagi, K. Uesugi, and S. T. Mudie, "On the origin of speckle in x-ray phase contrast images of lung tissue," *Phys. Med. Biol.* **49**(18), 4335–4348 (2004).
17. K. K. W. Siu, K. S. Morgan, D. M. Paganin, R. Boucher, K. Uesugi, N. Yagi, and D. W. Parsons, "Phase contrast X-ray imaging for the non-invasive detection of airway surfaces and lumen characteristics in mouse models of airway disease," *Eur. J. Radiol.* **68**(3 Suppl), S22–S26 (2008).
18. M. Born, and E. Wolf, *Principles of Optics*, 7th ed. (Cambridge University Press, Cambridge, 1999).
19. G. Margaritondo, and G. Tromba, "Coherence-based edge diffraction sharpening of x-ray images: A simple model," *J. Appl. Phys.* **85**(7), 3406–3408 (1999).

## 1. Introduction

X-rays are a powerful tool in biomedical imaging, traditionally using the absorption properties of the structure in question to reveal features of morphological (*e.g.* anatomical, structural) interest. Such absorptive imaging has the capacity to easily display bones and highly attenuating materials [1]. In addition to this well established mode, propagation-based phase contrast x-ray imaging (PCXI) demonstrates that even soft tissue may be seen using sufficiently coherent x-rays, using the phase changes that occur when a wave passes through a structure [2,3]. In particular, PCXI makes use of the transverse phase differences that are seen in a wave when it exits a scattering volume containing regions of different materials. In propagation based phase contrast, these phase variations are observed as intensity variations upon free-space propagation from the object to the detector, producing marked light and dark intensity interference fringes along the boundary of the two differing regions [4]. These high contrast fringes make the edges of tissue regions, for example an airway lumen, easily seen. As x-ray detector technology develops, smaller pixels enable such structures to be observed at high resolution in excellent detail. The use of synchrotron x-rays, characterised by their brightness and coherence, has also played an important part in realising detailed and informative PCXI [2,3].

Having established methods for biomedical PCXI, the balance of work is now moving from qualitative observations to quantitative measures of biological function (see, *e.g.*, [5]). While PCXI resolves the edges of soft tissue well [6], it is the phase contrast fringe which can reveal quantitative information about the phase changes effected by different materials, hence the spatial distribution and characteristics of those materials [5,7]. The projection approximation (PA) is a valuable tool in simulating the phase contrast process and in the development of phase retrieval algorithms (see, *e.g.*, [7,8]). This approximation describes the passage of rays through an object, by defining a nominal exit surface, immediately "downstream" of the irradiated object, at which transverse phase and intensity changes are imprinted. The projection approximation assumes that all scattering within the object is fully described by this exit wave, with negligible diffraction within the scattering volume. This simplification is very useful in recovering quantitative information from phase contrast images, and as theory is pushed further, it is timely to re-examine the projection approximation and edge contrast detail.

Here we look at the case of propagation-based x-ray phase contrast imaging of a cylinder or cylindrical edge, a simple model for the edges of many biological samples. A cylinder can model airways, blood vessels and other anatomical passages. The boundary between tissue and air is particularly suited for PCXI; an airway may be easily seen which would appear near invisible if observing attenuation only [9]. More generally, a cylinder can also be a good approximation to a rounded edge in projection, such as features *A*, *B*, *C* and *D* of Fig. 1. In this figure the imaging geometry is shown, with a monochromatic scalar electromagnetic

plane wave propagating in the positive  $z$  direction, incident on a cylinder or cylindrically modelled edge. The incident wave incurs changes in phase during its passage through the various regions of the object. As mentioned earlier, propagation based PCXI makes use of these phase changes by converting them into intensity variations through free-space propagation after the scatterer [2,3,10]. For sufficiently short propagation distances, propagation-based phase contrast exhibits fringes that become more visible the greater the propagation distance and for a greater difference in projected refractive index between neighbouring regions in the scatterer.

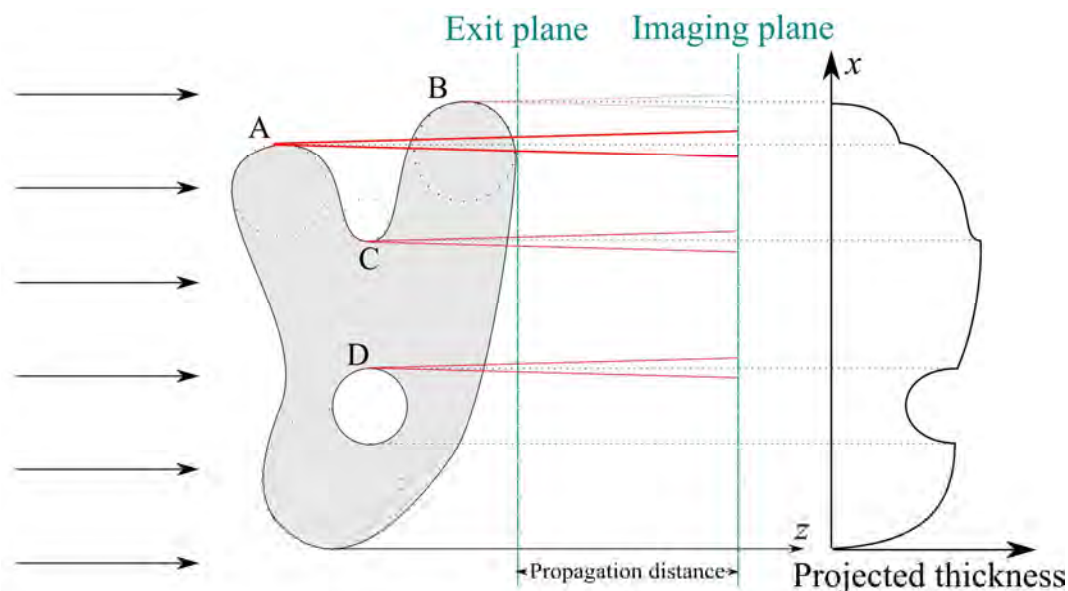


Fig. 1. Imaging geometry showing the projected thickness of a sample object, as used by the projection approximation, along with the associated exit plane.

As previously mentioned, the projection approximation assumes no diffraction occurs within the object volume, and hence phase and intensity variations at the scatterer's exit surface arise only from the projected complex refractive index. Further propagation from the exit plane to the imaging plane is required to then convert transverse phase gradients into phase contrast, visualised as intensity fringes. However, any diffraction within the object volume will mean that narrow intensity fringes will be observed at the “exit plane”, *e.g.* from each feature marked *A-D* in Fig. 1. In other words, the diffraction between the  $z$  position of edges *A-D* and the exit plane will be sufficient for the wave that has passed on one side of the feature to interfere with the wave passing on the other side of the feature. As shown by the red traces in Fig. 1, features such as *A*, which are further from the exit plane, will produce wider, more intense fringes than closer features such as *B*. Application of the projection approximation to simulate this process will predict only absorption contrast at the exit plane, requiring further propagation to produce phase contrast.

The study of edge contrast from such shapes is approached through a simulation which takes the exit wave as predicted by the projection approximation, and propagates to the detector surface, as described in section 2. Section 3 then looks at the signature of the resulting complex wavefield in the Argand plane. The simulation results are then validated by comparison with x-ray phase contrast images of a perspex cylinder taken at the SPring-8 synchrotron in Japan, in section 4.

## 2. X-ray image simulation using the projection approximation

The projection approximation is a consequence of the paraxial equation in an inhomogeneous medium (called the inhomogeneous paraxial equation hereafter), under the assumption that the scattering introduced by the sample is not strong enough to significantly disturb the ray

paths compared to the ray paths which would have existed within the same volume in the absence of the scatterer. This “semi-classical” approximation, which is somewhat reminiscent of the geometrical theory of diffraction described by Keller [11] in so far as it ascribes a phase to each ray path, approximates the phase and amplitude variation of a wave on travelling through a scatterer (for a textbook account see *e.g.* reference 7). The inhomogeneous paraxial equation, for a single wavelength, is given in Eq. (1):

$$\left[ 2ik \frac{\partial}{\partial z} + \nabla_{\perp}^2 + k^2(n^2(x, y, z) - 1) \right] \psi(x, y, z) = 0, \quad (1)$$

where  $\nabla_{\perp}^2 = \frac{\partial^2}{\partial x^2} + \frac{\partial^2}{\partial y^2}$  is the transverse Laplacian operator,  $k$  is the wavenumber,  $n$  is the position dependent refractive index and  $\psi$  is the envelope of the spatial wavefunction  $\psi e^{ikz}$ , describing the spatial part of a coherent scalar wavefield with intensity  $I = |\psi|^2$  and phase  $\varphi = \arg \psi$ . Each material is described by a complex refractive index  $n = 1 - \delta + i\beta$ , where  $\beta = \mu/2k$  ( $\mu$  is the linear attenuation coefficient) and  $\delta$  describes the refractive properties of the material.

The projection approximation states that waves passing through space with this refractive index  $n$  will undergo a phase shift, as denoted by the second term on the right-hand side of Eq. (2) and experience attenuation, as denoted by the third term of Eq. (2), where  $T_j$  is the projected thickness of each material  $j$  along the  $z$  direction [7]:

$$\psi_{\text{exit surface}} = \psi_{\text{incident}} \times \exp(-i\sum_j k \delta_j T_j) \times \exp(-\sum_j k \beta_j T_j). \quad (2)$$

The projection approximation may be used to simulate an x-ray phase contrast image, similar to the use of the projected charge-density approximation in electron microscopy [12]. Using this approach, the projection approximation was applied to the x-ray plane wave incident upon the object in question to give the exit wavefield. We look at the case of a cylinder, such as those approximating edges in Fig. 1 (*e.g.* B), so  $n$  is defined throughout the object and the total projected thickness ( $T$ ) of each material may be determined by the position  $x$  on the plane where the image is to be evaluated. As the projection approximation effectively projects all material to the exit surface, the diffraction and interference of waves is not described until after propagating the wavefunction from the exit plane to the image plane. This propagation was done by applying the wavefield propagator, then the modulus squared of the projected wavefield was calculated to obtain the intensity phase contrast image. The propagation was implemented using the angular spectrum representation of the Rayleigh-Sommerfeld diffraction integral of the first kind [13,14]. This method for simulation has been previously used in the field of synchrotron imaging (see, *e.g.* [15]) and biomedical x-ray imaging (see, *e.g.* [16]). The technique is particularly useful in that phase contrast images may be quickly and easily simulated. This allows optimisation of experimental configurations when the sample composition is well-known.

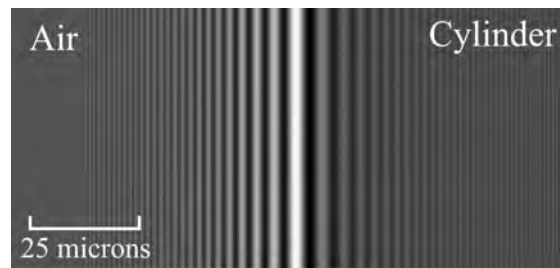


Fig. 2. Phase contrast fringes from the simulation for light of wavelength  $\lambda = 0.5$  Angstrom incident on the left edge of a 3 mm diameter perspex cylinder (using  $\delta_{\text{air}} = 4.13 \times 10^{-10}$ ,  $\beta_{\text{air}} = 0$ ,  $\delta_{\text{perspex}} = 4.00 \times 10^{-7}$ ,  $\beta_{\text{perspex}} = 3.1998 \times 10^{-10}$ ), propagated 50 cm.

Simulations produced images showing the edge of a cylinder (or rounded edge), as seen in Fig. 2, where fringes grow wider and more intense as a result of increased propagation (up to several metres for hard x-rays). Images experimentally obtained using a monochromatic 25keV synchrotron source of low divergence, as seen in Fig. 3, agree with simulations when simulated images are smoothed with the point spread function (PSF) appropriate to the detector characteristics, after adding noise and sampling at the same pixel size - see details below. The simulated and observed profiles show the same width and positioning of the multiple fringes from the cylinder edge, as well as the same maximum intensity from the fringe set. The smoother fringe envelope in the observed image is likely due to a PSF with broader tails than was measured experimentally (by knife-edge image) and used to smooth the simulated image. Here the projected edge of a 3 mm diameter cylinder is imaged with 50 cm and 100 cm propagation before the detector, distances typical of PCXI.

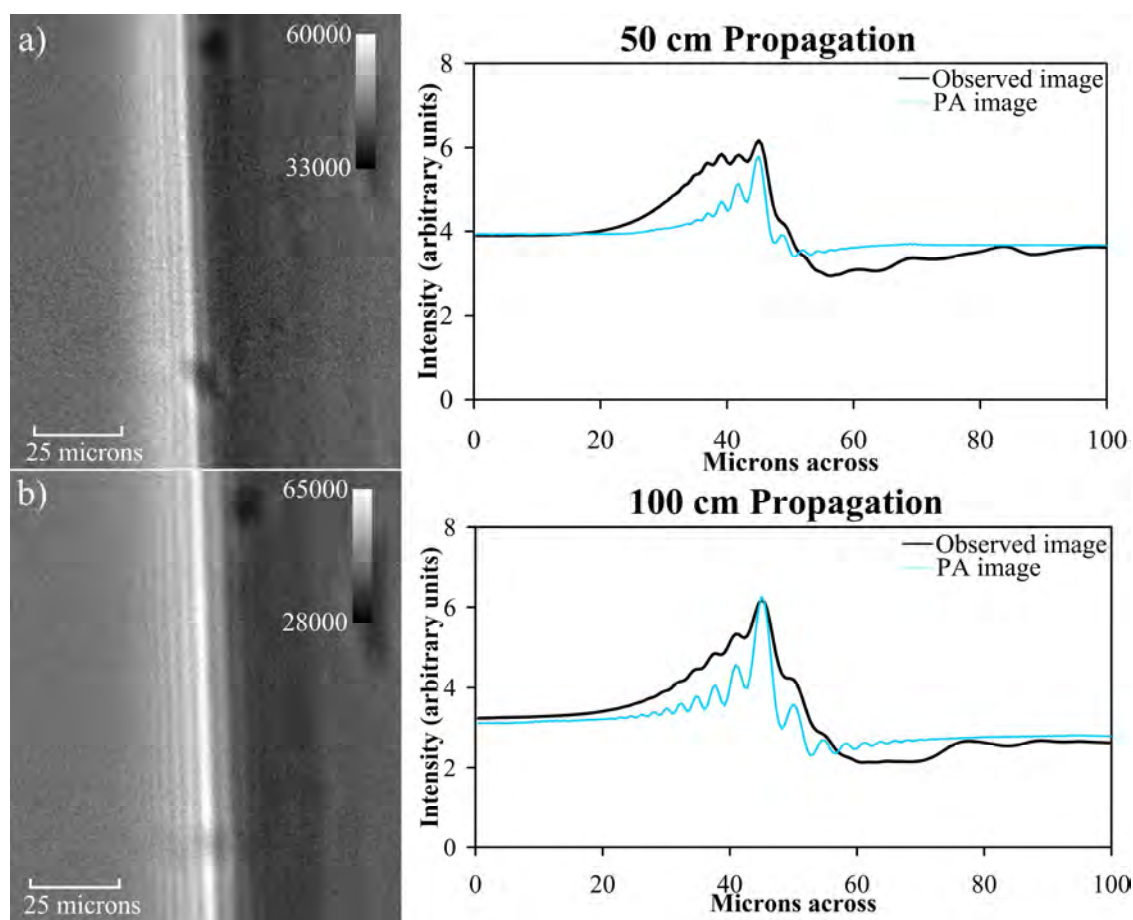


Fig. 3. Phase contrast images show the projection approximation correctly predicts the fringes seen at sufficiently long propagation distances. Images taken at the upstream hutch of BL20XU, SPring-8, of a 3 mm diameter perspex cylinder at 25keV for a propagation of *a*) 50 cm and *b*) 100 cm. The observed profile is shown in black and the simulated in blue.

An experimental image will usually not show many more than a few Fresnel fringes, due to the limited coherence of the source as well as the PSF of the imaging set-up, which is dependent on both the source size and the detector system (here most significantly due to scattering in the phosphor screen used to convert x-rays to visible/UV light for CCD capture as a digital image). A biomedical phase contrast image (for example, of an airway in a mouse or rabbit) often shows only one or two fringes, due to the overlying textured tissue and scattering within the volume [17]. The detector system used consisted of a phosphor screen, lens and a CCD, resulting in a pixel size of 0.45 microns and observed point spread function (PSF) of full width half maximum 3.8 microns. The cylinder was at an angle  $\theta$  to the columns

of the pixel array. Hence, to improve the signal to noise ratio, each row was shifted by aligning the fringe peaks to allow an average of the edge fringe over many rows. Since a true profile of the fringes should be taken perpendicular to the edge, correction by a factor of  $\cos(\theta)$  was made to the horizontal axis (*i.e.* via the pixel size).

### 3. Argand representation of the complex wavefield at the imaging plane

The wavefield at the exit plane or at the image plane (see Fig. 1) may be mapped to the Argand plane. For the case of a cylinder edge, a characteristic curve is formed from a Cornu spiral and a kind of hypocycloid (a cycloid inscribed on a circle). The Argand trace is parameterized by position in the imaging plane, with intensity described as square of the distance from the Argand origin and phase as the angle from the positive real axis.

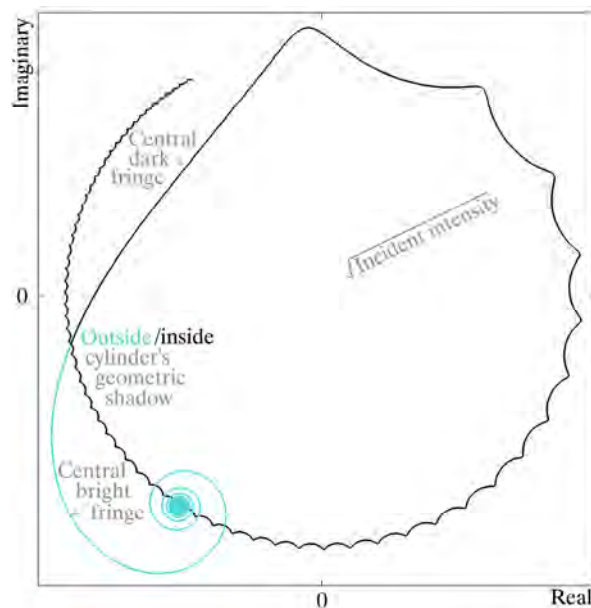


Fig. 4. Argand plot of 1 Angstrom waves incident on a 3 mm cylinder, propagated 5 mm, corresponding to 8 micron either side of the cylinder's geometric shadow, producing a connected Cornu spiral (blue) and hypocycloid (black).

Depending on the wavelength, object size and propagation, the wavefield across a plane downstream of the cylindrical edge will trace out an Argand-plane trace similar to that seen in Fig. 4. The centre of the blue spiral corresponds to far outside the geometric shadow of the cylinder (*i.e.* large  $x$ ), so has the uniform intensity and phase of the unscattered plane wave over a plane of constant  $z$ . Cycling outwards around the blue spiral increases and decreases the intensity in increasingly large bands, producing the increasingly wide, intense Fresnel fringes seen when approaching (from the outside) the phase contrast fringe arising from the edge of the cylinder.

The black hypocycloid in Fig. 4 describes the wavefield when moving inside the geometric shadow of the cylinder. In this example the absorption contrast is negligible compared to the phase contrast, so the trace moves along a circle of almost uniform radius/intensity, slowly changing in phase, according to the projection approximation. Oscillations in and out of this circle become light/dark bands of decreasing width and intensity, as seen in the phase contrast image (Fig. 2).

The diffraction pattern and hence the Argand plot can be explained by conceptually separating the x-ray wavefield scattered by the cylinder into two components, as seen in Fig. 5.

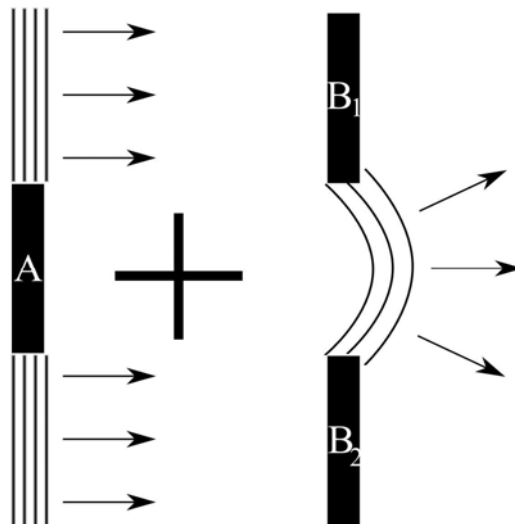


Fig. 5. Propagation based phase contrast imaging of a cylinder separated into edge diffraction and a distorted transmitted wave.

The first component, that of a plane wave diffracting around an opaque black screen A (bounded by the edges of the projected cylinder), is seen as the blue Cornu spiral in Fig. 4 [18]. The second component, the cylindrically distorted wave diffracted between two black screens, B<sub>1</sub> and B<sub>2</sub>, is seen as the hypocycloid; this hypocycloid results from a combination of the projection approximation and diffraction from the edge of the cylinder/opaque barrier. Note that screen A is complementary to the screen formed by B<sub>1</sub> and B<sub>2</sub>. We examine each of the diffracted components in detail below.

A Cornu spiral is typically plotted with  $C(u)$  and  $S(u)$  as the Fresnel integrals on the  $x$  and  $y$  axes respectively [18], where  $u$  is a reduced variable proportional to  $z$ , the distance across the imaging plane. In order to calculate the diffracted wavefield along a plane which is downstream of an opaque edge, the Cornu spiral is shifted by  $+1/2$  in both  $x$  and  $y$  directions, rotated about the origin by  $-\pi/4$  and divided by  $\sqrt{2}$  as in Eq. (3) [18]:

$$\psi \propto \left\{ \left[ \frac{1}{2} + C(u) \right] - \left[ \frac{1}{2} + S(u) \right] \right\} + \left\{ \left[ \frac{1}{2} + C(u) \right] - \left[ \frac{1}{2} + S(u) \right] \right\}. \quad (3)$$

This will place the centre of the spiral a distance from the origin equal to the square root of the wave intensity. The square of the distance from the origin will then give the intensity of the wave, giving local maxima and minima while moving around the spiral, closer to and further from the origin. This links to the elegant edge diffraction model described by Margaritondo and Tromba [19], although the cylindrical nature of the edge considered here will slightly distort the diffraction pattern from that which would be seen from a rectangular edge, as they describe. Their model also uses Fresnel integrals to look at diffraction of a wave, this time from an absorbing, but not completely opaque edge. The wavefield is then altered to Eq. (4) [19]:

$$\begin{aligned} \psi \propto & \left\{ \left[ \frac{1}{2} + C(u) \right] + \left[ \frac{1}{2} + S(u) \right] \right\} + i \left\{ \left[ \frac{1}{2} + C(u) \right] - \left[ \frac{1}{2} + S(u) \right] \right\} \\ & + \exp(-ik\delta T) \times \exp(-k\beta T) \left\{ \left[ \frac{1}{2} + C(-u) \right] - i \left[ \frac{1}{2} + S(-u) \right] \right\}. \end{aligned} \quad (4)$$

The addition of the projection approximation, multiplied by a Cornu spiral around the origin, will produce phase contrast fringes within the geometric shadow of the non-opaque edge. This signature, as a trace in the Argand plane, is seen in our simulations of a cylindrical edge using the projection approximation (*cf.* Fig. 4 and Fig. 7).

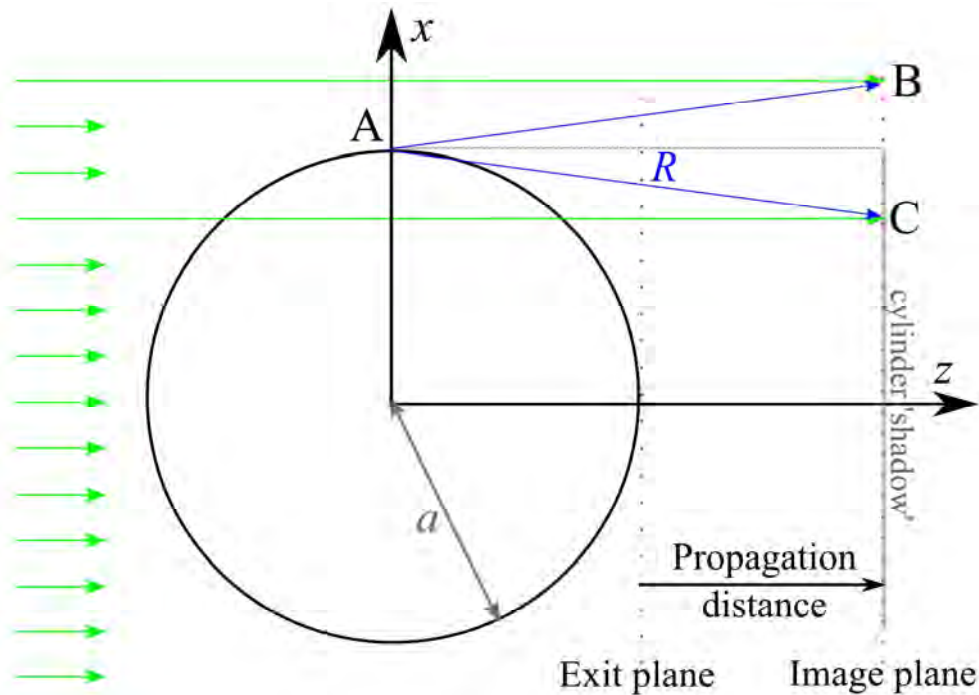


Fig. 6. Geometry of rays incident on a cylinder, showing the rays which interfere to form a Cornu spiral and a hypocycloid.

The spiral shape of the Cornu spiral (the blue trace in Fig. 4) is due to the phasor addition of the unscattered plane wave passing outside the cylinder in Fig. 6 with the cylindrical wave scattered from the edge of the cylinder, such as ray  $AB$ . These can also be described by the interference of the incident plane wave and a cylindrical wave scattered from the edge of the cylinder, using the rays seen in Fig. 6. The projection approximation will incur a phase change, as given in Eq. (2), on the incident plane wave travelling through the cylinder and landing at  $C$ . This distorted plane wave, as estimated via the projection approximation, will then interfere with the cylindrical edge wave  $AC$ . The resulting wave, as described by Eq. (5), will then be the sum of a plane wave ( $e^{ikz}$ ) multiplied by the projection-approximation phase shift  $e^{-ik\delta T}$ , and this spherical wave scattered from the edge of the cylinder;

$$\psi_{\text{image plane}} = e^{ikz} \times e^{-ik\delta T} + S e^{ikR} / \sqrt{R}, \quad (5)$$

where  $S$  is a coefficient describing the amplitude of the edge wave and  $R$  is the distance from the edge  $A$  of the cylinder to a given point on the image plane (shown in Fig. 6).

$R$  will be increased as the point  $C$  moves deeper into the geometric shadow of the cylinder, and in the projection approximation,  $T = \sqrt{a^2 - x^2}$ , will also be increasing. This means that as the projection approximation traces out a uniform-intensity circle in the Argand plane, interference between the distorted plane wave landing at  $C$  and the spherical wave  $AC$  will cycle with decreasing amplitude in the same way as a Cornu spiral. The effect of a Cornu spiral moving anti-clockwise around the Argand plane, following the projection approximation, is therefore seen as a hypocycloid in which the “epicycle” has reducing radius. If there is significant attenuation from the cylinder or rounded edge, the projection approximation will also show a decrease in the amplitude of the wavefield, as seen in Fig. 7. Interestingly, this Argand-plane trace exhibits a transition from classic hypocycloid-type cusps (e.g. feature  $\alpha$  in Fig. 7) to a looped structure (e.g. feature  $\beta$  in Fig. 7), indicative of “retrograde” Argand-plane motion. The amplitude of this scattered edge wave,  $S$ , as related to where the phase begins “retrograde” Argand-plane behaviour, is explored mathematically in the appendix.

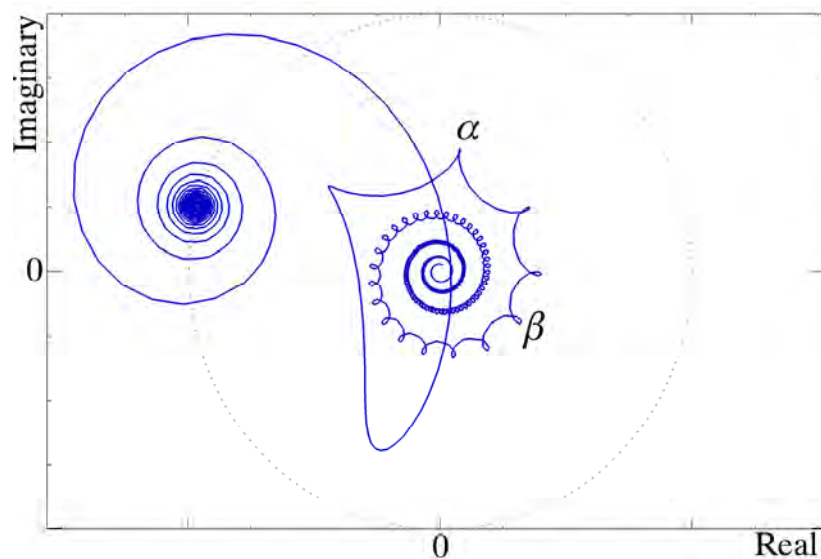


Fig. 7. Argand plot of 0.5 Angstrom waves incident on a 1 mm diameter cylinder, propagated 1 mm, corresponding 8 micron either side of the cylinder's geometric shadow, with significant attenuation by the cylinder ( $\beta_{\text{Fig. 7}} = 500 \times \beta_{\text{Fig. 4}}$ ). The dotted circle indicates the uniform intensity of the unscattered wave.

As the wavefield is further propagated from the cylinder to an image plane, the size of the Cornu spiral increases, as does the amplitude of the hypocycloid oscillations. This will produce more intense, wider Fresnel fringes. The pixel size and point spread function, relative to the size of the fringes, will be significant when phase contrast is observed with many fringes. Given small enough pixels, a holographic region fringe set will be observed, as would be seen by taking the absolute value squared of the Argand trace in Fig. 4. Larger pixels would give an image in the “edge detection” region, showing a single light/dark fringe at the boundary. As the pixel size increases further, the image will be less able to detect fringes, eventually leading to an absorption-only image. This smoothing of fringes is also observed with a decrease in the transverse coherence of the beam, the effect of which is well approximated by smoothing of the simulated image with a demagnified image of the source. As well as decreasing fringe visibility, this could smooth out the phase “loops” seen in Fig. 7.

Regardless of pixel size, the projection approximation's prediction of no intensity fringes due to phase contrast at the “exit” surface can be seen in an Argand plot for zero object-to-detector propagation distance.

#### 4. Underestimation of fringes by the PA at short object-to-detector propagation distance

Here we examine how the PA underestimates phase contrast fringe visibility and width close to the object, both through the Argand trace and in practice. The origin of this underestimation is that the projection approximation omits the Young-type boundary wave [18] given by the final term of Eq. (5), over the exit-plane of the object. The associated underestimation of phase-contrast fringe visibility carries over to sufficiently-small object-to-detector propagation distances, as examined below.

Figure 8 shows the Argand-plane trace for 25keV x-rays falling on the edge of a 3 mm diameter cylinder with increased propagation before the image plane, as used in our experiment. The intensity and phase of the trace has been blurred with a Gaussian of standard deviation  $0.18\mu\text{m}$  to describe the effect on the observable fringes of using  $0.18\mu\text{m}$  effective pixel size. As mentioned earlier, the angular-spectrum formalism has been used to numerically propagate from the nominal planar exit surface of the object, to the surface of the detector.

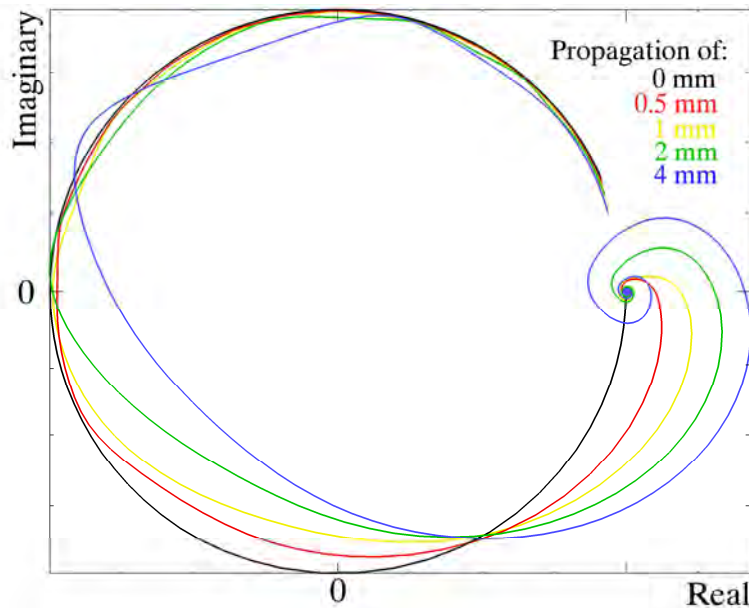


Fig. 8. Argand plot of 0.5 Angstrom waves incident on a 3 mm cylinder, smoothed by a Gaussian of pixel size 0.18 micron, showing the introduction of multiple intense, wider fringes with propagation, viewing 1 micron either side of the interface.

In Fig. 8, it can be seen that the projection approximation shows no fringes at 0 mm propagation, simply uniform intensity with slowly varying phase behind the cylinder. With 1.5 mm propagation from the exit plane, using the projection approximation, a single faint light/dark fringe is predicted, closer to that theoretically expected at the exit plane, which will itself sit 1.5 mm from the edge of the 1 mm cylinder. This illustrates the assertion that the propagation within a scattering volume upstream of the nominal exit plane will not be taken into account by the projection approximation. Propagations of 4 mm and greater are predicted to show multiple observable fringes both behind and outside the cylinder shadow.

A comparison between Fig. 8 and Fig. 4 shows that, as predicted by the projection approximation, a greater phase change is incurred with a short wavelength or a stronger phase object. This is seen when across the imaging plane a short wavelength (*e.g.* the 0.5 Angstrom hard x-rays of Fig. 8) passes through a full  $2\pi$  phase change within a micron of the cylinder edge shadow, while a longer wavelength (*e.g.* the 1 Angstrom softer x-rays of Fig. 4) wraps more slowly (requiring 4 microns across the image plane for a  $2\pi$  phase change in Fig. 4). It is for this reason that small propagation lengths on the order of millimeters (hence narrow fringes) and small pixels have been used in Fig. 8, to avoid wrapping the trace around upon itself.

The inability of the projection approximation to predict fringes at very short propagations was confirmed by imaging the same 3 mm perspex cylinder at propagation lengths comparable to the cylinder radius. Figure 9(a) shows that at 25keV there was no fringe predicted by the projection approximation at contact, but a fringe was observed in the image, as predicted by Eq. (5). When the propagation distance is increased to the radius, and then to the diameter of the cylinder, the fringes predicted by the PA become much more similar to those observed. The simulated fringes are not only more similar in amplitude, but also in fringe width. At 1m propagation, a typical distance as would be used for medical phase contrast imaging to produce good edge contrast (see, *e.g.*, [2–6]), the images are correctly simulated using the projection approximation, as was seen in Fig. 3(b). This demonstrates how the projection approximation will only underestimate phase contrast intensity fringes when a significant amount of the total diffraction occurs within the scattering volume.

Therefore, for typically-large propagation distance as used in small animal PCI (as seen in Fig. 3), where the relative error in the propagation distance is small, the projection approximation is a fast and accurate tool in the simulation of x-ray phase contrast imaging.

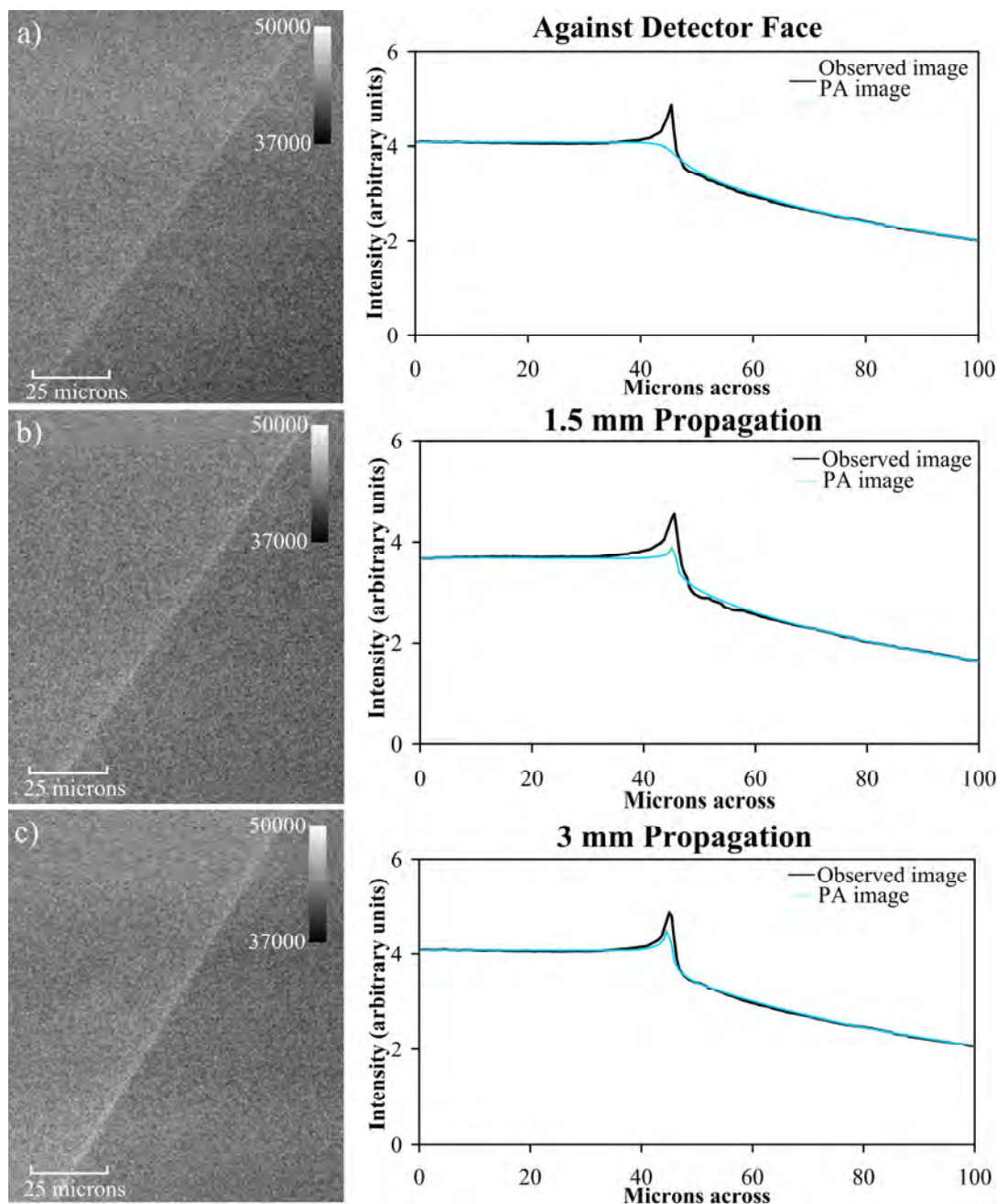


Fig. 9. Experimental phase contrast images show the projection approximation does not predict the fringes seen at very short propagation distances, but the simulated fringes become more accurate as the propagation distance increases. Images taken of the same 3 mm diameter perspex cylinder as Fig. 3, at 25keV for a propagation of *a)* contact, *b)* 1.5 mm, *c)* 3 mm. At these short propagation distances, the pixel size and point spread function prevent multiple fringes being resolved at the edge interface. The shorter propagation distance means that the signal to noise ratio is reduced. The observed profile is shown in black and that simulated using the projection approximation (then smoothed with detector characteristics as in Fig. 3) in blue.

## 5. Conclusion

It has been seen that the projection approximation is indeed accurate in predicting propagation-based phase contrast x-ray images of a cylinder given that the propagation distance is significant compared to the radius of the cylinder. This observation can be extended to other volumes in a general sense, in that the approximation is valid provided that there is not significant space for diffraction within the scattering volume compared to the propagation distance. The projection approximation is therefore very useful in efficiently simulating phase contrast as part of the journey to recovering quantitative information from images. We have also seen the “signature” of the projection approximation in the Argand plane, winding the phase around at uniform intensity turning a Cornu spiral into a hypocycloid in the geometric shadow of the rounded edge. The magnitude of these Cornu/hypocycloid oscillations was seen to increase with propagation.

## Appendix

The scattered wavefield from the cylinder edge will produce the Argand plane loops as seen in Fig. 7. Whether the cycloid shape seen in the complex wavefield behind the geometric shadow of the cylinder will be seen to “loop the loop” (*i.e.*, exhibit a retrograde-like trace) will be determined by the propagation distance, refractive index and edge gradient of the cylinder. This looping will mean that the Argand-plane trace due to phase along the image plane is moving slightly backwards (due to the scattered field from the edge of the cylinder) before continuing to increase while moving further behind the increasingly thick volume of the cylinder.

Given Eq. (5), we look at the relationship between the slow moving phase due to the projection approximation for the increasingly thick object and the small fast cycles due to edge cylindrical waves. In Fig. 7 a transition from where the hypocycloid goes from showing cusps (*e.g.* feature  $\alpha$  in Fig. 7) to loops (*e.g.* feature  $\beta$  in Fig. 7) is seen. This is where the gradient of the cylinder is sufficiently small that the projection approximation is no longer moving the phase around the Argand plane fast enough to keep up with the fast cycles of the fringes from edge wave interference. Figure 10 shows a perfect hypocycloid, where a small circle moves along the inside of a bigger circle without any slipping. In order to avoid slipping, the distance along which it travels between peaks must be  $2\pi d$ , the circumference of the cylinder. If the distance is smaller (or the circle turns faster, slipping as it moves across the surface), loops will be seen.

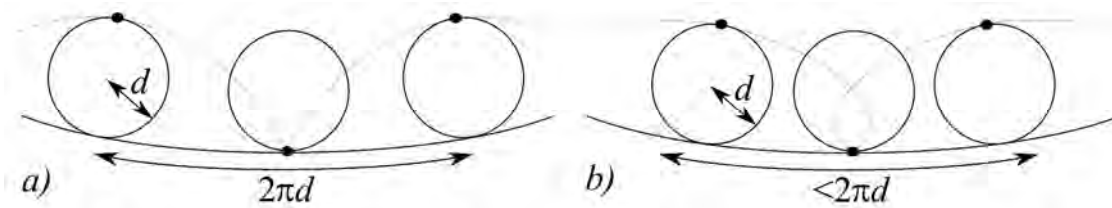


Fig. 10. A hypocycloid is traced by a circle turning, *a*) without slipping and *b*) with slipping, around the inside of a bigger circle.

In the case considered, looking at the loops in the Argand plane of the wavefield observed along an image plane, the wave is given by Eq. (A1) [*c.f.* Eq. (5)]:

$$\psi_{\text{image plane}} = e^{ikz} \times e^{i\varphi_{\text{object}}} + \frac{S}{\sqrt{R}} e^{i\varphi_{\text{edge}}}. \quad (\text{A1})$$

Note that the object phase,  $\varphi_{\text{object}} = -k\delta T$ , is decreasing when moving further behind the cylinder, while the edge phase,  $\varphi_{\text{edge}} = kR$ , is increasing. In the Argand plane considered, the large circle (see *e.g.* dotted line in Fig. 4 or Fig. 7) is created by the first term of Eq. (A1)

varying slowly in phase and the smaller circle comes from the second term varying quickly in phase. The critical case of a perfect hypocycloid with no slipping [Fig. 10(a)] will require two conditions to be fulfilled for a section of the trace (hence a section of the image plane);

- The slowly moving phase from the first term in Eq. (A1),  $\varphi_{object}$ , changes by the circumference of the smaller circle ( $2\pi d$ ) so that a full cycloid cycle can be traced by the edge of a “non-slipping” circle.
- The fast moving phase from the second term in Eq. (A1),  $\varphi_{edge}$ , changes by a full cycle ( $2\pi$ ) within the same distance.

This distance or section of the image plane is defined as  $\Delta x$ , in addressing the first requirement. The smaller circle will have radius  $d = S/\sqrt{R}$  (from the second term in Eq. (A1)) and will require the arc length  $2\pi d$  in the Argand plane on which to complete a full rotation without slipping. This arc length will come from the slow moving phase due to the slowly increasing projected thickness of the object. The change in phase across  $\Delta x$  is given in Eq. (A2):

$$\varphi_{object}(x + \Delta x) - \varphi_{object}(x) = \varphi'_{object}(x) \times \Delta x, \quad (\text{A2})$$

with a dash denoting differentiation with respect to  $x$ . This angle swept out by the phase change given in Eq. (A2) will also be the arc length traversed in the Argand plane for a circle of radius 1 (*i.e.* intensity = 1). This means the critical case of a perfect hypocycloid is now described by Eq. (A3):

$$2\pi d = 2\pi \frac{S}{\sqrt{R(x)}} = \varphi'_{object}(x) \times \Delta x. \quad (\text{A3})$$

To satisfy the second condition, we require the condition given in Eq. (A4), that the phase changes from the cylindrical wave [ $\varphi_{edge}$  in Eq. (A1)] change by  $2\pi$  (or less, to avoid loops) over the length  $\Delta x$ :

$$\varphi'_{edge}(x) \Delta x \leq 2\pi. \quad (\text{A4})$$

Substituting Eq. (A3) into Eq. (A4) to eliminate  $\Delta x$  gives Eq. (A5):

$$\varphi'_{edge}(x) \frac{2\pi S}{\sqrt{R(x)} \varphi'_{object}(x)} \leq 2\pi. \quad (\text{A5})$$

Simplifying produces Eq. (A6)

$$S \varphi'_{edge}(x) \leq \sqrt{R(x)} \varphi'_{object}(x). \quad (\text{A6})$$

Putting in the expressions for each of  $\varphi_{object}$  and  $\varphi_{edge}$  as determined by the object and by the edge wave {Eq. (5) gives Eq. (A7)}:

$$SkR'(x) \leq \sqrt{R(x)} k \delta T'(x). \quad (\text{A7})$$

where  $k$  is the wavenumber,  $R(x)$  the distance from the edge and  $T(x)$  the projected thickness of the object, as previously defined. In all edge cases,  $R(x) = \sqrt{z^2 + x^2}$  for the origin in  $x$  (*i.e.*  $x = 0$ ) set at the edge of the object. This will produce a requirement for a cycloid without loops, Eq. (A8):

$$T'(x) \geq \frac{Sx}{\delta(z^2 + x^2)^{3/4}}. \quad (\text{A8})$$

Assuming that  $x$  is small compared to  $z$ , *i.e.* fringes are seen close to the edge for long propagations, this simplifies to Eq. (A9) for a non-retrograde Argand-plane trace:

$$T'(x) \geq \frac{Sx}{\delta z^{3/2}}. \quad (\text{A9})$$

This describes how the sample thickness gradient must be sufficiently large that the slowly varying phase from the projection approximation moves around the Argand plane quickly enough to keep up with the fast loops from the edge wave. More specifically, tighter loops will be seen for any of shorter propagation  $z$  (where the spherical edge wave has greater variations across  $\Delta x$ ), smaller  $\delta$  (a weak phase object will not wrap the slow moving phase from the object around as quickly) or greater distance ( $x$ ) from the edge, where the reduced radius of the hypocycloid means it can complete a circuit more quickly. The increase in retrograde behaviour with position  $x$  in the imaging plane when moving behind the cylinder has already been observed in Fig. 7.

For the specific case of the edge of a cylinder, the projected thickness  $T(x)$  can be described as  $T(x) = 2\sqrt{a^2 - (x-a)^2}$ , where  $a$  is the radius of the cylinder and  $|x| \leq a$ . Substituting into Eq. (A9) and again assuming that  $x$  is close to the edge, and small compared to the radius  $a$ , gives Eq. (A10);

$$x \leq z \sqrt[3]{\frac{2a\delta^2}{S^2}}. \quad (\text{A10})$$

This means that the scattered edge wave coefficient,  $S$  [from Eq. (5)], could be determined from a plot such as Fig. 7, simply from the  $x$  coordinate at which the hypocycloid begins to loop around. With significant attenuation, this  $x$  coordinate will change slightly, with the condition given in Eq. (A9) now divided by  $e^{-k\beta T}$  on the right hand side.

### Acknowledgments

The authors thank the Japan Synchrotron Radiation Research Institute and beamline 20XU scientists Kentaro Uesugi, Yoshio Sukuji and Akihisa Takeuchi for the privilege of using the SPring-8 facility in obtaining the experimental images. We acknowledge funding for the travel to SPring-8 from the Access to Major Research Facilities Program, which is supported by the Commonwealth of Australia under the International Science Linkages program. Kaye Morgan acknowledges the support of an Australian Postgraduate Award and a J.L. William Scholarship from Monash University. David Paganin acknowledges the Australian Research Council, together with useful advice from Christian Dwyer, Timur Gureyev and Freda Werdiger. Karen Siu acknowledges the National Health and Medical Research Council.

---

## Exact Modelling of Propagation-Based PCXI of Cylindrical Interfaces

---

*The projection approximation versus an exact solution for x-ray phase contrast imaging, with a plane wave scattered by a dielectric cylinder.*

by Kaye S. Morgan, Karen K. W. Siu and David M. Paganin.

Published in Optics Communications **283**, pp. 4601-4608, 2010.

---

This second paper follows on directly from Chapter 2, now comparing simulated PB-PCXI images (produced using the model described in section 1.1.1.2 and Chapter 2) with images from an exact wavefield solution for a sample consisting of one or more concentric cylinders.

This is again relevant for the modelling of any rounded interface and mathematically verifies the assertions made in Chapter 2 that phase contrast fringes will be underestimated in intensity and width at propagation distances comparable to the longitudinal dimension of the sample, but will match at those longer propagation distances typically used in biomedical PB-PCXI. This is important in the simulation work of Chapters 4-6. Comparisons are made both between the intensity images and between the Argand plane plots (see section 1.1.1.3 and Chapter 2) of the complex wavefield.

The mathematical argument showing how the exact solution becomes the projection approximation in the centre of the cylinder, for a small wavelength relative to the sample, complements the numerical comparisons.

### Declaration for Thesis Chapter 3

In the case of Chapter 3, contributions to the work involved the following:

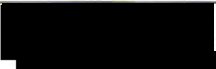
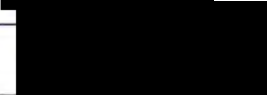
Name	% contribution	Nature of contribution
Kaye Morgan	90%	Solved for and evaluated the exact solution, wrote the code for and analysed the numerical simulations, developed the theoretical aspects, worked through the mathematics of the asymptotic approximations to the exact solution and wrote up the paper
Karen Siu		Contributed to the theoretical discussions, provided supervisory advice, aided proofreading and drafting
David Paganin		Contributed to the theoretical discussions, provided supervisory advice, aided proofreading and drafting

#### Declaration by co-authors

The undersigned hereby certify that:

1. the above declaration correctly reflects the nature and extent of the candidate's contribution to this work, and the nature of the contribution of each of the co-authors.
2. they meet the criteria for authorship in that they have participated in the conception, execution, or interpretation, of at least that part of the publication in their field of expertise;
3. they take public responsibility for their part of the publication, except for the responsible author who accepts overall responsibility for the publication;
4. there are no other authors of the publication according to these criteria;
5. potential conflicts of interest have been disclosed to (a) granting bodies, (b) the editor or publisher of journals or other publications, and (c) the head of the responsible academic unit; and
6. the original data are stored at the following location(s) and will be held for at least five years from the date indicated below: School of Physics and Monash Centre for Synchrotron Science, Clayton Campus, Monash University, Australia.

#### Signatures:

Kaye Morgan:		Date: 19/10/10
Karen Siu:		Date: 19.10.2010
David Paganin:		Date: 18/10/10

---

This paper was published in Optics Communications and is made available as an electronic reprint with the permission of Elsevier. The paper can be found on the ScienceDirect website under doi:10.1016/j.optcom.2010.07.012. Systematic or multiple reproduction or distribution to multiple locations via electronic or other means is prohibited and is subject to penalties under law.

---



Contents lists available at ScienceDirect

Optics Communications

journal homepage: www.elsevier.com/locate/optcom



## The projection approximation versus an exact solution for X-ray phase contrast imaging, with a plane wave scattered by a dielectric cylinder

Kaye S. Morgan<sup>a,\*</sup>, Karen K.W. Siu<sup>a,b</sup>, David M. Paganin<sup>a</sup>

<sup>a</sup> School of Physics, Monash University, Victoria, 3800, Australia

<sup>b</sup> Monash Centre for Synchrotron Science, Monash University, Victoria, 3800, Australia

### ARTICLE INFO

#### Article history:

Received 7 May 2010

Accepted 2 July 2010

#### Keywords:

Phase contrast imaging  
Synchrotron hard X-rays  
Projection approximation

### ABSTRACT

We show that exact solutions for an X-ray plane wave scattered by a dielectric cylinder with radius large compared to the radiation wavelength, give almost the same intensity fringes as seen when using the projection approximation (PA) to simulate propagation based phase contrast imaging. The characteristic Argand plane Cornu spiral and hypocycloid from the complex wavefield beyond the cylinder was observed to agree with the PA simulations. Asymptotic approximations to the exact analytical solution simplify to the projection approximation at the centre of the cylinder. The projection approximation underestimates observed fringes at a propagation distance comparable with the cylinder radius, but converges to the exact solution at larger propagation distances. This demonstrates that the complex ray approach of the projection approximation is insufficient, in comparison to the exact approach, when the propagation distances are sufficiently small.

© 2010 Elsevier B.V. All rights reserved.

### 1. Introduction

The complexity of models required to describe a given optical system is often determined by the scale or regime in which that system is considered. As one example of this, geometric optics may be used over sufficiently large length scales, with wave optics being required to analyze smaller-scale wavefield features. This paper looks at modelling wave optics, focusing on propagation-based phase contrast X-ray imaging (PCXI) [1–3]. It takes a complex ray approach, using the projection approximation (PA), and compares this to a full analytic solution. It is shown that phase contrast fringes are underestimated at propagation distances comparable to or smaller than the longitudinal dimension of the volume, a result of the PA neglecting the effects of transverse scattering or diffraction within the volume.

Here we study the case of imaging a cylinder, following on from our previous work looking at the application of the projection approximation to a cylinder [4]. Fig. 1 shows the geometry of such a set-up, with a monochromatic scalar electromagnetic plane X-ray wave propagating in the positive  $z$  direction incident on a cylindrical dielectric object of inner radius  $a$ , and outer radius  $b$ . This may be considered, for example, as an idealized model of a fluid-lined biological airway, which is of direct relevance to our ongoing work in imaging such fluid linings in the context of cystic fibrosis [5].

As the wave passes through the cylinder(s), the complex refractive index (specified as uniform within each region) will mean the wave is not only attenuated, but also undergoes a relative phase change. This phase change is made visible in X-ray propagation-based phase contrast imaging when the interference of phase-differing waves creates bright/dark intensity fringes [1–3,6]. As the strongest transverse difference in phase occurs at the edges of objects, this is where the fringes will be most readily observed in the phase-contrast image. These fringes will be increased in amplitude and width with an increased propagation distance. A typical propagation distance, in the PCXI of biomedical structures with millimetre length scales, is on the order of 1 m [5].

This process is often simulated using the projection approximation for regions of specified constant refractive index (see, e.g., [7]),

$$\psi_{\text{exit surface}} = \psi_{\text{initial}} \times \exp\left(-ik \sum_j \delta_j T_j\right) \times \exp\left(-k \sum_j \beta_j T_j\right). \quad (1)$$

Here  $\psi$  is the spatial part of the complex monochromatic scalar X-ray wavefield,  $k$  is the wavenumber, and  $n = 1 - \delta + i\beta$  is the refractive index of material  $j$  which has total thickness  $T_j$  when projected along the optic axis  $z$ . The projection approximation comes from the inhomogeneous paraxial equation (see, e.g., [7]),

$$\left[2ik \frac{\partial}{\partial z} + \nabla_{\perp}^2 + k^2(n^2(x, y, z) - 1)\right] \psi(x, y, z) = 0. \quad (2)$$

\* Corresponding author. Tel.: +61 3 9905 3611; fax: +61 3 9905 3637.  
E-mail address: Kaye.Morgan@monash.edu (K.S. Morgan).

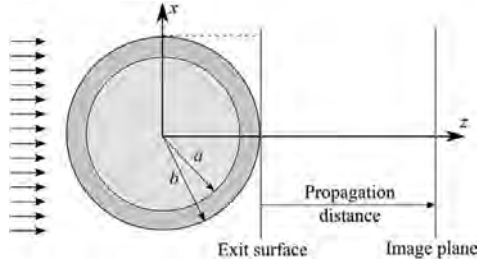


Fig. 1. Two concentric cylinders, of radius  $a$  and  $b$ , each of different composition to their surroundings, scattering a plane wave incident from the left.

where  $\nabla_{\perp}^2$  is the transverse Laplacian operator. Neglecting  $\nabla_{\perp}^2\psi$  as small relative to the other terms in the square brackets results in the projection approximation. More generally, if paraxiality is not assumed,  $\psi$  obeys the inhomogeneous Helmholtz equation,

$$[\nabla^2 + k^2 n^2(x, y, z)]\psi(x, y, z) = 0. \quad (3)$$

In simulation, the projection approximation describes the changes in intensity and phase after propagation through a volume and then from the exit plane (Fig. 1) to the imaging plane, using the angular spectrum representation of the Rayleigh–Sommerfeld diffraction integral of the first kind [8]. The algorithm is very fast to evaluate numerically, primarily due to the fact that the angular-spectrum formalism is very readily coded using fast Fourier transforms (FFTs) [9]. The intensity of the resulting wavefield shows phase contrast fringes as expected, but does not take into account any diffraction within the scattering volume itself [4], or more generally within the half-space upstream of the nominally plane exit surface. In the case of a cylinder, this means that the propagation from the edge of the cylinder (e.g.,  $z=0$ ,  $x=a, b$ ) to the exit plane will not be taken into account by the projection approximation. Therefore the simulated image will exhibit phase contrast fringes that are more similar to those seen at a propagation distance which is shorter by the order of the cylinder radius. The PA-simulated fringes will therefore be both narrower and of decreased visibility.

Here we look at comparing the results from this simulation model to an exact solution for a plane wave incident on a cylinder. This provides meaningful insights into the complexity of model required to adequately describe a wave problem. For example, a simple geometrical optics description will be bettered in this situation by using the projection approximation with complex rays. Rigorous wave theory [10], such as an exact solution to the inhomogeneous Helmholtz equation Eq. (3), will best describe the expected images for all regimes (e.g. all propagation distances).

We outline such an exact solution, for the case of a dielectric cylinder (as was first considered by Lord Rayleigh in 1881 [11,12]), and how this solution may be numerically evaluated, in Section 2. This exact result is then compared to the projection approximation model in Section 3.1 in terms of both the observed image and the complex wavefield in the Argand plane. The final part of this comparison, Section 3.2, details how the exact solution simplifies to the projection approximation for the special case at the centre of the cylinder. We offer a discussion in Section 4 and conclude with Section 5.

## 2. An analytical solution

An exact solution to Eq. (3) was desired in order to assess the discrepancies expected between simulated data using the projection approximation and experimental images. This was found for a simple

cylinder, as well as for two or more concentric cylinders as shown in Fig. 1, and the exact series solution was then evaluated numerically at the image plane in order to compute an exact phase contrast image. This required a solution to the inhomogeneous Helmholtz equation Eq. (3) such that the following conditions are met for the wavefunction  $\psi$  (starting with the case of a single cylinder):

- Far upstream of the scatterer there is only an incident plane wave;
- The scattered component of  $\psi$  is outgoing at infinity (Sommerfeld radiation condition);
- $\psi$  is finite at the origin;
- $\psi$  is continuous at the interface between the two regions, i.e.  $\psi_{\text{outside}}|_{r=a} = \psi_{\text{inside}}|_{r=a}$ ;
- $\psi$  is smooth at the interface between the two regions, i.e.  $\partial\psi_{\text{outside}}/\partial r|_{r=a} = \partial\psi_{\text{inside}}/\partial r|_{r=a}$ .

The first two conditions mean, for the case of a simple cylinder, that the wavefunctions must have the following form [13]:

- Inside cylinder:  $\psi_{\text{inside}} =$  Scattered radially expanding wave + Scattered radially contracting wave

$$\psi_{\text{inside}} = e^{-i\omega t} \sum_{m=0}^{\infty} D_m H_m^{(1)}(n_a k r) \cos(m\phi) + e^{-i\omega t} \sum_{m=0}^{\infty} E_m H_m^{(2)}(n_a k r) \cos(m\phi); \quad (4)$$

- Outside cylinder:  $\psi_{\text{outside}} =$  Unscattered plane wave + Scattered radially expanding wave

$$\psi_{\text{outside}} = e^{-i\omega t} \sum_{m=0}^{\infty} A_{\epsilon_m} i^m J_m(n_b k r) \cos(m\phi) + e^{-i\omega t} \sum_{m=0}^{\infty} B_m H_m^{(1)}(n_b k r) \cos(m\phi). \quad (5)$$

Here,  $\omega$  is the angular frequency of the wave,  $n_a$  and  $n_b$  the refractive index inside and outside the cylinder respectively,  $r$  the distance from the coordinate origin in the  $x$ - $z$  plane,  $\phi$  the angle from the  $z$  axis, and  $\epsilon_m$  defined as  $\epsilon_0=1$ ,  $\epsilon_m=2$  for all  $m \geq 1$ .  $A$  is the amplitude of the incident plane wave, with  $D_m$ ,  $E_m$  and  $B_m$  the coefficients of the scattered waves, still to be determined.  $J_m(x)$  denotes an  $m$ th order Bessel function of the first kind and  $H_m^{(1)}(x)$  and  $H_m^{(2)}(x)$  are type 1 and 2 Hankel functions, where  $H_m^{(1)}(x) = J_m(x) + iY_m(x)$  and  $H_m^{(2)}(x) = J_m(x) - iY_m(x)$ , with  $Y_m(x)$  the Bessel function of the second kind [14].

The third condition, finiteness at the origin, means that  $D_m = E_m$  in order to have no  $Y_m(n_a k r)$  terms at the origin (since  $Y_m(0) \rightarrow \infty$ ). The final two conditions of continuity and smoothness require:

$$\begin{bmatrix} J_m(n_a k a) & -H_m^{(1)}(n_b k a) \\ n_a J_m'(n_a k a) & -n_b H_m^{(1)'}(n_b k a) \end{bmatrix} \begin{bmatrix} 2D_m \\ B_m \end{bmatrix} = \begin{bmatrix} A_{\epsilon_m} i^m J_m(n_b k a) \\ A_{\epsilon_m} i^m n_b J_m(n_b k a) \end{bmatrix}, \quad (6)$$

with a dash denoting differentiation with respect to  $r$ .

Solving this system of simultaneous linear equations gives:

$$D_m = E_m = \frac{1}{2} \frac{A_{\epsilon_m} i^m (J_m(n_b k a) H_m^{(1)'}(n_b k a) - J_m'(n_b k a) H_m^{(1)}(n_b k a))}{J_m(n_a k a) H_m^{(1)'}(n_b k a) - \frac{n_a}{n_b} J_m'(n_a k a) H_m^{(1)}(n_b k a)}, \quad (7)$$

$$B_m = \frac{E_m J_m(n_a k a) - A_{\epsilon_m} i^m J_m(n_b k a)}{H_m^{(1)}(n_b k a)}. \quad (8)$$

The case of two concentric cylinders may be solved using the same method. The wavefunctions inside the inner cylinder and outside both cylinders may again be described using Eqs. (4) and (5). The wavefunction for the region between the two cylinders has the same form as for that inside the cylinder (radially expanding and contracting waves), with coefficients  $F_m$  and  $G_m$  instead of  $D_m$  and  $E_m$  in Eq. (4). The condition requiring the wavefunction to be finite at the

origin again gives  $D_m = E_m$  and the four remaining boundary conditions (requiring continuity and smoothness at each of the boundaries  $r = a$  and  $r = b$ ) are summarised in the following system of equations:

$$\begin{bmatrix} J_m(n_a ka) & -H_m^{(1)}(n_b ka) & -H_m^{(2)}(n_b ka) & 0 \\ n_c J_m(n_a ka) & -n_b H_m^{(1)'}(n_b ka) & -n_b H_m^{(2)'}(n_b ka) & 0 \\ 0 & H_m^{(1)}(n_b ka) & H_m^{(2)}(n_b ka) & -H_m^{(1)}(n_c kb) \\ 0 & n_b H_m^{(1)}(n_b kb) & n_b H_m^{(2)}(n_b kb) & -n_c H_m^{(1)}(n_c kb) \end{bmatrix} \quad (9)$$

$$\times \begin{bmatrix} 2D_m \\ F_m \\ C_m \\ B_m \end{bmatrix} = \begin{bmatrix} 0 \\ 0 \\ A \epsilon_m i^m J_m(n_c kb) \\ A \epsilon_m i^m n_c J_m(n_c kb) \end{bmatrix}$$

which may then be solved to find the required coefficients.

For each additional cylinder boundary, there will be one additional coefficient for the radially expanding wave and one for the radially contracting wave in the new region. There will also be an additional two conditions on the solution, i.e., smoothness and continuity at the new boundary, which therefore specify sufficient conditions to solve for all scattered wave coefficients.

Given that the non-zero terms within Eq. (9) are very similar in magnitude (different by only a very small order for small wavelengths, such as X-rays incident on millimetre size objects with  $n$  close to 1), solving by numerical matrix inversion or numerical singular value decomposition [9] was not sufficient to give accurate results. This could be seen by evaluating the intensity of the wavefield in the  $x$ - $z$  plane and looking at the boundaries of the cylinder. In order to have a smooth and continuous intensity at these boundaries, the full expression for each coefficient (as given in Eqs. (7) and (8) for a single cylinder) had to be evaluated numerically.

Fig. 2 shows the scattered coefficient  $B_m$  converging to zero for large  $m$ , clearly specifying the number of terms required when evaluating the solution (e.g. just over 4000 terms in 2 a) and c)). The cut-off term number is equal to  $ka$ , which expresses the number of X-ray wavelengths that fit into half the cylinder. The scattering coefficients for the wavefunction(s) inside the cylinder(s) continue to oscillate with significant magnitude around zero for much larger  $m$ , however only  $B_m$  is required for evaluation of phase contrast images outside the cylinder. For each additional concentric cylinder, another half-ellipse outline may be seen in the form of the plot for  $B_m$ , as in 2 c). Fig. 2 a) and b) clearly demonstrate that evaluating the wavefield either with shorter wavelength or incident on a larger radius cylinder will require more terms, in accordance with the cut-off at  $ka$ .

This means the number of terms required increases inversely with the wavelength of light used. In order to numerically evaluate images for wavelengths in the region of X-rays incident on millimetre-size objects, millions of terms are required, and hence significant computation time. Since both Bessel and Hankel functions are given by an integral over the summing coefficient ( $m$ ), evaluating these functions recursively during evaluation of  $B_m$  and the final wavefield decreases computation time significantly. Evaluation of different pixels from the same image may also be executed on several computer nodes to decrease the required time per image. However, a  $2000 \times 1$  pixel image of 1 Å radiation scattered from a 1 mm cylinder will still require 26 h to evaluate on the VPAC (Victorian Partnership for Advanced Computing) Tango cluster (using two nodes each with 2 AMD 2356 quad core processors and 32 GB RAM). This demonstrates the utility of the projection approximation, which takes less than a second to simulate the same image on a single desktop computer.

The solution was evaluated at a given propagation distance, determining  $\phi$  and  $r$  at each pixel position and evaluating Eq. (5) through the addition of a plane wave to the sum as given in the second half of the expression.

### 3. Comparison of exact solution to the projection approximation simulation

The exact description of the wavefield scattered by a dielectric cylinder is compared to the field predicted for the projection approximation via simulated phase contrast images. This is done first through comparison of intensity images, and then via the complex wavefield mapped to the Argand plane. Finally, the projection approximation is revealed as a result of an asymptotic approximation to the exact solution.

#### 3.1. Numerical comparisons

##### 3.1.1. Intensity images

The simulated PCXI images produced by both the projection approximation and the exact solution appeared as expected for an X-ray plane wave scattered from a single cylinder of radius  $a$ , with  $a$  being much larger than the radiation wavelength. Diffraction fringes were seen showing the edges of the cylinder, growing wider and more intense as a result of increased propagation, as seen in Fig. 3. The fringes will also be narrower and stronger in intensity as a result of a larger radius cylinder, which will produce a sharper image of the edge between the two regions.

According to the projection approximation, there is no intensity variation due to phase contrast along the exit plane, but in fact the

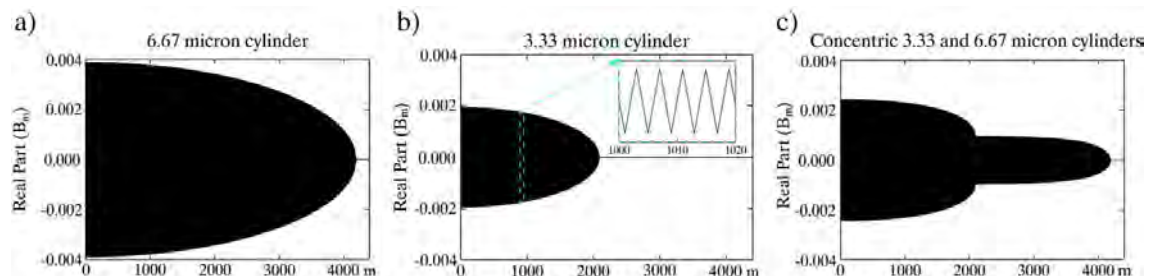


Fig. 2. The real part of the scattered wave coefficient  $B_m$ , showing an ellipse-like shape for each of the scattering cylinders of radius a) 6.67  $\mu\text{m}$ , b) 3.33  $\mu\text{m}$  and c) concentric 3.33  $\mu\text{m}$  and 6.67  $\mu\text{m}$  cylinders, hence specifying the number of terms ( $= ka$ ) required when evaluating a phase contrast image outside of the cylinders. High frequency oscillations present in all three are shown in the inset of b). (Simulated using wavelength of 100 Å and refractive indices  $\delta_{\text{inside}} = 4.5 \times 10^{-7}$ ,  $\beta_{\text{inside}} = 4.2 \times 10^{-8}$ ,  $\delta_{\text{between}} = 2 \times 10^{-7}$ ,  $\beta_{\text{between}} = 4 \times 10^{-8}$ ,  $\delta_{\text{outside}} = 0$ ,  $\beta_{\text{outside}} = 0$ ). The imaginary part of  $B_m$  converges to zero in the same way, simply with a quarter-wave phase difference in the high frequency oscillations.



**Fig. 3.** Phase contrast fringes from the exact analytical solution for light of  $\lambda = 100 \text{ \AA}$  incident on the edge of a 1 mm diameter cylinder (using  $\delta = 4.00 \times 10^{-7}$ ,  $\beta = 3.6889 \times 10^{-10}$ ), propagated a) 1  $\mu\text{m}$ , b) 1 mm and c) 5 mm.

exact solution should have some very narrow fringes due to the small propagation distance shown by the dotted line in Fig. 1. The diffraction that occurs in the space around  $x = \pm a$  between the edge position ( $z = 0$ ) and the exit surface ( $z = a$ ) will be sufficient for the wave that has passed through the edge of the cylinder to interfere with the wave passing outside the cylinder. While these resulting fringes at  $z = a$  should not be very strong or wide, they will be present. As the projection approximation effectively projects each material to be an infinitely thin phase-amplitude screen coincident with the exit surface, the diffraction and interference of waves is not described until after propagating the wavefunction downstream of the exit surface.

When evaluating the two models over a range of propagation distances, the expected discrepancy was observed at short propagation. Not only on contact, but also for small propagations, where the distance

was of the order of the cylinder radius, the projection approximation differed from the exact model. This is seen in Fig. 4 a), b) and c), where the projection approximation predicts smaller amplitude fringes than those expected and seen in the exact solution. The simulated fringes from the projection approximation model are smaller in both intensity and in width or fringe spacing, as would be seen at a shorter propagation.

This discrepancy was not seen when the propagation between the edge of the cylinder (at  $z = 0$ ) and the exit surface (at  $z = a$ ) was small compared to the total propagation distance  $z$ , i.e.  $z \gg a$ . At such large propagation distances, similar to those that are typically used in phase contrast imaging, the two approaches converge, as seen even with the comparatively short 10 mm propagation of Fig. 4 d), validating the use of the projection approximation. Fig. 4 also shows that the fringe as predicted by the projection approximation at 0.5 mm propagation

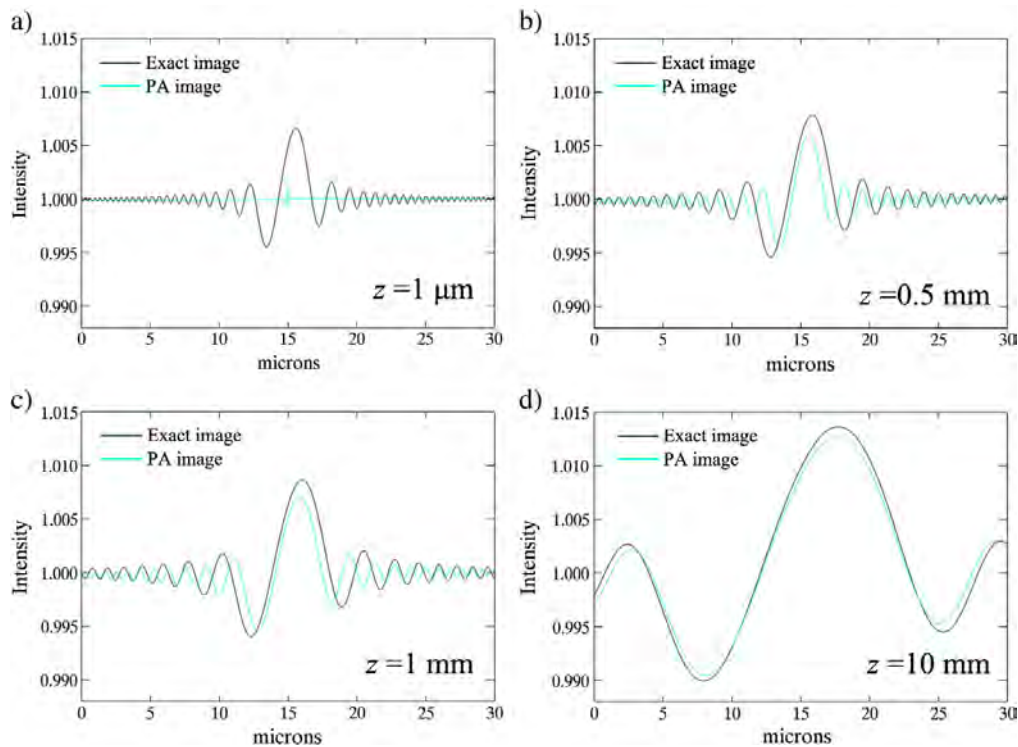


**Fig. 4.** Phase contrast fringes are underestimated by the projection approximation at propagation distances  $z$  comparable to the cylinder diameter (propagation = a) 1  $\mu\text{m}$ , b) 0.5 mm, c) 1 mm), but become much closer in amplitude and spacing for significantly larger propagation (propagation = d) 10 mm). Simulated with 100  $\text{\AA}$  wavelength radiation incident on a 1 mm diameter cylinder with  $\delta = 4.0 \times 10^{-7}$ ,  $\beta = 3.6889 \times 10^{-10}$ . The projection approximation is shown in blue and the exact solution in black.

(Fig. 4 b)) is very similar to that predicted by the exact solution on negligible propagation (Fig. 4 a)). This is due to the effective propagation of 0.5 mm, the radius of the cylinder, in the exact solution.

This effective propagation within the volume is best illustrated by an  $x$ - $z$  intensity distribution, as seen in Fig. 5 (similar to intensity distributions produced by Janowicz when summing the scattered field from a large number of dipoles positioned on a circle [15]). At the “exit” plane,  $z = a$ , there are phase contrast fringes present, due to  $a$  metres of propagation from the edge (at the origin  $z = 0$ ). It is also interesting to note in Fig. 5 b) that there is a cusp caustic  $\alpha$  on the inside of the cylinder, similar to that seen when sunlight hits the inside of a cup. This caustic surface, which is singular in the zero-

wavelength limit of geometric optics, is modified into a non-singular albeit peaked intensity distribution by the non-zero wavelength [16].

The build-up of phase lag through the cylinder is seen in Fig. 5 c), with a “shadow” behind the cylinder, as predicted by the projection approximation. However, there are also diffraction-induced phase variations from the edge of the cylinder at the “exit” plane. The vertical stripes seen in the phase distribution inside the cylinder are a numerical effect of subtracting the incident plane wave from a region where the largely planar wavefield comes from the sum of many cylindrical functions, hence lacks the required micro-radian precision in phase.

It should be noted that most experimental images will not show many more than a few diffraction fringes per edge, due to the finer fringes being suppressed by the point spread function of the imaging set-up. A biomedical phase contrast image (for example, of an airway in a mouse or rabbit) often shows only one or two fringes, due to the overlying textured tissue and scattering within the volume [5].

### 3.1.2. Complex wavefield Argand-plane signatures

The signature of the projection approximation and propagation based phase contrast in the Argand plane has been shown in earlier work [4]. This maps the complex wavefield at a given image plane of constant  $z$  to an Argand-plane trace, with phase and intensity parameterized by transverse position  $x$  along a plane downstream of the cylinder. The intensity of the image will therefore be given by the absolute value of the complex phasor in the Argand plane, the distance from the origin to the tip of the phasor. The exact solution gives the same shape as seen in our earlier work [4], a combination of a Cornu spiral [17] and a hypocycloid winding its way around the complex plane, slowly changing in phase in accordance with the projection approximation. The Cornu spiral describes the diffracted wavefield outside the geometric shadow of the cylinder, where the fringes increase in intensity and width closer to the edge. These are created by the addition of the incident plane wave to a cylindrical wave originating from the edge of the cylinder. The same fringes are seen moving inside the geometric shadow of the cylinder, but here the increasing projected thickness slowly increases the phase difference. This means a moving Cornu spiral is seen as a hypocycloid.

A comparison between the traces formed by the projection approximation simulation and the exact solution shows the discrepancy observed at short propagation distances. As seen in Fig. 6 a), at 1 micron propagation, the projection approximation predicts no intensity contrast due to phase effects, with almost uniform intensity (apart from attenuation effects) near the edge of the geometric shadow of the cylinder. The analytical solution however, does show intensity fringes, clearly seen in the cycloid extending along nearly the entire trace, due to the propagation between the edge of the cylinder and the exit plane. The traces here correspond with the intensity profiles in Fig. 4. It is seen again that at long propagations, the two approaches become more similar with the same intensity fringes.

However, it can also be seen that there is a difference in the phase change incurred from the cylinder itself, with the exact solution traversing a longer arc in the uniform-intensity Argand-plane circle. This is likely due to the phase difference which is incurred due to intensity gradients within the scattering volume, which can be viewed as an altering of the local refractive index  $n$ , as a function of intensity  $I$ , according to [7]:

$$n \rightarrow n \sqrt{1 + \frac{1}{n^2 k^2} \frac{\nabla^2 \sqrt{I}}{\sqrt{I}}}. \quad (10)$$

These intensity gradients are seen in the intensity distribution of Fig. 5, and using this intensity distribution the difference in the phase shift was calculated across the cylinder. Evaluating the expected diffraction-induced phase difference using this altered  $n$  value within the projection approximation gave differences of the same order of magnitude as seen in the Cornu spirals (adequate

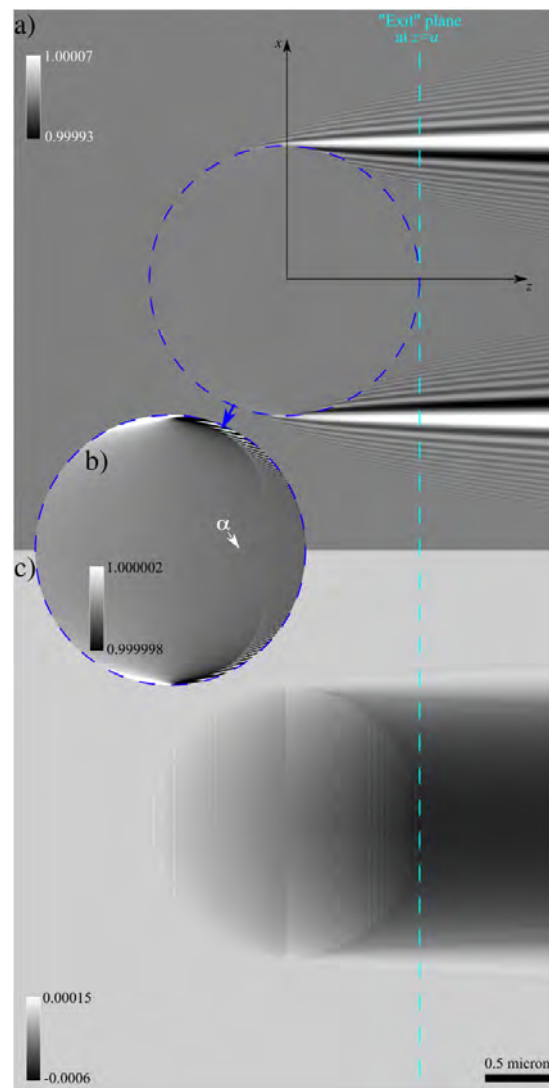


**Fig. 5.** The  $x$ - $z$  plane wavefield for 100 Å waves incident from the left on a 1 μm radius cylinder, showing phase contrast before and after the “exit surface”, in a) Intensity and c) Phase. The intensity for the region inside the cylinder is shown in high contrast in b) to visualise the cusp caustic  $\alpha$ . A small cylinder is used to reduce numerical evaluation time, particularly given the number of terms required to evaluate the field within the cylinder (see the end of Section 2).

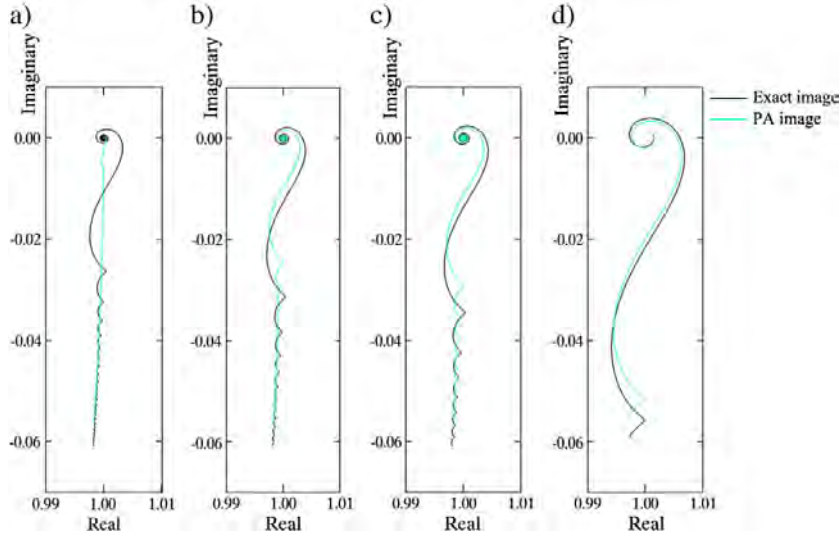


**Fig. 6.** Argand plane traces for the intensity profiles given in Fig. 4, for propagations of a) 1 μm, b) 0.5 mm, c) 1 mm, d) 10 mm; analytic solution shown in black and the projection approximation shown in blue. Since the traces rapidly rotate around the origin with propagation, a full  $2\pi$  rotation for each wavelength, the analytical solution and the projection approximation do not match in starting phase for any propagation length, due to sub-wavelength differences introduced when not taking into account propagation within the volume. Each trace is rotated to begin at zero phase angle for easy comparison between the two traces.

sampling of the complicated wavefield created by the small wavelength in a large cylinder was difficult), suggesting that this is a likely cause of the difference. In the case of Fig. 5, this difference is of the order of tens of microradians. This would mean the inability of the projection approximation to take into account diffraction-induced phase shifts within the scattering volume predicts a phase arc in the Argand plane that is not strictly accurate. A larger difference in phase arc length was also observed at shorter wavelengths, consistent with Eq. (10).

3.2. Mathematical comparisons

The exact solution rigorously solves the inhomogeneous Helmholtz equation (Eq. (3)), with the projection approximation corresponding to paraxial radiation with negligible diffraction within the scattering volume. This means that the projection approximation should result from suitable approximations applied to the exact solution. As expected, evaluating the exact solution for no object ( $n_a = n_b = n_c \dots$ ) gives a plane wave; a trivial solution of the homogeneous Helmholtz equation. While it is expected that introducing asymptotic approximations for the Hankel and Bessel functions into the analytical solution should lead to the projection approximation at longer propagations, this problem is not tractable for all positions. This is due to the fact that the exact solution is a sum from 0 to  $ka$ , hence the approximations for the Hankel and Bessel functions must be valid for orders from 0 up to the argument ( $ka$ ). An approximation valid for this entire region is due to Debye [18], given by:

$$J_m(m \sec \beta) \approx \left(\frac{2}{m \tan \beta}\right)^{\frac{1}{2}} \left[ \cos\left(m \tan \beta - m\beta - \frac{\pi}{4}\right) \sum_{s=0}^{\infty} \frac{(-)^s \Gamma(2s + \frac{1}{2})}{\Gamma(\frac{1}{2})} \frac{A_{2s}}{(\frac{1}{2} m \tan \beta)^{2s}} + \sin\left(m \tan \beta - m\beta - \frac{\pi}{4}\right) \sum_{s=0}^{\infty} \frac{(-)^s \Gamma(2s + \frac{3}{2})}{\Gamma(\frac{3}{2})} \frac{A_{2s+1}}{(\frac{1}{2} m \tan \beta)^{2s+1}} \right] \tag{11}$$

where  $A_0 = 1, A_1 = \frac{1}{8} + \frac{5}{24} \cot^2 \beta, A_2 = \frac{3}{128} + \frac{77}{576} \cot^2 \beta + \frac{385}{3456} \cot^4 \beta$  and  $\Gamma(x)$  is the Gamma function. The first factor in the sum over  $s$  has a denominator which increases with  $s$ , given that  $\Gamma(n/2) = \sqrt{\pi}(n-2)!!/2^{(n-1)/2}$ . However, the second factor has  $m \tan \beta = \sqrt{z^2 - m^2}$  in the denominator which will go from many millions down towards 0 as  $m$  goes from 0 to many millions in the sum over  $m$ . While this will be the simple case for the first term in  $s$ , the second term in  $s$  will square this factor and the third raise this factor to the power four, resulting in a very large denominator. This will mean that the second factor in this sum over  $s$  will decrease very quickly with increasing  $s$ . Given that  $A_s$  also decreases in magnitude for larger  $s$ , the first term in  $s$  may be sufficient to give a good approximation for the Bessel function. Using only the first term in the sum over  $s$  gives:

$$J_m(m \sec \beta) \approx \left(\frac{2}{m \tan \beta}\right)^{\frac{1}{2}} \left[ \cos\left(m \tan \beta - m\beta - \frac{\pi}{4}\right) + \sin\left(m \tan \beta - m\beta - \frac{\pi}{4}\right) \left(\frac{1}{2} \times \frac{1}{8} + \frac{5}{24} \cot^2 \beta\right) \right] \tag{12}$$

This may then expressed in terms of an argument  $z$  as

$$J_m(z) \approx \left(\frac{2}{\pi \sqrt{z^2 - m^2}}\right)^{\frac{1}{2}} \left[ \cos\left(\sqrt{z^2 - m^2} - m \arctan\left(\frac{\sqrt{z^2 - m^2}}{m}\right) - \frac{\pi}{4}\right) + \sin\left(\sqrt{z^2 - m^2} - m \arctan\left(\frac{\sqrt{z^2 - m^2}}{m}\right) - \frac{\pi}{4}\right) \times \left(\frac{1}{8\sqrt{z^2 - m^2}} + \frac{5m^2}{24(z^2 - m^2)^{\frac{3}{2}}}\right) \right] \tag{13}$$

The Hankel function of the second kind (also required to describe the wavefield outside the cylinder) is approximated by Debye as:

$$H_m^{(2)}(m \sec \beta) \approx \frac{e^{-mi(\tan \beta - \beta) + \frac{\pi i}{4}}}{\sqrt{\frac{m}{2} \tan \beta}} \sum_{s=0}^{\infty} \frac{\Gamma(s + \frac{1}{2})}{\Gamma(\frac{1}{2})} \frac{A_s}{(-\frac{1}{2}mi \tan \beta)^s}. \quad (14)$$

Taking only the first term in the sum over  $s$  and expressing in terms of a single argument  $z$  gives,

$$H_m^{(2)}(z) \approx \frac{e^{-i\sqrt{\chi^2 - m^2} + im \arctan\left(\frac{\sqrt{\chi^2 - m^2}}{m}\right) + \frac{\pi i}{4}}}{\sqrt{\frac{\pi}{2}(\chi^2 - m^2)^{\frac{1}{2}}}}, \quad (15)$$

which is a good approximation for large-order Hankel functions of the second kind. The complexity of these expressions means that neither computer algebraic simplification packages Matlab 7.4 or Mathematica 6 nor manual simplification has been able to simplify the coefficients  $B_m$  and  $D_m$  within the full wavefield expression, and hence reach a simplified description of the wavefield.

However, at the origin ( $r=0$ ), a special case arises, where the exact solution may be simplified and will become the projection approximation, predicting a phase change and attenuation for thickness  $T=a$ , the radius of the cylinder. Eq. (4), with the result  $D_m = E_m$  from the boundary conditions, is

$$\psi_{\text{inside}}(r, \phi) = e^{-i\omega t} \sum_{m=0}^{\infty} 2D_m J_m(n_a k r) \cos(m\phi). \quad (16)$$

Evaluating this internal wavefield at the origin, or centre of the circle, will give:

$$\psi_{\text{inside}(0,0)} = e^{-i\omega t} \sum_{m=0}^{\infty} 2D_m J_m(0). \quad (17)$$

Given that  $J_0(0) = 1$  and all other  $J_{m \neq 0}(0) = 0$ , this leaves:

$$\psi_{\text{inside}(0,0)} = e^{-i\omega t} 2D_0. \quad (18)$$

The coefficient  $D_m$  (Eq. (7)), found from the boundary conditions, may then be simplified using asymptotic forms of the Bessel and Hankel functions at the cylinder boundaries. Given the short wavelengths involved, the following asymptotic forms of the Bessel and Hankel functions for large argument ( $>2$ ) and small order may be taken [14]:

$$J_m(z) \rightarrow \sqrt{\frac{2}{\pi z}} \cos\left(z - \frac{m\pi}{2} - \frac{\pi}{4}\right), \quad (19)$$

$$H_m^{(1)}(z) \rightarrow \sqrt{\frac{2}{\pi z}} e^{i\left(z - \frac{m\pi}{2} - \frac{\pi}{4}\right)}. \quad (20)$$

The recurrence relations  $C'_m(z) = -C_{m+1}(z) + \frac{m}{z}C_m(z)$ , where  $C(z) = H_m^{(1)}(z), H_m^{(2)}(z)$  or  $J_m(z)$  [14] will also be required for the derivatives. Given that we require order  $m=0$  only, this becomes:

$$C'_0(z) = -C_1(z). \quad (21)$$

Substituting Eqs. (19)–(21) into Eq. (7) to evaluate  $D_0$ , and simplifying, yields:

$$D_0 = \frac{1}{2}A \frac{2i\sqrt{n_a}}{\sqrt{n_b}((1-n_a/n_b)e^{i(n_a+n_b)ka} + i(1+n_a/n_b)e^{i(n_b-n_a)ka})}. \quad (22)$$

Given that  $n_a$  and  $n_b$  are very close to 1,  $1+n_a/n_b \gg 1-n_a/n_b$ :

$$D_0 = \frac{1}{2}A \frac{\sqrt{n_a n_b}}{n_a + n_b} 2e^{i(n_a - n_b)ka}. \quad (23)$$

Given again that  $n_a$  and  $n_b$  are very close to 1,  $\sqrt{n_a n_b} / (n_a + n_b)$  is very close to one half, and expanding the refractive index into complex parts gives:

$$D_0 = \frac{1}{2}Ae^{-i(\delta_a - \delta_b - i\beta_a + i\beta_b)ka}. \quad (24)$$

Putting this back into the expression for the wave at the origin gives:

$$\psi_{\text{inside}}(0, 0) = Ae^{-i\omega t} e^{-ik(\delta_a - \delta_b)a} e^{-k(\beta_a - \beta_b)a}. \quad (25)$$

The exact solution has therefore become the projection approximation at the centre of the cylinder. For example, if the region outside the cylinder has refractive index 1 ( $\delta_b = \beta_b = 0$ ), having passed through thickness  $a$ , the radius of the cylinder, the resulting wavefield corresponds to Eq. (1), the projection approximation.

4. Discussion

This work has shown that the projection approximation consistently underestimates the visibility and width of phase contrast fringes at short propagation in simulation, complementing experimental comparisons made in earlier work [4]. The underestimated fringes occur when a significant amount of the total diffraction may occur within the volume to which the approximation is applied. This prompts a discussion on the relative complexity of optical models, starting from the simplest ray models and increasing in sophistication to a wave-optical description, illustrated schematically in Fig. 7.

This hierarchy of models in optics is an analogue of that in mechanics, in which the inner oval would represent classical mechanics, appropriate in some cases. There is then a regime where a semi-classical mechanics model (the middle oval) is required [19], making use, for example, of the Wentzel–Brillouin–Kramers (WKB) method, with quantum mechanics then forming the outer and most general oval in such a diagram. Similarly, it is the limit between wave optics and a complex ray model which is discussed in this paper, as indicated in Fig. 7.

A simple ray description is adequate in situations when it is acceptable to effectively ‘walk along rays’, while ignoring any interference

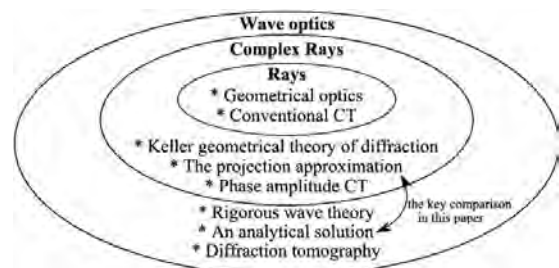


Fig. 7. The concepts by which optics may be described and the ideas which fall under each concept.

between overlapping rays [20]. For example, computed tomography (CT) reconstructions from projection images make the assumption that rays pass through the imaged volume in a straight line, simply undergoing absorption, in order to reconstruct a three dimensional volume [21]. However, Keller's geometrical theory of diffraction [22] is required to extend the theory to describe phase-amplitude CT [23]. Similarly, the projection approximation describes the intensity and phase changes on single rays through a scattering volume assuming they simply travel in a straight line through the volume. Even further, diffraction tomography [24–27] requires a full wave description, albeit under the first Born approximation. As with the tomographic techniques, a rigorous classical wave theory is required in phase contrast imaging when diffraction within the volume is significant (e.g., PCXI with a very short propagation distance). It may be necessary to pay attention to diffraction within a volume, not only when there are voids inside the object imaged, but also when the volume is not coincident with (flat against) the exit plane. A comparison between the projection approximation and an analytical solution for a plane wave incident on a cylinder, as studied here, exemplifies this difference.

The straight line approximation can also be seen in treating the projection approximation as an Ewald sphere [28], where the scattered wave vector is always pointing in much the same direction as incident wave vector. In such a case (angles are of the order of picoradians) it is a valid approximation to treat the Ewald sphere as flat, given only a very small scattering angle is ever observed [29]. This corresponds to the key assumption of the projection approximation, that the scatterer is not sufficiently strong to disturb ray paths, therefore fitting within the middle circle of Fig. 7. A weak scattering case satisfying the first Born approximation may therefore also be a case which is valid within the projection approximation.

## 5. Conclusion

An exact solution to the wavefield resulting from an X-ray plane wave incident on one or more concentric cylinders has been studied. This has shown that the projection approximation can be used to efficiently and accurately simulate biomedical PCXI. The comparison has also shown that the projection approximation will predict smaller fringes than observed at propagations comparable to empty spaces within the volume, due to the additional diffraction which occurs within the scattering volume. Mathematical approximations have shown that in the special case of within the scattering volume, where diffraction will not be significant, the projection approximation may be directly obtained from the exact solution. Given that evaluation of the exact solution requires significantly more computation time than the PA model and that the distances used in PCXI are typically much larger than the volumes imaged, the projection approximation is a good model for the study of phase contrast X-ray imaging.

## Acknowledgements

Kaye Morgan would like to acknowledge the support of an Australian Postgraduate Award and a J.L. William Scholarship from Monash University. David Paganin acknowledges the Australian Research Council, together with useful discussions with Christian Dwyer, Timur Gureyev and Freda Werdiger. Karen Siu acknowledges the National Health and Medical Research Council. The computational parts of this work were supported by the Victorian Partnership for Advanced Computing HPC Facility and Support Services.

## References

- [1] A. Snigirev, I. Snigireva, V. Kohn, S. Kuznetsov, I. Schelokov, *J. Phys. D Appl. Phys.* 29 (1995) 133.
- [2] P. Cloetens, R. Barrett, J. Baruchel, J.P. Guigay, *J. Phys. D Appl. Phys.* 29 (1996) 133.
- [3] S.W. Wilkins, T.E. Gureyev, D. Gao, A. Pogany, A.W. Stevenson, *Nature* 384 (6607) (1996) 335.
- [4] K.S. Morgan, K.K.W. Siu, D.M. Paganin, *Opt. Express* 18 (2010) 9865.
- [5] K.K.W. Siu, K.S. Morgan, D.M. Paganin, R. Boucher, K. Uesugi, N. Yagi, D.W. Parsons, *Eur. J. Radiol.* 68 (2008) S22.
- [6] P. Cloetens, L. Wolfgang, J. Baruchel, J.G.P. Pernot-Rejmánková, M. Salomé-Pateyron, M. Schlenker, J. Buffière, E. Maire, G. Peix, *J. Phys. D Appl. Phys.* 32 (1999) A145.
- [7] D.M. Paganin, *Coherent X-ray Optics*, Oxford University Press, New York, 2006.
- [8] M. Nieto-Vesperinas, *Scattering and Diffraction in Physical Optics*, 2nd Edition, World Scientific Publishing, New Jersey, 2006.
- [9] W.H. Press, B.P. Flannery, S.A. Teukolsky, W.T. Vetterling, *Numerical Recipes in C: The Art of Scientific Computing*, 2nd Edition, Cambridge University Press, Cambridge, 1992.
- [10] A.N. Tikhonov, A.A. Samarskii, *Equations of Mathematic Physics*, Pergamon Press, Oxford, 1963.
- [11] L. Rayleigh, *Philos. Mag.* 12 (1881) 81.
- [12] J. Wait, *Can. J. Phys.* 33 (5) (1955) 189.
- [13] P.M. Morse, H. Feshbach, *Methods of Theoretical Physics*, McGraw-Hill Book Company, New York, 1953.
- [14] M. Abramowitz, I.A. Stegun (Eds.), *Handbook of Mathematical Functions*, 10th Edition, National Bureau of Standards, Applied Mathematics Series - 55, New York, 1972.
- [15] M. Janowicz, *J. Mod. Opt.* 57 (2010) 366.
- [16] J.F. Nye, *Natural Focusing and Fine Structure of Light*, Institute of Physics Publishing, Bristol and Philadelphia, 1999.
- [17] M. Born, E. Wolf, *Principles of Optics: Electromagnetic Theory of Propagation, Interference and Diffraction of Light*, Cambridge University Press, Cambridge, 1999.
- [18] G.N. Watson, *A Treatise on the Theory of Bessel Functions*, 2nd Edition, Cambridge University Press, Cambridge, 1944.
- [19] S.M. Kennedy, D.M. Paganin, D.E. Jesson, *Am. J. Phys.* 72 (2008) 158.
- [20] M. Berry, *Proc. SPIE* 3487 (1998) 1.
- [21] A.C. Kak, M. Slaney, *Principles of Computerized Tomographic Imaging*, Society of Industrial and Applied Mathematics, New York, 2001.
- [22] J.B. Keller, *J. Opt. Soc. Am.* 52 (1962) 116.
- [23] P. Cloetens, M. Salomé-Pateyron, J. Buffière, G. Peix, J. Baruchel, F. Peyrin, M. Schlenker, *J. Appl. Phys.* 81 (1997) 5878.
- [24] E. Wolf, *Opt. Commun.* 1 (1969) 153.
- [25] G. Harding, J. Kosanetzky, *Phys. Med. Biol.* 30 (1985) 183.
- [26] J. Kosanetzky, B. Knoerr, G. Harding, U. Neitzel, *Med. Phys.* 14 (1987) 526.
- [27] K.M. Pavlov, C.M. Kewish, J.R. Davis, M.J. Morgan, *J. Phys. D Appl. Phys.* 33 (2000) 1596.
- [28] P.P. Ewald, *Phys. Z.* 14 (1913) 465.
- [29] H.A. Cohen, M.F. Schmid, W. Chiu, *Ultramicroscopy* 14 (1984) 219.

---

## X-ray Coherence when using a Spinning Phase Diffuser

---

*Measurement of hard x-ray coherence in the presence of a rotating random-phase-screen diffuser.*

by Kaye S. Morgan\*, Sarah C. Irvine\*, Yoshio Suzuki, Kentaro Uesugi, Akihisa Takeuchi, David M. Paganin and Karen K. W. Siu. \*Both authors contributed equally to this work.

Published in Optics Communications **283**, pp. 216-225, 2010.

---

Having established a method of modelling ideal propagation-based phase contrast images of interfaces (Chapters 2 and 3), we now move to looking at the non-ideal imaging set-up used in experiment, specifically beamline 20XU of the SPring-8 synchrotron. This beamline is used in the application work of Chapter 6, and provides a high degree of both temporal and spatial coherence (see section 1.3), producing sharp, high contrast fringes from interfaces. However, the transverse coherence width will change by almost an order of magnitude depending on which imaging hutch is used ( $\sim 75$  m or  $\sim 250$  m from the source), the dimensions of the aperture collimating the beam in the optics hutch and the presence or absence of a spinning phase diffuser. Optimisation of the set-up for maximal phase contrast is required to reveal the indistinct biological interfaces studied in Chapter 6. It is also valuable to have a measure of the coherence width observed with each set-up for use in accurately modelling the creation of propagation-based phase contrast images at BL20XU.

This paper details measurements of the transverse coherence width, taken at beamline 20XU with 25 keV x-rays (as used for small animal imaging in Chapter 6). In particular, we study the decrease in the magnitude of the complex degree of coherence observed when a spinning random-phase-screen diffuser is introduced. This diffuser is used to produce a more even area of illumination and remove unwanted phase images due to optical elements along the beamline. The coherence width seen from the Gaussian storage ring electron beam, behind a square aperture, is also considered and modelled, both for cases where the apertures is comparable to and different from the source size.

The results of this study influence the choice of diffuser, aperture and imaging hutch in the application work of Chapter 6.

## Declaration for Thesis Chapter 4

In the case of Chapter 4, contributions to the work involved the following:

Name	% contribution	Nature of contribution
Kaye Morgan	45%	Contributed to the original experiments, the data analysis, numerical simulations and the write-up
Sarah Irvine	45%	Contributed to the original experiments, the data analysis, numerical simulations and the write-up
Yoshio Suzuki		Contributed to the original experiments
Kentaro Uesugi		Contributed to the original experiments
Akihisa Takeuchi		Contributed to the original experiments
David Paganin		Provided supervisory advice, aided proofreading and drafting
Karen Siu		Contributed to the original experiments, provided supervisory advice, aided proofreading and drafting

### Declaration by co-authors

The undersigned hereby certify that:

1. the above declaration correctly reflects the nature and extent of the candidate's contribution to this work, and the nature of the contribution of each of the co-authors.
2. they meet the criteria for authorship in that they have participated in the conception, execution, or interpretation, of at least that part of the publication in their field of expertise;
3. they take public responsibility for their part of the publication, except for the responsible author who accepts overall responsibility for the publication;
4. there are no other authors of the publication according to these criteria;
5. potential conflicts of interest have been disclosed to (a) granting bodies, (b) the editor or publisher of journals or other publications, and (c) the head of the responsible academic unit; and
6. the original data are stored at the following location(s) and will be held for at least five years from the date indicated below: School of Physics and Monash Centre for Synchrotron Science, Clayton Campus, Monash University, Australia.

### Signatures:

Kaye Morgan:		Date: 19/10/10
Sarah Irvine:		Date: 18/10/2010
Yoshio Suzuki:		Date: 18/10/2010
Kentaro Uesugi:		Date: 18/10/2010
Akihisa Takeuchi:		Date: 18/10/2010
David Paganin:		Date: 18/10/2010
Karen Siu:		Date: 19.10.2010

---

This paper was published in Optics Communications and is made available as an electronic reprint with the permission of Elsevier. The paper can be found on the ScienceDirect website under doi:10.1016/j.optcom.2009.09.023. Systematic or multiple reproduction or distribution to multiple locations via electronic or other means is prohibited and is subject to penalties under law.

---



Contents lists available at ScienceDirect

Optics Communications

journal homepage: [www.elsevier.com/locate/optcom](http://www.elsevier.com/locate/optcom)

## Measurement of hard X-ray coherence in the presence of a rotating random-phase-screen diffuser

Kaye S. Morgan<sup>a,\*</sup>, Sarah C. Irvine<sup>a,\*</sup>, Yoshio Suzuki<sup>b</sup>, Kentaro Uesugi<sup>b</sup>, Akihisa Takeuchi<sup>b</sup>, David M. Paganin<sup>a</sup>, Karen K.W. Siu<sup>a,c</sup>

<sup>a</sup>School of Physics, Monash University, Victoria 3800, Australia

<sup>b</sup>Japan Synchrotron Radiation Research Institute (JASRI), SPring-8, Mikazuki, Hyogo 679-5198, Japan

<sup>c</sup>Monash Centre for Synchrotron Science, Monash University, Victoria 3800, Australia

### ARTICLE INFO

#### Article history:

Received 26 February 2009  
Received in revised form 10 September 2009  
Accepted 10 September 2009

#### PACS:

42.25.Kb  
41.60.-m  
41.50.+h  
29.20.dk  
07.85.Qe  
42.79.Bh  
87.64.mh

#### Keywords:

Coherence  
Synchrotron hard X-rays  
Prism interferometer  
Bio-medical phase contrast imaging

### ABSTRACT

A suitably large coherence area is important in coherent X-ray optics, when using techniques such as interferometry or phase contrast imaging (PCI). The work done by Suzuki using a prism interferometer to measure X-ray coherence at 12.4 keV [1] is here extended to consider the use of a diffuser at the bio-medical imaging energy of 25 keV. In order to achieve a broader, more even X-ray field and eliminate speckle, a spinning piece of paper may be used as a rotating random-phase screen to diffuse the hard X-ray beam, but this will concomitantly decrease the magnitude of the complex degree of second-order coherence. We also study the effect of source size and source-to-sample distance on coherence, where imaging area and required flux must be considered. Coherence measurements at the 20XU beamline at the SPring-8 synchrotron are compared to results from wave-optical computer modelling. These show that while the diffuser will decrease the magnitude of the complex degree of coherence, further free-space propagation will lessen this effect. In the design of an experiment, the collimating slit size and use of a diffuser must therefore be balanced with distance from the source, in order to maximise coherence while maintaining the desired field of view and exposure time.

© 2009 Elsevier B.V. All rights reserved.

### 1. Introduction

Coherent imaging techniques, such as interferometry and holography, rely on a high degree of correlation between wavefronts at different points in space and time. With poor coherence, key image features may be blurred out due to the associated incoherent summation of intensity, and those techniques which utilise the interference of waves will encounter problems such as inadequate interference-fringe visibility. When using synchrotron X-rays, high temporal coherence is achievable with undulators and monochromators, but in the context of propagation-based X-ray phase contrast this is not as important as a sufficiently high degree of spatial coherence [2]. In this paper, we will look at the complex

degree of second-order spatial coherence, measured by the correlation coefficient between two points, to give a measure of their statistical similarity [3]. Additionally we will look at the width of the spatially coherent area, hereafter referred to as the coherence width. This is considered to be the minimum transverse distance across a wavefield at which two points can be taken as spatially incoherent. In other words, when measuring the complex degree of coherence over an increasing distance between a pair of transverse points, this is the first distance across which the magnitude of the complex degree of coherence becomes zero. The coherence width is discussed since this is the limiting dimension in this experiment, given use of a synchrotron undulator source, where the electron beam profile is significantly wider than it is high. In third-generation synchrotrons, the electron beam trajectory and source profile may be considered fixed, however the spatial coherence may be improved with the use of suitable beam-line optics. While the X-ray field at the source may typically be considered incoherent (i.e., delta correlated) [4], with significant propagation

\* Corresponding authors. Tel.: +61 3 9905 3611; fax: +61 3 9905 3637.  
E-mail addresses: [Kaye.Morgan@sci.monash.edu.au](mailto:Kaye.Morgan@sci.monash.edu.au) (K.S. Morgan), [Sally.Irvine@sci.monash.edu.au](mailto:Sally.Irvine@sci.monash.edu.au) (S.C. Irvine).

<sup>1</sup> They contributed equally to this work.

the wavefunction increases in coherence, according to the van Cittert–Zernike theorem [5–7]. In fact the transverse coherence width is proportional to the propagation distance [8,9], hence the utility of working with a longer X-ray beamline in many coherent X-ray-optics contexts [10]. The use of apertures, slits or pinholes to create secondary sources may also significantly increase the coherence width at the sample and detector.

Some coherent X-ray imaging experiments, which necessitate very short exposure times, are perhaps best carried out closer to the source, where the achievable photon flux will be much higher. An upstream hutch position (where the sample position is closest to the source) is often preferred for such short exposure times, but is worse in terms of coherence. Electron orbit instabilities cause the X-ray beam centre to vary in position at the imaging plane, an effect which is exacerbated when the imaging hutch is at long distances from the source. To produce a more regular intensity field, sometimes an X-ray diffuser may be employed. This optical element is also used to even out unwanted speckle or corrugations in the illuminating wavefronts, introduced by various beam-line optics and other components such as windows [11].

One simple X-ray diffuser is a spinning piece of paper, placed across the X-ray beam soon after the monochromator to even out the field of view (cf. [12,13]). The diffuser spin period is much smaller than the exposure times, leading to a coherent-optics scenario that may be well approximated by incoherent averaging over an ensemble of spatially-random transverse phase screens. A diffuser of this kind has proven to be particularly useful on the X-ray undulator BL20XU at the SPring-8 synchrotron in Hyogo, Japan; it not only compensates for instabilities but also provides a beam with a larger area of uniform intensity. This beamline has two experimental hutches; the ‘upstream’ hutch, at 80 m from the source, and the ‘downstream’ hutch, at 245 m from the source, providing a choice of imaging locations. The monochromator is located in a separate optics hutch 40 m from the source, and the diffuser

sits 31.5 m further downstream, as close as practicable to the source side of the ‘upstream’ hutch.

A large area of uniform intensity is particularly valuable in biomedical applications of propagation-based phase contrast imaging [14]. Typical samples, such as small animals, have a thickness of up to a few centimetres. To achieve adequate flux for high resolution imaging after absorption by such samples, a higher energy such as 25 keV or even 30 keV is often used [15]. Importantly, it is also known that contrast from phase effects decreases with increasing energy much more slowly than absorption contrast [16], so quality phase images may be acquired at a reduced dose level [17].

Quantitative measurements of spatial coherence are important in the design of experiments using coherent X-ray optics techniques [18]. The idea of coherence is traditionally linked to interferometry [7], and most techniques for synchrotron-based X-ray coherence measurement are interferometric, or may be construed as such [19]. Conventional methods such as a Young’s double slit apparatus are effective, but often difficult to implement, due to the requirement for a range of precise slit separations (see, e.g. [20]). A Hanbury Brown–Twiss intensity interferometer [21] may be used for precise transverse coherence characterisation, but in addition to a high precision diffractometer, this requires extremely small-bandpass monochromators. These monochromators are required to achieve a sufficiently-small bandwidth that coincidence of photons may be counted. Inline holographic methods (also known as Gabor holography [22]) regard the Fresnel diffraction patterns of illuminated samples such as fibres and slits as interferograms from which source size and coherence width may be inferred (see, e.g. [16]). Another important method for coherence measurement makes use of a uniformly redundant array (URA), as a complex phase mask which diffracts the incident beam equivalently to the parallelized superposition of multiple Young’s experiments [23].

As an elegantly simple alternative to costly crystals and precisely machined masks, Suzuki has documented the use of a simple

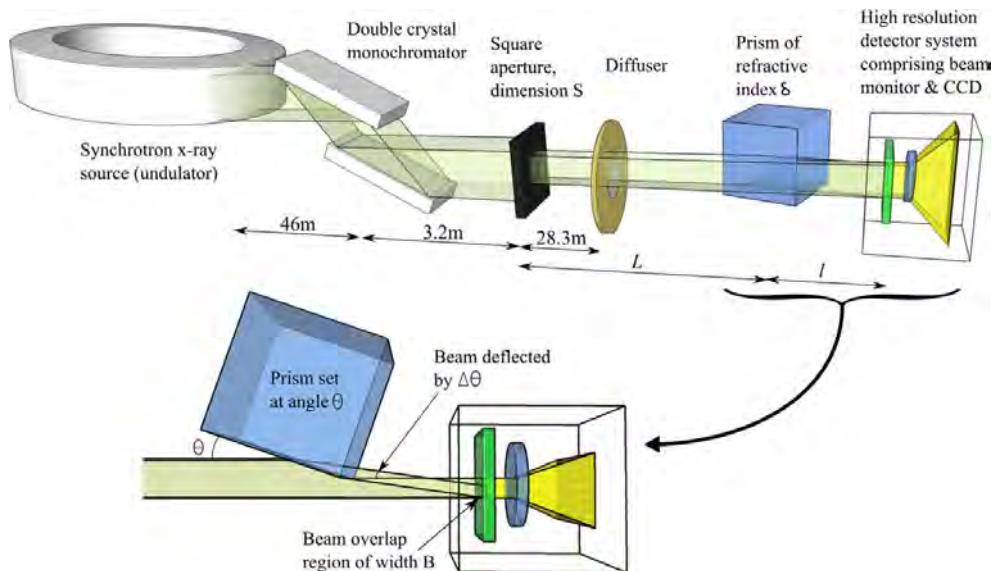


**Fig. 1.** Experimental set-up, using BL20XU at the SPring-8 synchrotron, with monochromator and aperture in the optics hutch, diffuser at the front of the upstream hutch, prism and camera in either the upstream or downstream hutch. Images taken with CCD detector coupled to a Hamamatsu AA50 X-ray converter, 50 $\times$  objective lens to give 0.18  $\mu\text{m}$  pixels. Mirror at 45 $^\circ$  between the lens and CCD omitted for simplicity in the above diagram.

Perspex prism interferometer [24] that works by interference of an X-ray beam with a refracted beam. This merely requires rotation of a very inexpensive (approx. ¥300) prism to vary the angle of refraction and hence the visibility of the resulting interference fringes [1] (see Fig. 1). In this paper we expand upon his work [1], which took a set of coherence measurements at the longer source-sample distance (downstream) at an energy of 12.4 keV, to a wavelength more suited to thicker samples (25 keV), in both upstream and downstream positions. In addition, we quantitatively observe the effect of a diffuser on the coherence properties, both in experiment and when simulating the diffuser as a random-phase screen. We see that the higher X-ray energy results in some additional difficulty in terms of larger fringe spacing and a smaller area of beam overlap. This results in fewer observable fringes, as well as increased variation in the fringe spacing. We show that the fringe visibility model used in Suzuki's paper [1] may be applied to the higher energy but a main assumption of the model, that a small square aperture may be viewed as an extended incoherent source, is less valid when larger apertures are used.

## 2. X-ray coherence measurement using a prism interferometer

As in Suzuki's experiment [1], the X-ray coherence was measured using a two-beam interferometer, in which a prism is used to deflect one half of the beam to interfere with the other half [24]. This arrangement is somewhat similar to that used in two-beam holography by Leith and Upatnieks [25], albeit for smaller than usual sample-to-detector propagation distances and in the absence of a sample for the latter technique. The prism-interferometer method was used to take measurements with 25 keV hard X-rays at both the upstream and downstream synchrotron-beamline hutches, with and without a diffuser comprised of a piece of conventional copy paper (80 g/m<sup>2</sup>) that was made to rotate within a plane perpendicular to the optic axis. The downstream hutch is typically chosen for the higher coherence afforded by the longer source-detector distance. It was also expected that without a diffuser in the beam, the degree of coherence would be increased.

Fig. 1 shows the experimental set-up, where a square aperture of width 20 μm, 50 μm or 100 μm is placed in front of the beam in the optics hutch to create an effective secondary source for the monochromatised synchrotron light. After  $L$  metres of propagation downstream of the square pinhole, a prism is then used to split the beam into two components, where one half passes outside of the prism and the other is refracted as it traverses the prism. The two beams then interfere after propagating  $l$  metres to form fringes, the visibility of which may be measured as defined by Michelson [9,26]:

$$V = \frac{I_{\max} - I_{\min}}{I_{\max} + I_{\min}}, \quad (1)$$

with  $I_{\max}$  and  $I_{\min}$  being the local maximum and minimum intensity respectively. This visibility will give the absolute value of the complex degree of coherence [8], so when the visibility is zero, the magnitude of the complex degree of coherence will also be zero.

The interference fringes created in the beam-overlap region will be seen with visibility and spacing dependent on the deflected angle ( $\Delta\theta$ ) of the second half of the beam.

Assuming that there is negligible refraction at the prism exit surface, where the beam is close to perpendicular to the prism face, the deflection is determined by incidence angle ( $\theta$ ) according to [1],

$$\Delta\theta = \frac{\delta}{\tan \theta}. \quad (2)$$

Here  $\delta$  is the refractive index decrement from unity, which is  $4.20 \times 10^{-7}$  for an acrylic resin prism at 25 keV [27].

As the incidence angle is increased by rotation of the prism, the distance over which the complex degree of coherence is measured increases, therefore decreasing the visibility of observed fringes. The phase difference between the interfering beams is also increased, producing narrower, more closely spaced fringes.

Given an extended incoherent source of size  $S$ , the fringe visibility can then be fitted to the model [1]

$$V = \frac{\sin(\pi\Delta\theta l S / \lambda L)}{\pi\Delta\theta l S / \lambda L} = \frac{\sin(\pi B / C)}{\pi B / C}, \quad (3)$$

where  $\lambda$  is the wavelength,  $l$  and  $L$  are shown in Fig. 1,  $B = \Delta\theta l$  is the beam overlap (the distance over which the coherence measurement is made) and  $C$  is the coherent width [8]:

$$C = \frac{\lambda L}{S}. \quad (4)$$

The interference-fringe visibility described in Eq. (3) is plotted as a function of incidence angle in Fig. 2. The first point of zero visibility (where the magnitude of the complex degree of coherence is zero) is produced when the distance over which this measurement is made is equal to the coherence width.

The fringe spacing,  $x$ , will be given by

$$x = \frac{\lambda}{\Delta\theta} = \frac{\lambda \tan \theta}{\delta} \propto \frac{\lambda \tan \theta}{\lambda^2} \propto \frac{\tan \theta}{\lambda}. \quad (5)$$

Using this model, incidence angles were selected at which to image the fringes, as shown in Fig. 2, aiming to maximise the range of fringe visibility for each set-up while maintaining a sufficient number of fringes and observable spacing. The shorter wavelength (compared to that used in Suzuki's study [1]) will refract less, producing both a smaller region of beam overlap and wider observed fringe spacing, and consequently far fewer observable fringes than in Suzuki's experiment [1]. These fringes are imaged using a CCD coupled to a scintillator via a lens, with magnification giving an effective pixel size of 0.18 μm.

Fringe profiles were obtained by averaging over the height of each fringe image. An image of a knife edge in the same orientation as the fringes (i.e., vertical) was used to measure the edge spread function. The knife edge image was differentiated to enable a horizontal point spread function (PSF) correction [28] on the profile. The spread is determined by both the source size and the detector system (contributions due to the latter are predominantly due to scattering effects within the detector's 10 μm thick phosphor screen). The horizontal PSF was measured to have a full-width at half maximum (FWHM) of 1.15 μm. The observed fringes were deconvolved with the measured PSF in Fourier space, which significantly increased the visibility of narrow fringes, as seen in Fig. 3. Fringe spacing and visibility could then be measured precisely.

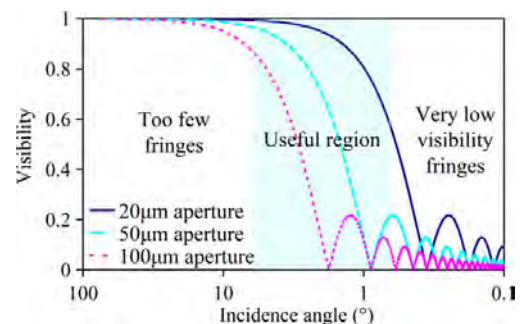


Fig. 2. Model for fringe visibility using the prism interferometer with 25 keV X-rays. The shaded region indicates the useful working region of incidence angles.

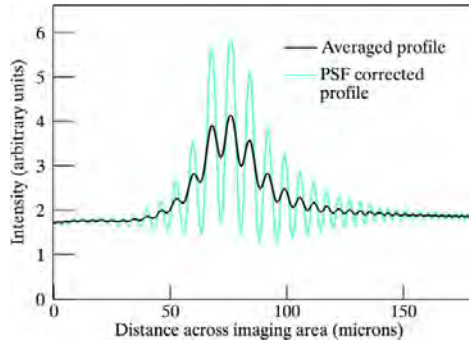


Fig. 3. Averaged profile of visibility fringes observed with prism at  $4.3^\circ$  at the downstream hutch using the  $20\ \mu\text{m}$  aperture, before and after PSF correction.

The resulting visibility points, as a function of incidence angle, were then least-squares fitted to the curve in Fig. 2 (described by Eq. (3)), varying the source size between 0 and  $300\ \mu\text{m}$ , thereby determining the effective source size.

### 3. Effects of synchrotron beamline parameters on X-ray coherence

Both measurements and modelling of the prism interferometer showed that measurement of the coherence width is dependent on a number of key parameters, including source size, energy and the presence of a diffuser. Here we look at the results of modelling these parameters in comparison with the experimental results obtained using the SPring-8 synchrotron. Our simulations of the imaging conditions, which modelled the behaviour of the observed fringes at each of the two hutches, were written in Interactive Data Language (IDL) version 6.3 (ITT Visual Information Solutions).

The present section is divided into three sub-sections. Section 3.1 looks at whether the assumption of an extended incoherent secondary source (corresponding to the square pinhole in Fig. 1) is valid and how the source will be seen at each hutch. Section 3.2 studies how the interference fringes will be affected by the introduction of a diffuser composed of a rotating random-phase screen, through use of our wave-optical simulation model. Finally, the changes to the observed fringes and the beam-overlap area when moving from 12.4 keV to 25 keV are discussed in Section 3.3.

#### 3.1. Effective source size

The source size will have a significant impact on the experimental observations obtained in the context of coherent X-ray imaging techniques such as interferometry, holography, propagation-based phase contrast, analyser-crystal phase contrast, etc. [28]. While the mathematical model in Suzuki's analysis [1] assumes the square aperture to be an incoherent source, the primary source  $49.2\ \text{m}$  further upstream is well approximated by an extended and incoherent source, resulting in partial coherence at the aperture. This will give a different result to that seen for either a point source behind the aperture or an extended incoherent source that uniformly fills the aperture. As seen from the van Cittert–Zernike theorem (applicable only to incoherent sources), coherence width is inversely proportional to source size and proportional to distance from the source [5,6,8]. In this case, the presence of an extended primary source some distance behind the aperture, means that the effective size of the secondary source at the aperture is not equal to the aperture size. The secondary source cannot be simply represented as an extended incoherent area.

The effect of the size of the primary source (such as the electron beam) seen through the aperture is investigated through wave-optical modelling using IDL. Each image is created using an array of mutually incoherent monochromatic point sources to build up the shape of the primary source [29]. For each source point, the field is propagated using the Fourier representation of the angular spectrum [30] to the aperture, cropped according to slit size, then propagated to the prism where a phase change occurs in half the field according to incidence angle. The resulting field is then propagated to the detector position (again using the angular-spectrum formalism) to give an intensity fringe image. The simulation used  $1.3\ \mu\text{m}$  pixels and took around 36 h on a 2.67 GHz, 3.25 GB RAM desktop computer to simulate a single fringe image (such as seen in the insets of Fig. 4) for an extended primary source the size of the electron beam.

Note that the angular-spectrum formalism (used for propagation in the simulations) is derived in the classic textbook accounts of Mandel and Wolf [8], Goodman [30] and Nieto-Vesperinas [31]; see also the text by Paganin [19]. This formalism relates the spatial part  $\psi_\omega(x, y, z = 0)$  of a forward-propagating, coherent, scalar wavefield of angular frequency  $\omega$ , to the propagated field  $\psi_\omega(x, y, z = \Delta)$ , by the formula:

$$\psi_\omega(x, y, z = \Delta > 0) = \mathfrak{T}^{-1} \exp \left[ i\Delta \sqrt{k^2 - k_x^2 - k_y^2} \right] \mathfrak{T} \psi_\omega(x, y, z = 0). \quad (6)$$

Here,  $(x, y)$  are the Cartesian coordinates perpendicular to the optic axis  $z$ ,  $\omega$  denotes angular frequency,  $k$  is the wavenumber of the radiation,  $(k_x, k_y)$  are Fourier coordinates dual to  $(x, y)$ ,  $\mathfrak{T}$  denotes Fourier transformation with respect to  $(x, y)$  and  $\mathfrak{T}^{-1}$  denotes the corresponding inverse transformation. Both  $\mathfrak{T}$  and  $\mathfrak{T}^{-1}$  may be numerically implemented using the Fast Fourier Transform [32].

As expected, a point source  $49.2\ \text{m}$  behind the aperture gives the fringes with the highest visibility, in comparison to extended incoherent sources located at the aperture position. For an extended source, the fringes are seen in an envelope in the shape of the source itself, as in the insets of Fig. 4. A decrease in visibility is seen, as in the profile plot of Fig. 4. We assume that the electron beam size of the 20XU SPring-8 source is as modelled by SPECTRA [33], i.e.,  $300\ \mu\text{m}$  (H) by  $6\ \mu\text{m}$  (V) FWHM, which is wider than the apertures used, but slightly smaller in the vertical direction.

When the slit size is increased, the X-ray wavefield at the exit surface of the slit is less meaningfully described as a 'secondary source' and becomes more meaningfully considered as a 'window' through which the primary source is 'seen'. This intuitive interpretation is consistent with our simulations. When the model of an extended incoherent source is compared to that of a point source, the

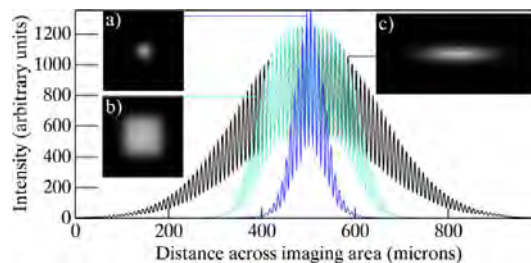


Fig. 4. Simulated fringes from (a) a point source, an extended incoherent (b) square source and (c) Gaussian source the size of the electron beam as seen through a  $50\ \mu\text{m}$  square aperture at the upstream hutch, prism at  $4^\circ$ . Fringe profiles are taken horizontally through the centre of the fringe image. Fringe images for the point and square source are  $500\ \mu\text{m}$  square and the image from the full source is  $1000\ \mu\text{m}$  by  $500\ \mu\text{m}$ .

results do not show a significant decrease in visibility for an extended source behind the 20  $\mu\text{m}$  slit, but as the slit size is increased and more of the source is 'seen' from the imaging position, there is a growing difference in the observed visibility, as in Fig. 5. This figure also shows that the presence of an extended primary source behind the apertures shifts the visibility curve to the left, indicating a larger effective source size.

Simulations also showed that an extended source has a greater effect downstream, due to penumbral blurring [34]. This will serve to blur the fringes and decrease the visibility.

### 3.2. Effects of diffuser on hard-X-ray coherence

During the experiment, the addition of a diffuser between the aperture and the prism 'smooths' the X-ray field over a larger field

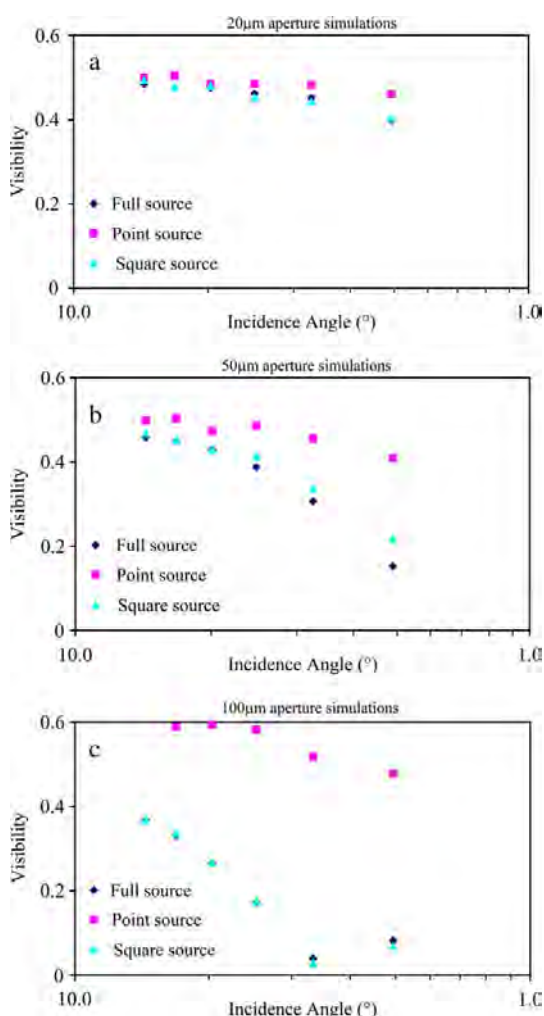


**Fig. 5.** Simulated fringe visibility for modelled sources as a function of incidence angle, for (a) 20  $\mu\text{m}$  aperture, (b) 50  $\mu\text{m}$  aperture and (c) 100  $\mu\text{m}$  aperture at the upstream hutch. 'Full' refers to the full 300  $\times$  6  $\mu\text{m}$  Gaussian source, and the square source is the size of the relevant aperture.

of view, but also decreases the fringe visibility, as seen in Fig. 6a, where the amplitude of fringes is slightly decreased. The magnitude of the complex degree of coherence is decreased when random phase variations are introduced by the diffuser.

Such smoothing has been studied by Cloetens et al. when taking a beam topograph on a bending magnet soft X-ray beamline, using a spinning piece of wood to blur out the overlying image of corrugations on the beryllium window [12]. Another application was that of White et al. [13], who used a sliding perforated photoresist in front of an undulator beam to decrease the amount of phase contrast, hence high frequency artefacts, to produce a smoother lithograph. In bio-medical X-ray imaging at SPring-8's 20XU beamline, spinning paper is used to even out the X-ray field in time and space, as well as to blur out phase contrast artefacts introduced by the beam-line optics and other components.

We developed a model to describe the effect of a spinning diffuser. This was incorporated in the simulation as a sum of random phase deviations, incurred at the position of the diffuser, and characteristic of the thickness and fibre size of the diffuser paper. For each term in the time-sum, an uncorrelated two-dimensional array of white noise was drawn from a standard Normal distribution. The array was then computationally smoothed using a Gaussian filter with a FWHM of 7  $\mu\text{m}$  to create random transverse spatial variations characteristic of the paper fibre size. This array is then used as the 'random screen' to determine the phase change due to the

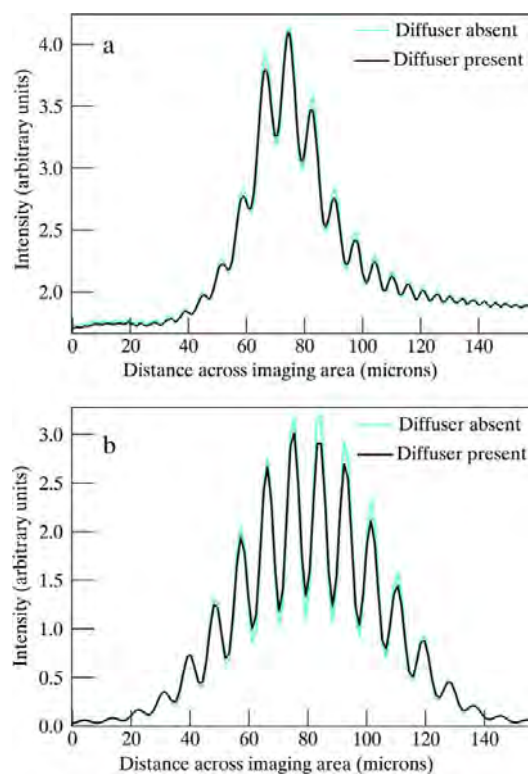


**Fig. 6.** A decrease in fringe visibility due to the presence of a diffuser is observed in (a) experiment (downstream, 20  $\mu\text{m}$  aperture, prism at 4°) (note: profile shown without PSF correction; 'Diffuser absent' required compensation for attenuation in the diffuser, so the profile was multiplied by 1.145, as determined by baseline comparison) and (b) point source simulation (upstream, 20  $\mu\text{m}$  aperture, prism at 4°, 200 terms of random phase deviations).

diffuser, using the projection approximation [18] (where phase is denoted by  $\varphi$ ):

$$\phi_{\text{after diffuser}}(x, y) = \phi_{\text{before diffuser}}(x, y) - \frac{2\pi}{\lambda} \delta_{\text{paper}} T_{\text{paper}} \times \text{Random Screen}(x, y). \quad (7)$$

Here  $\delta$  is again the refractive index decrement from unity, which for the diffuser paper is  $2.75 \times 10^{-7}$ , the thickness of the paper is given by  $T_{\text{paper}}$  (taken as  $100 \mu\text{m}$  here) and  $\text{Random Screen}(x, y)$  is the previously-mentioned smoothed white noise map. The resulting phase changes are described by a Gaussian distribution with a mean of 0.0 and a standard deviation of 0.44 radians. Visibility would go to zero, if these phase changes were to exceed a range of  $-\pi$  to  $\pi$  [35]. These changes were implemented 28.3 m after the aperture, as shown in the experimental set-up of Fig. 1. The field was then propagated to the prism, using a Fast Fourier Transform (FFT) implementation of the angular-spectrum formalism [30], and then treated in the same way as in the source size model.

A single image obtained from one term in the time-sum, i.e., a stationary diffuser, gives uneven, noisy fringes. However, the incoherent sum of many such images (200 in the simulation) over the whole exposure time gives fringes with decreased visibility, as observed in practice (Fig. 6).

Increasing the paper thickness in the simulation decreases the visibility further, as expected. PCI also requires adequate coherence to create interference fringes at the sample, from the incoherent addition of points which make up the source. Cloetens et al. [12] studied the effect of increasing the diffuser thickness on the observed crystal rocking curve used in their analyser based PCI. Our model is currently being extended to predict the effects of diffuser thickness on propagation based PCI, and describe how the presence of a diffuser decreases the visibility of phase contrast fringes.

The drop in visibility is seen as a fixed percentage of the initial visibility. Fig. 7 shows a drop to 80% of the initial visibility for the upstream data. Although the visibility of fringes decreases with a diffuser (for a fixed beam overlap size), the first point of zero visibility on the visibility curve (as seen in Fig. 7) does not change (i.e., there is a scaling in the  $y$ -direction, rather than a shift in the  $x$ -direction as a source size change incurs). Consequently, we modified Eq. (3) to include a new parameter, the multiplicative constant  $\kappa$ , which defines this percentage drop in visibility. The model then becomes

$$r' = \kappa \times \frac{\sin(\pi B/C)}{\pi B/C}, \quad (8)$$

with a least-squares fit of  $\kappa = 0.80$  for the measurements taken at the upstream hutch.

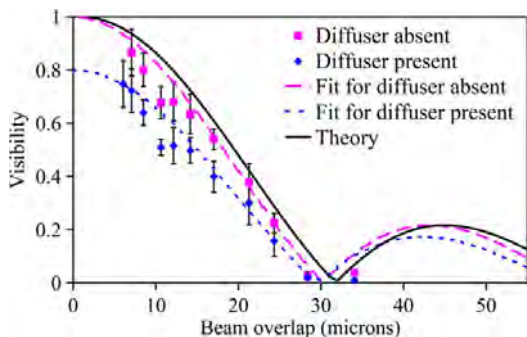


Fig. 7. Measured visibility for  $50 \mu\text{m}$  aperture taken at the upstream hutch, showing a fixed percentage drop in visibility when a diffuser is present.

The visibility curve fit is heavily reliant on the first point of zero visibility, which shifts horizontally with source size. Given that the first point of zero visibility does not shift when a diffuser is introduced, the impact of the diffuser on coherence cannot be expressed as a simple change in effective source size. This is confirmed when measurements yielded the same source size when fitting to Eq. (8) with the diffuser present, as to fitting to Eq. (3) without the diffuser present (seen in Fig. 7).

Simulations and observations both showed that this visibility drop is substantially greater at the upstream hutch than the downstream hutch. The visibility of observed fringes increases when moving to the downstream hutch from the upstream position, resulting in an increase in amplitude of the visibility curve. In the experimental data,  $\kappa$  was seen to increase by  $24 \pm 8\%$ . To evaluate the effect of the diffuser on visibility, simulations were performed using a point source (simulations using the full source were prohibitively time consuming). These indicated that  $\kappa$  should increase by  $27 \pm 3\%$  moving to the downstream hutch from upstream. It seems apparent that the free-space propagation distance of around 200 m to the downstream hutch is sufficient for the beam to recover some of the coherence lost in the upstream hutch due to the presence of the diffuser, in accord with the van Cittert–Zernike theorem [5–7].

It is seen from this experiment that the effect of a diffuser is not actually on the effective source size, and thus coherence width. The addition of many speckled interference fringe images over an exposure means that the sum shows fringes of reduced visibility. This means that the effective magnitude of the complex degree of coherence of the beam is instead altered. Further investigation could be carried out theoretically through analysis of the correlation function of a wave, showing how this correlation will be affected by a phase screen and by propagation [36].

### 3.3. Energy considerations

Moving from 12.4 keV ( $\lambda = 1 \text{ \AA}$ ) to 25 keV ( $\lambda = 0.5 \text{ \AA}$ ), in order to match the energy often used in bio-medical imaging, will change the relative scaling between the wavelength used and the physical geometry. A given path difference (between a refracted and a reference beam) will now be quite different when expressed in wavelengths. In this case, the path difference in wavelengths is approximately doubled for the harder radiation.

The effect of the shorter wavelength radiation was directly observable on the fringe images, in which the effects of Fresnel diffraction from the edge of the prism are apparent as varying fringe spacing across the horizontal extent of the image. The origin of this variation is as follows: Two interfering planar waves will give uniform fringe spacing across the fringe envelope, but at 25 keV the fringe spacing is observed to vary noticeably across the beam-overlap area, unlike at 12.4 keV. The diffracted spherical wavefront from the corner of the prism (a form of Young boundary wave [9]) will interfere with the planar wavefront passing outside the prism, as seen in Fig. 8a, where both waves are propagating from left to right. The curvature introduces an additional path difference, which will vary across the overlap region. The range of this path difference (the variation in the length of the black arrows in Fig. 8a) becomes significant when expressed in terms of a short wavelength. This will be observed as a spread in the fringe spacing over the area, with maximum spacing seen in the centre of the fringe set. Fig. 3 shows an example, where the sides of the beam-overlap area show very narrow fringes compared to the centre.

A simulated model of the interference of a planar wavefront and a parabolic wave from the prism, as in Fig. 8b and c, shows such a range of fringe spacing. The effect of Fresnel diffraction from the edge of the prism does not significantly change the fringe spacing across the beam-overlap area at 12.4 keV, but at 25 keV the fringe

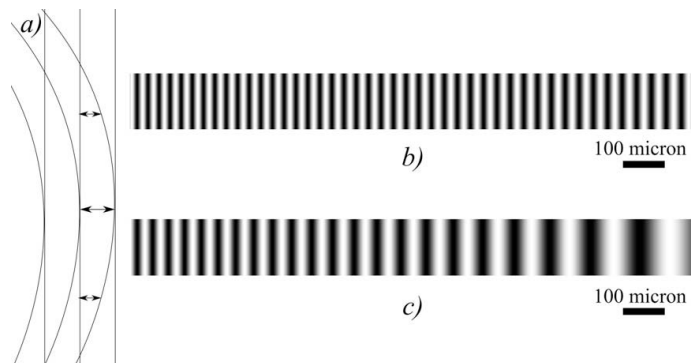


Fig. 8. (a) The simulated interference of a plane wave and a parabolic wave for (b) 12.4 keV X-rays and (c) 25 keV X-rays.

width changes significantly over the same distance. For example, over a set number of fringes, there is a change of 40% in the fringe spacing at 25 keV, but the variation is less than 5% at 12.4 keV, when the prism is set at  $2^\circ$ .

Fig. 8 also shows that fringe spacing is larger at the shorter wavelength (see Eq. (5)). It should likewise be noted that the area of beam overlap will be approximately one quarter as wide for 25 keV compared to 12.4 keV, for a given incidence angle and propagation distance, providing insufficient space for many of these fringes to be seen.

When the incidence angle  $\theta$  is less than  $\hat{\theta} \approx 7^\circ$ , fringe spacing varies approximately linearly with  $\theta$  as expected from Eq. (5); see Fig. 9. A too large prism angle results in a smaller beam overlap with too large fringe spacing, together with distorting effects of Fresnel diffraction. These factors account for the deviations from the theory, for points in Fig. 9 corresponding to  $\theta > \hat{\theta}$ ; such points are discarded when fitting visibility curves.

#### 4. Measured source sizes and coherence widths

Each visibility curve, as in Fig. 7, was fitted according to Eq. (3) using least squares regression, varying the source size parameter to determine the effective source size, as shown in Table 1. Eq. (4) relates a given source size to coherence width, also shown in Table 1. It can be seen in Fig. 7, where the visibility is shown as a function of

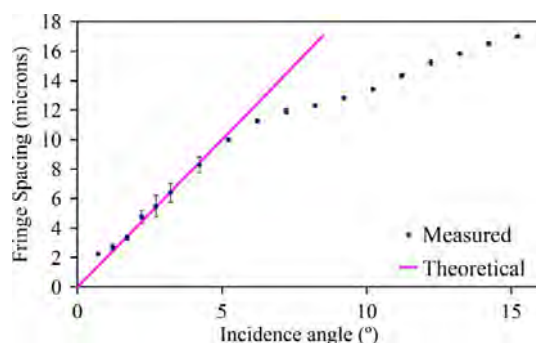


Fig. 9. Measured fringe spacing at the downstream hutch as a function of prism rotation angle, in agreement with theory for angles less than  $7^\circ$ . Therefore points beyond  $7^\circ$  were discarded when analysing fringe visibility, as the beam-overlap area was insufficient to fit the fringes, without significant distortion due to the curved wavefront.

Table 1

Effective source size from fitting the experimental results to Eq. (3) and the resulting coherent widths from Eq. (4).

Aperture size ( $\mu\text{m}$ )	Fitted effective source size upstream ( $\mu\text{m}$ )	Fitted effective source size downstream ( $\mu\text{m}$ )	Coherent width upstream ( $\mu\text{m}$ )	Coherent width downstream ( $\mu\text{m}$ )
20	$33 \pm 2$	$116 \pm 22$	$47 \pm 2$	$84 \pm 16$
50	$51 \pm 5$	$146 \pm 24$	$30 \pm 3$	$66 \pm 11$
100	$150 \pm 35$	$190 \pm 36$	$10 \pm 3$	$51 \pm 10$

beam overlap, that the coherence width is the beam overlap at the first point of zero visibility ( $30 \mu\text{m}$  coherence width for the  $50 \mu\text{m}$  slit observed at upstream). It should also be remembered that these measurements apply for both cases of with and without a diffuser, since this zero visibility point is the same for both.

These show that the extra propagation to the downstream hutch significantly increases the coherence width, despite the effect of penumbral blurring on the visibility of interference fringes. The larger aperture sizes, where more of the extended source is seen, fit least well to the model. The aperture is not simply a delta-correlated square source, so the visibility curve is not precisely as seen in Fig. 2. In consequence the larger apertures had the largest uncertainty in final fit, as expected from the source simulations.

#### 5. Discussion and summary

The choice of experimental set-up for synchrotron imaging, particularly when high coherence is desired, requires prioritization of the other experimental requirements. We have seen that the coherence width is maximised when imaging far from the source, without a diffuser and with a small aperture to collimate the beam. This should however be balanced with any requirements regarding a large imaging area or high flux, requiring a diffuser, larger aperture or a shorter source-sample distance.

The prism interferometer works effectively to create interference fringes from which coherence may be measured. The original model of Suzuki [1] shows some limitations in terms of the energy at which measurements may be taken and how the effect of a diffuser may be quantified in the model. Two main assumptions of the model were also evaluated; that of negligible prism exit-surface refraction and that of negligible attenuation by the prism.

Suzuki's model [1] assumes that there is negligible refraction of the beam at the exit surface of the prism, where the incident angle is close to perpendicular. Calculations showed that in our experi-

ment, the additional change in angle upon the beam exiting the prism is less than 1.5% of the change in angle incurred by the initial refraction for the range of points taken. Further detail is given in Appendix A.

Attenuation by the prism will also mean the interfering beams are of different intensity, hence cannot achieve the same fringe visibility. The visibility will be decreased by a multiplicative factor according to [9]:

$$\mathcal{V}_{new} = \frac{2\sqrt{I_1 I_2}}{I_1 + I_2} \mathcal{V}_{old}. \quad (9)$$

Here  $\mathcal{V}_{new}$  is the visibility given the differing intensity beams,  $\mathcal{V}_{old}$  is the visibility seen for two beams of the same intensity, and  $I_1$  and  $I_2$  are the intensities of the two beams. Given that the path length through the prism is less than 4 mm for incidence angles greater than  $1.5^\circ$  and generally much smaller for larger angles, this does not make a significant difference to the results. This is particularly true at higher energies, where the attenuation is less.

These two assumptions are therefore quite valid, and it is the source description which is most responsible for discrepancies between Suzuki's model and measurements. This means that the data taken with larger aperture sizes, where more of the extended source behind the aperture is seen, fit least well to the model. This results in lower-visibility fringes, hence a larger observed source size than expected. When the secondary source is small, the set-up is closer to the theoretical model of an extended incoherent source and the problem of penumbral blurring is decreased. Simulation at a range of wavelengths (including that used by Suzuki) of a full source behind the aperture could provide some measure of where the model used by Suzuki is valid.

Suzuki's original model (Eq. (3)) also cannot describe the decrease in the magnitude of the complex degree of coherence due to a diffuser. The effect of the diffuser is to decrease the fringe visibility by a fixed percentage, rather than shifting the curve in relation to incidence angle when the source size is altered (Fig. 7). While our modified model (Eq. (8)) describes the effect of the diffuser on the interference-fringe visibility, it shows that there is no change in measured coherence width. The diffuser decreases the magnitude of the degree of coherence through the introduction of random phase variations, but this effect cannot be viewed as a change in effective source size. Simulations of this diffuser effect demonstrate that a thicker diffuser will decrease fringe visibility further. A coarser diffuser will require longer exposures to smooth out the variations from each part of the diffuser and obtain a cleaner set of fringes. The authors are currently looking at the effect of a diffuser on propagation-based phase contrast imaging, through application of this model.

The 25 keV X-rays used in these measurements mean that Fresnel diffraction from the prism edge is significant compared to at 12.4 keV, observed as a variation of fringe spacing across the fringe envelope. The wide fringes and narrow beam-overlap region mean that it is difficult to take a large range of measurements in practice, even when the propagation distance is maximised.

The visibility of interference fringes in this experiment was affected by a number of parameters. The presence of a diffuser decreases the magnitude of the complex degree of coherence of a beam, hence the visibility of interference fringes. Propagation beyond a diffuser serves to recover coherence, in the sense implied by the van Cittert–Zernike theorem, and hence the diffuser does not have such a significant effect on coherence at the downstream hutch. An extended source will decrease the visibility of fringes, particularly downstream where penumbral blurring is seen. Decreases in fringe visibility, whether due to a diffuser or penumbra from an extended source, will be most significant at small incidence angles where the fringe spacing is small.

In general, the coherence width of BL20XU for these slit sizes at 25 keV at SPring-8 increases by 36–40  $\mu\text{m}$  when moving from upstream to the downstream hutch, although flux at the sample is reduced. The magnitude of the complex degree of coherence is decreased when a diffuser is introduced to even out the beam, reducing the visibility of interference fringes by a factor of 0.80 at the upstream hutch for the diffuser tested.

#### Acknowledgements

We thank the Japan Synchrotron Radiation Research Institute (Proposal number 2008A1334) for the privilege of using the SPring-8 facility to conduct these experiments. We acknowledge the Access to Major Research Facilities Programme (managed by the Australian Nuclear Science and Technology Organization) for supporting this work and funding the necessary trips to SPring-8 for the Australian co-authors. Kaye Morgan and Sally Irvine acknowledge the support of an Australian Postgraduate Award. Kaye Morgan also acknowledges a J.L. William Scholarship at Monash University. David Paganin acknowledges the Australian Research Council.

#### Appendix A

Section 5 discusses the assumptions present in the model of Suzuki et al. [1], noting negligible exit-surface refraction and uniform fringe spacing given by the first equality in Eq. (5). This appendix will first derive an approximate expression for the exit-surface angle of deflection and second, the phase difference associated with the path difference for a beam travelling through the prism as a function of its depth.

##### A.1. Entrance-surface deflection angle

We define  $\theta$  as the angle of the incident beam parallel to the surface of the prism, as shown in Fig. 10. From Snell's Law, the deflection angle at the entrance surface  $\Delta\theta_1$  is governed by:

$$\sin(90 - \theta) = n \sin(90 - \theta + \Delta\theta_1), \quad (A.1)$$

where  $n$  is the refraction index of the prism material. It follows that:

$$\cos(\theta) = n[\cos(\theta) \cos(\Delta\theta_1) + \sin(\theta) \sin(\Delta\theta_1)], \quad (A.2)$$

and with negligible absorption ( $n \cong 1 - \delta$ , where  $\delta$  is the standard refractive index decrement) and application of the small-angle approximation,

$$\cos(\theta) = (1 - \delta)[\cos(\theta) + \sin(\theta)\Delta\theta_1]. \quad (A.3)$$

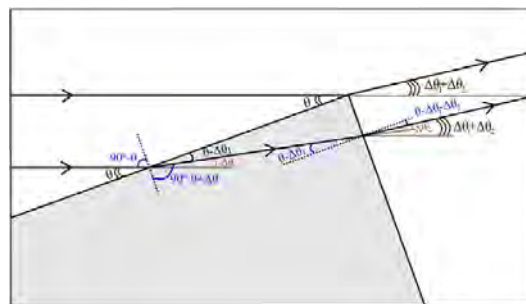


Fig. 10. Ray diagram showing angles of deflection at entrance and exit surfaces of prism. For X-rays, the angles of deflection may be measured in microradians: here they are exaggerated for clarity.

As both  $\delta$  and  $\Delta\theta_1$  are small, their product is ignored and the above equation is rearranged to give for the first angle of deflection:

$$\Delta\theta_1 = \frac{\delta}{\tan \theta}. \tag{A.4}$$

A.2. Exit angle of deflection

From Snell's Law, the angles of the beam inside the prism relate to the second angle of deflection  $\Delta\theta_2$  via:

$$n \sin(\theta - \Delta\theta_1) = \sin(\theta - \Delta\theta_1 - \Delta\theta_2). \tag{A.5}$$

As in the previous angle derivation, trigonometric identities may then be applied to give the equation:

$$(1 - \delta) \sin(\theta - \Delta\theta_1) = \sin(\theta - \Delta\theta_1) \cos(\Delta\theta_2) - \cos(\theta - \Delta\theta_1) \sin(\Delta\theta_2). \tag{A.6}$$

Again by the small-angle approximation,

$$\sin(\theta - \Delta\theta_1) - \delta \sin(\theta - \Delta\theta_1) = \sin(\theta - \Delta\theta_1) + \cos(\theta - \Delta\theta_1) \Delta\theta_2, \tag{A.7}$$

which is then rearranged to give

$$\Delta\theta_2 = \delta \tan(\theta - \Delta\theta_1), \tag{A.8}$$

or

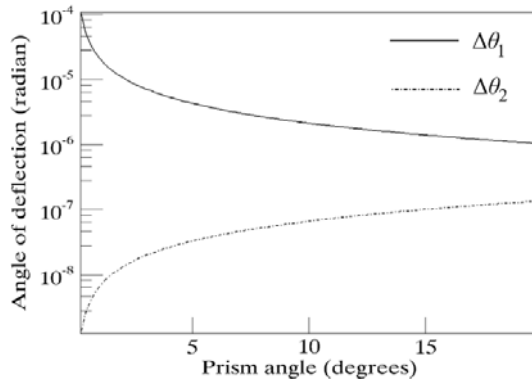


Fig. 11. The two deflection angles as a function of incident angle, demonstrating that at small angles of incidence, the exit angle of deflection ( $\Delta\theta_2$ ) is negligible relative to the entrance angle of deflection ( $\Delta\theta_1$ ).

$$\Delta\theta_2 = \delta \tan \left( \theta - \frac{\delta}{\tan \theta} \right). \tag{A.9}$$

These two angles of deflection  $\Delta\theta_1$  and  $\Delta\theta_2$  add to give the total deflection from the incident angle:

$$\Delta\theta \equiv \Delta\theta_1 + \Delta\theta_2 \equiv \frac{\delta}{\tan \theta} + \delta \tan \left( \theta - \frac{\delta}{\tan \theta} \right). \tag{A.10}$$

When plotted,  $\Delta\theta_2$  is negligible compared to  $\Delta\theta_1$ , as seen in Fig. 11, and hence may be omitted as in Suzuki's calculations [1].

A.3. Path length through prism

Fig. 12 shows the prism set-up, various representative rays, and the beam-overlap at the detector-plane. The pathlength of a ray traversing the prism may be calculated relative to a variable  $x$  which describes the depth of penetration into the prism, perpendicular to the direction of propagation within. This is equivalent in the diagram to  $T_1 + T_2$ , which is given by the following:

$$PL_{total} = \frac{x}{\tan(\theta - \Delta\theta_1)} + x \tan(\theta - \Delta\theta_2). \tag{A.11}$$

This can be written purely as a function of the incident angle  $\theta$  using Eq. (A.4) as:

$$PL_{total} = \frac{x}{\tan \left( \theta - \frac{\delta}{\tan \theta} \right)} + x \tan \left( \theta - \frac{\delta}{\tan \theta} \right). \tag{A.12}$$

The phase difference between a reference ray and a prism-deflected ray is given by the following:

$$\varphi_{diff} = k[n(T_1 + T_2) + T_3 - T_4 - T_5 - T_6] \tag{A.13}$$

where:

$$T_1 = \frac{x}{\tan(\theta - \Delta\theta_1)}, \tag{A.14}$$

$$T_2 = x \tan(\theta - \Delta\theta_1), \tag{A.15}$$

$$T_3 = \frac{T_6}{\cos(\Delta\theta_1 + \Delta\theta_2)}, \tag{A.16}$$

$$T_4 = \frac{T_1 \cos \theta}{\cos(\theta - \Delta\theta_1)}, \tag{A.17}$$

$$T_5 = \frac{T_2 \sin \theta}{\sin(\theta - \Delta\theta_1)}, \tag{A.18}$$

and

$$T_6 = L - T_5. \tag{A.19}$$

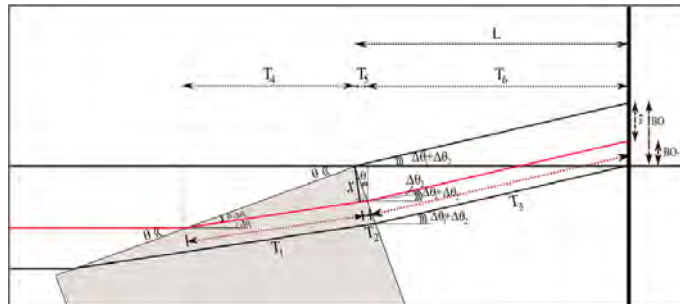


Fig. 12. Ray diagram of prism interferometer. Parts of the beam which hit the prism and are thus deflected by it interfere with the undeflected reference beam in a region of overlap (BO) at the detector-plane. The path-length difference between the two parts of beam is represented by  $(T_1 + T_2 + T_3) - (T_4 + T_5 + T_6)$ , which may be given as a function of depth into the prism ( $x$ ), angle of incidence ( $\theta$ ) and distance to the detector ( $L$ ).

Substituting Eqs. (A.14)–(A.19) into (A.13) gives the following:

$$\varphi_{diff}(x) = k \left\{ x \left[ \frac{(1-\delta)}{\tan(\theta-\Delta\theta_1)} + (1-\delta) \tan(\theta-\Delta\theta_1) - \frac{\sin\theta}{\cos(\theta-\Delta\theta_1)\cos(\Delta\theta_1+\Delta\theta_2)} \right] - \frac{\cos\theta}{\sin(\theta-\Delta\theta_1)} \right\} + L \left[ \frac{1}{\cos(\Delta\theta_1+\Delta\theta_2)} - 1 \right], \quad (\text{A.20})$$

where  $\delta$ ,  $\Delta\theta_1$  and  $\Delta\theta_2$  are as previously defined, and  $L$  is the sample-to-detector distance, measured from the top-corner of the prism.

The variable  $x$  may be related linearly to the vertical distance  $\hat{x}$  from the top of the beam-overlap area ( $BO = L \tan(\Delta\theta_1 + \Delta\theta_2)$ ) as:

$$\hat{x} = T_5 \tan(\Delta\theta_1 + \Delta\theta_2) + \frac{T_5}{\tan\theta} = \frac{x(\sin\theta \tan(\Delta\theta_1 + \Delta\theta_2) + \cos\theta)}{\cos(\theta - \Delta\theta_1)}. \quad (\text{A.21})$$

As  $\Delta\theta_1$  and  $\Delta\theta_2$  are very small in magnitude compared to unity,  $\hat{x} \approx x$ .

Given that the angles of refraction at X-ray wavelengths are so small, the difference between the full geometric expression given in Eq. (A.20) and the general approximation for the linear phase difference as a function of  $x$  [37], i.e.:

$$\varphi_{diff}(x) \approx kx\Delta\theta_1, \quad (\text{A.22})$$

is indeed negligible. This model does not, however, take into account the Fresnel diffraction from the sharp edge of the prism, which is known to produce a varying fringe spacing as discussed in Section 3.3.

## References

- [1] Y. Suzuki, *Rev. Sci. Instrum.* 75 (2004) 1026.
- [2] S.W. Wilkins, T.E. Gureyev, D. Gao, A. Pogany, A.W. Stevenson, *Nature* 384 (1996) 355.
- [3] E. Wolf, *Introduction to the Theory of Coherence and Polarization of Light*, Cambridge University Press, New York, 2007.
- [4] R. Coisson, *Appl. Opt.* 34 (1995) 904.
- [5] P.H. van Cittert, *Physica* 1 (1934) 201.
- [6] P.H. van Cittert, *Physica* 6 (1939) 1129.
- [7] F. Zernike, *Physica* 5 (1938) 785.
- [8] L. Mandel, E. Wolf, *Optical Coherence and Quantum Optics*, Cambridge University Press, 1995.
- [9] M. Born, E. Wolf, *Principles of Optics*, seventh ed., Cambridge University Press, 1999.
- [10] T. Ishikawa, K. Tamasaku, M. Yabashi, S. Goto, Y. Tanaka, H. Yamazaki, K. Takeshita, H. Kimura, H. Ohashi, T. Matsushita, T. Ohata, *Proc. SPIE* 4145 (2003) 1.
- [11] A. Snigirev, I. Snigireva, V.G. Kohn, S.M. Kuznetsov, *Nucl. Instr. Meth. Phys. Res., A* 370 (1996) 634.
- [12] P. Cloetens, R. Barrett, J. Baruchel, J. Guigay, M. Schlenker, *J. Phys. D: Appl. Phys.* 29 (1996) 133.
- [13] D.L. White, O.R. Wood II, J.E. Bjorkholm, S. Spector, A.A. MacDowell, B. LaFontaine, *Rev. Sci. Instrum.* 66 (1994) 1930.
- [14] T.E. Gureyev, S.C. Mayo, D.E. Myers, Y.A. Nesterets, D.M. Paganin, A. Pogany, A.W. Stevenson, S.W. Wilkins, *J. Appl. Phys.* 105 (2009) 102005 (invited review).
- [15] M.J. Kitchen, D. Paganin, R.A. Lewis, N. Yagi, K. Uesugi, S.T. Mudie, *Phys. Med. Biol.* 49 (2004) 4335.
- [16] T.E. Gureyev, S. Mayo, S.W. Wilkins, D. Paganin, A.W. Stevenson, *Phys. Rev. Lett.* 86 (2001) 5827.
- [17] R.A. Lewis, K.D. Rogers, C.J. Hall, A.P. Hufton, S. Evans, R.H. Menk, G. Tromba, F. Arfelli, L. Rigon, A. Olivo, A. Evans, S.E. Pinder, E. Jacobs, I.O. Ellis, D.R. Dance, in: L.E. Antonuk, M.J. Yaffe (Eds.), *Medical Imaging 2002: Physics of Medical Imaging*, *Proc. SPIE* 4682 (2002) 286.
- [18] V. Kohn, I. Snigireva, A. Snigirev, *Phys. Rev. Lett.* 85 (2000) 2745.
- [19] D.M. Paganin, *Coherent X-Ray Optics*, Oxford University Press, New York, 2006.
- [20] D. Paterson, B.E. Allman, P.J. McMahon, J. Lin, N. Moldovan, K. Nugent, I. McNulty, C.T. Chantler, C.C. Retsch, T.H.K. Irving, D.C. Mancini, *Opt. Commun.* 195 (1) (2001) 79.
- [21] M. Yabashi, K. Tamasaku, T. Ishikawa, *Phys. Rev. Lett.* 87 (2001) 140801-1.
- [22] D. Gabor, *Nature* 161 (1948) 777.
- [23] J.J.A. Lin, D. Paterson, A.G. Peele, P.J. McMahon, C.T. Chantler, K.A. Nugent, *Phys. Rev. Lett.* 90 (2003) 074801-1.
- [24] Y. Suzuki, *Jpn. J. Appl. Phys.* 41 (2002) L1019.
- [25] E.N. Leith, J. Upatnieks, *J. Opt. Soc. Am.* 52 (1962) 1123.
- [26] A.A. Michelson, *Studies in Optics*, Chicago Press, 1927. Reprinted by Dover Publications Inc., 1995.
- [27] B.L. Henke, E.M. Gullikson, J.C. Davis, *Atomic Data Nucl. Data Tables* 54 (2) (1993) 181.
- [28] W. Leitenberger, H. Wendrock, L. Bischoff, T. Weitkamp, *J. Synchrotron Rad.* 11 (2004) 190.
- [29] J.M. Cowley, *Diffraction Physics*, third ed., North Holland, 1995.
- [30] J.W. Goodman, *Introduction to Fourier Optics*, Roberts and Company Publishers, 2005.
- [31] M. Nieto-Vesperinas, *Scattering and Diffraction in Physical Optics*, second ed., World Scientific Publishing Company, 2006.
- [32] W.H. Press, B.P. Flannery, S.A. Teukolsky, W.T. Vetterling, *Numerical Recipes in C: The Art of Scientific Computing*, Cambridge University Press, 2007, p. 602.
- [33] T. Tanaka, H. Kitamura, *J. Synchrotron Rad.* 8 (2001) 1221.
- [34] L. Beese, R. Feder, D. Sayre, *Biophys. J.* 49 (1986) 259.
- [35] J.W. Goodman, *Speckle Phenomena in Optics*, Roberts and Company, Englewood, Colorado, 2007.
- [36] M.V. Berry, *J. Phys. A* 11 (1978) 27.
- [37] B.E.A. Saleh, B.C. Teich, *Fundamentals of Photonics*, Wiley Interscience, New York, 1991.

---

## Propagation-Based PCXI using a Spinning Phase Diffuser

---

*Assessment of the use of a diffuser in propagation-based x-ray phase contrast imaging.*

by S. C. Irvine\*, K. S. Morgan\*, Y. Suzuki, K. Uesugi, A. Takeuchi, D. M. Paganin and K. K. W. Siu. *\*Both authors contributed equally to this work.*

Published in Optics Express **18**, pp. 13478-13491, 2010.

---

Chapter 5 follows directly on from the results of Chapter 4, looking at the effect of the random phase screen diffuser (used to produce a more even beam area and remove unwanted phase artefacts) on propagation-based phase contrast x-ray images. As shown in Chapter 4, the diffuser decreases the magnitude of the complex degree of second-order coherence, which will reduce the visibility of phase contrast effects. This chapter links the coherence measurements of Chapter 4 with the need to increase interface fringe visibility discussed in Chapter 6.

Images of a rounded interface are taken with and without the diffuser, both in the original position and after moving it upstream, once again at beamline 20XU, SPring-8. Further justification is given on the advantages of using a diffuser, and it is found that these advantages may be retained by increasing the distance between the diffuser and the sample. This extra propagation will increase the degree of coherence in accordance with the van Cittert-Zernike theorem (Eqn. 1.35). The diffuser material is also considered, looking at the effect of increased total thickness, and/or increased feature length scales, upon an interface phase contrast fringe.

As a result of this work, a diffuser has been placed close to the source for future imaging studies, in the Optics hutch of BL20XU, 27.3 metres upstream of the original position.

## Declaration for Thesis Chapter 5

In the case of Chapter 5, contributions to the work involved the following:

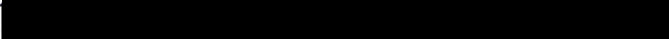
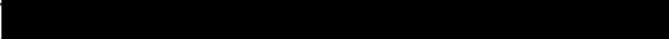
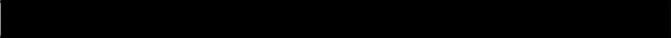
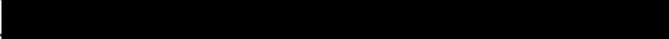
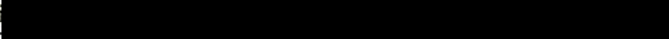
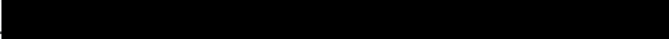
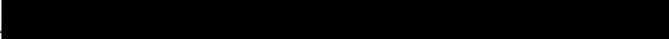
Name	% contribution	Nature of contribution
Sarah Irvine	45%	Contributed to the original experiments, the data analysis, numerical simulations and the write-up
Kaye Morgan	45%	Contributed to the original experiments, the data analysis, numerical simulations and the write-up
Yoshio Suzuki		Contributed to the original experiments
Kentaro Uesugi		Contributed to the original experiments
Akihisa Takeuchi		Contributed to the original experiments
David Paganin		Provided supervisory advice, aided proofreading and drafting
Karen Siu		Contributed to the original experiments, provided supervisory advice, aided proofreading and drafting

### Declaration by co-authors

The undersigned hereby certify that:

1. the above declaration correctly reflects the nature and extent of the candidate's contribution to this work, and the nature of the contribution of each of the co-authors.
2. they meet the criteria for authorship in that they have participated in the conception, execution, or interpretation, of at least that part of the publication in their field of expertise;
3. they take public responsibility for their part of the publication, except for the responsible author who accepts overall responsibility for the publication;
4. there are no other authors of the publication according to these criteria;
5. potential conflicts of interest have been disclosed to (a) granting bodies, (b) the editor or publisher of journals or other publications, and (c) the head of the responsible academic unit; and
6. the original data are stored at the following location(s) and will be held for at least five years from the date indicated below: School of Physics and Monash Centre for Synchrotron Science, Clayton Campus, Monash University, Australia.

### Signatures:

Kaye Morgan:		Date: 19/10/10
Sarah Irvine:		Date: 18/10/2010
Yoshio Suzuki:		Date: 18/10/10
Kentaro Uesugi:		Date: 18/10/10
Akihisa Takeuchi:		Date: 18/10/10
David Paganin:		Date: 18/10/10
Karen Siu:		Date: 19.10.2010

---

This paper was published in Optics Express and is made available as an electronic reprint with the permission of OSA. The paper can be found at the following URL on the OSA website: <http://www.opticsinfobase.org/abstract.cfm?uri=oe-18-13-13478>. Systematic or multiple reproduction or distribution to multiple locations via electronic or other means is prohibited and is subject to penalties under law.

---

# Assessment of the use of a diffuser in propagation-based x-ray phase contrast imaging

S. C. Irvine<sup>1,4,\*</sup>, K. S. Morgan<sup>1,4,5</sup>, Y. Suzuki<sup>2</sup>, K. Uesugi<sup>2</sup>, A. Takeuchi<sup>2</sup>, D. M. Paganin<sup>1</sup>, and K. K. W. Siu<sup>1,3</sup>

<sup>1</sup>*School of Physics, Monash University, Victoria 3800, Australia*

<sup>2</sup>*Japan Synchrotron Radiation Research Institute (JASRI), SPring-8, Mikazuki, Hyogo, 679-5198, Japan*

<sup>3</sup>*Monash Centre for Synchrotron Science, Victoria 3800, Australia*

<sup>4</sup>*S. Irvine and K. Morgan contributed equally to this work*

<sup>5</sup>*Kaye.Morgan@sci.monash.edu.au*

*\*Sally.Irvine@sci.monash.edu.au*

**Abstract:** A rotating random-phase-screen diffuser is sometimes employed on synchrotron x-ray imaging beamlines to ameliorate field-of-view inhomogeneities due to electron-beam instabilities and beamline optics phase artifacts. The ideal result is a broader, more uniformly illuminated beam intensity for cleaner coherent x-ray images. The spinning diffuser may be modeled as an ensemble of transversely random thin phase screens, with the resulting set of intensity maps over the detector plane being incoherently averaged over the ensemble. Whilst the coherence width associated with the source is unaffected by the diffuser, the magnitude of the complex degree of second-order coherence may be significantly reduced [K. S. Morgan, S. C. Irvine, Y. Suzuki, K. Uesugi, A. Takeuchi, D. M. Paganin, and K. K. W. Siu, *Opt. Commun.* **283**, 216 (2010)]. Through use of a computational model and experimental data obtained on x-ray beamline BL20XU at SPring-8, Japan, we investigate the effects of such a diffuser on the quality of Fresnel diffraction fringes in propagation-based x-ray phase contrast imaging. We show that careful choice of diffuser characteristics such as thickness and fiber size, together with appropriate placement of the diffuser, can result in the ideal scenario of negligible reduction in fringe contrast whilst the desired diffusing properties are retained.

©2010 Optical Society of America

**OCIS codes:** (030.1670) Coherent optical effects, (030.6140) Speckle, (110.4980) Partial coherence in imaging, (230.1980) Diffusers, (110.7440) X-ray imaging, (340.7440) X-ray imaging.

---

## References and links

1. K. S. Morgan, S. C. Irvine, Y. Suzuki, K. Uesugi, A. Takeuchi, D. M. Paganin, and K. K. W. Siu, "Measurement of hard x-ray coherence in the presence of a rotating random-phase-screen diffuser," *Opt. Commun.* **283**(2), 216–225 (2010).
2. A. Snigirev, I. Snigireva, V. Kohn, S. Kuznetsov, and I. Schelokov, "On the possibilities of x-ray phase contrast microimaging by coherent high-energy synchrotron radiation," *Rev. Sci. Instrum.* **66**(12), 5486–5492 (1995).
3. P. Cloetens, R. Barrett, J. Baruchel, J. P. Guigay, and M. Schlenker, "Phase objects in synchrotron radiation hard x-ray imaging," *J. Phys. D Appl. Phys.* **29**(1), 133–146 (1996).
4. S. W. Wilkins, T. E. Gureyev, D. Gao, A. Pogany, and A. W. Stevenson, "Phase-contrast imaging using polychromatic hard X-rays," *Nature* **384**(6607), 335–338 (1996).
5. T. E. Gureyev, S. C. Mayo, D. E. Myers, Y. Nesterets, D. M. Paganin, A. Pogany, A. W. Stevenson, and S. W. Wilkins, "Refracting Röntgen's rays: Propagation-based x-ray phase contrast for biomedical imaging," *J. Appl. Phys.* **105**(10), 102005–102012 (2009).
6. S. C. Irvine, D. M. Paganin, S. Dubsy, R. A. Lewis, and A. Fouras, "Phase retrieval for improved three-dimensional velocimetry of dynamic x-ray blood speckle," *Appl. Phys. Lett.* **93**(15), 153901 (2008).
7. S. C. Irvine, D. M. Paganin, A. Jamison, S. Dubsy, and A. Fouras, "Vector tomographic X-ray phase contrast velocimetry utilizing dynamic blood speckle," *Opt. Express* **18**, 2368–2379 (2010).
8. J. M. Cowley, *Diffraction physics (third edition)* (Amsterdam: North-Holland Publication, and New York: Elsevier Publication Co., 1995).
9. D. L. White, O. R. Wood, J. E. Bjorkholm, S. Spector, A. A. MacDowell, and B. LaFontaine, "Modification of the coherence of undulator radiation," *Rev. Sci. Instrum.* **66**(2), 1930 (1995).

10. R. A. Lewis, "Medical phase contrast x-ray imaging: current status and future prospects," *Phys. Med. Biol.* **49**(16), 3573–3583 (2004).
11. E. Wolf, *Introduction to the Theory of Coherence and Polarization of Light* (Cambridge University Press, New York, 2007).
12. L. Mandel, and E. Wolf, *Optical Coherence and Quantum Optics* (Cambridge Univ Pr, Cambridge, 1995).
13. A. Pogany, D. Gao, and S. W. Wilkins, "Contrast and resolution in imaging with a microfocus x-ray source," *Rev. Sci. Instrum.* **68**(7), 2774–2782 (1997).
14. Ya. I. Nesterets, "On the origins of decoherence and extinction contrast in phase-contrast imaging," *Opt. Commun.* **281**(4), 533–542 (2008).
15. K. A. Nugent, C. Q. Tran, and A. Roberts, "Coherence transport through imperfect x-ray optical systems," *Opt. Express* **11**(19), 2323–2328 (2003).
16. T. E. Gureyev, A. Pogany, D. M. Paganin, and S. W. Wilkins, "Linear algorithms for phase retrieval in the Fresnel region," *Opt. Commun.* **231**(1-6), 53–70 (2004).
17. K. K. W. Siu, K. S. Morgan, D. M. Paganin, R. Boucher, K. Uesugi, N. Yagi, and D. W. Parsons, "Phase contrast X-ray imaging for the non-invasive detection of airway surfaces and lumen characteristics in mouse models of airway disease," *Eur. J. Radiol.* **68**(3 Suppl), S22–S26 (2008).
18. D. M. Paganin, *Coherent X-Ray Optics* (Oxford University Press, New York, 2006).
19. J. W. Goodman, *Introduction to Fourier Optics* (Roberts and Company Publishers, 2005).
20. W. H. Press, B. P. Flannery, S. A. Teukolsky, and W. T. Vetterling, *Numerical Recipes in C: The Art of Scientific Computing* (Cambridge University Press, Cambridge Greenwood Village, 2007).
21. VPAC, "Victorian Partnership for Advanced Computing," (2010), <http://www.vpac.org/>.
22. A. Barty, "Quantitative Phase-Amplitude Microscopy, PhD Thesis," (University of Melbourne, Melbourne, 1999).
23. W. Leitenberger, H. Wendrock, L. Bischoff, and T. Weitkamp, "Pinhole interferometry with coherent hard X-rays," *J. Synchrotron Radiat.* **11**(2), 190–197 (2004).
24. A. A. Michelson, *Studies in Optics* (University of Chicago Press, Chicago, 1927).
25. M. Born, and E. Wolf, *Principles of Optics* (Cambridge University Press, Cambridge, 1999).
26. P. H. van Cittert, "Die Wahrscheinliche Schwingungsverteilung in Einer von Einer Lichtquelle Direkt Oder Mittels Einer Linse Beleuchteten Ebene," *Physica* **1**(1-6), 201–210 (1934).
27. P. H. van Cittert, "Kohaerenz-probleme," *Physica* **6**(7-12), 1129–1138 (1939).
28. F. Zernike, "The concept of degree of coherence and its application to optical problems," *Physica* **5**(8), 785–795 (1938).

## 1. Introduction

Propagation based phase contrast imaging [2–4] using a synchrotron x-ray source is a powerful and flexible tool in the study of biological soft tissues [5]. To achieve quality phase contrast images, a transversely uniform field of incident coherent x-rays is desired. Division of the phase-contrast image by a flat field image (*i.e.*, division by an image taken in the absence of the sample) can remove some transverse intensity variations due to a non-uniform incident beam. However, frame-to-frame movement of the beam image will not be corrected. Additionally, this correction does not necessarily remove image inhomogeneities created by undesired transverse phase variations in the x-ray beam illuminating the sample, for example those introduced by optical elements. The use of a diffuser to remove such phase defects and to even out the illuminating beam intensity may therefore be required. This must be balanced with coherence requirements, as the presence of a diffuser will simultaneously decrease the observed degree of coherence of the illuminating beam [1]. Notwithstanding their utility in the context of propagation-based x-ray phase contrast imaging, little attention has been paid to developing a physical model for phase contrast image formation in the presence of a diffuser. Here we develop such a model, which is readily implemented computationally, and which we anticipate to be of particular utility in computer simulations of propagation-based phase contrast imaging employing a phase diffuser. We apply this model to investigate the effect of the spinning paper diffuser used at synchrotron x-ray beamline BL20XU at SPring-8, Japan. Our simple computational model correlates well with our experimental data.

As mentioned previously, the need for a diffuser stems from the difficulty in achieving a perfectly uniform x-ray beam for the full field of view using a synchrotron source. This is particularly evident when the area to be illuminated is relatively large (*e.g.* several millimeters to centimeters in extent), as required in biomedical small animal *in vivo* imaging [5], where the frame-to-frame movement of the beam is particularly problematic. Further to this, short exposure times (*e.g.* on the order of 100ms) are helpful in avoiding image blur due to animal movement, and those experiments which attempt to observe rapid biomedical dynamics such

as blood flow [6,7], require even shorter exposures. With such short exposures it becomes more apparent that fluctuations in the electron-beam stability are causing a time-varying beam, which imposes undesirable inhomogeneities in propagation-based x-ray phase contrast images.

Further image inhomogeneities may be imposed by imperfections in various beamline components [8,3]. Indeed, it is precisely because propagation-based x-ray phase contrast is so sensitive to transverse phase variations, that even minute variations (due *e.g.* to beryllium windows, insufficiently flat reflecting optics, inhomogeneities in beam curvature *etc.*) may lead to artifacts in the image of a sample. The introduction of a diffuser will both minimize the presence of these phase artifacts in the final image of the sample, as well as creating a more stable area of uniform intensity [2,3,9]. One thereby remains sensitive to transverse phase gradients imposed by the sample, whilst simultaneously being *insensitive* to transverse phase gradients which are not due to the sample.

As an example of the non-uniform illumination which will be present in even the best of third-generation synchrotrons, a 25keV (as used in biomedical imaging [10]) flat field image observed at the bio-medical imaging hutch of beamline 20XU at SPring-8, Japan, is shown in Fig. 1. Without a diffuser present (Fig. 1a), the beam shows a high intensity peak (visible as a red stripe in the false-color map), which represents the temporally-varying incident intensity averaged over a single exposure. As shown in the movie supplementary to Fig. 1 ([Media 1](#)), consecutive image frames show significant frame-to-frame variation. There is also propagation-based phase contrast introduced by the non-ideal optics, as indicated by the arrows. As shown in Fig. 1b, when a stationary diffuser (see Sec. 2 for details) is introduced, the illuminating area becomes significantly more uniform, but still shows some movement with time (supplementary Fig. 1 ([Media 1](#))). The flat field has phase images and intensity variations characteristic of the part of the diffuser positioned in the beam. Rotating the diffuser, so that the illuminated area changes over time, will mean that these variations are averaged out over the exposure time. This will produce a field that is even in space and over time, provided that the image exposure time is long compared to the characteristic timescale of the rotating diffuser (Fig. 1c and supplementary Fig. 1 ([Media 1](#))). The placement of this random phase screen directly after the optics means that the phase artifacts in the flat-field image are blurred out.

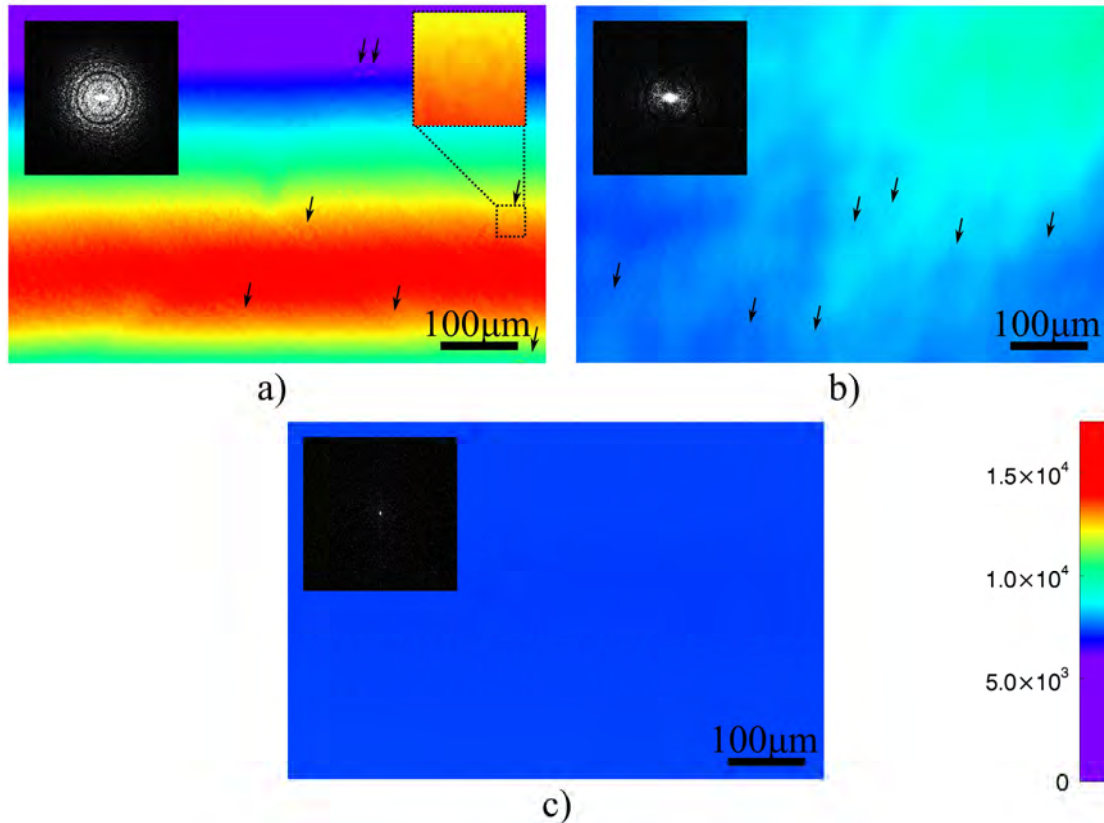


Fig. 1. Flat field at BL20XU as seen (a) without a diffuser, (b) with a stationary diffuser and (c) with a spinning diffuser. Power spectra ( $|FFT\{I\}|^2$ ) are shown inset. (Media 1).

As seen in the inset to Fig. 1c, the impulse-like power spectrum of the spinning diffuser flat-field map clearly indicates a uniform intensity. However with either the stationary diffuser or no diffuser, further components are introduced in the low frequency (beam shape), medium frequency (diffuser pattern) and high frequency (beam-line optics phase artifacts) spatial regions of the power spectra. Note that the dark rings, present in the insets to Figs. 1a and 1b, are zeros in the phase contrast transfer function for the coherent x-ray imaging system [8].

While the series of flat field images in Fig. 1 (Media 1) suggests that the use of a diffuser will be beneficial during synchrotron x-ray imaging, the effect on the transverse coherence of the beam should also be considered. The ensemble-averaged intensity due to many phase screens over the exposure time (*cf.* Sec. 3) means that the magnitude of the complex degree of second order spatial coherence [11] will be decreased, although the coherence width (the width is dominant given the large horizontal size of the undulator beam compared to the vertical size) will be unchanged [1]. In this case, the coherence width is defined as the minimum distance over which two transversely separated points of a wavefield may be considered as spatially incoherent [12]. When a sample is placed in the beam for propagation-based phase contrast imaging, the phase-distorted incident beam will produce a speckled, ‘warped’ phase contrast image dependent on the instantaneous position of the diffuser (*cf.* Fig. 5b), which is incoherently summed over time. Consequently, the visibility and number of fringes in the phase contrast fringe set from a single interface in the sample will be significantly reduced [13]. The link between unresolved phase variations (resulting in speckle) and observed decoherence effects has been previously discussed (*e.g.* [14], [15]) in the context of spatial ensemble averaging by the detector (in our case it is predominantly an effect of temporal averaging).

In some bio-medical imaging applications, a single bright/dark phase contrast fringe is all that is desired, to reveal the position of an interface [4]. Other applications require multiple

fringes, either to permit use of a phase retrieval algorithm [16], or so that the fringe pattern may be easily identified amid surrounding intensity variations [17]. It is for this reason that we study the optimal diffuser set-up in this paper.

This analysis looks at both simulated and experimental propagation-based phase contrast images with 25keV energy and an object-to-detector propagation distance of between 0.5 and 1.45 meters. The computer simulation is based on a diffuser model described in [1], evaluating the incoherent sum of a number of simulated phase contrast images, each produced with an incident field that has incurred random transverse phase variations of a specified characteristic depth and width at the the diffuser position. The incoherent ensemble average, due to these many diffuser positions over a complete exposure, forms the phase contrast image.

We close the introduction with a summary of the remainder of the paper. In section 2, we outline our phase contrast x-ray imaging experiment and describe the key observations relating to the effect of a phase diffuser on our phase contrast images. The numerical simulation, based on our model for the phase diffuser, is detailed and implemented in section 3. The final section compares theory and experiment, quantifying the effect of a diffuser on the visibility and number of observable fringes in a phase-contrast x-ray image of an edge. We conclude with some practical recommendations for future experiments. The most important recommendation is to place the diffuser as close as possible to the x-ray source, in order to retain desired fringe information while simultaneously suppressing phase-contrast artifacts due to imperfections in the illuminating beam.

## 2. Experiment on propagation-based phase contrast imaging with a diffuser

X-ray images were acquired on BL20XU, an undulator-source beamline at the SPring-8 synchrotron in Japan. We worked at the downstream hutch, which gives a source-sample distance of 240m. A double crystal Si-111 monochromator was used to select x-rays at an energy of 25keV. The high resolution detector system used comprised a  $4008 \times 2672$  pixel CCD camera coupled to a Hamamatsu AA50 x-ray converter with a  $50\times$  objective lens, yielding an effective pixel size of  $0.18\mu\text{m}$ .

The diffuser utilized at this beamline consists of a  $\approx 12\text{cm}$  diameter circular disk of conventional office-grade white copy paper ( $80\text{ g/m}^2$ ) which was made to rotate within a plane perpendicular to the x-ray optical axis. A set of slits created a  $300\mu\text{m} \times 300\mu\text{m}$  aperture which acted as a secondary source. The diffuser used on this beamline was located approximately 78m from the source and 29m from the aperture (see Fig. 2).

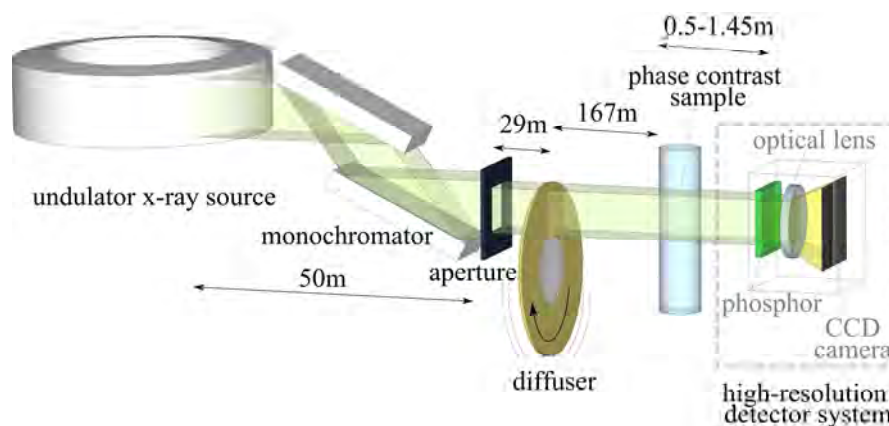


Fig. 2. Experimental set-up at SPring-8 x-ray synchrotron beamline BL20XU, using 25keV x-rays to produce propagation based phase contrast images (object-to-detector propagation distance between 0.5 and 1.45m). Images recorded on a CCD camera coupled to a phosphor screen and optical lens, producing  $0.18\mu\text{m}$  effective pixel size.

Samples for this experiment were a cylindrical perspex rod (diameter 3.0mm), and two perspex spheres of 1.5mm diameter which in projection overlapped very slightly (region of overlap was approximately  $30\mu\text{m}$  at its widest point, see inset to Fig. 3a). On this beamline, at

sample-to-detector propagation distances ranging from 0.5 to 1.45m, these objects produce tens of Fresnel-regime phase contrast fringes. In the case of the overlapping spheres, these fringes intersect, forming lattice-like sets of intensity peaks whose visibility is highly sensitive to the effect of a diffuser. Such a region is shown in Figs. 3b and 3c, clearly demonstrating the reduction in area and visibility of fringes when a diffuser is introduced in the experiment.

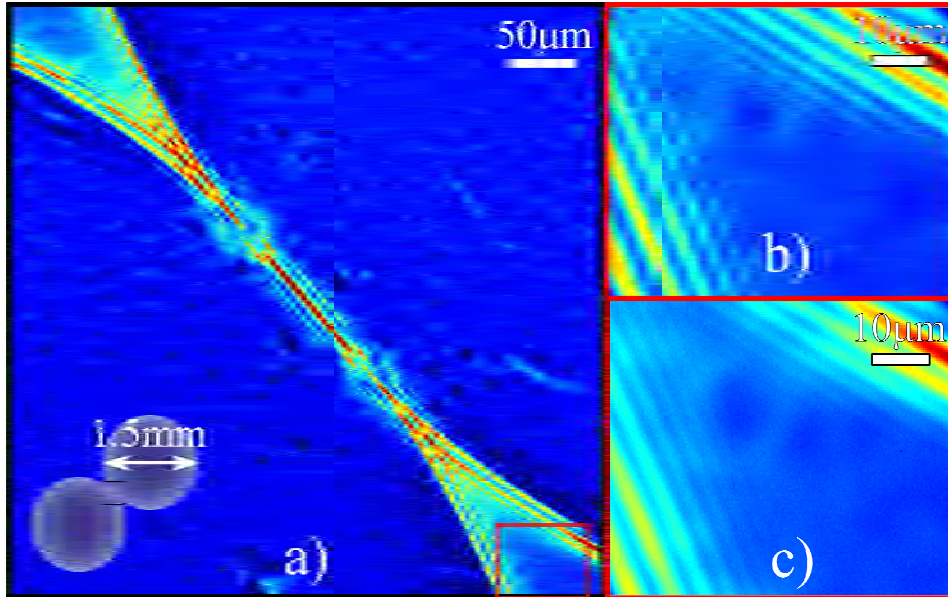


Fig. 3. The observed effects of a diffuser on the visibility of fringes in the propagation-based phase contrast image of two 1.5mm diameter Perspex spheres at 1.45m object-to-detector propagation distance. In projection, the spheres share an overlap region of up to 30µm, which results in a complex interference pattern. (a) Image in the absence of a diffuser. The field-of-view here is illustrated by the black box in the inset, which shows the projected thickness image of the two spheres. (b) Magnified region of lattice-like interference pattern in Fig. 3a (region denoted by red box), still in the absence of a diffuser. (c) The same region, this time taken with diffuser present. Note the absence of central intersecting fringes in (c), when compared to (b).

### 3. Model for x-ray diffuser in propagation-based phase contrast imaging

The effect of the spinning diffuser is computationally modeled as a series of random transverse phase perturbations, each added to the phase of the simulated x-ray wavefield at the position of the diffuser, propagated and the resulting intensity map summed incoherently at the detector plane. The random transverse phase distribution is characteristic of the thickness and fiber size of the paper. An optical microscopic image of the paper surface (at 12.5× magnification) is shown in Fig. 4, demonstrating a range of features ranging from coarse (*e.g.*  $\alpha$ ) to fine (*e.g.*  $\beta$ ). The azimuthally-averaged power spectrum of this image is well approximated by a two-dimensional Lorentzian whose full width at half maximum (FWHM) corresponds in real space to 7µm. For each term in the time-sum, a particular random phase screen realization is generated beginning with a normally-distributed white-noise random two-dimensional array which is then spatially smoothed by Fourier-space multiplication with the normalized Lorentzian. The smoothed transversely random array is multiplied by the mean paper thickness  $T_{paper}$ , the vacuum x-ray wavenumber ( $2\pi/\lambda$ ) and the refractive index phase decrement  $\delta$  according to the projection approximation (see [18]) (Eq. (1)). This phase shift is then added to the diffuser-incident phase  $\varphi_{before\ diffuser}(x, y)$ , to give the diffuser-exit phase  $\varphi_{after\ diffuser}(x, y)$  as a function of coordinates  $(x, y)$  perpendicular to the optic axis:

$$\varphi_{after\ diffuser}(x, y) = \varphi_{before\ diffuser}(x, y) - \frac{2\pi}{\lambda} \delta_{paper} T_{paper} \times Random\ Screen(x, y). \quad (1)$$

We used  $\delta = 2.75 \times 10^{-7}$  for paper, producing phase depths with a standard deviation of approximately 1.25 radian at 25keV, illustrated by the example profile in Fig. 4b.

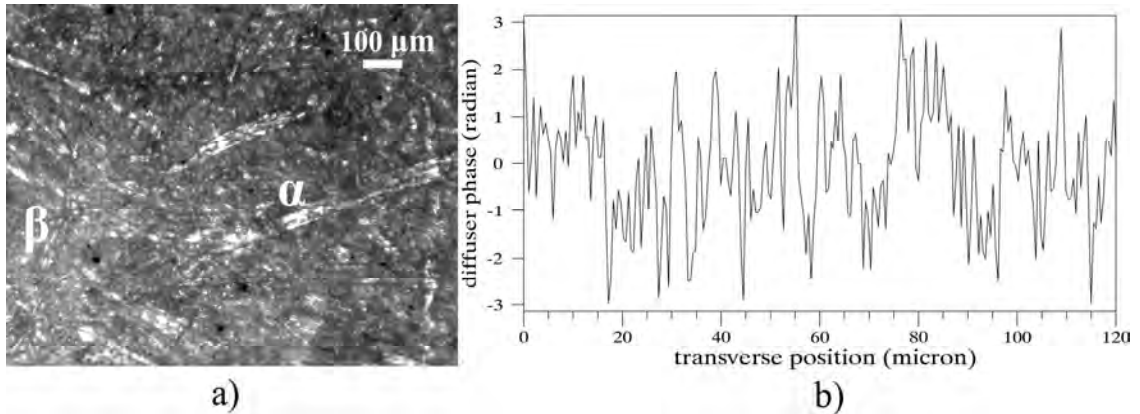


Fig. 4. (a) Optical microscope image of the diffuser paper used. (b) Line profile through one two-dimensional realization of the transversely random phase map used to simulate the diffuser as a thin phase screen, before propagation.

All simulations were performed using the Interactive Data Language (IDL 7.0), with a final pixel size of  $0.18\mu\text{m}$ , as in the experiment (see Sec. 2). To determine only the relative effects of the diffuser and avoid prohibitively long calculation times, the model assumes a point source. The effects of an extended source on the transverse coherence properties in this set-up have been considered in a previous work by the authors [1]. The complex monochromatic scalar wavefield  $\Psi$  from such a source was calculated directly at the plane of the square aperture, cropped in accordance with the Kirchhoff approximation to simulate the effect of the aperture, and then propagated through a distance  $\Delta$  from the aperture to the diffuser position. For propagation of a coherent scalar x-ray wavefield we make use of a Fourier representation of the angular spectrum [19], employing the Fast Fourier Transform [20]:

$$\Psi(x, y, z = \Delta) = \mathfrak{F}^{-1} \exp\left\{i\Delta\sqrt{k^2 - k_x^2 - k_y^2}\right\} \mathfrak{F}\Psi(x, y, z = 0). \quad (2)$$

Here,  $\mathfrak{F}$  denotes two-dimensional Fourier transformation,  $\mathfrak{F}^{-1}$  denotes the corresponding inverse transformation, and  $(k_x, k_y)$  are Fourier coordinates dual to  $(x, y)$ .

In the diffuser plane, the phase shift of the modeled paper is added to the wavefield phase, which is then propagated to the sample position. The projection approximation is again utilized to calculate the relative phase change and attenuation due to the sample of material components  $j$ :

$$\Psi(x, y, z = z_0) = \exp\left\{-ik\sum_j [\delta_j - i\beta_j]dz\right\} \Psi(x, y, z = 0). \quad (3)$$

Parameters  $\delta_j$  and  $\beta_j = \lambda\mu_j/4\pi$  respectively quantify the refractive and absorptive properties of material  $j$ , where  $\mu_j$  is the linear absorption coefficient.

The angular-spectrum formalism (Eq. (2)) is then used once more to simulate the propagation over the object-to-detector distance. A single intensity image over the detector plane then simulates a single position of the diffuser. The incoherent ensemble average over many such diffuser positions produces a smooth background in the final image, simulating the observed image for a complete exposure.

Note that the very long propagation distances from diffuser to object (over 150m), and an object resolution of micrometers, necessitated use of the 32GB RAM VPAC computer cluster [21] to sustain very large array calculations (up to  $8000 \times 8000$  pixels) for accurate resolution

of the free-space propagator (for small wavelengths, the limiting propagation distance is proportional to the array dimensions and the square of the pixel size) [22].

Figures 5a-5c, shown below, illustrate the effect of this process. In Fig. 5a, simulated phase contrast fringes present due to Fresnel diffraction from the edges of a 3mm diameter perspex cylinder are seen. Figure 5b shows a single realization of the diffuser model, with distorted fringes and overlying 'image' of the diffuser. Interestingly, the speckle from the given realization of the diffuser's thin random phase screen, has a visibility comparable to the fringes produced by the object. (The intensity variations of Fig. 5b are greater than that seen in the observed stationary diffuser flat field of Fig. 1b due to the finite length of the exposure time and beam movement within this time.) These random undulations in the phase incident on the sample locally distort the image for each diffuser realization. Figure 5c is the incoherent sum of 1000 realizations of the diffuser model, wherein the phase contrast fringes of Fig. 5a are once again apparent but at a reduced visibility. Several of the narrowest fringes are no longer visible. The speckles due to the diffuser itself are no longer seen, as the ensemble average of many random realizations over the full exposure time becomes a smooth background of unresolved x-ray speckle.

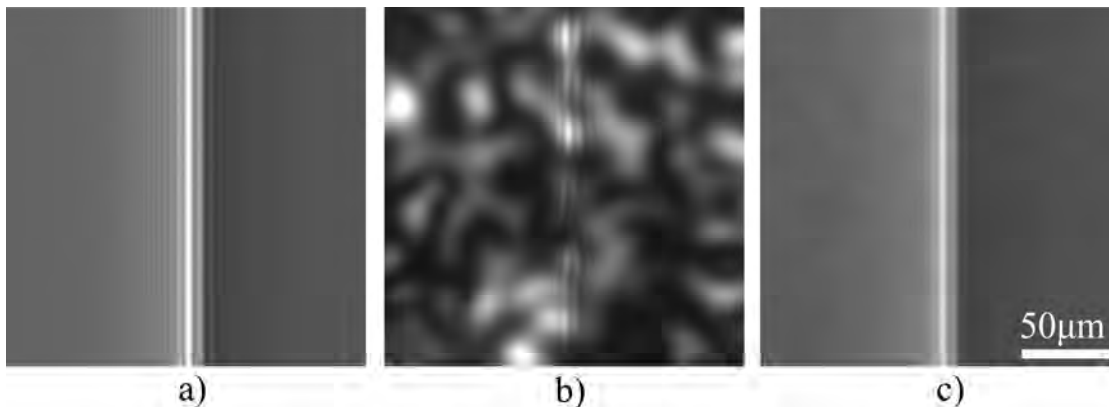


Fig. 5. Simulated phase contrast images of a 3mm diameter cylinder with 1.45m propagation, using (a) no diffuser, (b) a single diffuser position and (c) the incoherent sum over 1000 diffuser realizations.

To complete the simulations, the modelled phase contrast images were convolved with the detector point spread function (PSF). The 1D PSF was measured from experiment as the derivative of a knife-edge image [23], yielding a PSF of 1.2 $\mu$ m FWHM.

The results of this simulation modeling the same two spheres as in Fig. 3, are shown below in Fig. 6, matching very well in terms of the fringe patterns and visibility. Again, both the contrast and number of visible fringes are greatly reduced when the diffuser is present (Fig. 6c) compared to when the diffuser is not used (Fig. 6b). The effect is exacerbated when a small degree of noise (approx 2%, consistent with experimental noise levels), is added to the simulated images (not shown).

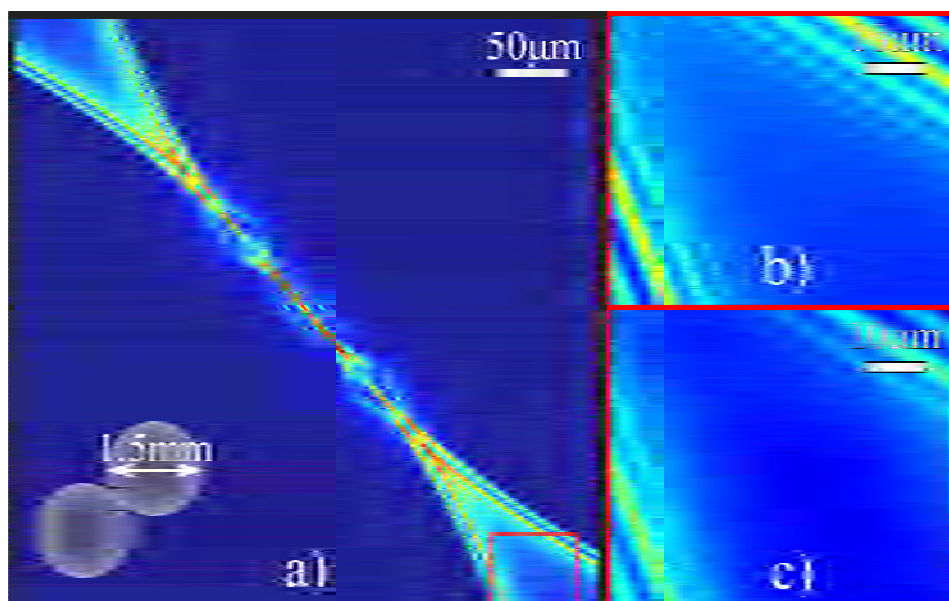


Fig. 6. Simulated phase contrast images of 1.5mm diameter spheres seen experimentally in Fig. 3, modelled without, then with a diffuser. (a) Image in the absence of a diffuser. (b) Magnified region of the lattice-like interference pattern (region denoted by red box) in (a). (c) The same region of a similar image, this time modelled with diffuser present.

#### 4. Comparison between modeling and experiment, for x-ray phase contrast diffuser

In order to quantitatively determine the effect of the diffuser on propagation-based x-ray phase contrast images, in both simulation and experiment, we applied Michelson's measure for interference fringe visibility  $V$  over the entire fringe set [24,25]:

$$V = \frac{I_{\max} - I_{\min}}{I_{\max} + I_{\min}}. \quad (4)$$

To obtain a single phase-contrast intensity profile for this analysis, cylinder images were row-averaged, showing reasonable agreement between experimental results and our model, as shown in Fig. 7. The diffuser is seen to decrease both the visibility and number of phase contrast fringes, in both experiment and in simulation. This detailed fringe information may be valuable in quantitative image analysis, *e.g.* in the context of phase-retrieval algorithms which utilize such information [16], however the narrowest fringes are suppressed by the diffuser.

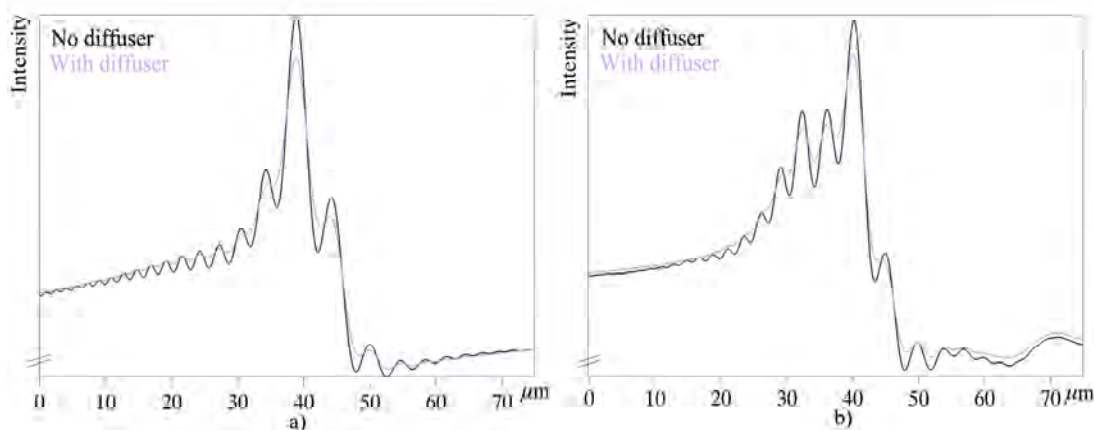


Fig. 7. Observed decrease in visibility of phase contrast fringes seen at the edge of a 3mm cylinder, taken with 1.45m propagation, (a) in simulation and (b) observed.

The relative effect of the diffuser on fringe visibility is dependent on the propagation-distance between sample and detector. In the Fresnel regime, increasing propagation causes an increase in fringe contrast and spacing. The visibility of the wider fringes seen at large propagation distances is also less affected by the point spread function of the detector, when compared to the narrower fringes obtained at smaller propagation distances. The rate of increase of fringe visibility as a function of propagation distance is reduced when the diffuser is introduced. This means that the diffuser makes more of a difference at the greater sample-to-detector propagation distances, as shown in Fig. 8a. The percentage decrease in visibility incurred by a diffuser increases by a factor of around 9% when moving from 0.5 to 1.5m propagation.

This decrease in visibility is due to the smoothing effect the presence of a diffuser has on the observed phase contrast fringes (*cf.* Figs. 3, 5 and 6). Consequently the narrowest fringes, which are generally also the fringes with smallest local contrast, are lost when a diffuser is introduced. In a similar trend to visibility, the rate of increase, with propagation, in the width of the interference fringe area from a single edge is lessened when a diffuser is present, as seen in Fig. 8b. Measurements from simulation based on our model agree with the observed changes, showing the trends described above. There are some discrepancies at short propagation distances, where the width of the phase contrast fringes becomes comparable to the pixel size.

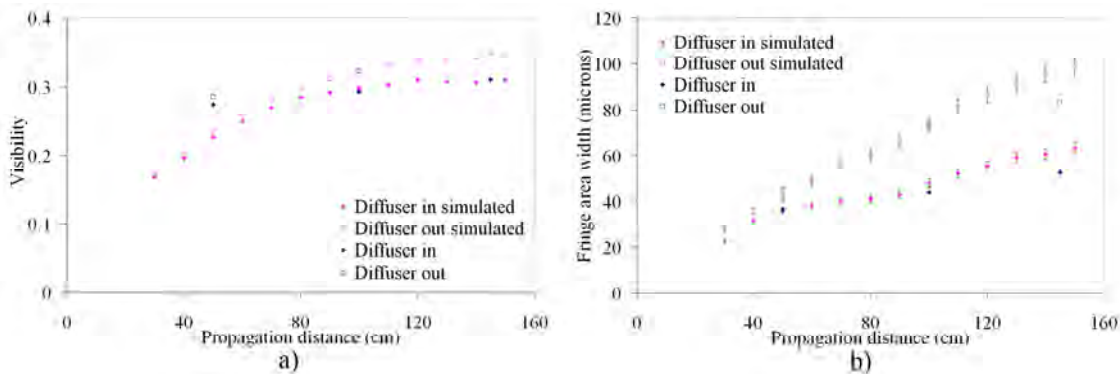


Fig. 8. (a) Visibility and (b) Width across which fringes from the edge of a 3mm decreases when a diffuser is introduced, with most effect at long propagation distance, both observed and in simulation.

The phase variations which determine the efficacy of the diffuser may be described by both the phase depth  $\Delta\phi$  and characteristic transverse length scale  $l$  of the resulting wavefield phase. Speaking only of the un-propagated wavefield (*i.e.*, the wavefield at the exit-surface of the diffuser), the phase depth of the wavefield is determined according to the projection approximation, which incorporates x-ray energy, the phase decrement  $\delta$  of the diffuser material and the variations in the projected thickness of the material. The characteristic transverse length scale  $l$  is determined by the size distribution of the diffuser constituent materials which give rise to those projected thickness variations, together with the thickness of the diffuser.

A simple descriptor which combines the properties  $\Delta\phi$  and  $l$  is that of a ‘root-mean-square (RMS) transverse phase gradient’; roughly speaking it is given by  $\Delta\phi/l$ . In Figs. 9a and 9b are shown the simulated effects of changing these properties, on the Fresnel-regime fringes of the Perspex cylinder image. For simplicity the phase of each cylinder-entrance wavefield was generated directly, *i.e.* without prior propagation, using Gaussian length-scale distributions. Figure 9a keeps  $l$  constant at 20 $\mu$ m FWHM and varies the phase-depth  $\Delta\phi$  from a standard deviation of 0.2 rad to 2.0, whilst Fig. 9b keeps  $\Delta\phi$  constant at a standard deviation of 1.0 rad and varies  $l$  from 2 $\mu$ m to 20 $\mu$ m.

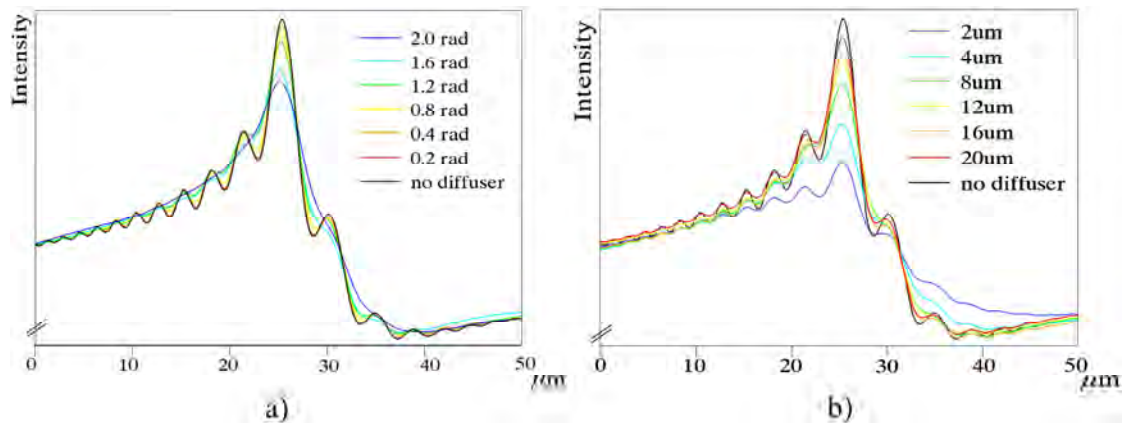


Fig. 9. Visibility of phase contrast fringes decreasing with (a) increasing phase depth  $\Delta\phi$ , (b) decreasing characteristic length  $l$ . Propagation distance is 1.0 m.

In Fig. 9a the profile with a  $\Delta\phi = 0.2$  rad is almost indistinguishable from the profile simulated without any diffuser. As the phase depth is increased the profile is increasingly strongly smoothed until the  $\Delta\phi = 2.0$  rad profile is so strongly smoothed as to have lost all fringe information altogether. These profiles are visually comparable to convolution of the no-diffuser profile with a Gaussian whose FWHM varies with the square of the phase depth.

In Fig. 9b, where the characteristic length scale  $l$  of the diffuser material is varied, the effect at large length scales (or small phase gradient) is consistent with a slight smoothing effect. As the length scale is decreased, the fringe contrast is further reduced however the smallest fringes are still apparent. The  $2\mu\text{m}$  FWHM length-scale profile has a much smaller absolute visibility than the largest phase depth profile in Fig. 9a and yet has retained significant fringe information. As such, it appears that the larger length scale variations in phase must also be present to smooth out the narrow fringes, as was observed in experiment.

Propagation of the wavefield from diffuser to sample was shown in simulations to result in negligible changes in phase depth. However, due to the relatively large propagation distances involved (see Fig. 2) and the corresponding scaling associated with Fraunhofer diffraction, the characteristic transverse length scale is increased as the whole wavefield is magnified with distance by the factor:

$$M = \frac{R'_1 + R_2}{R'_1}, \quad (5)$$

where  $R'_1$  is the effective source-to-diffuser distance (corresponding to a point source), and  $R_2$  is the diffuser-to-sample distance.  $R'_1$  in our case was determined by the size of the aperture, and found to be approximately 37m upstream of the aperture.

Figure 10 shows experimentally the effect of changing the diffuser position relative to source and sample. The resulting magnification with increased propagation means that the RMS phase gradient at the sample is decreased (and the degree of coherence increased), reducing the dampening of the fringes by the diffuser. All of the diffuser measurements described thus far were conducted with the diffuser in its customary location, *i.e.* the experimental hutch which is 29 m from the aperture (see Fig. 2). However, as a result of these and previous studies [1], the diffuser has now been permanently relocated to the closer optics hutch, and placed 1.7m from the aperture, hence the reduction in visibility is now insignificant.

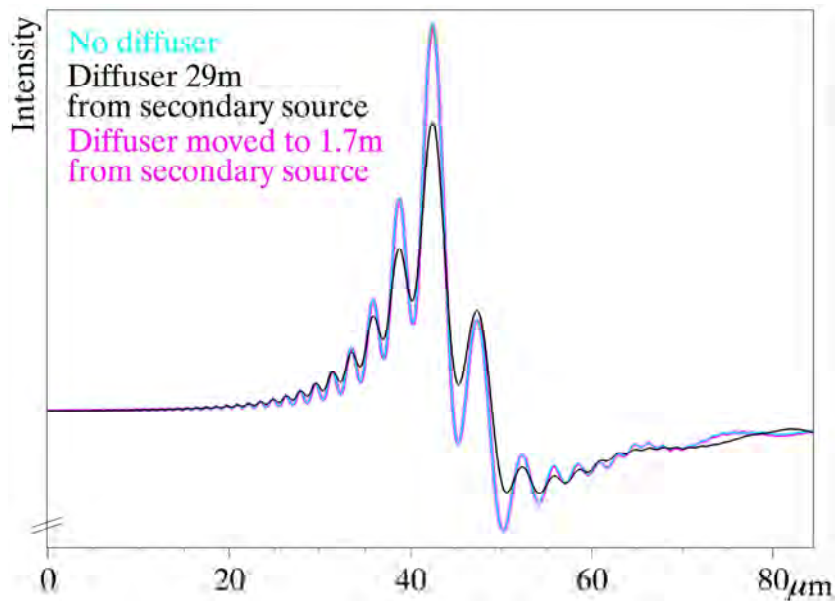


Fig. 10. Visibility decrease in phase contrast fringes from the edge of a 1mm Perspex cylinder observed experimentally in the presence of a diffuser is more significant for a diffuser placed in the upstream experimental hutch 29m from the aperture secondary source, than at the optics hutch 1.7m from the aperture.

Figure 11 is a plot showing the simulated effects of changing RMS phase gradient on fringe visibility. The decrease in visibility when changing characteristic transverse length scale is shown on the same axis as when changing phase depth. As always the visibility was calculated from the global maxima and minima of the fringes. There is general overlap between the two series of points, which is consistent with the idea of the RMS phase gradient as the determining factor. The series differ most at higher phase gradients, where the length scale was smallest (and less physically likely).

The simulated visibility at the two diffuser positions are also indicated in Fig. 11. It was seen that by moving the diffuser close to the source, the magnification increase led to a relative phase length which was effectively doubled, *i.e.* halving the phase gradient. This change is consistent with the effect observed in Fig. 10. The additional propagation from the diffuser to the sample increases the observed coherence, in accord with the van Cittert-Zernike theorem [26–28].

Figure 11 may thus be viewed as a plot which summarizes the deleterious effect of the diffuser on the phase contrast fringe information for a given sample-detector distance. The RMS phase gradient of the x-ray wavefield at the sample entrance plane is characterized by the diffuser position and material, and indicates the strength of the diffuser. The visibility of the resulting detected fringes from a typical sample, relative to their visibility in the absence of the diffuser, is proportional to the factor decrease in the observed degree of coherence which the diffuser causes. Use of too strong a diffuser yields a part of the curve where the decrease in observed fringe visibility and hence degree of coherence may be unacceptable to the user. On the other hand, this loss of coherence may be advantageous if the user wishes to remove phase contrast.

If the user wishes to conserve the observed degree of coherence as much as possible, and yet maintain the desired effects of the diffuser on the intensity homogeneity of the detected beam, it is perhaps easiest to move the position of the diffuser, away from the sample and closer to the source.

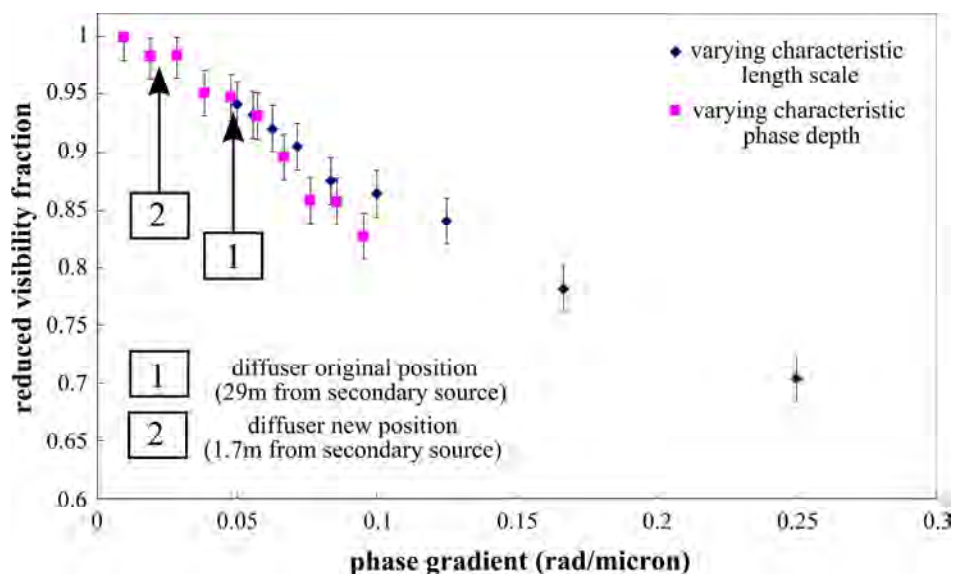


Fig. 11. The characteristics and position of the diffuser will determine the phase gradient in the field incident at the sample, hence the effect of the diffuser on the visibility of observed phase contrast fringes.

## 5. Summary and Conclusion

A spinning piece of paper represents an extremely simple and low-cost method for the diffusion of hard x-ray beams in the context of propagation-based phase contrast imaging. Use of such a diffuser is of particular benefit to imaging experiments which require close to homogeneous intensity over a broad area and increasingly shorter exposure times, for example in many *in vivo* biomedical imaging applications. As many of these applications depend on a sufficiently high degree of partial transverse coherence for phase contrast, it is important to minimize the potential associated deleterious effects of the diffuser on fringe visibility. In this work which combines experimental propagation-based phase contrast x-ray imaging data using a diffuser with simulations, we have modeled the effect of the diffuser as the time-averaged incoherent sum of random phase perturbations to the x-ray wavefield. Simulated Fresnel-regime fringes with and without a diffuser were consistent with experimental observations, displaying a significant decrease in both the number and visibility of fringes when the diffuser was introduced into its standard position. The effect was greatest at larger sample-detector distances. The role of the phase distribution of the random screen representing the diffuser, in terms of a characteristic phase depth and length scale, was investigated and discussed in terms of an average absolute 'phase gradient'. This leads to several practical suggestions for the optimization of a diffuser in terms of minimizing the effect on the degree of coherence at the object and detector. Primarily, it is desirable to place the diffuser as close to the source, or secondary source (*e.g.* aperture), as possible. The resulting increase in far-field propagation and consequent scaling serves to magnify the length scale of the phase distribution, decreasing the phase gradient and hence the effect on fringe contrast. The combination of thickness/roughness and fiber characteristics of the diffuser-material should also be considered given specific requirements for the detail and visibility of a phase contrast fringe set.

Conversely, it is also possible to apply these principles for opposite effect, in situations where a high degree of coherence is temporarily undesirable. One example of this would be on a synchrotron beamline where pure absorption-based CT is required but a contact (zero distance between sample and detector) image is unachievable.

The position of the diffuser along the beamline may therefore be chosen to produce the required degree of coherence for the imaging required. More importantly, the diffuser will spatially even out the beam and reduce phase effects in the final image.

## Acknowledgments

The authors thank the Japan Synchrotron Radiation Research Institute (Proposal number 2008B1985) for the privilege of using the SPring-8 facility to conduct these experiments. We acknowledge funding for the trips to SPring-8 for the Australian co-authors from the Access to Major Research Facilities Program, which is supported by the Commonwealth of Australia under the *International Science Linkages program*. The computational component of our project was supported by the Victorian Partnership for Advanced Computing HPC Facility and Support Services. Kaye Morgan and Sally Irvine acknowledge the support of an Australian Postgraduate Awards. Kaye Morgan also acknowledges a J. L. William Scholarship from Monash University. David Paganin acknowledges the Australian Research Council. We thank Andreas Fouras for the use of his PCO camera during the experiment, as well as Stephen Dubsky and Simon Higgins for their assistance and the use of their optical microscope for Fig. 4.

---

## Propagation-Based PCXI for the Study of Airway Interfaces

### 6.1 Introduction

The ability of phase contrast imaging to resolve soft tissue interfaces is particularly of use in the imaging of the airways. In this chapter, such an application is described, detailing the work undertaken in collaboration with a team from the Women's and Children's Hospital in Adelaide to develop a measure of airway health using PCXI. This collaboration aims to utilise the benefits of phase contrast imaging in a novel application: the assessment of a new treatment for cystic fibrosis. Cystic fibrosis (CF) is a genetic condition in which the cystic fibrosis transmembrane conductance regulator (CFTR) gene defect affects the fluid balance across airway surfaces (Boucher, 2004, 2007). The condition is seen in a number of ways, the most debilitating of which is associated airway disease (Welsh and Smith, 1995). Mucus retention, airway obstruction and inflammation continually degrade the health of the airways and lungs, resulting in a decreasing quality of life for sufferers and often death early in adulthood. Work done by Dr David Parsons and collaborators from the Women's and Children's Hospital in Adelaide, Australia offers potential for a cure, using an airway gene transfer method (Limberis et al., 2002). A key concept in the assessment of the therapy is the airway surface liquid (ASL). As shown schematically in Fig. 6.1, there is normally a thin layer of salty water coating the inside of an airway, a sufficient depth of which is critical in maintaining clear airways.

The ASL allows cilia along the airway surface to be active in clearing debris to protect the lungs. A decreased depth in ASL has been observed as a result of an airway cell ion imbalance (Tarran et al., 2001). An effective treatment for CF airway disease should result in an increase in ASL depth, restoring the ability of the cilia to clear debris. This depth is typically only 5 to 75  $\mu\text{m}$  (Song et al., 2003), depending on the animal and the airway site, and changes are of the order of several micron (Tarran et al., 2001). The ability to image and track this ASL depth *in vivo* would therefore provide immediate feedback on the effectiveness of the gene therapy or indeed any pharmaceutical therapy being developed. Their work on the treatment has used a mouse model, so live PCXI of the 1mm diameter murine<sup>1</sup> airways using a synchrotron x-ray source (specifically SPring-8, Japan) is the focus of this work. Future studies propose the use of sheep and marmosets to study the effects of treatment in a human size lung and primate lung, respectively.

This chapter first provides some background on the condition of cystic fibrosis in section 6.2. Section 6.3 describes the mouse airway imaging performed, including visualisation of airway

---

<sup>1</sup>Pertaining to a mouse.

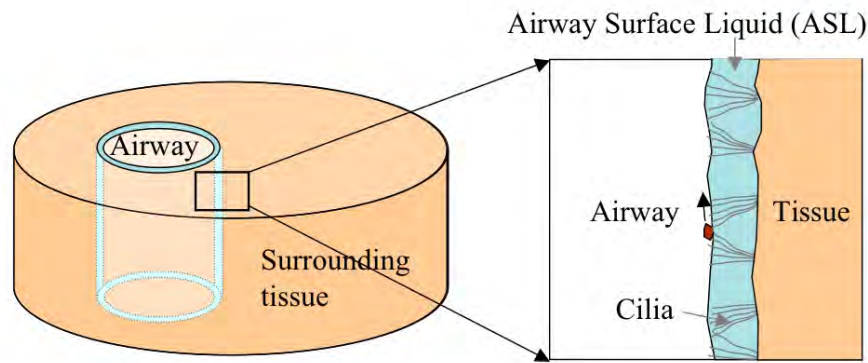


Figure 6.1: a) ASL coats the inside of the airway, b) enabling cilia to move back and forth to transit debris from the lungs.

imaging sites by both CT and by live airway observation. Several methods for extracting data from these live sequences are then described in section 6.4. Further optimisation of the imaging set-up and image analysis to obtain detailed interface fringe patterns, rather than simple edge enhancement, are detailed in section 6.5. Finally, section 6.6 describes an alternative airway health measure, using observation of the clearance of particles along the airways.

## 6.2 Cystic Fibrosis

### 6.2.1 The Condition

Cystic fibrosis, or Mucoviscidosis, is a condition affecting approximately 1 in 2500 people (Welsh and Smith, 1995). Passed on recessively, the gene defect is a mutation in the CFTR gene (McAuley and Elborn, 2000). This gene is responsible for the production of sweat, digestive juices and mucus. While most people have two normal CFTR genes, health is unaffected by having one normal and one mutated CFTR gene (*i.e.* in carriers). CF is only present when two carriers both pass on a mutated CFTR gene to their child. Testing is now possible to determine if a person is a carrier, but such tests are not routine. Screening of newborns for CF is much more common and usually picks up sufferers early (Welsh and Smith, 1995).

The condition affects a number of processes in the body. Chronic, progressive, infective and inflammatory lung disease is the major symptom. Sinus infections result from a dysfunction in the cell ion-balance, dehydrating and decreasing the ASL depth, compromising normal airway cleansing mechanisms. CF sufferers also have difficulty digesting food properly, resulting in diarrhoea and poor growth. Infertility is another symptom, affecting 97% of CF males and some females. Secondary problems include high blood pressure in the lungs, difficulty in circulating oxygen, heart failure, headaches and diabetes. Most of these symptoms may be treated or controlled in some way (Tonelli and Aitken, 2001). Enzyme tablets are taken to help to digest food, and a specialised diet can aid CF patients in gaining weight. There are now more alternatives to assist with reproduction and there are treatments available for secondary problems such as diabetes. However, lung disease remains the most dominant symptom, with a range of therapies helping to extend the life span of a patient, but never preventing the degradation of lung health. The airways of patients

progressively become infected and inflamed due to bacteria which are not normally dangerous for non-sufferers. This results in frequent and increasing coughing and difficulty exercising due to breathing restrictions. Antibiotics may be taken to control the infection and steroids to reduce inflammation. Regular physiotherapy also helps to clear the chest, through targeted percussion on the patient's back and chest (Marks, 2007). Mucus secretions are loosened using aerosolized medications, and broncodilator drugs help to open airways. Hypertonic saline is a more recently developed treatment, which increases ASL depth (Daviskas, 2006). Exercise is encouraged to help clear airways and keep the patient as healthy as possible. Nevertheless, the condition of the lungs is continually worsening, requiring regular visits to hospital.

### 6.2.2 Long-term Treatments

Currently, the only long-term treatment option that will halt further lung disease is a lung transplant. This involves many risks and hurdles, including long waiting lists, missing the time-window for transplant, side effects from a lifetime of anti-rejection medication after the operation, and possible complications during a long recovery period. Our collaborator Dr Parsons and his team are working on an alternative long-term option which promises to increase the lifespan and the quality of life for many sufferers of CF (Parsons, 2005). As a form of gene therapy, a lentivirus vector<sup>2</sup>, delivered by aerosol, instillation or spray, will be used to place normal CFTR genes into the airway cell chromosomes. The normalised CFTR-containing airway cells will take over proper physiological function from the mutated ones. As normal airway cells, they should increase the airway surface liquid (ASL) depth to that of normal, healthy airways. This will allow the re-hydrated airways to perform normal cleansing mechanisms, clearing mucus secretions from both the airways and the lungs. This motion of debris along the airway surface, out of the lungs, is known as Mucociliary Clearance (MCC) or Mucociliary Transport (MCT). Gene therapy that was able to incorporate correction into airway stem cells could result in continuing CFTR correction, so that the need for regular symptomatic airway treatment should cease.

### 6.2.3 Assessing Treatments

It is essential to assess the effectiveness, longevity and safety of gene therapy in the process of establishing the therapy as a viable treatment. Currently, monitoring of the effect of a treatment may require months or years, tracking small changes in the lung function in response to earlier changes in airway health. The pulmonary function tests used as a measure of airway health for humans (*e.g.* looking at the volume of air which a person can exhale) are not a direct measurement of the effect of a treatment on the airways and require a large number of trials over a long period for reliable results. The condition of a patient's lungs may also be evaluated using x-rays and computed tomography (CT) scans (Harm, 2006; Garcia-Pena and Lucaya, 2004), however this is also a fairly crude measure of airway health and function, reaching a resolution of 1mm at best. Immediate measurement of the direct effect of a treatment would clearly accelerate research. Currently, ASL structure may only be studied after death by histological sectioning. Given that the decreased ASL depth is due to defective chloride and sodium ion channels along the epithelial cells lining the airway surface, the electrical potential difference at the surface should change if the

---

<sup>2</sup>A lentivirus vector is a viral tool used by biologists as a means of delivering genes into cells *in vivo*.

channel behaviour is corrected, caused both directly and indirectly by the CFTR mutation. However electrical potential monitoring only provides local information, and tells us nothing about the extent or spread of the treatment. If the depth of the airway surface liquid could be non-invasively monitored using PCXI, increases in depth due to an effective treatment could be recorded. In the airways of a mouse, as studied here, this change will be of the order of up to 2  $\mu\text{m}$  in an ASL depth of 5-7  $\mu\text{m}$  in the nasal airways and an ASL depth of 50  $\mu\text{m}$  in the trachea. Alternatively, if the transport of debris out of the lungs (MCC) could be non-invasively observed, the speed of clearance will indicate the airway health, and so the effectiveness of treatment. Imaging by synchrotron-based phase contrast could provide detailed, immediate, non-invasive and direct feedback of the effect of a treatment on the airways in animal models.

## 6.3 Airway Imaging Methods

### 6.3.1 Introductory

Mouse models of cystic fibrosis have normally been employed for the testing of treatments. There have been four different strains of mice used for medical tests in Adelaide and imaged in Japan. These include C57 (normal) mice, hairless mice, Fabp mice who have the CFTR gene deficiency and BetaENaC mice who have a sodium channel defect and hence show CF-like symptoms. The live CF transgenic model cannot be taken from Australia to the SPring-8 synchrotron in Japan, due to quarantine regulations, so both the Fabp and BetaENaC were taken to Japan frozen for CT scans. The short lifetime of mice (around 2 years naturally) also means that the rapid disease onset and treatment effects may be observed in a timely manner. Airway imaging has almost exclusively been carried out at the medical imaging beamlines (BL20XU and BL20B2) at the SPring-8 synchrotron in Japan, with either the C57 or hairless mice. A successful pilot beamtime was carried out at the Australian Synchrotron in the 1B hutch of the Imaging and Therapy beamline, but this beamline is still in a construction phase and not yet open to general users. The results as presented below were all obtained at SPring-8, which is one of the few synchrotron imaging facilities with co-located animal care facilities.

The beamline 20XU is used for live imaging, the undulator source providing adequate flux for short exposures, required to avoid movement blur. The second medical imaging beamline, 20B2, has a bending magnet source and provides a larger imaging area, utilised in CT scans. Both have hutches situated 200-250m from the main storage ring (Suzuki et al., 2004), in the Biomedical Imaging Centre, as seen in Fig. 6.2. Beamline 20XU also has available an experimental hutch 75m from the source in the main experimental hall, as seen in Fig. 6.3, which was used in some of these studies. This set-up figure also shows the distances at which key components are placed from the source, as incorporated in simulation components of this work.

Hard x-rays of energy 25 keV are used throughout this study, bringing sufficient penetrating power to provide an adequate number of photons after passing through a small animal, while still enabling good phase contrast.

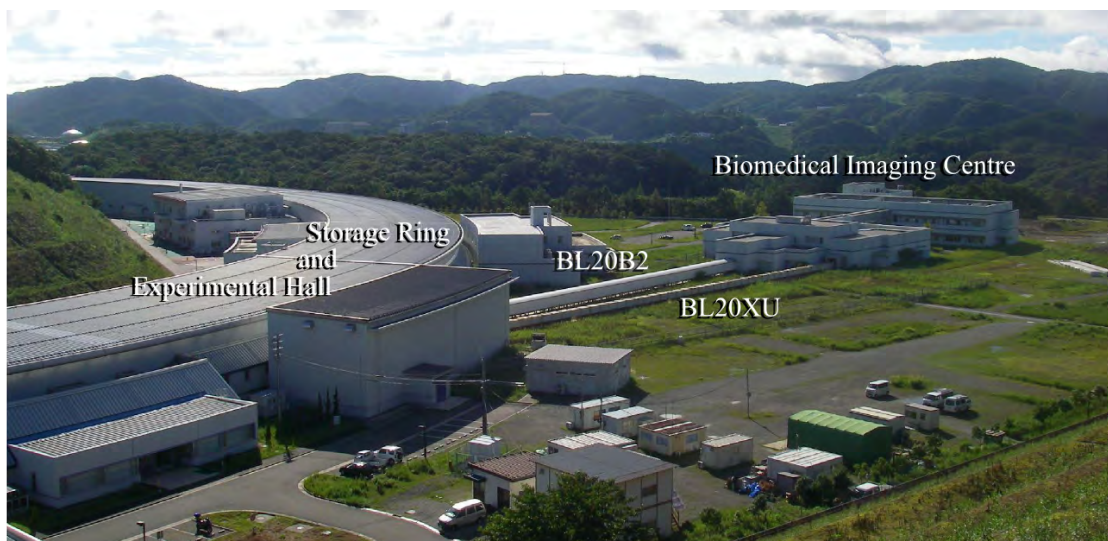


Figure 6.2: SPring-8 beamlines used for biomedical imaging, showing the Biomedical Imaging Centre 250 metres from the storage ring.

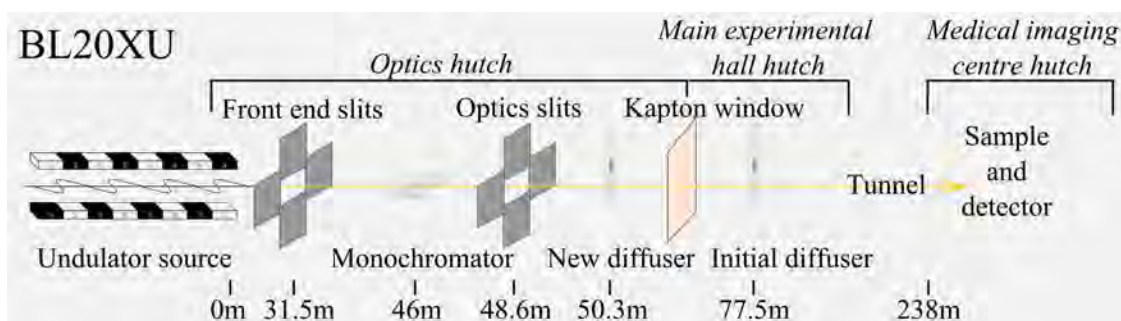


Figure 6.3: Main optical components in the BL20XU undulator beamline at SPring-8, used for the live imaging component of this project.

### 6.3.2 Gene Therapy Delivery Site Observation by CT

This project has used propagation-based phase contrast micro Computed Tomography (CT) (Kak and Slaney, 2001) to visualise the intricate airway structure of the mouse models.

Specifically, CT has been used for monitoring the treatment delivery site in the nasal passages of the mouse (the site of gene delivery in the CF mouse, as CF symptoms are expressed in the complex nasal passages, rather than in the lungs), looking at the placement of a cannula used in lab experiments by Dr David Parsons. Electrical potential difference measurements at the airway surfaces are a conventional measure of gene correction, as the electrical signal will change with correction of the ion imbalance, with the recording electrode placed in a cannula positioned in the nose of a mouse. In this work, it was important to discover the exact position in which the cannula was being placed, to ensure that the signal was coming from the correct region of the airway epithelium (Parsons et al., 2000).

CT has also been used to look at the lung and airway condition of the three mouse models. Figure 6.4 shows a slice through the lungs of one of these mice, a C57 type. The Fabp and BetaEnaC mice mentioned earlier were also imaged in order to compare the airway obstruction. This plays a role in evaluating the amount of mucus present before treatment.

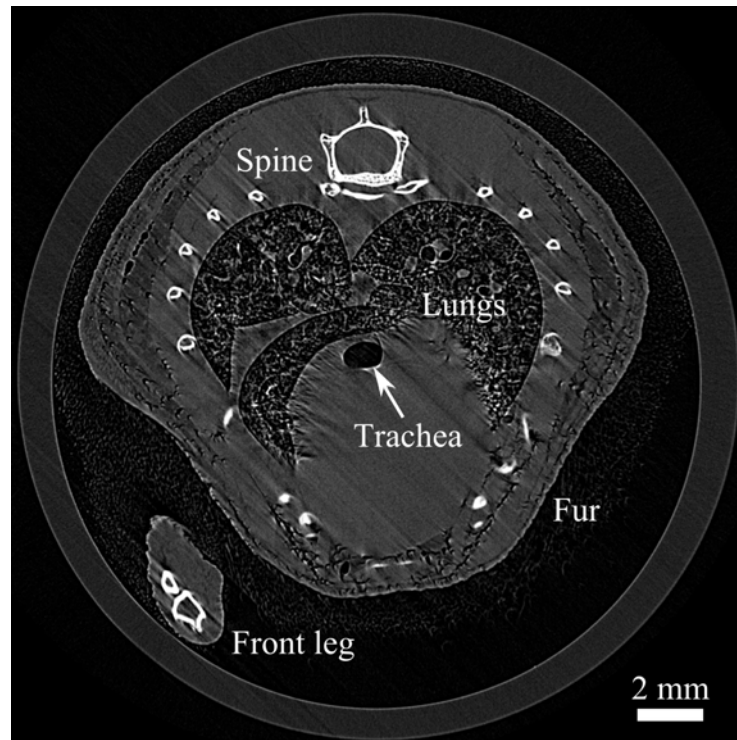


Figure 6.4: A CT slice of the upper lungs of a mouse, as reconstructed from 1500 projections, taken on BL20B2, using 25 keV x-rays and 12  $\mu\text{m}$  pixels, 95 cm propagation. Despite use of a frozen sample, some movement artifacts are evident in these scans, due to inadequate temperature control during imaging.

Using beamline 20B2, each mouse was rotated in front of the beam to take 1500 phase contrast enhanced projection images at equally spaced angles, using 25 keV x-rays, 12  $\mu\text{m}$  effective pixel size, 95 cm sample-to-detector propagation with a  $2632 \times 1648$  pixel CCD. The mice were frozen in an endeavor to reduce movement during the several hours required for each scan, and were returned to the Women's and Children's Hospital in Adelaide for histology after imaging.

The projections were then reconstructed by the candidate using the filtered back projection algorithm (Kak and Slaney, 2001), to give a series of horizontal slice images through the animal, such as that seen in Fig. 6.4, forming a 3D data-set. The edge enhancement produced in the propagation-based images is intentionally retained by reconstructing from PCXI images without phase retrieval or filtering, given that it is the airway interfaces that are of interest. Figure 6.5 shows the excellent detail, even of soft tissue structures, which can be seen in a rendering of the 3D dataset. The candidate used Amira 4 (Visage Imaging) to render both this figure and visualisation movies, an example of which is included on the attached CD as Fig. 6.5 supplementary, moving along the path down the airways by which a treatment would be delivered.

Further detail on this area of work may be found in Appendices B and C (Siu et al., 2008; Parsons et al., 2008).

### 6.3.3 ASL Monitoring by Live Imaging

The central area of work in this collaboration has been live imaging sequences, taken in order to observe changes in the airways over time (typically 40 minutes, imaging every 10 seconds)

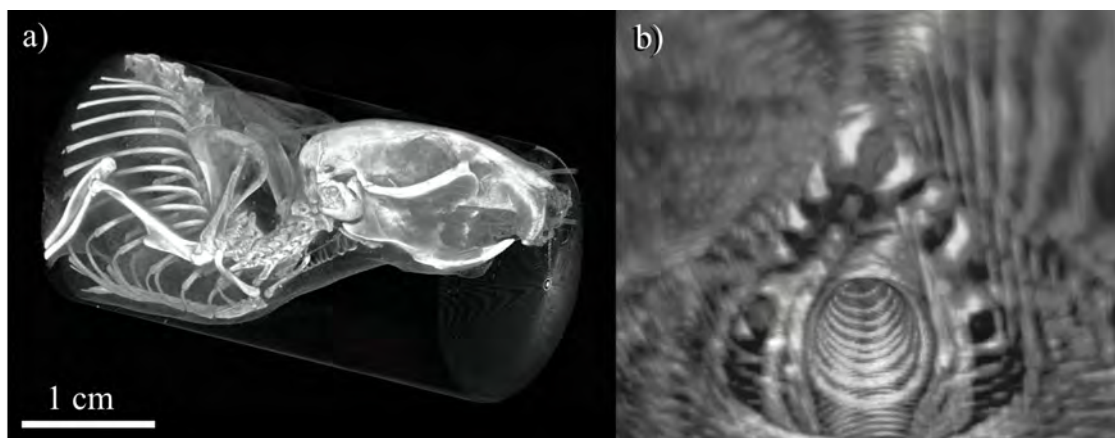


Figure 6.5: 3D rendering of a CT set taken of the upper half of a mouse, a) from outside and b) inside the trachea, looking down towards the lungs.

in response to treatments. As the mice cannot be kept completely still, phase imaging methods which require several images for phase retrieval are difficult. As it was also valuable to detect phase gradients in all directions, propagation-based phase contrast is used. In the initial set of experiments (§6.4), standard symptomatic CF treatments (David et al., 2002) such as mannitol and hypertonic saline (Wark et al., 2006) were administered partway through the imaging sequence, using a nebuliser<sup>3</sup>. These treatments were expected to temporarily increase the ASL depth by several microns over that observed in baseline measurements. These treatments provide a basis for testing of airway assessment methods while the gene therapy treatment is still in development. A second set of experiments was then conducted, aiming to increase the visibility of the indistinct ASL/tissue interface through the experimental set-up (§6.5), so that ASL depth may be measured.

### 6.3.3.1 Synchrotron Live Imaging Experimental Set-up

Imaging using BL20XU has been predominantly carried out in the Biomedical Imaging Centre of SPring-8 ( $\approx 240$  m from the source), although the experimental hall hutch ( $\approx 75$  m from the source) has also been used. The longer source to sample distance at the imaging centre is preferred for increased coherence (see Chapter 4), increased beam area and therefore better beam stability. Nevertheless, the higher flux obtained at the upstream hutch enables shorter exposures, which can be of use in preventing blurring when looking at the lower airways where motion from the animal breathing is significant. The use of a respirator triggered with imaging, including a short breath hold period, has also been important in reducing motion blur by holding the animal stationary in the breathing cycle at the time of imaging.

Mice are constrained in a stereotactic frame<sup>4</sup> so that the head is immobilised, and the body is held in a vertical position with tape, as seen in Fig. 6.6. This further reduces the probability of blurred images due to animal movement, particularly in the nasal airways. Appendix F (Donnelley et al., 2010a) describes the animal imaging setup in further detail.

A distance of around 1m (depending on the specific experiment, see section 6.3.3.3) is introduced between the mouse and the detector to provide propagation based phase contrast. The

<sup>3</sup>A nebuliser is a device used to aerosolize medication so that it may be inhaled as a mist.

<sup>4</sup>A stereotactic frame holds the mouse in an  $x$ - $y$ - $z$  co-ordinate system, as is required for stereotactic surgery.

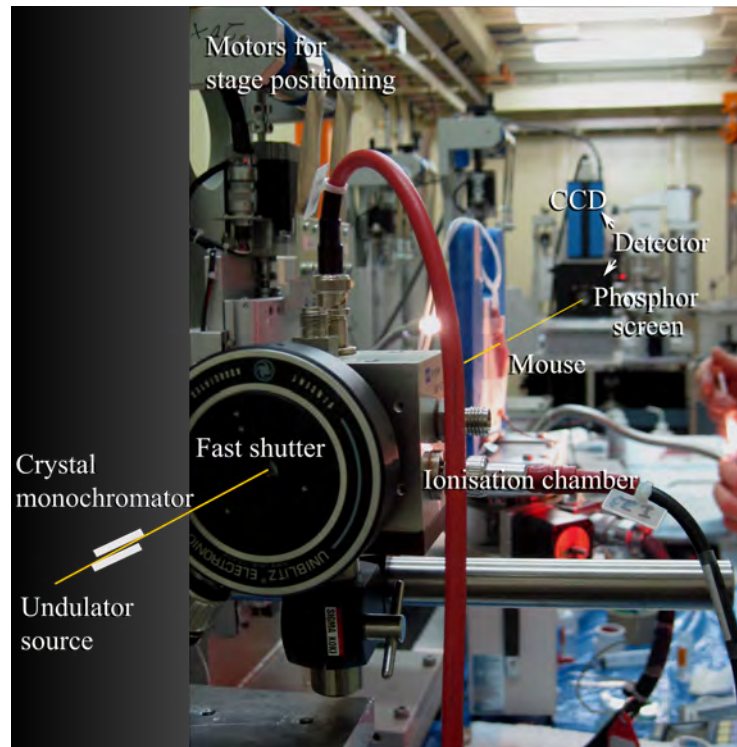


Figure 6.6: Experimental Setup in the Biomedical Imaging Centre of BL20XU, SPring-8, set up for the live imaging sequences.

detector uses a thin phosphor screen to convert x-rays to visible light, which then passes through a microscope objective lens and is reflected in a mirror to the CCD face. The use of an optical lens means that the effective pixel size may be altered to either provide a greater field of view or to look closer at an area of interest. The resolution will usually be ultimately limited by the thickness of the phosphor screen, broadening the point spread function of the detector (§6.5.2.1). The PCI CCD provided  $4008 \times 2762$  pixels, so that both sides of a 1 mm airway could be imaged with  $0.45 \mu\text{m}$  pixels ( $20\times$  lens, providing a 1.8 mm by 1.25 mm field of view (FOV)) or a single side with  $0.18 \mu\text{m}$  pixels ( $50\times$  lens, providing a 0.72 mm by 0.5 mm FOV).

A fast shutter is introduced upstream of the mouse in order to minimise the dose received by the mouse, since the main beam shutter opens and closes too slowly to be practical for obtaining multiple images. The shutter is connected to a timing box such that it opens immediately before the camera records and closes immediately after the end of image acquisition. Ionisation chambers positioned either side of the shutter enable the precise dose to be calculated. Exposure times are typically 280 ms long for *in vivo* imaging, with a dose of 0.13 Gy per image. Sufficient pixel counts were available with a thicker detector phosphor and 100 ms exposures in particulate tracking studies (§6.6).

The initial set of 40 minute image sequences were taken observing either the trachea or the nasal airway, with the 1 mm diameter airway running vertically through the image in both cases.

### 6.3.3.2 Modelling PB-PCXI Images of the ASL

These imaging sequences aimed to monitor the ASL depth directly. In the mouse model, the ASL will only be around 5-7  $\mu\text{m}$  deep in the nasal airways, compared to around 50  $\mu\text{m}$  in the trachea (Song et al., 2003). Note that the depth of liquid in the trachea will depend on the radial position. Changes of several microns in liquid depth are expected in response to an effective treatment. This imaging geometry was simulated using the model described in section 1.1.1.2, with the resulting image and associated simulation parameters shown in Fig. 6.7.

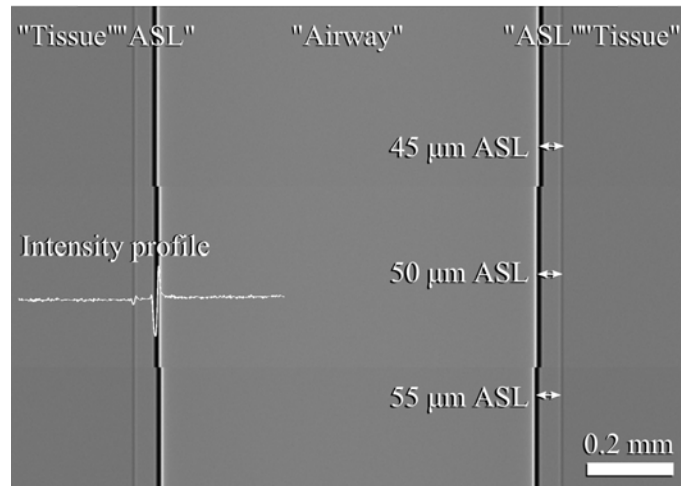


Figure 6.7: Simulated airway, using the model detailed in section 1.1.1.2 and refractive indices as below. Propagation distance of 1 m is used, with 25 keV x-rays, 0.45  $\mu\text{m}$  pixels, 245 m from a  $24 \times 1100 \mu\text{m}$  source with Poisson noise added. An intensity profile is shown across the left interfaces.

The projection approximation takes the refractive index values ( $n = 1 - \delta + i\beta$ ) to accurately describe tissue ( $\delta = 4.24 \times 10^{-7}$  and  $\beta = 3.20 \times 10^{-10}$ ), water ( $\delta = 3.69 \times 10^{-7}$  and  $\beta = 1.71 \times 10^{-10}$ ) and air ( $\delta = 4.13 \times 10^{-10}$ ) (NIST, 2007). The phase contrast fringe between the simulated ASL and the tissue is seen to be much weaker than that between air and ASL, demonstrating how similar the refractive indices of tissue and liquid are. The computer simulation incorporated the finite synchrotron source size, detector noise (drawing from a Poisson distribution of mean equal to each pixel value), pixel size and smoothed the interfaces slightly to describe how the fringe visibility would be suppressed in experimental images.

The simulation model was used to study the effect of imperfect imaging conditions on the visibility of the airway interfaces. This included varying the interface surface roughness, the interface surface gradient, the salt concentration in the ASL and the transverse coherence length. For each of these variables individually and together as a group, the decrease observed in fringe visibility (for a reasonable range of each variable) was insufficient to render the ASL/tissue boundary undetectable. Figure 6.8 shows an example of one such study, where the transverse coherence length is varied. Here it can be seen that the visibility of the ASL/tissue interface only drops below 0.1 for a transverse coherence length less than 5  $\mu\text{m}$ , which is significantly smaller than that measured for any of the beamline configurations considered in Chapter 4. Visibility below 0.1 would be insufficient to observe an interface fringe above the background noise and overlying patterns which have an average visibility of 0.07.

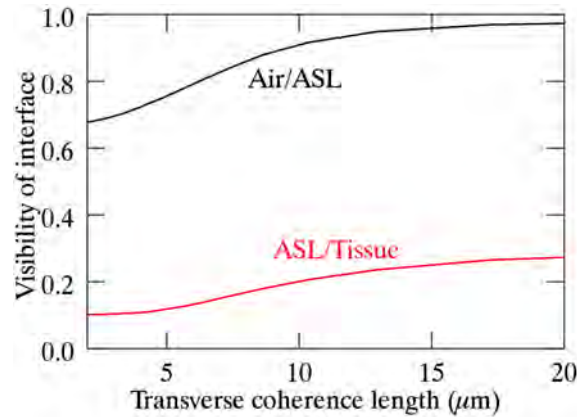


Figure 6.8: Simulated interface fringe visibility from each airway interface, using the same parameters as Fig. 6.7, while varying the source size.

In order to experimentally model a simple version of the expected images, imaging of phantom airways was also carried out. Phantoms were constructed using a rectangular block of perspex (which has a similar refractive index to tissue,  $\delta = 4.26 \times 10^{-7}$  and  $\beta = 1.53 \times 10^{-10}$ ), with holes drilled through of diameter 1mm (to model a mouse airway), as shown inset in Fig. 6.9. Each hole was coated on the inside using various materials of similar refractive index to water, such as cyanoacrylate (“superglue”) ( $\delta = 3.82 \times 10^{-7}$  and  $\beta = 1.41 \times 10^{-10}$ ), petroleum jelly (“Vaseline”), water or polyethylene, to simulate the ASL. These provide almost the same 12% decrease in  $\delta$  going from tissue to ASL as expected and as modelled in simulation.

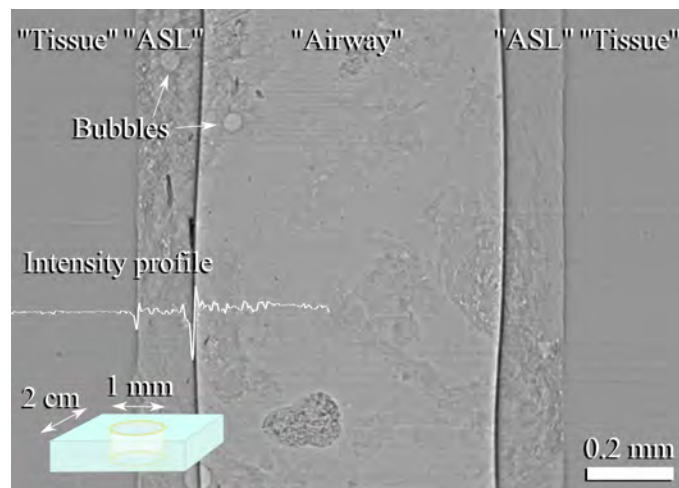


Figure 6.9: Perspex block phantom, with 1mm hole internally coated with Vaseline, imaged at 25 keV at the downstream hutch of BL20XU with a propagation distance of 0.7 metres, 100 ms exposure,  $0.45 \mu\text{m}$  pixels. A schematic of the phantom is shown inset and an intensity profile is shown across the left interfaces.

A phantom image, as seen in Fig. 6.9, shows the same two interfaces on each side of the “airway”, as expected to be seen in an airway image (note that the depth of the ASL is exaggerated here). Some bubbles in the simulated “ASL” can also be seen, with the lighter fringe seen on the inside of the bubble, just as the airway has a lighter fringe on the air-filled inside.

Both images (6.7 and 6.9) suggest that the boundaries between the three regions should be

visible as phase contrast fringes in the image. This would enable a simple measure between the two fringes to provide the ASL depth. Given that the radius of curvature of both interfaces is very similar and the propagation distance is the same, the width and shape of the fringe set seen at each of the two interfaces will be the same, and only the visibility (or magnitude) will differ.

### 6.3.3.3 Propagation Distance Selection

The propagation distance between the sample and detector was chosen to maximise the visibility of the phase contrast fringe at each interface (achieved with a longer propagation distance), without creating such wide fringe sets that the two interfaces could not be distinguished from each other. Figures 6.10 and 6.11 show the width and visibility of the ASL/airway interface increasing with propagation. A smaller propagation distance produces both finer detail and well separated interfaces, however weaker fringes in intensity. As the propagation distance is increased, both the visibility of the airway interfaces and of surrounding phase features will increase.

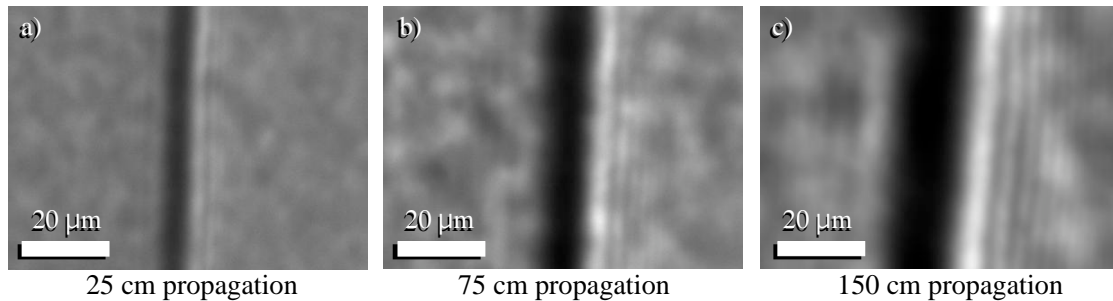


Figure 6.10: *In vivo* trachea edge images with increased propagation.

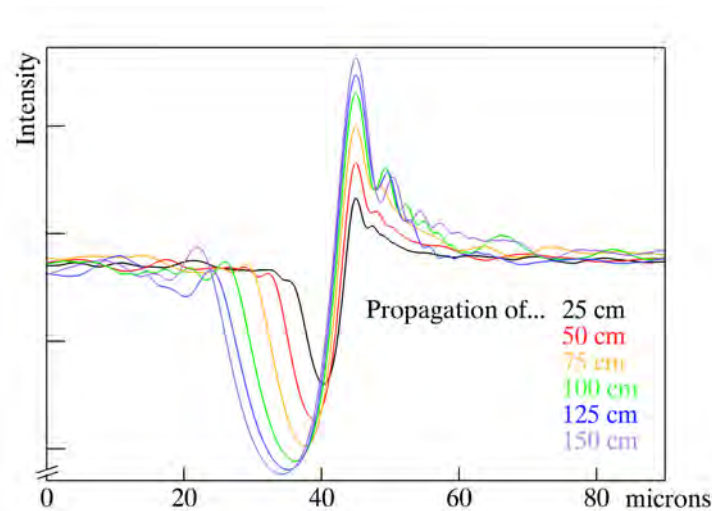


Figure 6.11: Intensity profile across the *in vivo* trachea edge for a range of propagation distances, showing more intense, wider fringes at longer propagation distances.

The optimal propagation distance, chosen from simulation and confirmed in experiment, is around 1 m for the 50 µm ASL in the trachea and 0.3 m for the 7 µm ASL in the nasal airways (see §6.3.3.4). The ASL should therefore be easier to visualise in the trachea, not only because of

less overlying anatomy, but also because a longer propagation distance may be used, which will produce stronger contrast.

### 6.3.3.4 Airway Live Imaging Sites

Live airway imaging was predominantly conducted in two positions within the mouse, the trachea and the nasal airways, as shown in Fig. 6.12. The propagation-based phase contrast makes even the fur on the outside of the mouse and the intricate nasal airway structure at the tip of the nose visible in Fig. 6.12 *a*).



Figure 6.12: *a*) Propagation based phase contrast image of a mouse head, imaged on BL20B2 using 25 keV x-rays, 300 ms exposure, 12  $\mu\text{m}$  pixels, *b*) Nasal airway imaging site and *c*) Trachea imaging site taken with a lateral view, imaged on BL20XU using 25 keV x-rays, 100 ms exposure, 0.45  $\mu\text{m}$  pixels, propagation distance of 1 m.

Fig. 6.12 *b*) shows the nasal airway site used during imaging, with the ASL/air interfaces on each side of the airway clearly visible. The central triangular shape is part of a bony suture on the skull of the mouse, and is used as a landmark to ensure imaging is done at the same position for all mice. This imaging site is stable because of the surrounding skull, so bulk movement is less of a problem than in the lower airways, however the ASL is much shallower here, hence more difficult to resolve.

Figure 6.12 *c*) also clearly shows the boundary between air and liquid, this time in the trachea. In this case, there are actually three edges visible on the left hand side of the image. This is

due to the kidney-like shape of the trachea, as depicted at the bottom right of this figure. When viewed laterally, these edges lead to three visible lines, two concave edges, seen with a strong dark fringe and one convex, which is seen with a stronger high intensity edge. While a perfectly square object would give a symmetric fringe pattern (see §1.1.1.3), curving the interface has the effect of expanding the central fringe on one side and compressing it on the other (see Chapter 2). The asymmetry of the fringe pattern will then indicate which way the surface is curving, as well as the radius of curvature. The trachea image also shows rings of cartilage around the airway, and the texture of the skin overlaid on the entire image (hair has been removed).

However, the interfaces on both sides of the ASL are not obvious in either of the two live imaging positions, Fig. 6.12 *b*) or *c*). While the ASL/air interface creates a strong phase contrast fringe, the tissue/ASL interface is not seen, unlike in Fig. 6.7 and Fig. 6.9.

This is partly due to attenuation and phase contrast from overlying features covering the ASL/tissue boundary. While fur (if present) was removed from the animal prior to imaging, other image features such as cartilage rings, skin folds and bone features cannot be easily removed. The overlying features in the trachea images were found to have a characteristic length scale of  $15 \pm 10 \mu\text{m}$ , which could then be incorporated in the simulation model (6.3.3.2).

It is also possible that the fainter fringe is not as strong as predicted due to a less-defined boundary. As seen in Fig. 6.1, the ASL is filled with cilia, which beat regularly back and forth in the liquid, moving any debris along the top of the ASL. The boundary between tissue and the ASL is irregular, hence does not provide the same phase contrast fringe as a binary sharp boundary would (*e.g.* the simulated fringe in Fig. 6.7).

The initial set of live imaging experiments sought to observe changes in ASL with proven short-term treatments, recording images over 40 minutes with 29 mice, using  $0.45 \mu\text{m}$  effective pixel size. The analysis done on these images is detailed in section 6.4. A series of experiments using phantoms and live imaging were carried out following this, aiming to visualise the ASL depth by enhancing the interface visibility to reveal the ASL/tissue interface, as described in section 6.5.

### 6.3.3.5 Image Processing

A standard “flat and dark” correction is made to all images in order to decrease the effects of the non-ideal source and detector. At the time of imaging, a “dark” image is taken, a capture with no incident x-rays, which is then subtracted from subsequent images in an effort to remove the effect of the dark current offset due to electronic noise. A “flat” image is also taken, simply an image of the incident beam, and subsequent images may then be divided by this flat in order to correct for the non-uniform illumination by the beam. This will also remove overlying artifacts due to beryllium windows and other optics. Therefore, corrected images are obtained by (Kwan and Seibert, 2006):

$$\text{Corrected} = \frac{\text{Image} - \text{Dark}}{\text{Flat} - \text{Dark}}. \quad (6.1)$$

All image processing code for the analysis of live images were written by the candidate using IDL 6.3, Research Systems, Inc.

## 6.4 Approaches to Measuring ASL depth

During the initial set of live imaging experiments both ASL interfaces were not observed (see Fig. 6.12), but the sequences of airway images provided data upon which several methods of extracting the ASL depth could be trialled. These are detailed below.

### 6.4.1 Obtaining an Interface Intensity Profile

While the ASL/tissue phase contrast fringe is not directly discernible in the image, it was possible that the feature could be enhanced by image processing. To minimise noise and small overlying features, the profile may be averaged over several rows of the image. The airway of a mouse is not perfectly straight and certainly does not align with the vertical or horizontal line of pixels, so it was necessary to align the fringe in each row before averaging. This was done using correlation to determine the position at which the subsequent fringe profiles most closely align with an arbitrarily chosen starting profile (pixel row). As a simple error checking device to avoid overlying anatomy or pixels with anomalous intensities corrupting the alignment process, subsequent aligned rows were compared for rapid deviations. If a deviation was observed, a combination of the minimum intensity and the steepest gradient in intensity was used to align that row. These two measures were much more consistent over a large number of rows, but did not give as exact an alignment as using correlation. Figure 6.13 shows a trachea edge image *a*), with the aligned edge *b*).

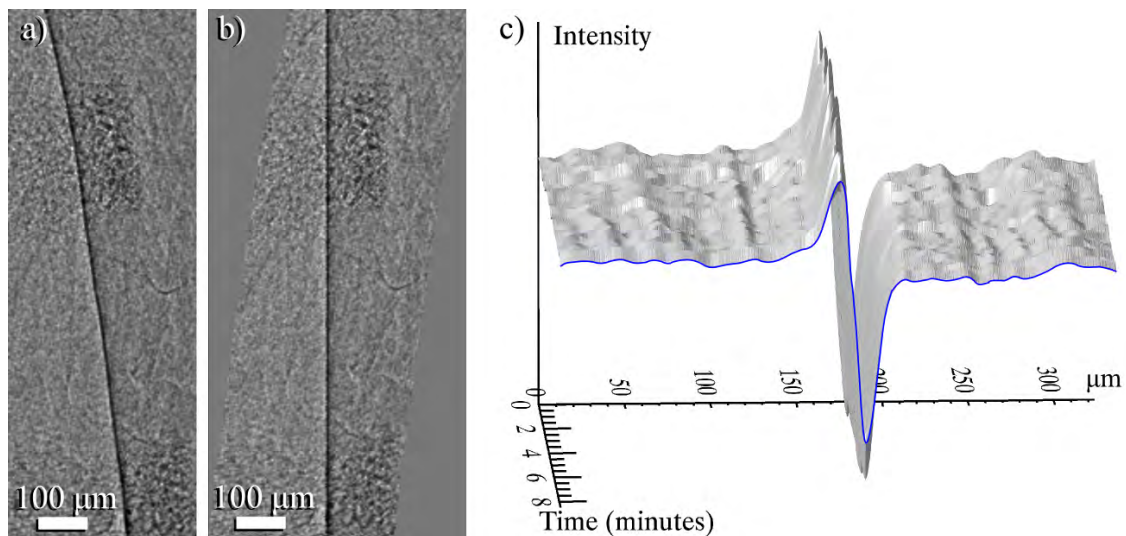


Figure 6.13: Aligning an edge image as shown in *a*) to produce a straightened edge *b*), which may be averaged to give *c*) a profile (as shown in blue). The plot *c*) shows the profile for a series of frames over several minutes of imaging. The sample is an *in vivo* mouse trachea with 25 keV x-rays, 0.45 μm pixels and 1 m propagation.

Averaging the straightened image produces a profile as seen in blue in Fig. 6.13 *c*), showing a phase contrast fringe profile less affected by overlying intensity undulations than a single row profile. It should be noted that a true profile of the fringe would be taken perpendicular to the edge, so a correction of a factor of  $\cos(\theta)$  should be made to the width of the fringe, where  $\theta$  is the angle subtended between the edge and the vertical. For images taken with a highly coherent source, exhibiting many narrow fringes from each interface, subpixel alignment was implemented,

interpolating pixel rows by a factor of 3 before aligning. Also note that the length of interface used to average to a single profile should be sufficiently small that the ASL depth will not vary over the length.

A clear edge intensity profile from each frame then allows quantification of variations in the profile over time, as in Fig. 6.13 c).

However, the ASL/tissue interface fringe, expected in the trachea to sit around 50  $\mu\text{m}$  to the right of the strong ASL/airway fringe is not evident. Profile averaging over the complete time series, producing a profile as a function of time as seen in Fig. 6.13 c), did not report any fringe from the ASL/Tissue boundary, neither stationary nor moving with time.

It was concluded that with this imaging set-up the depth of the ASL could not be consistently measured *in vivo* by simply taking the distance between the two ASL interface fringes from this set of live imaging, as the ASL/tissue boundary could not be reliably located.

#### 6.4.2 Tracking Airway Width over Time

Given the boundary between the ASL and the tissue could not be definitively observed, another approach was to look at the distance between the two ASL/Air walls of the airway. If the ASL was deepening in response to a treatment, the ASL/air edges on either side of the airway should move closer together at twice the rate of the ASL depth increase (assuming that the overall airway diameter remains constant). This measurement was performed on both the nasal airway and trachea images (Fig. 6.12). The process was most successful on the nasal airway images, with less bulk movement problems and only one interface seen on each side of the airway (unlike that produced by the kidney-like shape of the cross-section of the trachea, Fig. 6.12 c)). The measurement was done through the following steps;

- Filter the image to enhance the fringe, using a differential edge-detection filter of the same width as the fringe.

For each row in the image:

- Obtain a smooth profile by averaging with the previous and subsequent rows and smoothing the profile with a 4.5  $\mu\text{m}$  wide Gaussian smoothing filter to remove noise.
- Take the derivative of the smoothed profile to find the point at which the light/dark fringe occurs.
- Identify the 10 points across the profile of maximal gradient.
- Choose the key points that are closest to the position of the edges in the previous row and check that they are slowly-varying.

This enables a plot of the airway width over the height of the image, as each row was analysed. The median width over the image height was taken as a good indication of the overall airway width, as the change in airway width over the height of the image was significantly greater than the change in a single pixel row width over time. Stepping through the images in the time series then gave a plot of the airway width as a function of time, as in Fig. 6.14.

The changes in the median airway width were consistent with the changes in airway width at a given row (height) in the image. In order to compare mice, the change in airway width for each series was expressed as a fraction of the initial width. Live imaging sequences were taken with a

baseline of 5 minutes before treating the airways, followed by around 40 minutes of observation, imaging once every 10 seconds.

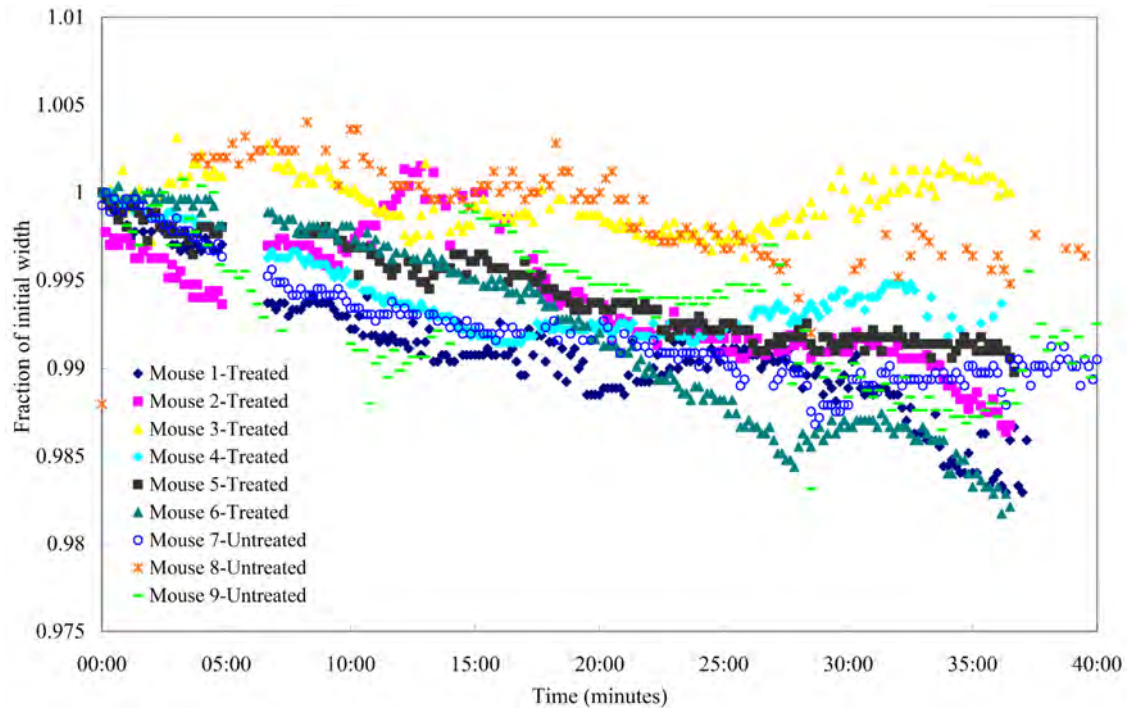


Figure 6.14: Distance between airway edges measured over treatment time, for mice treated with UTP-608 (UTP-608 is a mix of pharmaceutical agents specifically designed to increase ASL depth) or hypertonic saline, which increases ASL depth via osmotic forces. Control observations, where no treatment was given, are also shown.

As seen in Fig. 6.14, the width of the airway did decrease over time, suggesting that the ASL deepened. However, when mice were observed over 40 minutes with no treatment (see mice 7,8,9), some decrease in width was still observed. Hence, it is not clear that it is a change in the ASL which is observed rather than in the tissue or positioning of the mouse. This could be due to a stretching of the airway given the unnatural vertical position of the mouse, or due to anaesthetic effects.

### 6.4.3 Interface Fringe Visibility

Using the profiles in Fig. 6.13, the airway interface fringes could also be easily analysed across the imaging time in terms of the width and visibility of the central fringe. While no significant changes in either of these measures were observed in response to the standard treatments, changes were observed in live imaging sequences taken for other parts of the project, which study the clearance of particulates from the airways (§6.6, Appendices D and E).

This involved instilling glass beads with radii in the micron range, suspended in a saline solution, into the airways of the mice (§6.6). The clearance of these was to be observed, as discussed in section 6.6. However, it was also observed that after the instillation the visibility (as defined in Eqn. 1.25) of the airway edge was increased.

As seen in Fig. 6.15, there is a marked jump in visibility when glass beads are instilled (mice 1-4), not seen in any of the treatment imaging sequences (mice 5-7). The spatial distance between

the maximum and minimum of the fringes did not change with any significance over imaging time for either set.

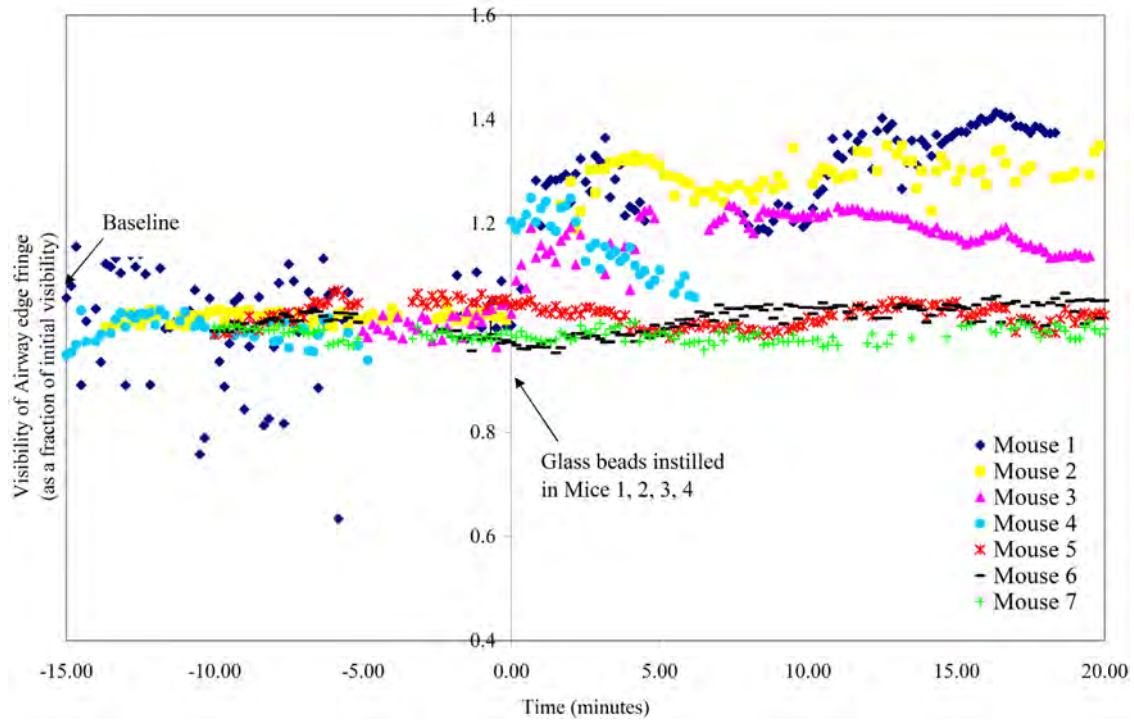


Figure 6.15: Visibility of the phase contrast fringe from the airway edge over the imaging time, with glass beads instilled in mannitol in mice 1, 2, 3 and 4 at time = 0.

It should be noted that a blurred image, due to animal movement, would give large changes in fringe visibility, such as seen for mouse 1 in the first few minutes of imaging.

The results seem to indicate that the bright phase contrast from beads adds to the bright fringe on the inside of the airway to increase the overall visibility.

#### 6.4.4 Fringe Visibility as a Function of ASL Depth

The simulation model detailed in section 1.1.1.2 may also be used to model the fringe visibility behaviour. If the fringes from the two ASL interfaces are sufficiently broad in extent, then the fringe patterns from the two interfaces will constructively or destructively interfere with each other and this may provide a method by which to measure the ASL depth. The resulting observed fringe pattern shape and visibility (as defined in equation 1.25) will change depending on how far apart the interfaces are. If there is a high intensity fringe from one fringe set overlapping the central maximum of the other, the visibility may be enhanced, but if there is a low intensity fringe overlapping the other's central maximum, the visibility will decrease. In this way, the visibility across the area in the vicinity of the two fringe sets will change according to the ASL depth. If this relationship is one-to-one for the range of expected ASL depths, or can be made so via an appropriate choice of wavelength and propagation, a simple look-up table could be employed, where the ASL depth is predicted by the visibility across the fringe region.

Using the simulation model for PB-PCXI mentioned in section 1.1.1.2, images for a range of ASL depths were used to create such a look-up table, as seen in Fig. 6.16. This shows the variation

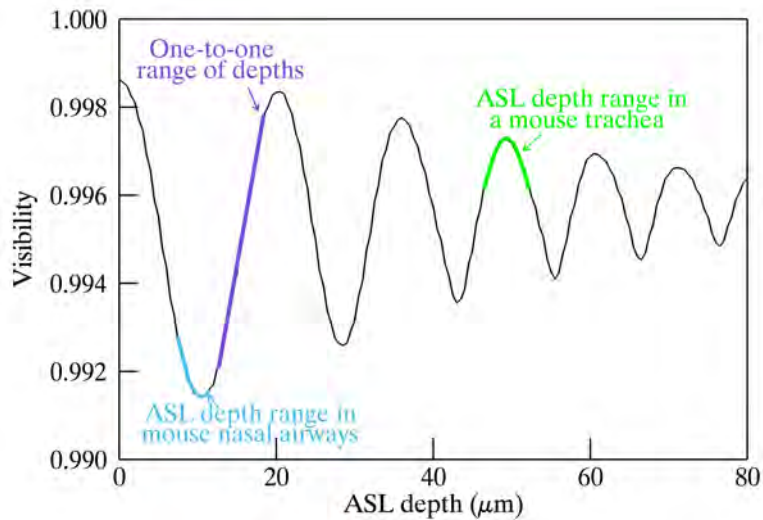


Figure 6.16: Simulated relationship between ASL depth and visibility using a  $300 \mu\text{m} \times 6 \mu\text{m}$  coherent source, for a propagation distance of 1 m.

in visibility with increasing distance between interfaces as each of the maximum intensity fringes from the weaker fringe set move past the central maximum and minimum of the stronger fringe set. Given that the expected variation in ASL depth is only a few microns, the sample-to-detector propagation distance may be chosen so that the relationship between visibility and ASL depth is one-to-one for the region of interest. The above theoretical look-up table for 1 m propagation shows the range of probable ASL depth in the nasal airways of a mouse in blue. In order to gain a one-to-one region, as shown in purple, the propagation distance could be adjusted. In the trachea, small changes in the larger ASL depths will not change the fringe visibility significantly, and require a longer propagation distance to produce broader fringe sets and larger variations in visibility. However, the results do show that if the range of possible ASL depths for the airway in question is known, it is therefore possible to define a one-to-one mapping from total fringe visibility to ASL depth.

Experimental images of a perspex phantom were studied for comparison, where the depth of the “ASL” varied with position (rather than time) along the edge of the tube, as shown and described in Fig. 6.17. Each row in the highlighted square was taken as a depth of ASL, fitting the depth linearly by the distance between fringe centres.

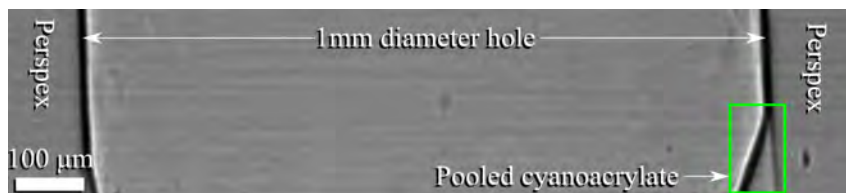


Figure 6.17: A 1mm diameter perspex phantom image, taken with propagation of 1 m in the Experimental Hall hutch of BL20XU, with a cyanoacrylate “ASL”. The green square shows the region used when measuring visibility.

Figure 6.18 shows two visibility look-up tables generated from phantom images, where *Phantom Edge 1* comes from the green square in Fig. 6.17. It can be seen that the visibility curve going

from 0 to 10 microns follows the same trend as seen in the theoretical plot, falling from a maximum at zero to a minimum at 10 microns. PSF correction (as in the coherence measurements described in Chapter 4) should enhance the visibility to a similar range to that predicted from the model. However, the imaging set-up provided only the central maximum and minimum to be seen in the solid phantom images, and the smaller fringes predicted to either side were not strong enough to produce the theoretically predicted oscillations in visibility for greater ASL depth that are seen in Fig. 6.16.

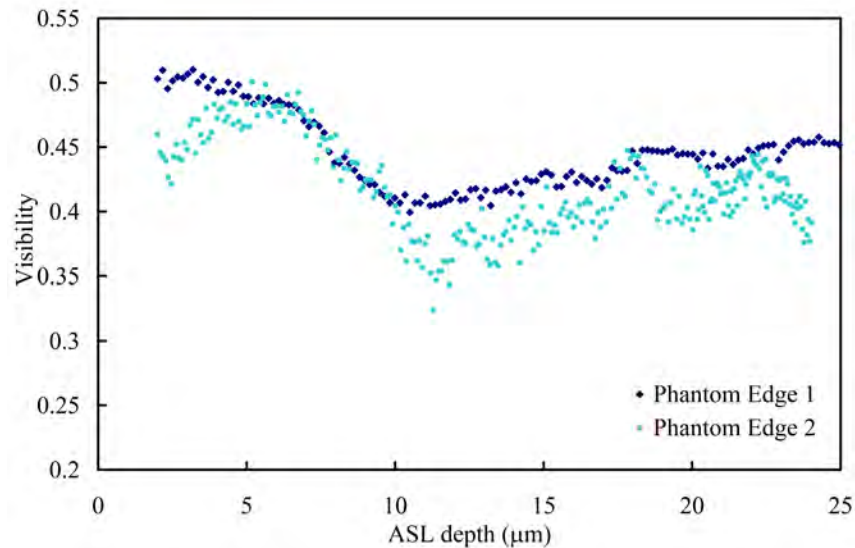


Figure 6.18: Measured visibility from perspex phantoms, Phantom 1 with a cyanoacrylate “ASL” and Phantom 2 with a Vaseline “ASL”, imaged on BL20XU, propagating 1 m.

These results show that for 1 m propagation, as used in live imaging, 1-2  $\mu\text{m}$  changes in a total depth of around 7  $\mu\text{m}$  (as in nasal airways) would be difficult to observe due to the visibility plot minimum at 10  $\mu\text{m}$ . This was evident in the visibility measurements done on treatment imaging sequences such as shown in Fig. 6.15, mice 5, 6 and 7. Changes in a total depth of around 0-5  $\mu\text{m}$ , where the gradient is steeper, would be more easily observable. A slightly longer propagation distance would widen the fringes, shifting the first visibility vs ASL depth minimum to a greater ASL depth, and the steeper gradient section up to 7  $\mu\text{m}$  ASL depth. Propagation of 1m would also not be optimum for observing changes at a greater ASL depth, like in the trachea, as figure 6.16 shows that visibility changes at 50  $\mu\text{m}$  ASL depth rely on the narrow low-intensity fringes from the sides of the interface fringe set, so the change in visibility is not significant in this experimental set-up. Increasing the propagation distance or the transverse coherence will increase the visibility and total breadth of the fringe sets and may allow more of these narrow fringes to be observed from each interface. This may enable more visibility variation to be observed at greater depths, but may result in images that are not as easy to interpret visually.

Nevertheless, the variation in fringe visibility from animal to animal would make it hard to draw conclusive measures. Similarly, changes in fringe visibility may be due to other factors such as the sharpness of the ASL/air interface. In conclusion, direct observation of both interfaces would be preferred.

## 6.5 Enhancing Interface Fringe Visibility

The experiments in section 6.4 suggested that the fringe visibility observed in this initial set of propagation-based imaging of the airways was insufficient to directly and conclusively observe the ASL directly. This section describes a series of experiments aiming to further enhance fringe visibility; to improve the information content of the fringes, and potentially apply more sophisticated methods of analysis. This imaging was conducted further to the initial live imaging set of 29 mice, and focuses simply on increasing interface visibility sufficiently such that the ASL/tissue interface may be visualised. Images are taken with a 50 $\times$  optical lens, rather than the 20 $\times$  optical lens used when imaging the full width of the airways, resulting in a new pixel size of 0.18  $\mu\text{m}$ . The associated point spread function of the imaging system, which will further limit the resolution, is discussed in section 6.5.2.1.

### 6.5.1 Enhancing Fringe Visibility by Experimental Set-up

#### 6.5.1.1 Sample Preparation

Firstly, if the trachea is excised, both blur from sample movement and the problems with overlying attenuation and phase images from skin and tissue will be decreased. If imaging is begun quickly after excising, the mucociliary mechanisms will continue to be active for some 30 minutes provided that the trachea is maintained in a moist environment to avoid dehydration (Button, 2009). As seen in Fig. 6.19, this *ex vivo*<sup>5</sup> imaging gives a much cleaner image, from which an accurate fringe intensity profile may be more easily extracted. Compared to *in vivo* images, see Fig. 6.20, the “signal” (interface fringes) to “noise” (overlying textures) ratio is increased. The smoother fringes will also enable averaging across several rows (§6.4.1) without suppressing fringes. This fringe suppression from the sum of many image rows, each with different overlying patterns from the anatomy, is analogous to the sum of many images each with a different realisation of the random phase screen diffuser (*i.e.* Compare Fig. 6.19 *a*) and *b*) with Chapter 5 Fig. 5 *a*) and *b*)).

#### 6.5.1.2 Increasing Coherence by Decreasing Effective Source Size

Secondly, the transverse coherence seen from the synchrotron x-ray source may be increased to maximise fringe visibility, and maximise the width across which fine fringes from a single interface will be detectable. The electron beam source size is intrinsically much smaller in the vertical direction than in the horizontal direction, and hence the transverse coherence in the vertical direction will be much greater (from Eqn. 1.24). An interface will therefore produce the sharpest phase contrast fringes when laid horizontally.

Similarly, moving further from the source by using the hutch in the Biomedical Imaging Centre, rather than in the main experimental hall, will significantly increase the coherence width, as shown in Chapter 4.

The observed source size may be decreased by closing the optics hutch slits to form a smaller aperture (see Fig. 6.3), as used during the coherence measurements of Chapter 4. As seen in Fig. 6.21, this increases the visibility of not only the central fringe, but also means that many narrow fringes to either side are now observable. This produces a more distinctive feature within the

---

<sup>5</sup>*Ex vivo* studies look at the biology while physiological processes are still functioning, but outside the animal.

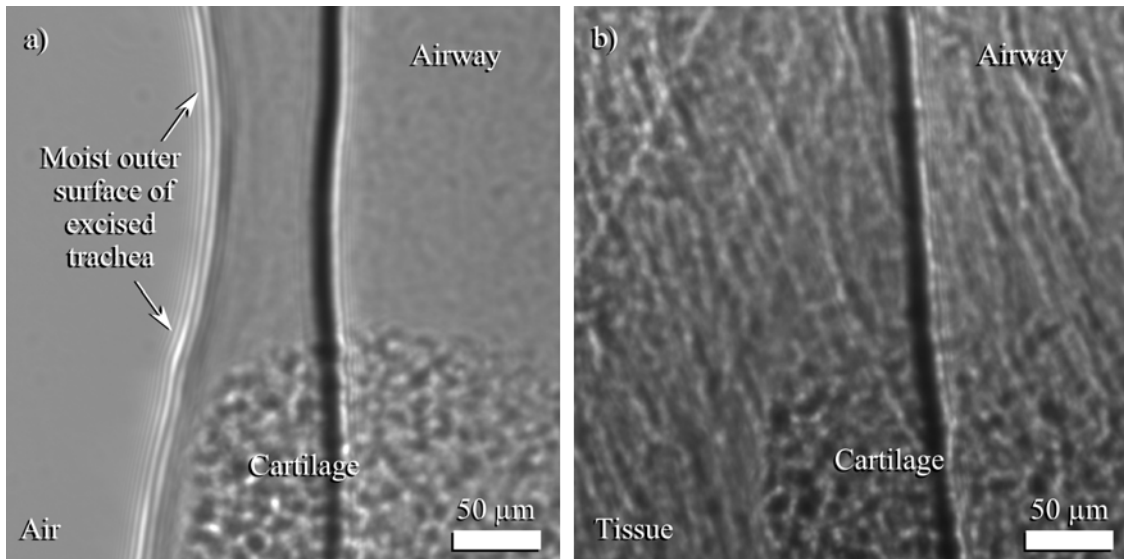


Figure 6.19: a) An excised (*ex vivo*) trachea and b) *in vivo* trachea, each with a cartilage ring in the lower part of the image, imaged with 25 keV x-rays, 100 ms exposure, 0.18  $\mu\text{m}$  pixels, 1 m propagation.

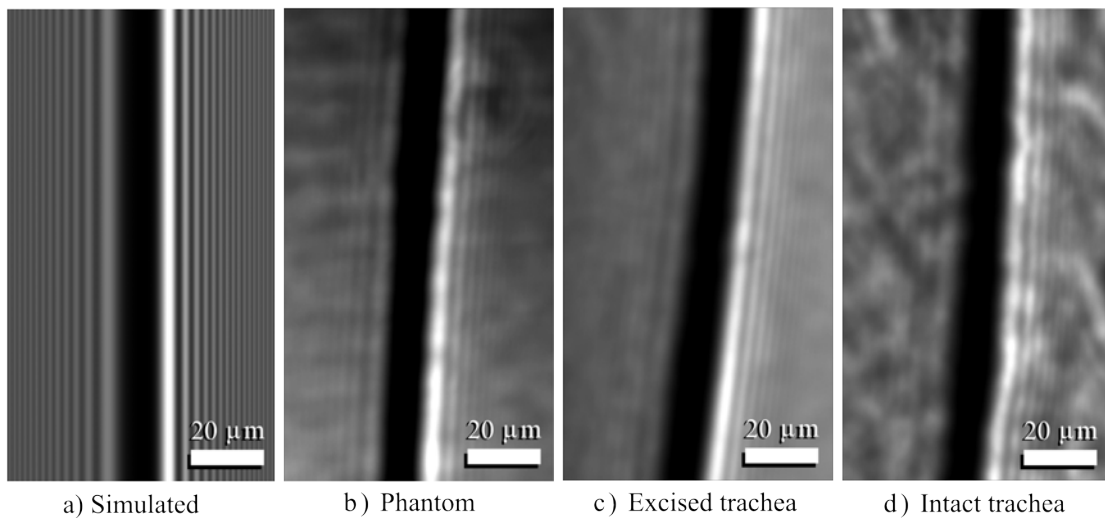


Figure 6.20: Fringe-dampening effect of moving from a simulated 1mm hole in perspex to an experimental 1 mm hole in perspex to an excised mouse trachea (1 mm diameter), to an intact mouse trachea (1 mm diameter), each taken/simulated with 0.18  $\mu\text{m}$  pixels and 25 keV x-rays, 1 m propagation.

intensity profile, more easily differentiated amongst surrounding variations due to attenuation and phase edges of different curvatures.

The penalty in decreasing the aperture size to less than 250  $\mu\text{m}$  square is that the flux decreases such that exposures must be greater than 1 second for the same pixel size and detector as used previously, which presents problems in terms of animal movement during the exposure.

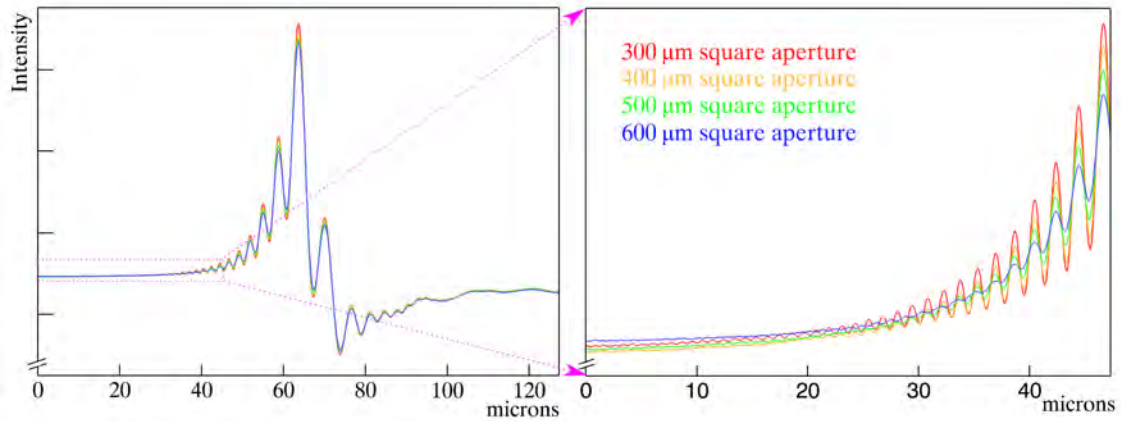


Figure 6.21: Reducing the observed source size increases the coherence width to produce many more high visibility fringes at interfaces, here from the outside of a 1 mm perspex cylinder, using 25 keV x-rays, propagation of 1 m and 0.18  $\mu\text{m}$  pixels. Profiles shown here are an average over the length of the interface, as described in Fig. 6.4.1.

### 6.5.1.3 Increasing Coherence by Diffuser Choice

As described in Chapters 4 and 5, the repositioning of the diffuser will also increase the observed degree of coherence and produce higher visibility fringes from an interface, as seen in Fig. 6.22. Placing the diffuser in the optics hutch, close to the source (see Fig. 6.3 for distances), and imaging in the Biomedical Imaging Centre, far from the source (and the diffuser), minimises the fringe-dampening effect of the diffuser.

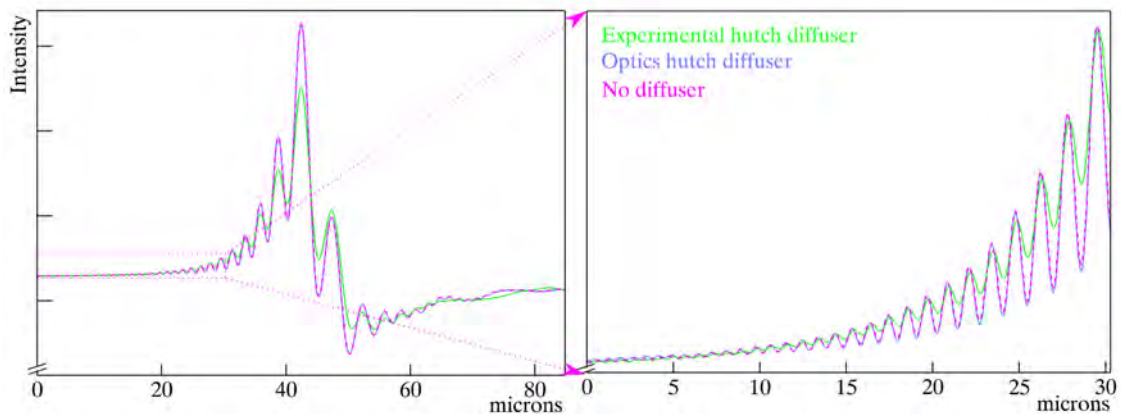


Figure 6.22: Moving the diffuser further from the sample or removing it increases the absolute value of the complex degree of second order coherence (Eqn. 1.28), producing higher visibility fringes, so that more fringes are visible, here from the outside of a 1 mm perspex cylinder, using 25 keV x-rays, 1 m propagation and 0.18  $\mu\text{m}$  pixels.

### 6.5.1.4 Increasing Phase Gradient by Sample Orientation

The edge fringe may be increased in visibility by imaging the airway tilted in the direction of propagation, as shown in Fig. 6.23 *b*), provided the airway is sufficiently cylindrical. This effectively increases the phase shift between rays passing through and beside the airway by a factor of the

cosine of the tilt angle. Figure 6.23 *a*) shows the associated increase in central fringe width and visibility. Angles of up to 55 degrees were possible with *in vivo* imaging before surrounding anatomy obscured the airway interface fringes and outweighed the advantage of the increased phase gradient.

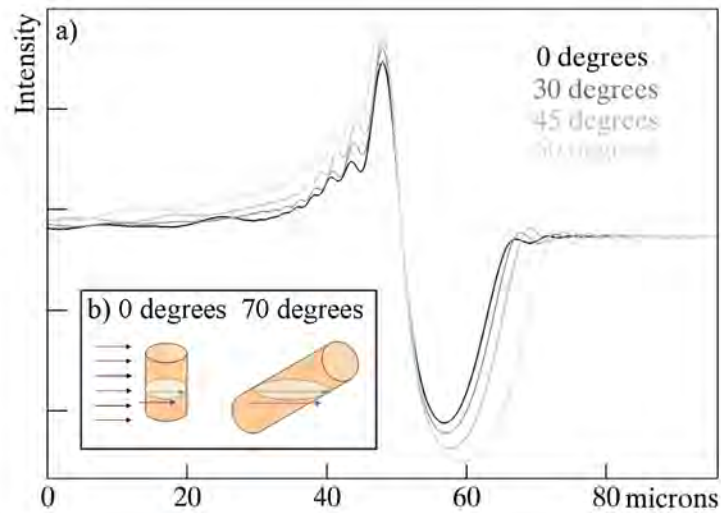


Figure 6.23: *a*) Higher visibility fringes are seen when *b*) rotating the airway in the direction of propagation incurs a greater effective thickness  $T$ , hence a greater phase change. Profiles are taken from images of a phantom with a 1 mm hole drilled in Perspex, taken with 25 keV x-rays and 0.18  $\mu\text{m}$  pixels, 1 m propagation.

The increase in visibility and detail of trachea interface fringes due to these alterations to the experimental set-up is significant, as seen in Fig. 6.24.

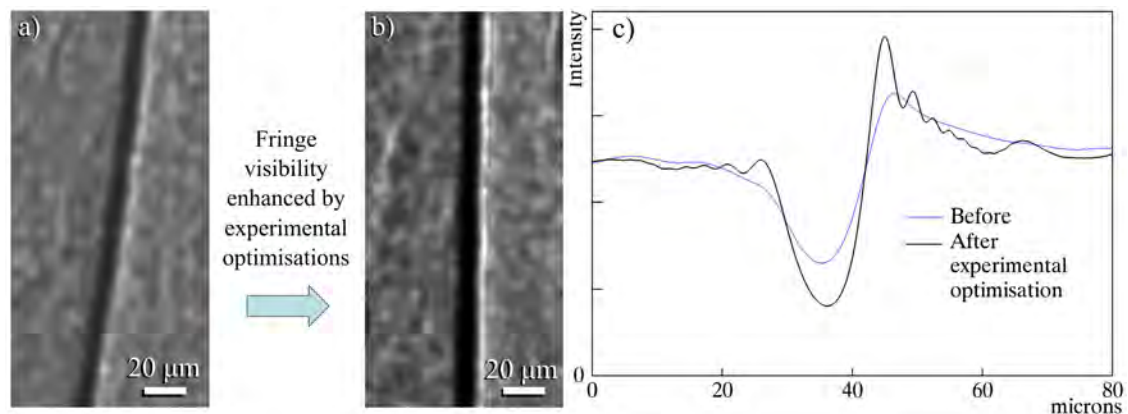


Figure 6.24: *In vivo* trachea ASL/air interface seen *a*) with 0.45  $\mu\text{m}$  pixels, diffuser in the experimental hall hutch, 0.4 mm optics hutch slits, oriented vertically, then *b*) with 0.18  $\mu\text{m}$  pixels, no diffuser, 0.3 mm optics hutch slits, oriented horizontally. Both are taken in the Biomedical Imaging Centre hutch with 1 m propagation. *c*) Averaged intensity profiles across the trachea edge for these two set-ups show the improvement in fringe visibility and detail.

The ASL/tissue interface is not apparent by direct inspection, so we investigate how the improved fringe visibility may allow edge information to be extracted in analysis.

## 6.5.2 Enhancing Fringe Visibility by Image Analysis

The small intensity variations in the PB-PCXI fringe arising from an interface may be extracted to better visualise interfaces post-experiment. It is important to maximise the signal to noise ratio from the inherently weak signal arising from the interface, and the relatively high noise arising from overlying anatomy in the samples. In the previous section we maximised the signal experimentally, and here we consider how the signal can be further enhanced in post-experiment image processing. Some of these methods of analysis are noise-sensitive, and require either several images to be averaged or a long exposure time to be used in order to provide good statistics in the image. While this may not be practical in live imaging, if ASL measurements are possible from these images, the ability to increase the pixel grey level count in a short exposure may be possible in future work, for example by using a more efficient detector.

### 6.5.2.1 PSF Correction on Fringe Intensity Profiles

One such method of fringe enhancement is a correction for the point spread function (PSF) of the detector. The PSF was measured experimentally by imaging a knife edge in both horizontal and vertical directions to give the edge spread function. The point spread function is then given by the derivative of the edge spread function. The resulting profile in the horizontal direction is shown in Fig. 6.25. The PSF was found not to change significantly in pixel width with different magnification optical lenses, since the spread is mainly due to scattering within the thickness of the phosphor screen which sits before the lens. A thicker phosphor screen, although creating more visible light and enabling shorter exposures, would therefore result in a broader PSF. The PSF width, measured at full width half maximum (FWHM), was  $0.45\ \mu\text{m}$  with  $0.18\ \mu\text{m}$  pixels and  $1.13\ \mu\text{m}$  with  $0.45\ \mu\text{m}$  pixels. The diffraction-limited resolution is  $0.2\ \mu\text{m}$  for 1 m propagation, hence is not the dominant factor in determining the resolution.

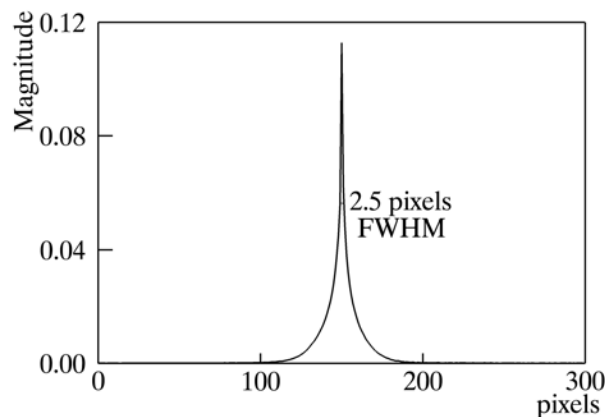


Figure 6.25: The point spread function of the imaging system, measured at the Biomedical Imaging Centre hutch of BL20XU, using  $0.18\ \mu\text{m}$  pixels from a vertical knife edge image.

The edge profile (provided it is sufficiently smooth) may then be then deconvolved with the PSF using the Fourier convolution theorem. The resulting profile is shown in Fig. 6.26, where the narrow fringes far from the central fringe are now easily visible. Also note the improved level of

detail in this profile, post experimental set-up optimisations, compared to the profile seen in Fig. 6.13.

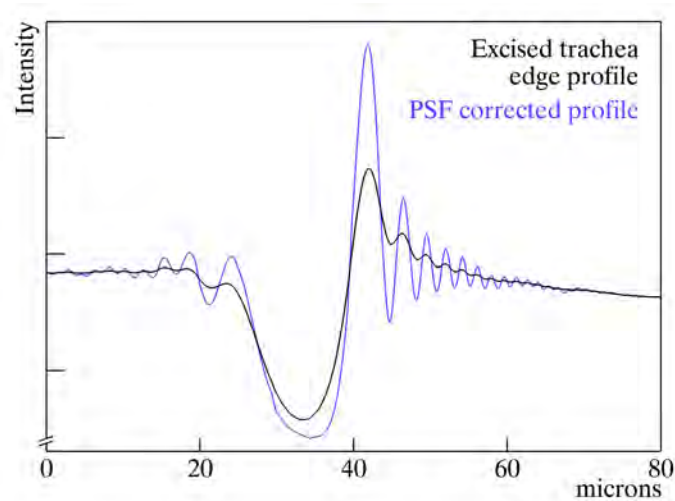


Figure 6.26: The profile from the edge of an *ex vivo* trachea, before and after correction for the measured point spread function (Fig. 6.25).

### 6.5.2.2 Fringe Intensity Profile Derivative

The derivative of a profile may be taken to enhance the visibility of these narrow fringes, as has been done in Fig. 6.27. In this example, fringes from the ASL/air interface in an excised trachea visible in the derivative profile at 80  $\mu\text{m}$ , are not visible by eye in the single exposure, which is promising in terms of detecting an ASL/tissue fringe which is not visible by eye during live imaging. This also shows that highly sensitive detectors, able to gain good image statistics within a short exposure, are critical to the development of live imaging.

### 6.5.2.3 Fringe Profile Correlation Analysis

Using this detailed edge profile, a correlation analysis may be performed, *i.e.* sliding a known edge pattern across the intensity profile, with an integration at each point, to search for points across the profile where the same pattern occurs. An example of such analysis using derivative profiles is shown below in Fig. 6.28, with first a simulated, and then an excised trachea profile. The weaker fringe between the tissue and ASL will be the same shape as that between the ASL and air (given they have almost the same radius of curvature and the same propagation distance). The visibility of the tissue/ASL interface fringe will be around 20% of the visibility of the ASL/airway interface fringe, due to the relative difference in densities across each of the interfaces. The ASL/air interface fringe set is taken as the kernel, and when convolved with the complete profile should pick out a strong correlation, seen as a peak, at the ASL/air interface and a weak correlation, seen as a smaller peak, at the tissue/ASL interface.

While this is seen in Fig. 6.28 *a*), the simulated intensity profile, it is not consistently seen in Fig 6.28 *b*), the mouse airway intensity profile.

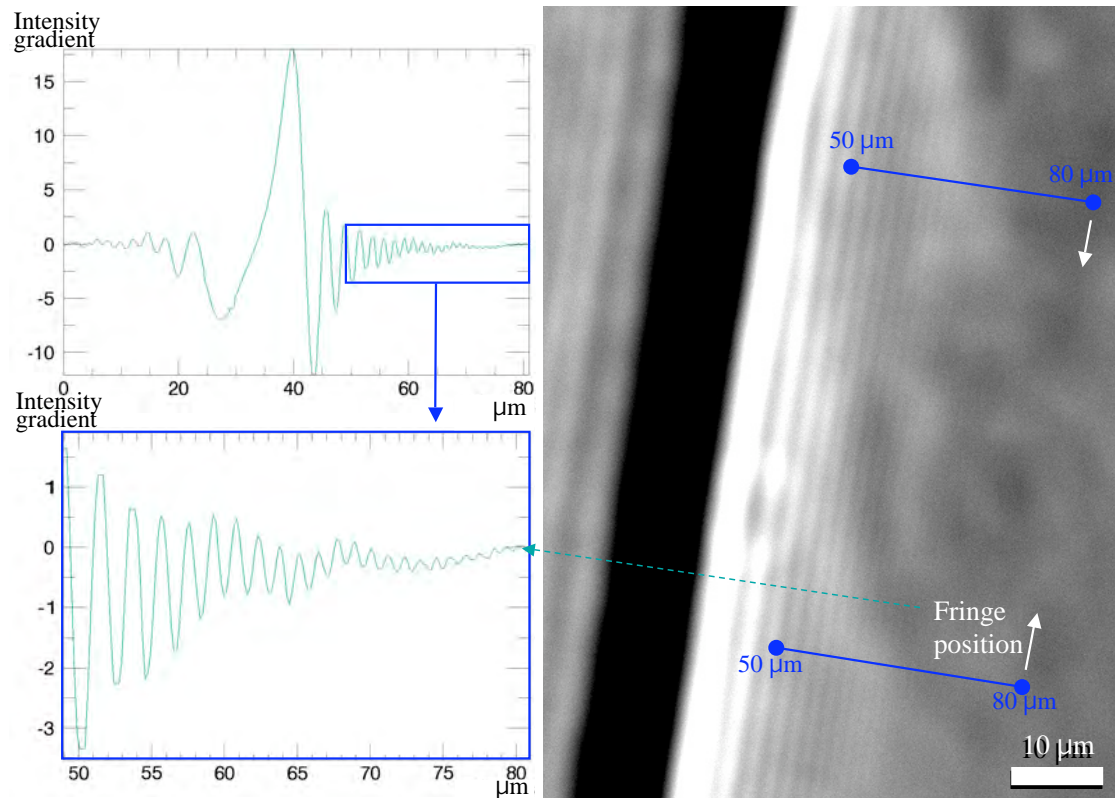


Figure 6.27: Narrow, low intensity fringes from an excised trachea edge, not visible by eye, can be detected after averaging and taking the profile derivative.

#### 6.5.2.4 Methods of Analysis using Phase Information

Single image phase retrieval (Paganin et al., 2002) and TIE phase retrieval were also trialed on the images, but just as there is insufficient contrast to identify both sides of the ASL in the raw image, there is insufficient contrast for the ASL depth to be revealed in phase-retrieved images.

Gabor holography was also attempted, in the hope that the many fine fringes around each interface would focus into an edge when back-propagated the same distance as used in the initial PB-PCXI. Once again, only the ASL/airway interface was apparent.

## 6.6 Mucociliary Clearance Monitoring

If the depth of the ASL may not be directly measured as an indicator of airway health, the signs of a properly functioning ASL (*i.e.* with correct depth) may instead be a good indicator. As previously mentioned (§§6.1-6.2) the purpose of the ASL is to facilitate the beating motion of the cilia in clearing debris and mucus from the lungs by moving these along the surface, a process called Mucociliary Clearance (MCC). Hence, insufficient ASL results in lower particle velocities for MCC than for normal ASL depths. Most of the naturally cleared particles are too small to be seen during direct imaging, hence larger particles must be introduced if MCC is to be observed. A large body of work, as described in Appendices D and E, has focused on this idea.

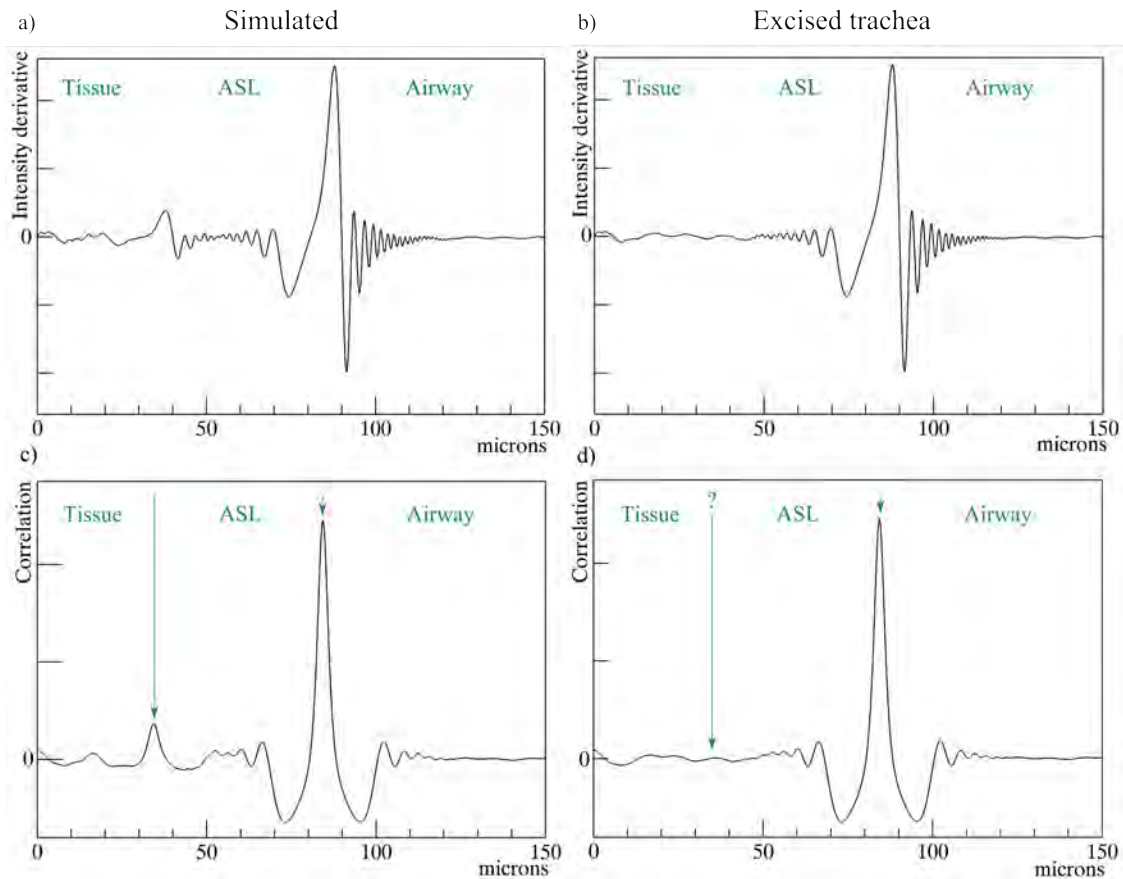


Figure 6.28: The derivative of the profile across airway interface images *a*) simulated, then *b*) from an excised trachea, is correlated with the fringe derivative profile kernel for *c*) simulated and *d*) excised trachea.

Small hollow glass beads, from 2  $\mu\text{m}$  to 30  $\mu\text{m}$  in diameter, are visible due to phase contrast effects when placed in the airways. These were delivered into the nose or trachea in a bolus of saline or distilled water, and observed using the same live imaging set-up as described in section 6.3.3.1. A healthy airway will then clear these beads once the carrier fluid is absorbed or otherwise lost and the beads stick to the sides of the airway.

This body of work has included trialling different fluids for the bead suspension and different types of beads, including those with high refractive index, those that are hollow and those coated with silver. The rate of clearance could then be calculated from the position of the bead at each time interval in the imaging sequence, with speeds typically around 0.2 mm/min (Donnelley et al., 2009). It was also known that MCC continues after death (§6.5.1.1), and it was seen that bead motion may then be more easily observed due to the lack of body movement. This also enables the trachea to be excised for MCC imaging, to reduce overlying phase images from overlying tissue. Figure 6.29 shows the motion of a bead along the edge of an *in vivo* trachea, most easily observed when taking the difference between consecutive frames.

This work has also looked at the clearance of different types of types of pollutants from the airways, including fibreglass, asbestos, lead and quarry dust (Appendix D and E) (Donnelley et al., 2009, 2010b). While long term effects of pollutant inhalation have been studied, no previous methods have been able to study the deposition and behaviour of these particulates as they arrive in

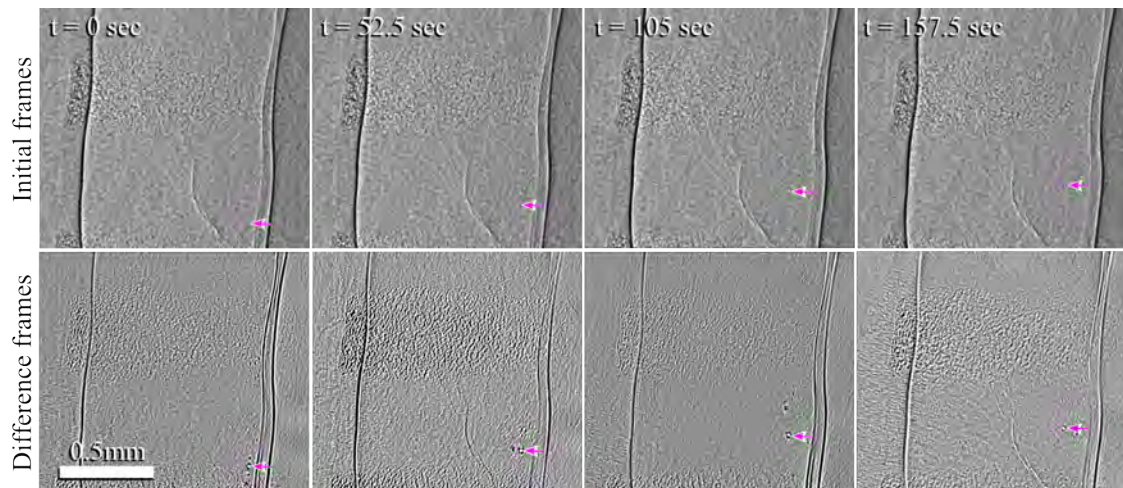


Figure 6.29: Introduced hollow glass beads move up away from the lungs, up the trachea. While difficult to identify in the original frames (top row), the beads are easily visible when the difference is taken between consecutive frames (lower row). The progress of a single bead is followed by the pink arrows. The full movies of both the initial frames and the difference frames are included in the supplementary materials as supplementary Fig. 6.29 a) and Fig. 6.29 b).

the airways. Examples of the different pollutants within an excised trachea are seen in Fig. 6.30, clearly differentiable from each other.

Full sets of results from the mucociliary clearance experiments are in Appendices D and E.

## 6.7 Conclusion

The phase contrast airway imaging work of the chapter has not revealed the depth of the airway surface liquid. Either a more sensitive method of imaging, or a different indicator of airway health is required to assess the effectiveness of treatments. An alternative measure of airway function was therefore presented in section 6.6 and we now describe an alternative live imaging method, sensitive to weak phase gradients, in Chapter 7.

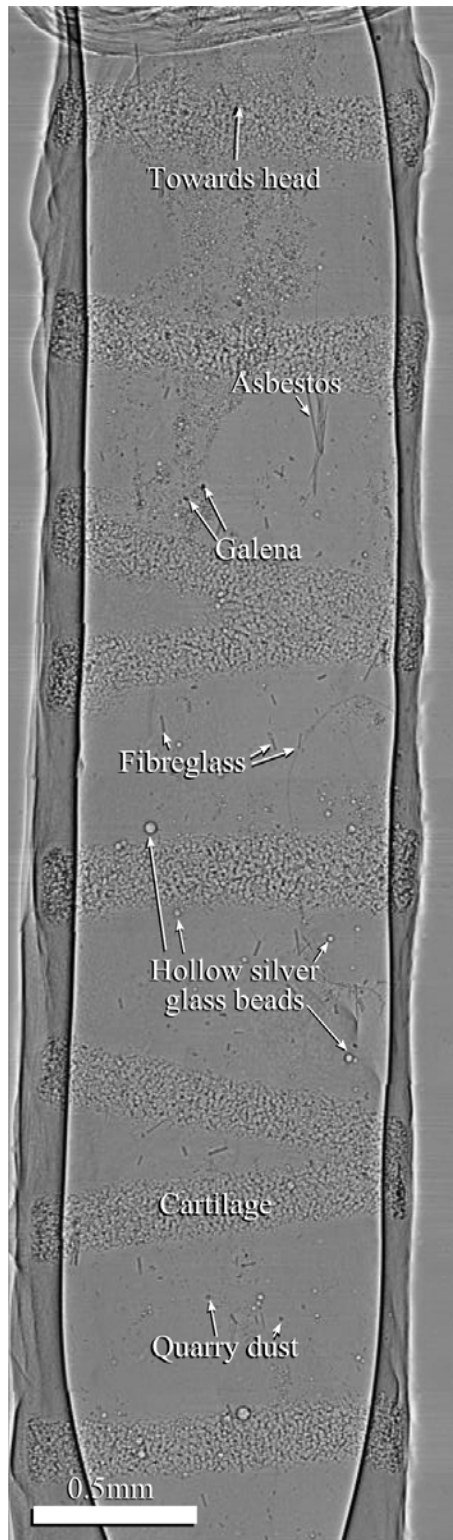


Figure 6.30: Asbestos, Galena, Glass beads, Quarry dust and Fibreglass are seen within an excised trachea (compiled from 8 images, each taken with 25 keV x-rays, 0.45  $\mu\text{m}$  pixels on BL20XU).



---

## PCXI for Live Imaging by a New Grating Method

---

*Quantitative x-ray phase contrast imaging using a single grating of comparable pitch to sample feature size.*

by Kaye S. Morgan, David M. Paganin and Karen K. W. Siu.

Published in Optics Letters **36**, pp. 55-57, 2011.

---

The need for a more sensitive method of imaging weak phase gradients in a live sample has been demonstrated by the results presented in Chapter 6 (see §6.7). The one-dimensional nature of an ASL depth measurement means that a two-dimensional image is not necessarily required, therefore an alternate method of phase imaging, perhaps only sensitive to gradients in one direction, may be employed. Imaging a live animal presents difficulties for techniques which require multiple exposures to retrieve a phase image, hence a single-exposure method is proposed.

This Letter details the idea of analysing how a high visibility reference pattern incident on a sample is warped by the phase gradients introduced by that sample. A method for quantitative retrieval of optical depth is given, which will produce a thickness map for a single-material object. Results from a perspex cylindrical interface verify the method and show the technique is sensitive to both high and low phase gradients.

This sensitivity is promising in terms of the application of Chapter 6; imaging the weak phase gradient produced at the interface between the ASL and tissue in the airways.

Other imaging applications, where a specific measurement is to be made on a non-static sample, may also benefit from this method.

## Declaration for Thesis Chapter 7

In the case of Chapter 7, contributions to the work involved the following:

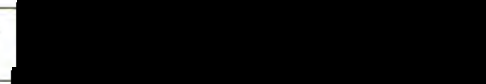
Name	% contribution	Nature of contribution
Kaye Morgan	90%	Led the original experiments and developed the theoretical basis, performed the data analysis, and wrote up the paper.
David Paganin		Contributed to the initial idea, theoretical discussions, provided supervisory advice, aided proofreading and drafting
Karen Siu		Contributed to the original experiments and the theoretical discussions, provided supervisory advice, aided proofreading and drafting

### Declaration by co-authors

The undersigned hereby certify that:

1. the above declaration correctly reflects the nature and extent of the candidate's contribution to this work, and the nature of the contribution of each of the co-authors.
2. they meet the criteria for authorship in that they have participated in the conception, execution, or interpretation, of at least that part of the publication in their field of expertise;
3. they take public responsibility for their part of the publication, except for the responsible author who accepts overall responsibility for the publication;
4. there are no other authors of the publication according to these criteria;
5. potential conflicts of interest have been disclosed to (a) granting bodies, (b) the editor or publisher of journals or other publications, and (c) the head of the responsible academic unit; and
6. the original data are stored at the following location(s) and will be held for at least five years from the date indicated below: School of Physics and Monash Centre for Synchrotron Science, Clayton Campus, Monash University, Australia.

### Signatures:

Kaye Morgan:		Date: 19/10/10
David Paganin:		Date: 19/10/10
Karen Siu:		Date: 19.10.2010.

---

This paper was published by Optics Letters and may be made available as an electronic reprint with the permission of OSA. The paper may in the future be found on the OSA website:

<http://www.opticsinfobase.org/ol/abstract.cfm?uri=ol-36-1-55>.

Systematic or multiple reproduction or distribution to multiple locations via electronic or other means is prohibited and is subject to penalties under law.

---

# Quantitative x-ray phase-contrast imaging using a single grating of comparable pitch to sample feature size

Kaye S. Morgan,<sup>1,\*</sup> David M. Paganin,<sup>1</sup> and Karen K. W. Siu<sup>1,2</sup>

<sup>1</sup>School of Physics, Monash University, Clayton, Victoria, Australia, 3800

<sup>2</sup>Monash Centre for Synchrotron Science, Monash University, Clayton, Victoria, Australia, 3800

\*Corresponding author: [kaye.morgan@monash.edu](mailto:kaye.morgan@monash.edu)

Received September 1, 2010; revised October 26, 2010; accepted November 13, 2010; posted December 2, 2010 (Doc. ID 133865); published December 27, 2010

The ability to quantitatively retrieve transverse phase maps during imaging by using coherent x rays often requires a precise grating or analyzer-crystal-based setup. Imaging of live animals presents further challenges when these methods require multiple exposures for image reconstruction. We present a simple method of single-exposure, single-grating quantitative phase contrast for a regime in which the grating period is much greater than the effective pixel size. A grating is used to create a high-visibility reference pattern incident on the sample, which is distorted according to the complex refractive index and thickness of the sample. The resolution, along a line parallel to the grating, is not restricted by the grating spacing, and the detector resolution becomes the primary determinant of the spatial resolution. We present a method of analysis that maps the displacement of interrogation windows in order to retrieve a quantitative phase map. Application of this analysis to the imaging of known phantoms shows excellent correspondence. © 2010 Optical Society of America

OCIS codes: 100.5070, 110.3010, 170.3880, 340.6720, 340.7440, 350.2770.

Noninvasive imaging of dynamic biological processes within animal models is being realized with the development of high temporal and spatial resolution coherent x-ray imaging [1,2]. In particular, phase-contrast techniques have made it possible to quantitatively image soft tissue and weakly attenuating materials (e.g., [3]). Although many different phase-imaging techniques of excellent sensitivity have been proposed and demonstrated, not all are possible with a single image or for a short exposure time, as is often desired during live animal imaging.

Distortion of a periodic high-visibility pattern to visualize a phase object was shown by Massig [4] using visible light and extended to a two-dimensional (2D) reference pattern by Perciante and Ferrari [5]. The source of this phase contrast may be described by the transport of intensity (TIE) equation for a coherent scalar paraxial wave [6],  $\nabla_{\perp} \cdot (I \nabla_{\perp} \phi) = -k \partial I / \partial z$ , where  $\phi$  is the phase,  $I$  is the intensity,  $k$  the wavenumber, and  $\nabla_{\perp}^2$  is the transverse Laplacian, in the plane perpendicular to the optic axis,  $z$ . For a small distance,  $z$ , between the contact plane ( $z = 0$ ) and image plane ( $z = z$ ), the TIE may be rearranged to give

$$I_{\text{image plane}} = I_{\text{contact}} - zk^{-1}(I \nabla_{\perp}^2 \phi + \nabla_{\perp} I \cdot \nabla_{\perp} \phi). \quad (1)$$

Although the “curvature” term of Eq. (1) ( $\nabla_{\perp}^2 \phi$ ) is most often the source of propagation-based phase contrast [3], if a large intensity gradient is introduced, the “prism” term ( $\nabla I \cdot \nabla \phi$ ) may become significant. For example, if the field is incident on a completely absorbing straight sharp edge normal to the vector  $\mathbf{n}_{\perp}$ , the intensity gradient will be equal to the Dirac-delta at the edge position ( $\delta_L$ ), and so Eq. (1) (taking  $\nabla_{\perp}^2 \phi$  as negligible) will become [7]

$$I_{\text{image plane}} = I_{\text{contact}} - zk^{-1} \delta_L \partial \phi / \partial \mathbf{n}_{\perp}, \quad (2)$$

directly describing the phase gradient in the direction perpendicular to the edge. A reference pattern may therefore

be designed to be most sensitive to gradients in the direction of interest for a particular sample.

A setup shown in Fig. 1(a) is proposed, translating Massig’s concept from visible light imaging to x-ray imaging [8]. This is analogous to a Shack–Hartmann wavefront sensor (cf. [9]). The grating introduces a high-visibility reference pattern, which is slightly distorted by the sample or phase object (cf. [10]); see Fig. 1(b). With further propagation, the transverse displacement ( $S$ ) of the pattern is increased so that the displacement can be easily visualized at the detector some distance downstream of the sample.

A single-grating setup has previously been used in differential phase-contrast imaging [11,12], using a procedure in which the grating is scanned across the sample and at least five images are taken to construct a differential phase image. In other work, a second or third grating has been scanned transversely after the sample, utilizing Talbot interferometry to map the refractive index of the phase object [13–18]. These techniques have enabled

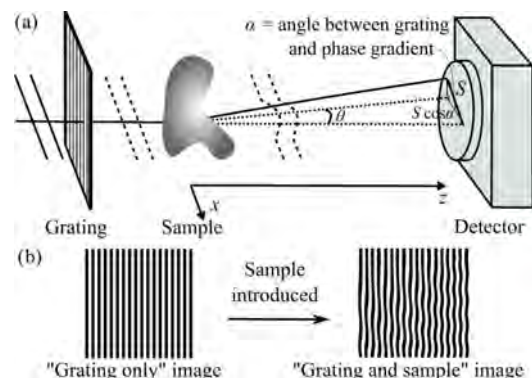


Fig. 1. (Color online) (a) Experimental setup. (b) Distorted grating pattern shown after passing through the sample.

high-resolution images of weak phase objects, including biological samples (e.g., [19]). However, multiple exposures are again required while translating the grating transversely, which makes these techniques challenging to apply to live imaging experiments.

Wen *et al.* [8] used a single-grating setup similar to the one proposed here for a grating period equal to around five pixels and a field of view thousands of times greater than the grating period. The grating frequency is well separated from the sample feature size in the Fourier domain, so Takeda's method of Fourier analysis [20] may be employed.

In our case, the effective pixel size is less than 1% of that used by Wen *et al.* and the grating period is closer to 60 pixels. The sample feature size is now smaller than or comparable to the grating period, hence Takeda's method is inapplicable. A complementary method of analysis is required to resolve distortions in the grating pattern and retrieve the sample function. Such a method is presented here, which compares a reference "grating only" image (taken at the start of imaging) with each "grating and sample" image [see Fig. 1(b)], looking at the displacement of grating lines (and their diffraction pattern if present).

Images taken with the setup of Fig. 1(a) may be analyzed as follows.

A reference incident ray will change direction in the plane perpendicular to the grid by angle  $\theta$ , according to the phase object through which it passes, as shown in Fig. 1(a). Such a ray may shift the edge of a feature of the grating pattern, hence a longer propagation,  $z$ , will result in a greater transverse shift,  $S$ , of this feature in the final image. For a line grating, this will be observed as  $S \cos \alpha$ , where  $\alpha$  is the angle between the normal to the grating lines and the phase gradient. A line grating should therefore be positioned to minimize this angle and maximize the observed shift. This relationship is

$$\tan \theta = (S \cos \alpha) / z. \quad (3)$$

For incident x rays of wavenumber  $k$ , phase  $\phi$  is introduced at position  $x$  (see Fig. 1) after passing through a sample of effective refractive index,  $\delta$ , and thickness,  $T$ , which means the ray angle  $\theta$  in the  $x-z$  plane will be

$$\theta(x) = \frac{1}{k} \frac{\partial \phi(x)}{\partial x} = \frac{1}{k} \frac{\partial (-k \delta T(x))}{\partial x} = -\delta \frac{\partial T(x)}{\partial x}. \quad (4)$$

Combining Eqs. (3) and (4), the observed shift of the reference pattern will be  $S(x) \cos \alpha = z \tan(\delta \partial T(x) / \partial x)$ . This may be rearranged in order to determine the thickness of a sample that creates such shifts; for a single-material sample:

$$T(x) = \frac{1}{\delta} \int \tan^{-1} \left( \frac{S(x) \cos \alpha}{z} \right) dx. \quad (5)$$

Therefore, for each pixel in the "grating and sample" image, a 40 pixel radius interrogation window was first normalized in intensity to, then compared with the corresponding position in the "grating only" image. The interrogation window was then shifted perpendicular to the grating lines until a position of least difference

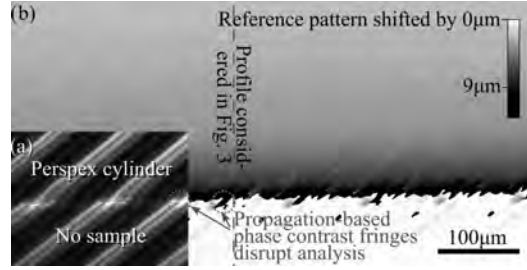


Fig. 2. (a) A 3 mm cylinder distorts the grating pattern, the image of which can then produce (b) a map of the perpendicular distance over which the pattern has been shifted, produced by image of grating pattern.

was reached. The shift required to achieve this position was then recorded as  $S \cos \alpha$ . Finally, Eq. (5) was used to convert the shift image  $[S(x)]$  to a thickness map  $[T(x)]$  for a given refractive index.

This method was applied to the imaging of a 3 mm diameter Perspex cylinder using 25 keV synchrotron undulator x rays incident on a 400 line pair per inch gold grating, with  $0.18 \mu\text{m}$  effective pixel size, 300 ms exposure, and propagation of  $z = 1.56 \text{ m}$ . Figure 2 shows the "grating and sample" image [Fig. 2(a)] and the subsequent shift image [Fig. 2(b)] for the 3 mm cylinder.

Diffraction from both the grating and the edge of the cylinder occurs with a highly coherent source, which creates a more detailed reference pattern, enabling a mapping to be made across the image, not just along a grating edge. However, analysis problems result in the local region where propagation-based phase contrast fringes appear near the edge of the cylinder: see circles in Fig. 2(b). The resulting retrieved thickness profile,  $T(x)$ , is shown in Fig. 3, for the profile  $S(x)$ , shown as a dashed line in Fig. 2. The 3 mm cylinder thickness profile shows excellent correspondence with an rms error of 1.8% from the expected profile.

A single-exposure propagation-based phase contrast image was also taken, and the resulting profile, reconstructed using a single-image phase retrieval method [21], is shown in Fig. 3 for comparison, with 16% rms error.

This method shows an advantage over single-image phase retrieval in the quantitative accuracy of the retrieval, achieved using a local approach rather than Fourier space analysis. Both the high phase gradient at

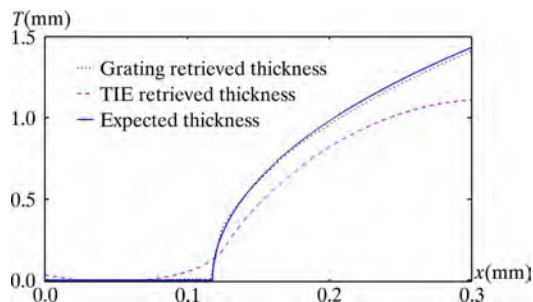


Fig. 3. (Color online) Reconstructed cylinder thickness  $[T(x)]$  along the dashed line shown in Fig. 2  $[S(x)]$  across the 3 mm diameter Perspex cylinder.

the cylinder edge and the low phase gradient far from the edge are better described than with the single-image phase retrieval.

This simple technique enables single-exposure phase contrast imaging for micrometer-size features in a sample without requiring micrometer pitch gratings or even regularly spaced grating/grid patterns. The method of analysis is also robust to beam intensity variations and hence does not require correction for a nonuniform flat field. The analysis looks only at the shifted position of a reference pattern and therefore cannot confuse absorption effects with phase effects. Consequently, a cone beam geometry or a polychromatic beam could also be used, which significantly expands its applicability. However, the presence of propagation-based contrast fringes at sharp interfaces makes phase retrieval in this local region difficult, hence this approach is of most value when imaging objects with slowly varying phase where features cannot be visualized with propagation-based phase-contrast x-ray imaging. Alternatively, a spinning diffuser could be introduced to the setup after the sample to decrease the magnitude of the complex degree of transverse coherence and to reduce propagation-based phase-contrast visibility [22,23].

Although this method may not always produce clear qualitative images, it may be of value in quantitatively observing certain micron size changes in soft tissue within a live animal (e.g., the depth of liquid lining an airway [24]). The value of this method has been shown in the accurate retrieval of known objects, including areas where the phase gradient is small (hence difficult to observe with propagation-based phase contrast alone).

We acknowledge the Japan Synchrotron Radiation Research Institute (JASRI) (proposal 2009B1922) and thank Yoshio Suzuki, Akihisa Takeuchi, and Aidan Jamison. We acknowledge travel funding provided by the International Synchrotron Access Program (ISAP) managed by the Australian Synchrotron, together with the support of the National Health and Medical Research Council (K. K. W. S.) and an Australian Postgraduate Award and a J. L. William Scholarship at Monash University (K. S. M.).

#### References

1. M. J. Kitchen, R. A. Lewis, M. J. Morgan, M. J. Wallace, M. L. Siew, K. K. W. Siu, A. Habib, A. Fouras, N. Yagi, K. Uesugi, and S. B. Hooper, *Phys. Med. Biol.* **53**, 6065 (2008).
2. M. Donnelley, K. S. Morgan, A. Fouras, W. Skinner, K. Uesugi, N. Yagi, K. K. W. Siu, and D. Parsons, *J. Synchrotron Radiat.* **16**, 553 (2009).
3. T. E. Gureyev, S. C. Mayo, D. E. Myers, Ya. Nesterets, D. M. Paganin, A. Pogany, A. W. Stevenson, and S. W. Wilkins, *J. Appl. Phys.* **105**, 102005 (2009).
4. J. H. Massig, *Appl. Opt.* **38**, 4103 (1999).
5. C. D. Perciante and J. A. Ferrari, *Appl. Opt.* **39**, 2081 (2000).
6. M. R. Teague, *J. Opt. Soc. Am.* **73**, 1434 (1983).
7. T. E. Gureyev, A. Roberts, and K. A. Nugent, *J. Opt. Soc. Am. A* **12**, 1932 (1995).
8. H. H. Wen, E. E. Bennett, R. Kopace, A. F. Stein, and V. Pai, *Opt. Lett.* **35**, 1932 (2010).
9. S. C. Mayo and B. Sexton, *Opt. Lett.* **29**, 866 (2004).
10. Y. J. Liu, B. Chen, E. R. Li, J. Y. Want, A. Marcelli, S. W. Wilkins, H. Ming, Y. C. Tian, K. A. Nugent, P. P. Zhu, and Z. Y. Wu, *Phys. Rev. A* **78**, 023817 (2008).
11. Y. Takeda, W. Yashiro, Y. Suzuki, and A. Momose, *AIP Conf. Proc.* **879**, 1361 (2007).
12. W. Yashiro, Y. Takeda, A. Takeuchi, Y. Suzuki, and A. Momose, *Phys. Rev. Lett.* **103**, 180801 (2009).
13. A. Momose, S. Kawamoto, I. Koyama, Y. Hamaishi, K. Takai, Y. Suzuki, *Jpn. J. Appl. Phys.* **42**, L866 (2003).
14. T. Weitkamp, A. Diaz, C. David, F. Pfeiffer, M. Stampanoni, P. Cloetens, and E. Ziegler, *Opt. Express* **13**, 6296 (2005).
15. F. Pfeiffer, T. Weitkamp, O. Bunk, and C. David, *Nature Phys.* **2**, 258 (2006).
16. A. Momose, W. Yashiro, Y. Takeda, Y. Suzuki, and T. Hattori, *Jpn. J. Appl. Phys.* **45**, 5254 (2006).
17. C. Kottler, C. David, F. Pfeiffer, and O. Bunk, *Opt. Express* **15**, 1175 (2007).
18. Y. Takeda, W. Yashiro, T. Hattori, A. Takeuchi, Y. Suzuki, and A. Momose, *Appl. Phys. Express* **1**, 117002 (2008).
19. F. Pfeiffer, O. Bunk, C. David, M. Bech, G. Le Duc, A. Bravin, and P. Cloetens, *Phys. Med. Biol.* **52**, 6923 (2007).
20. M. Takeda, *J. Opt. Soc. Am.* **72**, 156 (1982).
21. D. Paganin, S. C. Mayo, T. E. Gureyev, P. R. Miller, and S. W. Wilkins, *J. Microsc. (Oxf)* **206**, 33 (2002).
22. K. S. Morgan, S. C. Irvine, Y. Suzuki, K. Uesugi, A. Takeuchi, D. M. Paganin, and K. K. W. Siu, *Opt. Commun.* **283**, 216 (2010).
23. S. C. Irvine, K. S. Morgan, Y. Suzuki, K. Uesugi, A. Takeuchi, D. M. Paganin, and K. K. W. Siu, *Opt. Express* **18**, 13478 (2010).
24. K. S. Morgan, D. M. Paganin, D. W. Parsons, M. Donnelley, N. Yagi, K. Uesugi, Y. Suzuki, A. Takeuchi, and K. K. W. Siu, *IFMBE Proc.* **25**, 135 (2009).



---

## Conclusion

This thesis has explored theoretical, experimental and application-based aspects of phase contrast imaging of biological interfaces. While much of the work is also applicable to non-biological applications, the emphasis on live imaging has meant that single exposure techniques are the focus. A summary of the key results from the thesis regarding PCXI simulation, coherence considerations and biomedical applications is presented here, along with ideas for possible extensions to the body of work presented.

Chapters 2 and 3 described the modelling of phase contrast fringes seen with propagation from a rounded edge. The projection approximation, used to model the passage of the wavefield through the sample, does not fully describe diffraction and interference of initially-adjacent rays. This was observed as an underestimation of the visibility and width of the simulated fringes from a rounded interface, where the sample thickness was significant compared with the total free-space propagation. This was seen in comparison with both experimental images and an exact solution. However, for larger propagation distances, as used in biological phase contrast imaging, the simulation model using the projection approximation proved to be a time and memory efficient method of accurately simulating propagation-based phase contrast. The Argand plane signature of the complex wavefield downstream of a rounded edge provided further insight into the interference of the plane wave passing outside the edge, the wavefield with a phase-shift having passed through the sample and the wavefield emanating from the very edge of the sample.

These generalised Cornu spirals could be applied to the study of phase variations in other contexts. For example, the complex wavefield downstream of a curved wavefront incident on a sharp phase edge could be considered. This work could also be extended to evaluate the validity of other approximations instead of looking solely at the projection approximation. Simulated images obtained using the 2D method of stationary phase (Mandel and Wolf, 1995) or the geometrical theory of diffraction (Keller, 1962) could be compared to the exact solution images found in the thesis. This study could look analytically at the error terms associated with each of these approximations and how these relate to the exact solution in appropriate limits.

The original comparison could also be done for the case of an ellipsoid (given a cylinder is a limiting case of an ellipsoid). This would better describe more complicated three-dimensional interfaces within samples.

Chapters 4 and 5 looked at how much of this intricate fringe shape predicted by theory would be resolvable in a system with a finite coherence width. Measurements of the transverse coherence at beamline 20XU of SPring-8 confirmed that the extra propagation to the Biomedical Imaging

Centre hutch (~250m from the source) from the experimental hall hutch (~75m from the source) significantly increases the coherence width, as does decreasing the size of a beam defining aperture in front of the source. More particularly, it was found that the coherence width is unchanged when a spinning random phase screen diffuser is introduced upstream of the sample, in order to increase the homogeneity of the beam and remove unwanted phase images due to imperfections in the optics. However the sum of the many random phase screens over the exposure time means that the magnitude of the absolute value of the complex degree of second order coherence is decreased by a fixed percentage,  $\kappa$ . This results in a decrease in the observed visibility of a phase contrast fringe produced by an interface. Numerical modelling of the image formation process showed how this effect changes with diffuser characteristics and position. This provides a reference when considering the diffuser material, feature length scale and thickness. More importantly, the results of the modelling and experiment show that if the diffuser is positioned close to the source, the reduction in fringe visibility is not as great. This means the advantages of a diffuser may be retained without markedly affecting the contrast available in PCXI, and has resulted in a permanent change to BL20XU. Alternatively, in circumstances where pure-absorption images are desired (for example, in some tomographic applications), the diffuser may be placed close to the sample to reduce or eliminate the visibility of phase effects.

Generic optimisation questions for given scenarios could be further considered by this model, looking at the effect of, for example, polychromatic x-rays. Consideration of a polychromatic source is important in translating techniques to laboratory sources.

The numerical model for the diffuser in the imaging system could be applied to other forms of phase contrast imaging, such as analyser-based PCXI. Results could be compared with the experimental findings of Cloetens *et al.* (Cloetens *et al.*, 1996), where the change in shape of the rocking curve due to the presence of a sliding wooden diffuser is observed. An analytic approach could also be used to consider how the correlation function of the wavefield changes as it propagates through many realisations of a random phase screen over an exposure time (Berry, 1978). It would similarly be interesting to develop an analytic expression for  $\kappa$ , the multiplicative factor for the degree of coherence in the presence of a diffuser.

The application of PB-PCXI to the imaging of the airways was addressed in Chapter 6, with the aim to detect the interfaces on either side of the airway surface liquid (ASL) to provide the ASL depth as a measure of airway health. This would be of great value in assessing the effectiveness of new treatments for the airway disease associated with cystic fibrosis. Phantom imaging and simulation models suggested that the ASL/tissue interface, while much more subtle than the ASL/airway interface, should be visible in PCXI images. *In vivo* PB-PCXI of the nasal airways and the trachea in mice models showed that the ASL/air interface produced a strong phase contrast fringe, however the ASL/tissue interface was not directly visible. Methods of interface fringe analysis over images covering 40 minutes of airway treatment showed that changes in the overall width of the airway and the visibility of the ASL/air interface fringe could be tracked with high resolution, but were not sufficiently sensitive or reliable to detect changes in ASL depth.

The visibility of airway interfaces was significantly increased by looking at *ex vivo* airways, orienting the sample to maximise the phase gradient created, using an apertured source and placing the diffuser as close to the source as possible. Detailed interference patterns were extracted from the improved images, but the results could not discern the ASL/tissue interface.

An alternate method of assessing airway health by PCXI was described; measuring the rate of

clearance of introduced particles along the airway surface and out of the lungs. This is of wider use in studying how various forms of airborne pollutant particles interact with the airway surface.

The next step in this study is the application of the imaging method of Chapter 7 to the observation of the airway interfaces. This single-exposure method studies the local displacement of a high visibility reference pattern to quantitatively determine the sample phase gradients. The increased sensitivity of this method to weak phase gradients may prove to be what is required to detect the ASL/tissue interface.

Alternatively, the sensitivity of analyser-based imaging may be able to resolve this interface. Images taken at a high gradient region of the rocking curve should show increased sensitivity compared to PB-PCXI. If phase retrieval algorithms are to be applied, this would require an experimental set-up where two images may be taken simultaneously (given the imaging is to be performed on a live mouse), such as the Laue crystal set-up used by Kitchen *et al.* (Kitchen *et al.*, 2008, 2010) on BL20B2 at SPring-8. Their images showed high sensitivity to phase gradients, using 12  $\mu\text{m}$  pixels to image the lungs of new-born rabbit pups. In order to resolve the micron changes in ASL depth, the set-up would have to be adapted with two suitable detectors for BL20XU. The need for an increase in the exposure time to compensate for the decreased flux associated with ABI should also be considered, given the inherent movement problems with *in vivo* imaging.

Given the increase in fringe visibility and detail achieved in Chapter 6 (see Fig. 6.24), the work on fringe visibility as a function of ASL depth (section 6.4.4) may be applied, with optimal propagation length, to the observation of mouse airway interfaces while being treated. The additional visible fringes from each interface would enable several maxima within the ASL depth vs visibility curve, which may be sufficient to track changes in ASL depth. Given the indirect nature of this measure, a trial with a statistically significant number of mice would be required to produce conclusive results.

The sensitivity of future detectors will be critical in enabling shorter exposures with sufficient counts per pixel, so that animal movement is less of a problem and noise-sensitive methods of analysis may be applied. Sub-micron spatial resolution is also desired.

The capabilities of phase contrast x-ray imaging promise to be of great value in biomedical research, revealing soft-tissue structures and function in excellent detail, without requiring invasive procedures. It is hoped that the results of this thesis will contribute to the planning of future imaging work in this field, and inspire further sensitive phase imaging methods for new applications in the live observation of biological function.



---

## References

- Arfelli, F., Assante, M., Bonvicini, V., Bravin, A., Cantatore, G., Castelli, E., Dalla Palma, L., Di Michiel, M., Longo, R., Olivo, A. and Pani, S., Pontoni, D., Poropat, P., Prest, M., Rashevsky, A., Tromba, G., Vacchi, A., Vallazza, E., and Zanconati, F. (1998). Low-dose phase contrast x-ray medical imaging. *Phys. Med. Biol.*, 43:2845–2852.
- Arfelli, F., Bonvicini, V., Bravin, A., Cantatore, G., Castelli, E., Palma, L., Michiel, M., Fabrizioli, M., Longo, R., Menk, R., Olivo, A., Pani, S., Pontoni, D., Poropat, P., Prest, M., Rashevsky, A., Ratti, M., Rigon, L., Tromba, G., Vacchi, A., Vallazza, E., and Zanconati, F. (2000). Mammography with synchrotron radiation: Phase-detection techniques. *Radiology*, 215:286–293.
- Beltran, M. A., Paganin, D. M., Uesugi, K., and Kitchen, M. J. (2010). 2D and 3D x-ray phase retrieval of multi-material objects using a single defocus distance. *Opt. Express*, 18:6423–6436.
- Berry, M. V. (1978). Disruption of wavefronts: Statistics of dislocations in incoherent Gaussian random waves. *J. Phys. A*, 11:27–37.
- Beutel, J., Kundel, H. L., and Van Metter, R. L., editors (2000). *Handbook of Medical Imaging*. SPIE Publications, New York.
- Bonse, U. and Hart, M. (1965). An x-ray interferometer. *Appl. Phys. Lett.*, 6:155–156.
- Born, M. and Wolf, E. (1999). *Principles of Optics*. Cambridge University Press New York, 7th edition.
- Boucher, R. C. (2004). New concepts of the pathogenesis of cystic fibrosis lung disease. *Eur. Respir. J.*, 23:146–158.
- Boucher, R. C. (2007). Airway surface dehydration in Cystic Fibrosis: Pathogenesis and therapy. *Medicine*, 58:157–170.
- Bronnikov, A. (2002). Theory of quantitative phase-contrast computed tomography. *J. Opt. Soc. Am. A*, 19:472–480.
- Buffière, J. Y., Maire, E., Cloetens, P., Lormand, G., and Fougères, R. (1999). Characterization of internal damage in a MMC using x-ray synchrotron phase contrast microtomography. *Acta Mater.*, 47:1613–1625.
- Button, B. (2009). New insights into the periciliary layer and its role in mucus clearance. *Pediatr. Pulmonol.*, CF Conference Proceedings:109.
- Castelli, E., Arfelli, F., Dreossi, D., Longo, R., Rokvic, T., Cova, M. A., Quaia, E., Tonutti, M., Zanconati, F., Abrami, A., Chenda, V., Menk, R. H., Quai, E., Tromba, G., Bregant, P., and

- de Guarrini, F. (2007). Clinical mammography at the SYRMEP beam line. *Nucl. Instrum. Meth. A*, 572:237–240.
- Chapman, D., Thomlinson, W., Johnston, R. E., Washburn, D., Pisano, E., Gmur, N., Zhong, Z., Menk, R., Arfelli, F., and Sayers, D. (1997). Diffraction enhanced x-ray imaging. *Phys. Med. Biol.*, 42:2015–2025.
- Cloetens, P., Barrett, R., Baruchel, J., Guigay, J.-P., and Schlenker, M. (1996). Phase objects in synchrotron radiation hard x-ray imaging. *J. Phys. D: Appl. Phys.*, 29:133–146.
- Cloetens, P., Ludwig, W., Baruchel, J., Van Dyck, D., Van Landuyt, J., Guigay, J., and Schlenker, M. (1999). Holotomography: Quantitative phase tomography with micrometer resolution using hard synchrotron radiation x rays. *Appl. Phys. Lett.*, 75:2912–2914.
- Cloetens, P., Ludwig, W., Boller, E., Helfen, L., Salvo, L., Mache, R., and Schlenker, M. (2002). Quantitative phase contrast tomography using coherent synchrotron radiation. *Proc. SPIE*, 4503:82–91.
- Cloetens, P., Salomé-Pateyron, M., Buffière, J., Peix, G., Baruchel, J., Peyrin, F., and Schlenker, M. (1997). Observation of microstructure and damage in materials by phase sensitive radiography and tomography. *J. Appl. Phys.*, 81:5878–5886.
- Coan, P., Mollenhauer, J., Wagner, A., Muehleman, C., and Bravin, A. (2008). Analyzer-based imaging technique in tomography of cartilage and metal implants: A study at the ESRF. *Eur. J. Radiol.*, 68:S41–S48.
- Coan, P., Pagot, E., Fiedler, S., Cloetens, P., Baruchel, J., and Bravin, A. (2005). Phase-contrast x-ray imaging combining free space propagation and Bragg diffraction. *J. Synchrotron Radiat.*, 12:241–245.
- David, C., Nohammer, B., and Solak, H. (2002). Differential x-ray phase contrast imaging using a shearing interferometer. *Appl. Phys. Lett.*, 81:3287–3289.
- Davis, T. J., Gao, D., Guryev, T. E., Stevenson, A. W., and Wilkins, S. W. (1995a). Phase-contrast imaging of weakly absorbing materials using hard x-rays. *Nature*, 373:595–598.
- Davis, T. J., Gureyev, T. E., Gao, D., Stevenson, A. W., and Wilkins, S. W. (1995b). X-ray image contrast from a simple phase object. *Phys. Rev. Lett.*, 74:3173–3176.
- Daviskas, E. (2006). Hyperosmolar agents and clearance of mucus in the diseased airway. *J. Aerosol. Med.*, 19:100–109.
- de Jonge, M. D., Hornberger, B., Holzner, C., Legnini, D., Paterson, D., McNulty, I., Jacobsen, C., and Vogt, S. (2008). Quantitative phase imaging with a scanning transmission x-ray microscope. *Phys. Rev. Lett.*, 100:163902.
- Delen, N. and Hooker, B. (1998). Free-space beam propagation between arbitrarily oriented planes based on full diffraction theory: a fast Fourier transform approach. *J. Opt. Soc. Am. A*, 15:857–867.

- Donnelley, M., Morgan, K. S., Fouras, A., Skinner, W., Uesugi, K., Yagi, N., Siu, K. K. W., and Parsons, D. W. (2009). Real-time non-invasive detection of inhalable particulates delivered into live mouse airways. *J. Synchrotron Radiat.*, 16:553–561.
- Donnelley, M., Parsons, D., Morgan, K., and Siu, K. (2010a). Animals in synchrotrons: Overcoming challenges for high-resolution, live, small-animal imaging. *AIP Conf. Proc.*, 1266:30–34.
- Donnelley, M., Siu, K. K. W., Morgan, K. S., Skinner, W., Suzuki, Y., Takeuchi, A., Uesugi, K., Yagi, N., and Parsons, D. W. (2010b). A new technique to examine individual pollutant particle and fibre deposition and transit behaviour in live mouse trachea. *J. Synchrotron Radiat.*, 17.
- Dubsky, S., Jamison, R. A., Irvine, S. C., Siu, K. K. W., Hourigan, K., and Fouras, A. (2010). Computed tomographic x-ray velocimetry. *Appl. Phys. Lett.*, 96:023702.
- Feser, M., Jacobsen, C., Rehak, P., and DeGeronimo, G. (2003). Scanning transmission x-ray microscopy with a segmented detector. *J. Phys. IV France*, 104:529–534.
- Fienup, J. R. (1982). Phase retrieval algorithms: a comparison. *Appl. Optics*, 21:2758–2769.
- Fitzgerald, R. (2000). Phase-sensitive x-ray imaging. *Phys. Today*, 53(7):23–26.
- Förster, E., Goetz, K., and Zaumseil, P. (1980). Double crystal diffractometry for the characterization of targets for laser fusion experiments. *Krist. Tech.*, 15:937–945.
- Fouras, A., Dubsky, S., Nguyen, J., Hourigan, K., Kitchen, M. J., Allison, B. J., Wallace, M. J., Siew, M. L., Siu, K. K. W., Lewis, R. A., Uesugi, K., Yagi, N., and Hooper, S. B. (2009a). In vivo synchrotron PIV for the measurement of airway motion. *8th International Symposium on Particle Image Velocimetry Proceedings*.
- Fouras, A., Dusting, J., Lewis, R., and Hourigan, K. (2007). Three-dimensional synchrotron x-ray particle image velocimetry. *J. Appl. Phys.*, 102:064916.
- Fouras, A., Kitchen, M. J., Dubsky, S., Lewis, R. A., Hooper, S. B., and Hourigan, K. (2009b). The past, present, and future of x-ray technology for in vivo imaging of function and form. *J. Appl. Phys.*, 105:102009.
- Gabor, D. (1948). A new microscopic principle. *Nature*, 161:777–778.
- Garcia-Pena, P. and Lucaya, J. (2004). HRCT in children: technique and indications. *Eur. Radiol.*, 14:L13–L30.
- Gerchberg, R. W. and Saxton, W. O. (1972). A practical algorithm for the determination of the phase from image and diffraction plane pictures. *Optik*, 35:237–246.
- Goodman, J. W. (2005). *Introduction to Fourier Optics*. Roberts and Company Publishers, Greenwood Village.
- Guigay, J. P., Langer, M., Boistel, R., and Cloetens, P. (2007). Mixed transfer function and transport of intensity approach for phase retrieval in the Fresnel region. *Opt. Lett.*, 32:1617–1619.

- Gureyev, T. E. (1999). Transport of intensity equation for beams in an arbitrary state of temporal and spatial coherence. *Optik*, 110:263–266.
- Gureyev, T. E. (2003). Composite techniques for phase retrieval in the Fresnel region. *Opt. Commun.*, 220:49–58.
- Gureyev, T. E., Davis, T. J., Pogany, A., Mayo, S. C., and Wilkins, S. W. (2004a). Optical phase retrieval by use of first Born- and Rytov-type approximations. *Appl. Optics*, 43:2418–2430.
- Gureyev, T. E., Mayo, S., Wilkins, S. W., Paganin, D., and Stevenson, A. W. (2001). Quantitative in-line phase-contrast imaging with multienergy x rays. *Phys. Rev. Lett.*, 86:5827–5830.
- Gureyev, T. E., Mayo, S. C., Myers, D. E., Nesterets, Y. I., Paganin, D. M., Pogany, A., Stevenson, A. W., and Wilkins, S. W. (2009). Refracting Röntgen's rays: Propagation-based x-ray phase contrast for biomedical imaging. *J. Appl. Phys.*, 105:102005.
- Gureyev, T. E., Nesterets, Y. I., Paganin, D. M., Pogany, A., and Wilkins, S. W. (2005). Linear algorithms for phase retrieval in the Fresnel region. 2. Partially coherent illumination. *Opt. Commun.*, 259:569–580.
- Gureyev, T. E. and Nugent, K. A. (1997). Rapid quantitative phase imaging using the transport of intensity equation. *Opt. Commun.*, 133:339–346.
- Gureyev, T. E., Paganin, D. M., Stevenson, A. W., Mayo, S. C., and Wilkins, S. W. (2004b). Generalized eikonal of partially coherent beams and its use in quantitative imaging. *Phys. Rev. Lett.*, 93:068103.
- Gureyev, T. E., Pogany, A., Paganin, D. M., and Wilkins, S. W. (2004c). Linear algorithms for phase retrieval in the Fresnel region. *Opt. Commun.*, 231:53–70.
- Gureyev, T. E., Raven, C., Snigirev, A., Snigireva, I., and Wilkins, S. W. (1999). Hard x-ray quantitative non-interferometric phase-contrast microscopy. *J. Phys. D: Appl. Phys.*, 32:563–567.
- Gureyev, T. E., Roberts, A., and Nugent, K. A. (1995). Partially coherent fields, the transport of intensity equation and phase uniqueness. *J. Opt. Soc. Am. A.*, 12:1942–1946.
- Harm, A. (2006). Chest computed tomography scans should be considered as a routine investigation in cystic fibrosis. *Paed. Resp. Rev.*, 7:202–208.
- Hooper, S., Kitchen, M., Wallace, M., Yagi, N., Uesugi, K., Morgan, M., Hall, C., Siu, K., Williams, I., Siew, M., Irvine, S. C., Pavlov, K., and Lewis, R. A. (2007). Imaging lung aeration and lung liquid clearance at birth. *FASEB J.*, 21:3329–3337.
- Hooper, S. B., Kitchen, M. J., Siew, M. L. L., Lewis, R. A., Fouras, A., te Pas, A. B., Siu, K. K. W., Yagi, N., Uesugi, K., and Wallace, M. J. (2009). Imaging lung aeration and lung liquid clearance at birth using phase contrast x-ray imaging. *Clin. Exp. Pharmacol. Physiol.*, 36:117–125.
- Hwu, Y., Tsai, W., Chang, H., Yeh, H., Hsu, P., Yang, Y., Su, Y., Tsai, H., Chow, G., Ho, P., Li, S., Moser, H., Yang, P., Seol, S., Kim, C., Je, J., Stefanekova, E., Groso, A., and Margaritondo, G. (2004). Imaging cells and tissues with refractive index radiology. *Biophys. J.*, 87:4180–4187.

- Hwu, Y., Tsai, W., Groso, A., Margaritondo, G., and Je, J. (2002). Coherence-enhanced synchrotron radiology: Simple theory and practical applications. *J. Phys. D: Appl. Phys.*, 35:R105–R120.
- Ingal, V. and Beliaevskaya, E. (1995). X-ray plane-wave topography observation of the phase contrast from a non-crystalline object. *J. Phys. D: Appl. Phys.*, 28:2314–2317.
- Ingal, V. and Beliaevskaya, E. (1997). Imaging of biological objects in the plane-wave diffraction scheme. *Il Nuovo Cimento*, 19(2-4):553–560.
- Ingal, V., Beliaevskaya, E., Brianskaya, A., and Merkurieva, R. (1998). Phase mammography—a new technique for breast investigation. *Phys. Med. Biol.*, 43:2555–2567.
- Irvine, S. C., Paganin, D. M., Dubsky, S., Lewis, R. A., and Fouras, A. (2008). Phase retrieval for improved three-dimensional velocimetry of dynamic x-ray blood speckle. *Appl. Phys. Lett.*, 93:153901.
- Irvine, S. C., Paganin, D. M., Jamison, R. A., Dubsky, S., and Fouras, A. (2010). Vector tomographic x-ray phase contrast velocimetry utilizing dynamic blood speckle. *Opt. Express*, 18:2368–2379.
- Jackson, J. D. (1999). *Classical Electrodynamics*. Wiley, New York, 3rd edition.
- Kak, A. C. and Slaney, M. (2001). *Principles of Computerized Tomographic Imaging*. Society of Industrial and Applied Mathematics, New York.
- Kashyap, Y. S., Tushar, R., Sarkar, P. S., Yadav, P. S., Shukla, M., Sinha, A., Dasgupta, K., and Sathiyamoorthy, D. (2007). Characterization of pyrocarbon coated materials using laboratory based x-ray phase contrast imaging technique. *Rev. Sci. Instrum.*, 78:83703.
- Keller, J. B. (1962). Geometrical theory of diffraction. *J. Opt. Soc. Am.*, 52:116–130.
- Kitchen, M., Lewis, R., Hooper, S., Wallace, M., Siu, K., Williams, I., Irvine, S., Morgan, M., Paganin, D., Pavlov, K., Yagi, N., and Uesugi, K. (2007). Dynamic studies of lung fluid clearance with phase contrast imaging. *AIP Conf. Proc.*, 879:1903–1907.
- Kitchen, M., Paganin, D., Lewis, R., Yagi, N., and Uesugi, K. (2005a). Analysis of speckle patterns in phase-contrast images of lung tissue. *Nucl. Instrum. Meth. A*, 548:240–246.
- Kitchen, M., Paganin, D., Lewis, R., Yagi, N., Uesugi, K., and Mudie, S. (2004). On the origin of speckle in x-ray phase contrast images of lung tissue. *Phys. Med. Biol.*, 49:4335–4348.
- Kitchen, M., Paganin, D., Uesugi, K., Allison, B., Lewis, R., Hooper, S., and Pavlov, K. (2010). X-ray phase, absorption and scatter retrieval using two or more phase contrast images. *J. Opt. Soc. Am. A*, 18:19994–20012.
- Kitchen, M. J., Lewis, R. A., Morgan, M. J., Wallace, M. J., Siew, M. L., Siu, K. K. W., Habib, A., Fouras, A., Yagi, N., Uesugi, K., and Hooper, S. B. (2008). Dynamic measures of regional lung air volume using phase contrast x-ray imaging. *Phys. Med. Biol.*, 53:6065–6077.

- Kitchen, M. J., Lewis, R. A., Yagi, N., Uesugi, K., Paganin, D., Hooper, S. B., Adams, G., Jureczek, S., Singh, J., Christensen, C. R., Hufton, A. P., Hall, C. J., Cheung, K. C., and Pavlov, K. M. (2005b). Phase contrast x-ray imaging of mice and rabbit lungs: a comparative study. *Brit. J. Radiol.*, 78:1018–1027.
- Knox, W. H., Alonso, M., and Wolf, E. (2010). Spatial coherence from ducks. *Phys. Today*, 63(3):11.
- Kohn, V., Snigireva, I., and Snigirev, A. (2000). Direct measurement of transverse coherence length of hard x rays from interference fringes. *Phys. Rev. Lett.*, 85:2745–2748.
- Kono, M., Ohbayashi, C., Yamasaki, K., Ohno, Y., Adachi, S., Sugimura, K., and Suzuki, Y. (2001). Refraction imaging and histologic correlation in excised tissue from a normal human lung: preliminary report. *Acad. Radiol.*, 8:898–902.
- Kottler, C., David, C., Pfeiffer, F., and Bunk, O. (2007). A two-directional approach for grating based differential phase contrast imaging using hard x-rays. *Opt. Express*, 15:1175–1181.
- Kozioziemski, B. J., Koch, J. A., Martz, H. E., Lee, W.-K., and Fezzaa, K. (2005). Quantitative characterization of inertial confinement fusion capsules using phase contrast enhanced x-ray imaging. *J. Appl. Phys.*, 97:63103.
- Kwan, A. L. C. and Seibert, J. A. (2006). An improved method for flat-field correction of flat panel x-ray detector. *Med. Phys.*, 33:391–393.
- Leitenberger, W., Wendrock, H., Bischoff, L., and Weitkamp, T. (2004). Pinhole interferometry with coherent hard x-rays. *J. Synchrotron Radiat.*, 11:190–197.
- Lewis, R., Hall, C., Hufton, A., Evans, S., Menk, R., Arfelli, F., Rigon, L., Tromba, G., Dance, D., Ellis, I., Evans, A., Jacobs, E., Pinder, S., and Rogers, K. (2003). X-ray refraction effects: application to the imaging of biological tissues. *Brit. J. Radiol.*, 76:301–308.
- Lewis, R., Rogers, K., Hall, C., Hufton, A., Evans, S., Menk, R., Tromba, G., Arfelli, F., Rigon, L., Olivo, A., Evans, A., Pinder, S. E., Jacobs, E., Ellis, I. O., and Dance, D. R. (2002). Diffraction-enhanced imaging: improved contrast and lower dose x-ray imaging. *Proc. SPIE*, 4682:286–297.
- Lewis, R. A. (2004). Medical phase contrast x-ray imaging: current status and future prospects. *Phys. Med. Biol.*, 49:3573–3583.
- Lewis, R. A., Yagi, N., Kitchen, M. J., Morgan, M. J., Paganin, D., Siu, K. K. W., Pavlov, K., Williams, I., Uesugi, K., Wallace, M. J., Hall, C. J., Whitley, J., and Hooper, S. B. (2005). Dynamic imaging of the lungs using x-ray phase contrast. *Phys. Med. Biol.*, 50:5031–5040.
- Limberis, M., Anson, D., Fuller, M., and Parsons, D. (2002). Recovery of airway cystic fibrosis transmembrane conductance regulator function in mice with cystic fibrosis after single-dose lentivirus-mediated gene transfer. *Hum. Gene Ther.*, 13:1961–1970.
- Lin, J. J. A., Paterson, D., Peele, A. G., McMahon, P. J., Chantler, C. T., and Nugent, K. A. (2003). Measurement of the spatial coherence function of undulator radiation using a phase mask. *Phys. Rev. Lett.*, 90:074801.

- Liu, Y. J., Chen, B., Wang, J. Y., Marcelli, A., Wilkins, S. W., Ming, H., Tian, Y. C., Nugent, K. A., Zhu, P. P., and Wu, Z. Y. (2008). Phase retrieval in x-ray imaging based on using structured illumination. *Phys. Rev. A*, 78:023817.
- Mandel, L. and Wolf, E. (1995). *Optical Coherence and Quantum Optics*. Cambridge University Press, Cambridge.
- Margaritondo, G. (2002). *Elements of Synchrotron Light: For Biology, Chemistry, and Medical Research*. Oxford University Press, New York.
- Margaritondo, G. and Tromba, G. (1999). Coherence-based edge diffraction sharpening of x-ray images: A simple model. *J. Appl. Phys.*, 85:3406–3408.
- Marks, J. (2007). Airway clearance devices in cystic fibrosis. *Paed. Resp. Rev.*, 8:17–23.
- Massig, J. H. (1999). Measurement of phase objects by simple means. *Appl. Optics*, 38:4103–4105.
- Mayo, S. C. and Sexton, B. (2004). Refractive microlens array for wave-front analysis in the medium to hard x-ray range. *Opt. Lett.*, 29:866–868.
- McAuley, D. and Elborn, J. (2000). Cystic fibrosis: Basic science. *Paed. Resp. Rev.*, 1:93–100.
- McDonald, S. A., Marone, F., Hintermuller, C., Mikuljan, G., David, C., Pfeiffer, F., and Stamparoni, M. (2009). Advanced phase-contrast imaging using a grating interferometer. *J. Synchrotron Radiat.*, 16:562–572.
- Menk, R. (1999). Interference imaging and its application to material and medical imaging. *Nucl. Phys. B-Proc. Sup.*, 78:604–609.
- Miao, J., Charalambous, P., Kirz, J., and Sayre, D. (1999). Extending the methodology of x-ray crystallography to allow imaging of micrometre-sized non-crystalline specimens. *Nature*, 400:342–343.
- Michelson, A. A. (1995). *Studies in Optics*. Chicago Press, reprinted by Dover Publications Inc.
- Misell, D. L. (1973). A method for the solution of the phase problem in electron microscopy. *J. Phys. D: Appl. Phys.*, 6:L6–L9.
- Mollenhauer, J., Aurich, M. E., Zhong, Z., Muehleman, C., Cole, A. A., Hasnah, M., Oltulu, O., Kuettner, K. E., Margulis, A., and Chapman, L. D. (2002). Diffraction-enhanced x-ray imaging of articular cartilage. *Osteoartr. Cartilage*, 10:163–171.
- Momose, A. (2002). Phase-contrast x-ray imaging based on interferometry. *J. Synchrotron Radiat.*, 9:136–142.
- Momose, A., Kawamoto, S., Koyama, I., Hamaishi, Y., Takai, K., and Suzuki, Y. (2003). Demonstration of x-ray Talbot interferometry. *Jpn. J. Appl. Phys.*, 42:L866–L868.
- Momose, A., Takeda, T., and Itai, Y. (1995). Phase-contrast x-ray computed tomography for observing biological specimens and organic materials. *Rev. Sci. Instrum.*, 66:1434–1436.

- Momose, A., Takeda, T., and Itai, Y. (2000). Blood vessels: Depiction at phase contrast x-ray imaging without contrast agents in the mouse and rat-feasibility study. *Radiology*, 17:593–596.
- Momose, A., Takeda, T., Itai, Y., Yoneyama, A., and Hirano, K. (1998). Phase-contrast tomographic imaging using an x-ray interferometer. *J. Synchrotron Radiat.*, 5:309–314.
- Momose, A., Takeda, T., Yoneyama, A., Koyama, I., and Itai, Y. (2001). Wide-area phase-contrast x-ray imaging using large x-ray inteferometers. *Nucl. Instrum. Meth. A*, 467:917–920.
- Momose, A., Yashio, W., Takeda, Y., Suzuki, Y., and Hattori, T. (2006). Phase tomography by x-ray Talbot interferometry for biological imaging. *Jpn. J. Appl. Phys.*, 45:5254–5262.
- Momose, A., Yashiro, W., Kuwabara, H., and Kawabata, K. (2009). Grating-based x-ray phase imaging using multiline x-ray source. *Jpn. J. Appl. Opt.*, 48:076512.
- Morgan, K. S., Irvine, S. C., Suzuki, Y., Uesugi, K., Takeuchi, A., Paganin, D. M., and Siu, K. K. W. (2010a). Measurement of hard x-ray coherence in the presence of a rotating random-phase-screen diffuser. *Opt. Commun.*, 283:216–225.
- Morgan, K. S., Paganin, D. M., Parsons, D. W., Donnelley, M., Yagi, N., Uesugi, K., Suzuki, Y., Takeuchi, A., and Siu, K. K. W. (2009). Optimising coherence properties for phase contrast x-ray imaging (PCXI) to reveal airway surface liquid (ASL) as an airway health measure. *IFMBE Proc.*, 2502:135–138.
- Morgan, K. S., Paganin, D. P., and Siu, K. K. W. (2011). Quantitative x-ray phase contrast imaging using a single grating of comparable pitch to sample feature size. *Opt. Lett.*, 36:55–57.
- Morgan, K. S., Siu, K. K. W., and Paganin, D. M. (2010b). The projection approximation and edge contrast for x-ray propagation-based phase contrast imaging of a cylindrical edge. *Opt. Express*, 18:9865–9878.
- Morgan, K. S., Siu, K. K. W., and Paganin, D. M. (2010c). The projection approximation versus an exact solution for x-ray phase contrast imaging, with a plane wave scattered by a dielectric cylinder. *Opt. Commun.*, 283:4601–4608.
- Myers, G. R., Gureyev, T. E., Paganin, D. M., and Mayo, S. C. (2008a). The binary dissector: Phase contrast tomography of two- and three-material objects from few projections. *Opt. Express*, 16:16736–16749.
- Myers, G. R., Mayo, S. C., Gureyev, T. E., Paganin, D. M., and Wilkins, S. W. (2007). Polychromatic cone-beam phase-contrast tomography. *Phys. Rev. A*, 76:045804.
- Myers, G. R., Paganin, D. M., Gureyev, T. E., and Mayo, S. C. (2008b). Phase-contrast tomography of single-material objects from few projections. *Opt. Express*, 16:908–919.
- Nesterets, Y. (2008). On the origins of decoherence and extinction contrast in phase-contrast imaging. *Opt. Commun.*, 281:533–542.
- Neuhäusler, U., Schneider, G., Ludwig, W., Meyer, M. A., Zschech, E., and Hambach, D. (2003). X-ray microscopy in Zernike phase contrast mode at 4keV photon energy with 60 nm resolution. *J. Phys. D: Appl. Phys.*, 36:A79–A82.

- Nieto-Vesperinas, M. (2006). *Scattering and Diffraction in Physical Optics*. World Scientific Publishing, New Jersey, 2nd edition.
- NIST (Accessed March, 2007). Physical reference data. <http://physics.nist.gov/PhysRefData/XrayMassCoef/cover.html>.
- Nugent, K., Tran, C., and Roberts, A. (2003). Coherence transport through imperfect x-ray optical systems. *Opt. Express*, 11:2323–2328.
- Nugent, K. A. (2010). Coherent methods in the x-ray sciences. *Adv. Phys.*, 59:1–99.
- Nugent, K. A., Guryev, T. E., Cookson, D. F., Paganin, D., and Barnea, Z. (1996). Quantitative phase imaging using hard x-rays. *Phys. Rev. Lett.*, 77:2961–2964.
- Olivo, A., Rigon, L., Vinnicombe, S. J., Cheung, K. C., Ibison, M., and Speller, R. D. (2009). Phase contrast imaging of breast tumours with synchrotron radiation. *Appl. Radiat. Isot.*, 67:1033–1041.
- Paganin, D., Mayo, S. C., Guryev, T. E., Miller, P. R., and Wilkins, S. W. (2002). Simultaneous phase and amplitude extraction from a single defocused image of a homogeneous object. *J. Microsc.*, 206:33–40.
- Paganin, D. and Nugent, K. A. (1998). Noninterferometric phase imaging with partially coherent light. *Phys. Rev. Lett.*, 80:2586–2589.
- Paganin, D. M. (2006). *Coherent X-ray Optics*. Oxford University Press, New York.
- Parkinson, D. Y., McDermott, G., Etkin, L. D., Le Gros, M. A., and Larabell, C. A. (2008). Quantitative 3-D imaging of eukaryotic cells using soft x-ray tomography. *J. Struct. Biol.*, 162:380–386.
- Parsons, D. (2005). Airway gene therapy and cystic fibrosis. *J. Paediatr. Child Health*, 41:94–96.
- Parsons, D. W., Hopkins, P. J., Bourne, A. J., Boucher, R. C., and Martin, A. J. (2000). Airway gene transfer in mouse nasal-airways: Importance of identification of epithelial type for assessment of gene transfer. *Gene Ther.*, 7:1810–1815.
- Parsons, D. W., Morgan, K., Donnelley, M., Fouras, A., Crosbie, J., Williams, I., Boucher, R. C., Uesugi, K., Yagi, N., and Siu, K. K. W. (2008). High-resolution visualization of airspace structures in intact mice via synchrotron phase-contrast x-ray imaging (PCXI). *J. Anat.*, 213:217–227.
- Paterson, D., Allman, B. E., McMahon, P. J., Lin, J., Moldovan, N., Nugent, K. A., McNulty, I., Chantler, C. T., Retsch, C. C., Irving, T. H. K., and Mancini, D. C. (2001). Spatial coherence measurement of x-ray undulator radiation. *Opt. Commun.*, 195:79–84.
- Pavlov, K. M., Gureyev, T. E., Paganin, D., Nesterets, Y. I., Morgan, M. J., and Lewis, R. A. (2004). Linear systems with slowly varying transfer functions and their application to x-ray phase-contrast imaging. *J. Phys. D: Appl. Phys.*, 37:2746–2750.
- Perciante, C. D. and Ferrari, J. A. (2000). Visualization of two-dimensional phase gradients by subtraction of a reference periodic pattern. *Appl. Optics*, 39:2081–2083.

- Pfeiffer, F., Bunk, O., David, C., Bech, M., Le Duc, G., Bravin, A., and Cloetens, P. (2007). High-resolution brain tumor visualization using three-dimensional x-ray phase contrast tomography. *Phys. Med. Biol.*, 52:6923–6930.
- Pfeiffer, F., Weitkamp, T., Bunk, O., and David, C. (2006). Phase retrieval and differential phase-contrast imaging with low-brilliance x-ray sources. *Nature Physics*, 2:258–261.
- Press, W. H., Flannery, B. P., Teukolsky, S. A., and Vetterling, W. T. (1992). *Numerical Recipes in C: The Art of Scientific Computing*. Cambridge University Press, Cambridge, 2nd edition.
- Quiney, H. M. (2010). Coherent diffractive imaging using short wavelength light sources. *J. Mod. Opt.*, 57:1109–1149.
- Robinson, I. K., Kenney-Benson, C. A., and Vartanyants, I. A. (2003). Sources of decoherence in beamline optics. *Physica B: Condens. Matter*, 336:56–62.
- Röntgen, W. C. (1896). On a new kind of rays. *Nature*, 53(59):274–277.
- Saleh, B. E. A. and Teich, B. C. (1991). *Fundamentals of Photonics*. Wiley Interscience, New York.
- Salomé, M., Peyrin, F., Cloetens, P., Odet, C., Laval-Jeantet, A., Baruchel, J., and Spanne, P. (1999). A synchrotron radiation microtomography system for the analysis of trabecular bone samples. *Med. Phys.*, 26:2194–2204.
- Schmahl, G., Rudolph, D., Schneider, G., Guttman, P., and Niemann, B. (1994). Phase contrast x-ray microscopy studies. *Optik*, 97:181–182.
- Schuster, D., Kovacs, A., Garbow, J., and Piwnica-Worms, D. (2004). Recent advances in imaging the lungs of intact small animals. *Am. J. Respir. Cell. Mol. Biol.*, 30:129–38.
- Sera, T., Uesugi, K., and Yagi, N. (2005). Refraction-enhanced tomography of mouse and rabbit lungs. *Med. Phys.*, 32:2787–2792.
- Sherman, G. C. (1967). Application of the convolution theorem to Rayleigh's integral formulas. *J. Opt. Soc. Am.*, 57:546–547.
- Siu, K. K. W., Morgan, K. S., Paganin, D. M., Boucher, R., Uesugi, K., Yagi, N., and Parsons, D. W. (2008). Phase contrast x-ray imaging for the non-invasive detection of airway surfaces and lumen characteristics in mouse models of airway disease. *Eur. J. Radiol.*, 68:S22–6.
- Snigirev, A., Snigireva, I., Kohn, V., Kuznetsov, S., and Schelokov, I. (1995). On the possibilities of x-ray phase contrast microimaging by coherent high-energy synchrotron radiation. *Rev. Sci. Instrum.*, 66:5486–5492.
- Song, Y., Thiagarajah, J., and Verkman, A. S. (2003). Sodium and chloride concentrations, pH, and depth of airway surface liquid in distal airways. *J. Gen. Physiol.*, 122:511–519.

- Stevenson, A. W., Gureyev, T. E., Paganin, D., Wilkins, S. W., Weitkamp, T., Snigirev, A., Rau, C., Snigireva, I., Youn, H. S., Dolbnya, I. P., Yun, W., Lai, B., Garrett, R. F., Cookson, D. J., Hyodo, K., and Ando, M. (2003). Phase-contrast x-ray imaging with synchrotron radiation for materials science applications. *Nucl. Instrum. Meth. B*, 199:427–435.
- Stevenson, A. W., Mayo, S. C., Häusermann, D., Maxsimenko, A., Garrett, R. F., Hall, C. J., Wilkins, S. W., Lewis, R. A., and Myers, D. E. (2009). First experiments on the Australian Synchrotron Imaging and Medical beamline, including investigations of the effective source size in respect of x-ray imaging. *J. Synchrotron Radiat.*, 17:75–80.
- Suzuki, Y. (2004). Measurement of x-ray coherence using two-beam interferometer with prism optics. *Rev. Sci. Instrum.*, 75:1026–1029.
- Suzuki, Y., Takeuchi, A., and Harada, K. (2010). X-ray holographic microscopy by double-prism interferometer. *Jpn. J. Appl. Opt.*, 49:16601.
- Suzuki, Y., Uesugi, K., Takimoto, N., Fukui, T., Aoyama, K., and Takeuchi, A. (2004). Construction and commissioning of a 248 m long beamline with x-ray undulator light source. *AIP Conf. Proc.*, 705:344–347.
- Suzuki, Y., Yagi, N., and Uesugi, K. (2002). X-ray refraction-enhanced imaging and a method for phase retrieval for a simple object. *J. Synchrotron Radiat.*, 9:160–165.
- Takeda, M., Ina, H., and Kobayashi, S. (1982). Fourier-transform method of fringe-pattern analysis for computer-based tomography and interferometry. *J. Opt. Soc. Am. A*, 72:156–160.
- Takeda, T., Momose, A., Hirano, K., Haraoka, S., Watanabe, T., and Itai, Y. (2000). Human carcinoma: Early experience with phase-contrast x-ray CT with synchrotron radiation—comparative specimen study with optical microscopy. *Radiology*, 214:298–301.
- Takeda, T., Momose, A., Ueno, E., and Itai, Y. (1998). Phase-contrast x-ray CT image of breast tumor. *J. Synchrotron Radiat.*, 5:1133–1135.
- Takeda, T., Momose, A., Wu, J., Zeniya, T., Yu, Q., and Itai, Y. (2001). Phase-contrast x-ray computed tomography of non-formalin fixed biological objects. *Nucl. Instrum. Meth. A*, 467:1322–1325.
- Takeda, Y., Yashiro, W., Hattori, T., Takeuchi, A., Suzuki, Y., and Momose, A. (2008). Differential phase x-ray imaging microscopy with x-ray Talbot interferometer. *Appl. Phys. Express*, 1:117002.
- Takeda, Y., Yashiro, W., Suzuki, Y., and Momose, A. (2007). X-ray phase microtomography by single transmission grating. *AIP Conf. Proc.*, 879:1361–1364.
- Tarran, R., Grubb, B., and Parsons, D. (2001). The CF salt controversy: In vivo observations and therapeutic approaches. *Mol. Cell*, 8:149–158.
- Teague, M. R. (1983). Deterministic phase retrieval: a Green's function solution. *J. Opt. Soc. Am. A*, 73:1434.

- Thomlinson, W. (1992). Medical applications of synchrotron radiation. *Nucl. Instrum. Meth. A*, 319:295–304.
- Tonelli, M. and Aitken, M. (2001). New and emerging therapies for pulmonary complications of cystic fibrosis. *Drugs*, 61:1379–1385.
- Tromba, G., Longo, R., Abrami, A., Arfelli, F., Begant, P., Brun, F., Casarin, K., Chenda, V., Dreossi, D., Hola, M., Kaiser, J., Mancini, L., Menk, R. H., Quai, E., Quai, E., Rigon, L., Rokvic, T., Sodini, N., Sanabor, D., Schultke, E., Tonutti, M., Vascotto, A., Zanconati, F., Cova, M., and Castelli, E. (2010). The SYRMEP beamline of ELETTRA: Clinical mammography and bio-medical applications. *AIP Conf. Proc.*, 1266:18–23.
- Turner, L. D., Dhal, B. B., Hayes, J. P., Mancuso, A. P., Nugent, K. A., Paterson, D., Scholten, R. E., Tran, C. Q., and Peele, A. G. (2004). X-ray phase imaging: Demonstration of extended conditions with homogeneous objects. *Opt. Express*, 12:2960–2965.
- van Cittert, P. (1939). Kohärenz-probleme. *Physica*, 6(7-12):1129–1138.
- van Cittert, P. H. (1934). Die Wahrscheinliche Schwingungsverteilung in Einer von Einer Lichtquelle Direkt Oder Mittels Einer Linse Beleuchteten Ebene. *Physica*, 1(1-6):201–210.
- Vartanyants, I. A. and Robinson, I. K. (2003). Origins of decoherence in coherent x-ray diffraction experiments. *Opt. Commun.*, 222:29–50.
- Wark, P., McDonald, V., and Jones, A. (2006). Nebulised hypertonic saline for cystic fibrosis (review). *The Cochrane Collaboration*.
- Weitkamp, T., Diaz, A., David, C., Pfeiffer, F., Stampanoni, M., Cloetens, P., and Ziegler, E. (2005). X-ray phase imaging with a grating interferometer. *Opt. Express*, 13:6296–6304.
- Welsh, M. and Smith, A. (1995). Cystic fibrosis. *Scientific American*, 273(6):52–59.
- Wen, H. H., Bennett, E. E., Kopace, R., Stein, A. F., and Pai, V. (2010). Single-shot x-ray differential phase-contrast and diffraction imaging using two-dimensional transmission gratings. *Opt. Lett.*, 35:1932–1934.
- Westneat, M. W., Betz, O., Blob, R. W., Fezzaa, K., Cooper, W. J., and Lee, W.-K. (2003). Tracheal respiration in insects visualised with synchrotron x-ray imaging. *Science*, 24:555–580.
- Weyl, H. (1919). Ausbreitung elektromagnetischer Wellen über einem ebenen Leiter. *Ann. Phys.*, 60:481–500.
- White, D. L., Wood, O. R., Bjorkholm, J. E., Spector, S., MacDowell, A. A., and LaFontaine, B. (1994). Modification of the coherence of undulator radiation. *Rev. Sci. Instrum.*, 66:1930–1933.
- Wilkins, S. W., Gureyev, T. E., Gao, D., Pogany, A., and Stevenson, A. W. (1996). Phase-contrast imaging using polychromatic hard x-rays. *Nature*, 384:335–338.
- Williams, G. J., Quiney, H. M., Dhal, B. B., Tran, C. Q., Nugent, K. A., Peele, A. G., Paterson, D., and de Jonge, M. D. (2006). Fresnel coherent diffractive imaging. *Phys. Rev. Lett.*, 97:025506.

- Winthrop, J. T. and Worthington, C. R. (1966). Convolution formulation of Fresnel diffraction. *J. Opt. Soc. Am.*, 56:588–591.
- Wolf, E. (1954). Optics in terms of observable quantities. *Il Nuovo Cimento*, 12:884–888.
- Wolf, E. (2007). *Introduction to the Theory of Coherence and Polarization of Light*. Cambridge University Press, New York.
- Yabashi, M., Tamasaku, K., and Ishikawa, T. (2001). Characterisation of the transverse coherence of hard synchrotron radiation by intensity interferometry. *Phys. Rev. Lett.*, 87:140801.
- Yagi, N., Suzuki, Y., Umetani, K., Kohmura, Y., and Yamasaki, K. (1999). Refraction-enhanced x-ray imaging of mouse lung using synchrotron radiation source. *Med. Phys.*, 26:2190–2193.
- Yashiro, W., Takeda, Y., Takeuchi, A., Suzuki, Y., and Momose, A. (2009). Hard-x-ray phase-difference microscopy using a Fresnel zone plate and a transmission grating. *Phys. Rev. Lett.*, 103:180801.
- Young, T. (1804). The bakerian lecture: Experiments and calculations relative to physical optics. *Phil. Trans. R. Soc. London*, 94:1–16.
- Zernike, F. (1938). The concept of degree of coherence and its application to optical problems. *Physica*, 5:785–795.
- Zernike, F. (1942). Phase contrast, a new method for the microscopic observation of transparent objects. *Physica*, 7:686–698.



# **Appendices: Supplementary Papers on PCXI of the Airways**



---

## Appendix A

*Optimising Coherence Properties for Phase Contrast X-ray Imaging (PCXI) to reveal Airway Surface Liquid (ASL) as an Airway Health Measure.*

by K. S. Morgan, D. M. Paganin, D. W. Parsons, M. Donnelley, N. Yagi, K. Uesugi, Y. Suzuki, A. Takeuchi and K. K. W. Siu.

Published in IFMBE Proceedings **25**, pp. 135-138, 2009.

---

This paper was published in IFMBE and is made available as an electronic reprint with the permission of Springer. The paper can be found at the following URL on the Springer website: <http://www.springerlink.com/content/t7u56476qm05678w/>. Systematic or multiple reproduction or distribution to multiple locations via electronic or other means is prohibited and is subject to penalties under law.

---

### Declaration for Appendix A, work supplementary to Thesis Chapter 6

In the case of Appendix A, contributions to the work involved the following:

Name	% contribution	Nature of contribution
Kaye Morgan	80%	Contributed to the original live imaging experiments, led the phantom imaging and diffuser placement imaging, the numerical simulations, image analysis, and wrote up the paper
David Paganin		Provided supervisory advice, aided proofreading and drafting
David Parsons		Provided the context for the imaging problem, led the live imaging aspects of the diffuser placement experiments
Martin Donnelley		Contributed to the live imaging aspects of the diffuser placement experiments
Naoto Yagi		Contributed to the original experiments
Kentaro Uesugi		Contributed to the original experiments
Yoshio Suzuki		Contributed to the original experiments
Akihisa Takeuchi		Contributed to the original experiments
Karen Siu		Contributed to the live imaging, phantom and diffuser placement experiments, provided supervisory advice, aided proofreading and drafting

### Declaration by co-authors

The undersigned hereby certify that:

1. the above declaration correctly reflects the nature and extent of the candidate's contribution to this work, and the nature of the contribution of each of the co-authors.
2. they meet the criteria for authorship in that they have participated in the conception, execution, or interpretation, of at least that part of the publication in their field of expertise;
3. they take public responsibility for their part of the publication, except for the responsible author who accepts overall responsibility for the publication;
4. there are no other authors of the publication according to these criteria;
5. potential conflicts of interest have been disclosed to (a) granting bodies, (b) the editor or publisher of journals or other publications, and (c) the head of the responsible academic unit; and
6. the original data are stored at the following location(s) and will be held for at least five years from the date indicated below: School of Physics and Monash Centre for Synchrotron Science, Clayton Campus, Monash University, Australia.

### Signatures:

Kaye Morgan:		Date: 18/10/10
David Paganin:		Date: 19/10/10
David Parsons:		Date: 15-10-10
Martin Donnelley:		Date: 18-10-10
Naoto Yagi:		Date: 18/10/10
Kentaro Uesugi:		Date: 18/10/10
Yoshio Suzuki:		Date: 18/10/10
Akihisa Takeuchi:		Date: 18/10/10
Karen Siu:		Date: 19.10.10.

## Optimising Coherence Properties for Phase Contrast X-Ray Imaging (PCXI) to Reveal Airway Surface Liquid (ASL) as an Airway Health Measure

K.S. Morgan<sup>1</sup>, D.M. Paganin<sup>1</sup>, D.W. Parsons<sup>2</sup>, M. Donnelley<sup>2</sup>, N. Yagi<sup>3</sup>, K. Uesugi<sup>3</sup>, Y. Suzuki<sup>3</sup>,  
A. Takeuchi<sup>3</sup>, and K.K.W. Siu<sup>1,4</sup>

<sup>1</sup> School of Physics, Monash University, Victoria, 3800, Australia

<sup>2</sup> Women's and Children's Hospital Adelaide, Adelaide, 5006, Australia

<sup>3</sup> Japan Synchrotron Radiation Research Institute (JASRI), SPring-8, Hyogo 679-5198, Japan

<sup>4</sup> Monash Centre for Synchrotron Science, Victoria, 3800, Australia

**Abstract**—We demonstrate the potential of PCXI in achieving a non-invasive measure of airway health, for the assessment of new therapies for cystic fibrosis (CF). In particular, the advantages to an increased transverse coherence length are studied, revealing sharper and more detailed phase contrast fringes, well-suited to phase retrieval algorithms. Through the application of these algorithms, the depth of the ASL, a key measure of airway health, may be revealed. This will enable medical researchers at the Women's and Children's Hospital in Adelaide, Australia, to immediately receive feedback from the CF treatment delivery site in the airways, rather than waiting for the disease to develop in the lungs, as required previously.

**Keywords**—Phase contrast imaging, synchrotron, x-rays.

### I. INTRODUCTION AND MOTIVATION

Cystic fibrosis (CF) is a recessive genetic condition, caused by the CFTR gene defect [1]. This is seen in many ways, the most debilitating of which is associated airway disease. Mucus retention, airway obstruction and inflammation continually degrade the health of the airways and lungs, resulting in a decreased quality of life for sufferers and almost always death early in adulthood. Current treatment options, such as antibiotics to control the infection and physiotherapy to clear the chest, are short-term. The condition of the lungs continually worsens, requiring regular visits to hospital. However, work done by Dr David Parsons and collaborators from the Women's and Children's Hospital in Adelaide offers potential for a cure, using an airway gene transfer method [2].

In order to develop this treatment, a good measure of airway health is required. Previous assessment of airway health has been indirect, commonly by observation of deficits in lung function [3], hence requiring months or years for changes due to treatment to propagate and to develop in the biological system. The aim is to measure the airway health in a more direct way, through observation of the actual treatment site, so that real-time feedback may be achieved.

A key concept in our assessment of therapies is the airway surface liquid (ASL). This is a salty water coating on the inside of an airway, a sufficient depth of which is critical in maintaining clear airways. The ASL allows cilia along the airway surface to be active in clearing debris to protect the lungs. Dr Parsons has already observed a decreased depth in ASL as a result of an airway cell ion imbalance, as produced by the CFTR gene defect [4]. An effective treatment for CF airway disease should result in an increase in ASL depth, restoring the ability of the cilia to clear debris.

The aim of the present work is to image mouse airways before, during and after treatment in a time sequence, to continually observe the ASL depth. Preliminary testing can use short-term, well-known treatments, such as hypertonic saline, to observe changes in ASL depth. Mouse models include C57 (normal) mice, Fabp mice who have the CFTR gene deficiency and BetaENaC mice who show CF-like symptoms.

The challenge is then to image airways in a way so that changes of around 3 $\mu$ m may be measured in both the upper airway 7-10 $\mu$ m ASL depth and the tracheal 50 $\mu$ m ASL depth of mice [5].

### II. PHASE CONTRAST IMAGING OF THE AIRWAYS

Phase contrast x-ray imaging (PCXI) is a novel, non-invasive technique which uses not only the absorption of x-rays through different materials, but also the relative refractive indices of materials to give enhanced image contrast over using absorption information alone [6, 7]. As an incident wave passes through a material, the amplitude decreases according to the attenuation coefficient of the material. The intensity of the transmitted wave will be observed as the squared magnitude of the complex amplitude, so different regions of material will transmit waves of different intensities, and at boundaries between these regions phase

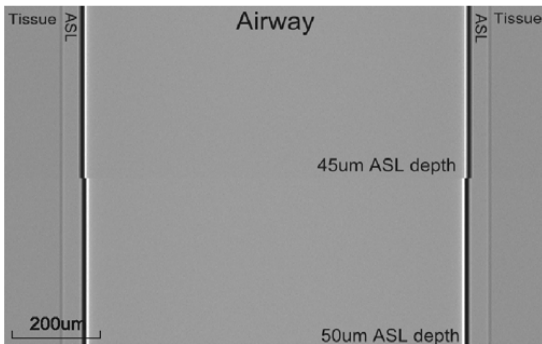


Fig. 1 Computer simulation of x-ray phase contrast imaging of a 1mm wide airway with 45/50µm ASL, showing both the air/ASL and the ASL/tissue interfaces, with 0.45 micron pixels

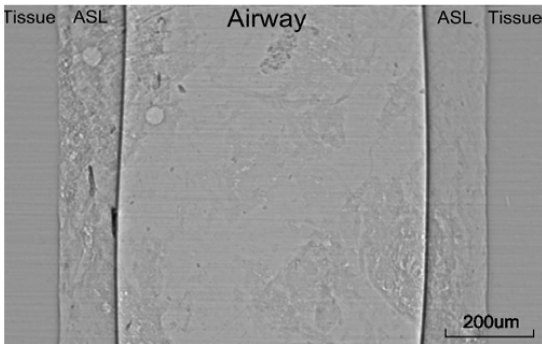


Fig. 2 Phase contrast image of 1mm wide perspex airway model, showing both interfaces, as in simulation results. Imaged with 0.45 micron pixels

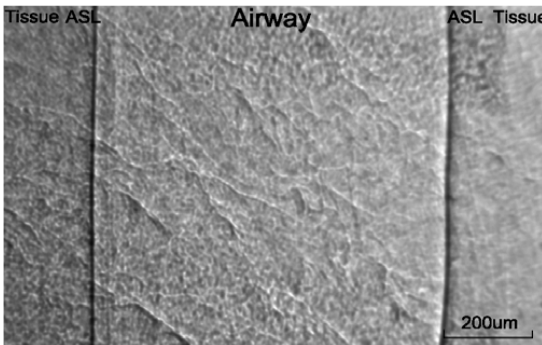


Fig. 3 Phase contrast image of a mouse trachea, with only the air/ASL interface seen clearly. Skin texture is seen overlying the image, and hairless mice are used to prevent images of hair, confounding the visibility of the ASL. Imaged with 0.45 micron pixels

shift will occur. Although regions with different refractive indices will incur different phase changes, these will not be directly observable. In order to use the extra information given by phase variations, they must be converted into intensity variations. In this case, this is done using propagation based phase contrast [6, 7, 8].

In this coherent x-ray imaging technique, a significant (centimeters to meters) distance is introduced between the imaged object and the detector. This allows the modified diffracted [9] wave at the boundaries to interfere during propagation, causing a bright/dark fringe pattern in the image where the boundary occurs between two material of different refractive indices.

This makes PCXI particularly suited to imaging soft tissue, where the absorption of adjoining tissues may be similar, but the real part of the refractive indices are different. The phase contrast fringe at a boundary between air and liquid is particularly visible in phase contrast images, recommending the technique for this application. The fine resolution in real time required to detect ASL changes of only a few micron in a 1mm diameter airway is enabled through phase contrast imaging with synchrotron x-rays. Imaging was performed using medical imaging beamline 20XU at the SPring-8 synchrotron in Japan [10, 11]. A 1m propagation distance between the airway and the detector is chosen. This balances the need for highly visible fringes (seen with longer propagation) with sufficiently narrow fringes (seen with shorter propagation) so that fine detail may be observed and the two sets of fringes do not overlap.

Figure 1 shows a simulated airway image, used in determining the optimal propagation distance. It can be seen in the simulation that the interface between the airway and ASL is of higher visibility than that between ASL and tissue. This is because the difference in refractive index is greater between air and ASL than between ASL and tissue.

The two interfaces are also seen in phantom imaging (Fig. 2), where a simple perspex model of an airway is imaged using the synchrotron source. A block of Perspex models the tissue, with a 1mm diameter hole interiorly coated with Vaseline as the airway. From this image, the ASL depth should simply be given by the distance between the airway/ASL fringe set and the ASL/tissue fringe set.

However, when imaging a live mouse airway, the ASL/tissue interfaces are not clearly visible, as in Fig 3. This is due to both the additional overlying tissue textures and a more complicated interface, which means that the step in refractive index is not as sharp.

In order to bring out this interface and enable measurement of the ASL, a highly coherent source is desired. A long coherence length is important in producing strong, sharp phase contrast fringes. Light with a short coherence length, such as that produced by an extended source, will

effectively blur the image. While it is not probable that an ASL/tissue fringe set will be revealed with the same clarity as in phantom imaging, optimization of the imaging conditions, in particular the coherence, offers promise in revealing sufficient information for the ASL depth to be recovered.

During imaging, a field of view of around 2mm by 1.5mm is required to observe a sufficient image of the airway. This is enabled through selection of the collimating slits through which the source is seen and through the use of a diffuser. A diffuser is a spinning piece of paper which is placed in front of the beam to even out the field, reducing fluctuations due to movement in the electron beam of the synchrotron. It also blurs out phase gradients introduced by beamline elements such as the beryllium window.

The use of the diffuser, effectively a random phase screen, means that the degree of transverse coherence of the beam is decreased [12]. The effective source size also affects the coherence of the beam, where a small source (or narrow collimating slits) results in a longer transverse coherence length. However, moving the collimating slits closer together will decrease the field of view. Less flux also results in the need for longer exposure times, which can become a problem in live imaging, introducing blur due to animal movement. There must therefore be a balance between a large imaging field of view and a high degree of coherence.

Figure 4 shows that the removal of the diffuser from the imaging set-up (increasing the degree of transverse coherence) results in a significant increase in the number of observable fringes at each boundary. While only two bright fringes are seen with the diffuser present (Fig. 4 (a)), when it is removed up to ten bright fringes are visible (Fig. 4 (b)).

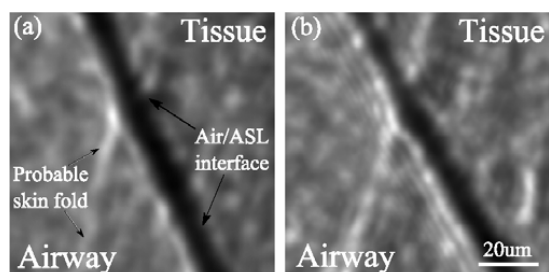


Fig. 4 (a) Mouse trachea edge imaged with a diffuser present, showing a single light/dark fringe at the interface, (b) Mouse trachea edge imaged without a diffuser present, with more detailed fringes seen, imaged with 0.18 micron pixels

The addition of detailed fringes means that an interface is more easily identified within the surrounding speckle. The

information provided by the detailed fringes in Fig. 4 (b) is valuable in techniques such as phase retrieval. Phase retrieval algorithms take information about the intensity of a wave and apply constraints such as the refractive index and position of the sample to reconstruct an image of the wave phase at the exit surface of the sample. This can then reveal the projected thickness of the imaged object.

Preliminary application of a single-material phase retrieval algorithm [13] to an intensity image (eg. Fig. 4(b)) suggests that a region may be identified in the expected position of the ASL, as in Fig. 5. A bright stripe, which has a width approximately equal to that expected of the ASL, is seen in the image at the airway edge, whereas the phase contrast fringe which was running in the opposite diagonal direction, most probably due to a skin fold, shows a simple step. The stripe, which is not obvious in the phase contrast image, may be seen in this phase retrieval, resulting in a more readily interpretable image.

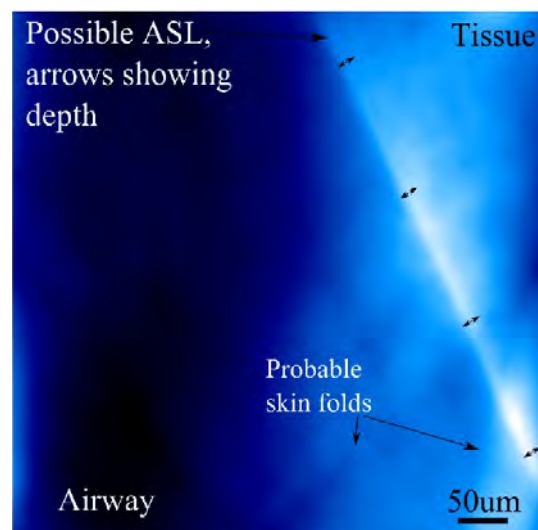


Fig. 5 Phase retrieved from an expanded region of Fig 4 (b), showing a possible ASL region, imaged with 0.18 micron pixels

The ability to quantify this ASL depth will enable examination of the airway changes in response to treatment over time. There are challenges arising from in-vivo imaging, such as the reduction of exposures times to minimize blur due to movement. Also, the imaging of different airways, high in the nasal passages or lower towards the lung, will change the overlying tissue textures. Nevertheless, PCXI lends itself to this application, with promising results regarding the observation of the airway surface liquid.

### III. CONCLUSIONS

Through optimization of the synchrotron imaging set-up to increase coherence, and use of specialized image analysis techniques such as phase retrieval, information about the airway surface may be revealed. This will be of immense value if it permits the non-invasive, real-time observation of the effectiveness of treatments for CF and other airway diseases.

### ACKNOWLEDGMENT

Kaye Morgan recognizes support by an Australian Post-graduate Award, a Monash University JL William Scholarship and a Cystic Fibrosis Australia Studentship. Studies supported in part by the NH&MRC Australia, USA CF Foundation and philanthropic donors via Cure4CF. SPring-8 experiments conducted under proposal 2008A1334 and 2008B1985. DMP acknowledges the Australian Research Council.

### REFERENCES

1. Welsh MJ, Smith AE (1995) Cystic Fibrosis, *Scientific American* 273:52-59
2. Limberis M, Anson DS, Fuller M, Parsons DW (2002) Recovery of airway cystic fibrosis transmembrane conductance regulator function in mice with cystic fibrosis after single-dose lentivirus-mediated Gene transfer. *Human Gene Therapy* 13:1961-70 DOI 10.1089/10430340260335365
3. Copley SJ, Padley SP (2001) High-resolution CT of paediatric lung disease. *Eur Radiol.* 11(12):2564-75 DOI 10.1007/s003300100865
4. Tarran R, Grubb BR, Parsons D, Picher M, Hirsh AJ, Davis CW, Boucher RC (2001) The CF salt controversy: In vivo observations and therapeutic approaches. *Molecular Cell* 8:149-158 DOI 10.1016/S1097-2765(01)00286-6
5. Song Y, Thiagarajah J, Verkman AS (2003) Sodium and chloride concentrations, pH, and depth of airway surface liquid in distal airways. *J Gen Physiol.* 122(5):511-519 DOI 10.1085/jgp.200308866
6. Snigirev A, Snigirev I (1995) On the possibilities of x-ray phase contrast microimaging by coherent high-energy synchrotron radiation. *Rev. Sci. Instrum.* 66:5486 DOI 10.1063/1.1146073
7. Wilkins SW, (1996) Phase-contrast imaging using polychromatic hard x-rays. *Nature* 384:335-338 DOI 10.1038/384335a0
8. Cloetens P, Ludwig W, Baruchel J (1999) Hard x-ray phase imaging using simple propagation of a coherent synchrotron radiation beam. *J. Phys. D: Appl. Phys.* 32:A145-A151.
9. Keller JB (1962) Geometrical theory of diffraction. *J. Opt. Soc. Of Am*
10. Parsons DW, Morgan K, Donnelley M, Fouras A, Crosbie J, Williams I, Boucher R, Uesugi K, Yagi N, Siu KKW (2008) High-resolution visualization of airspace structures in intact mice via synchrotron phase-contrast X-ray imaging (PCXI). *J. Anat.* DOI 10.1111/j.1469-7580.2008.00950.x
11. Siu KKW, Morgan KS, Paganin DM, Boucher R, Uesugi K, Yagi N, Parsons DW (2008) Phase contrast X-ray imaging for the non-invasive detection of airway surfaces and lumen characteristics in mouse models of airway disease. *Eur. J. of Radiol.* DOI 10.1016/j.era.2008.04.029
12. Morgan KS, Irvine, SC, Suzuki Y, Uesugi K, Takeuchi A, Paganin DM, Siu KKW (submitted Feb 2009 to Optics Communications) Measurement of hard-x-ray coherence in the presence of a rotating random-phase-screen diffuser.
13. Paganin D, Mayo SC, Gureyev TE, Miller PR, Wilkins SW (2002) Simultaneous phase and amplitude extraction from a single defocused image of homogeneous object. *J. Microscopy.* DOI 10.1046/j.1365-2818.2002.01010.x

Author: Kaye Morgan  
 Institute: Monash University  
 Street: Clayton Campus, Wellington Road  
 City: Clayton 3800  
 Country: Australia  
 Email: Kaye.Morgan@sci.monash.edu.au

---

## Appendix B

*Phase contrast x-ray imaging for the non-invasive detection of airway surfaces and lumen characteristics in mouse models of airway disease.*

by K. K. W. Siu, K. S. Morgan, D. M. Paganin, R. Boucher, K. Uesugi, N. Yagi and D. W. Parsons.

Published in the European Journal of Radiology **68S**, pp. S22-S26, 2008.

---

This paper was published in the European Journal of Radiology and is made available as an electronic reprint with the permission of Springer. The paper can be found on the Elsevier website under doi 10.1016/j.ejrad.2008.04.029. Systematic or multiple reproduction or distribution to multiple locations via electronic or other means is prohibited and is subject to penalties under law.

---

### Declaration for Appendix B, work supplementary to Thesis Chapter 6

In the case of Appendix B, contributions to the work involved the following:

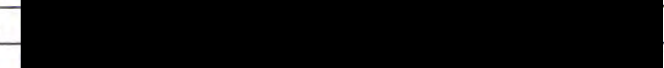
Name	% contribution	Nature of contribution
Karen Siu		Contributed to the original CT and live imaging experiments, the data analysis and visualisation and wrote up the paper
Kaye Morgan	20%	Contributed to the original live imaging experiments, image processing, numerical simulations and proofreading
David Paganin		Contributed to planning for the numerical simulations, aided proofreading
Richard Boucher		Contributed to the context of the imaging problem and planning
Kentaro Uesugi		Contributed to the original experiments
Naoto Yagi		Contributed to the original experiments
David Parsons		Provided the context of the imaging problem, contributed to the original CT and live imaging experiments, interpretation of data and the write-up

#### Declaration by co-authors

The undersigned hereby certify that:

1. the above declaration correctly reflects the nature and extent of the candidate's contribution to this work, and the nature of the contribution of each of the co-authors.
2. they meet the criteria for authorship in that they have participated in the conception, execution, or interpretation, of at least that part of the publication in their field of expertise;
3. they take public responsibility for their part of the publication, except for the responsible author who accepts overall responsibility for the publication;
4. there are no other authors of the publication according to these criteria;
5. potential conflicts of interest have been disclosed to (a) granting bodies, (b) the editor or publisher of journals or other publications, and (c) the head of the responsible academic unit; and
6. the original data are stored at the following location(s) and will be held for at least five years from the date indicated below: School of Physics and Monash Centre for Synchrotron Science, Clayton Campus, Monash University, Australia.

#### Signatures:

Karen Siu:		Date: 19.10.2010.
Kaye Morgan:		Date: 18/10/10
David Paganin:		Date: 15-10-10
Richard Boucher:		Date:
Kentaro Uesugi:		Date: 18/10/10
Naoto Yagi:		Date: 18/10/10
David Parsons:		Date: 15-10-10



## Phase contrast X-ray imaging for the non-invasive detection of airway surfaces and lumen characteristics in mouse models of airway disease

K.K.W. Siu<sup>a,b,\*</sup>, K.S. Morgan<sup>a</sup>, D.M. Paganin<sup>a</sup>, R. Boucher<sup>c</sup>,  
K. Uesugi<sup>d</sup>, N. Yagi<sup>d</sup>, D.W. Parsons<sup>e,f,g</sup>

<sup>a</sup> School of Physics, Monash University, Victoria 3800, Australia

<sup>b</sup> Monash Centre for Synchrotron Science, Monash University, Victoria 3800, Australia

<sup>c</sup> CF Research and Treatment Center, University of North Carolina at Chapel Hill, USA

<sup>d</sup> SPring-8/JASRI, Hyogo 679-5198, Japan

<sup>e</sup> Department of Pulmonary Medicine, Women's and Children's Hospital, South Australia 5006, Australia

<sup>f</sup> Department of Paediatrics, University of Adelaide, South Australia, 5006, Australia

<sup>g</sup> Women's and Children's Health Research Institute, South Australia, 5006, Australia

Received 15 April 2008; accepted 25 April 2008

### Abstract

We seek to establish non-invasive imaging able to detect and measure aspects of the biology and physiology of surface fluids present on airways, in order to develop novel outcome measures able to validate the success of proposed genetic or pharmaceutical therapies for cystic fibrosis (CF) airway disease. Reduction of the thin airway surface liquid (ASL) is thought to be a central pathophysiological process in CF, causing reduced mucociliary clearance that supports ongoing infection and destruction of lung and airways. Current outcome measures in animal models, or humans, are insensitive to the small changes in ASL depth that ought to accompany successful airway therapies. Using phase contrast X-ray imaging (PCXI), we have directly examined the airway surfaces in the nasal airways and tracheas of anaesthetised mice, currently to a resolution of  $\sim 2 \mu\text{m}$ . We have also achieved high resolution three-dimensional (3D) imaging of the small airways in mice using phase-contrast enhanced computed tomography (PC-CT) to elucidate the structure-function relationships produced by airway disease. As the resolution of these techniques improves they may permit non-invasive monitoring of changes in ASL depth with therapeutic intervention, and the use of 3D airway and imaging in monitoring of lung health and disease. Phase contrast imaging of airway surfaces has promise for diagnostic and monitoring options in animal models of CF, and the potential for future human airway imaging methodologies is also apparent.

© 2008 Elsevier Ireland Ltd. All rights reserved.

**Keywords:** Cystic fibrosis; Airway surface; Phase contrast imaging; Computed tomography; Synchrotron

### 1. Introduction

Cystic fibrosis (CF) is a genetic condition which, despite advances in ameliorative treatments, remains a debilitating disease for which there is no cure or long-lasting therapy. This means a substantial and progressively decreased quality of life for many sufferers, eventually resulting in death for many from lung failure in early adulthood. This single group of patients in the community imposes substantial resourcing and financing burdens on federal, state and community health services. For example, in 1 year at the Women's and Children's Hospital,

Adelaide, Australia, approximately 21% of the hospital's annual drug needs were devoted to approximately 150 CF children and youths.

The underlying problems in CF organ diseases are due to a defective gene, CFTR, which in lung causes dysfunction of the airway-cell ion-balance across the apical (lumen-facing) cell surface. The end result is a reduction of the depth/volume of the airway surface liquid (ASL) [1], a thin film of fluid that overlies airway cells. In this environment the normal mucociliary clearance (MCC) mechanism that maintains airway health is defective, so unstoppable infection, tissue damage, and eventual lung failure occurs. Compromised MCC function is also a hallmark of other common airspace diseases such as chronic bronchitis, asthma, and chronic obstructive pulmonary disease (COPD). Correction of the defective CFTR gene should return

\* Corresponding author. Tel.: +61 3 99054922; fax: +61 3 99053637.  
E-mail address: Karen.Siu@sync.monash.edu.au (K.K.W. Siu).

ASL depth to, or sufficiently towards, normal levels, providing a rational basis for a lifelong cure. Members of our group are developing corrective gene-delivery vectors in normal and CF transgenic mice [2,3] as well as other animals.

A major practical limitation in CF animal model research is the inability to non-invasively measure the functional effects and longevity of airway gene correction. If an ultimate use in humans is envisaged, a successful assessment tool must also be feasible for airways of children with CF without causing harm, and must also be repeatable to track effect persistence. Most importantly, there must be sufficient spatial resolution (to less than 1  $\mu\text{m}$ ) to detect any increase in ASL depth that ought to correlate with the correction of CFTR ion-channel activity resulting from the CFTR gene-transfer process [4,5]. Currently, animal researchers have one relatively invasive electrophysiological measurement available to test for improved CFTR function [6], while clinical researchers must wait many months, or years, to know if treatment has been successful. The primary outcome measure in humans is lung function tests (spirometry) but changes are small and slow to appear. Such delayed and indirect measures are inadequate for rapid assessment of therapeutic CFTR corrective gene expression and its longevity.

We report here on pilot studies assessing synchrotron-based phase contrast X-ray imaging (PCXI) as a novel and effective measure of airway health in mouse models. PCXI utilizes changes in the phase of propagating X-rays as they traverse a sample to greatly enhance image contrast. The resulting image contrast can be several orders of magnitude larger than that produced by conventional (absorption) X-ray imaging [7]. While absorption contrast effectively maps the density distribution of tissues, phase contrast imaging is particularly sensitive to the boundaries between different tissues. X-ray phase changes at boundaries manifest as intensity changes in the final image, due to the very slight deviations in the X-ray propagation direction. In the propagation-based variant of PCXI, this results in visible edge enhancement in which a characteristic bright “fringe” appears near tissue interfaces, provided the distance between the sample and the detector is sufficiently large (tens of centimetres to several metres apart) [8–10]. This enhancement has been exploited for imaging of the airways, and in particular, for imaging the airway lumen/ASL/tissue boundary.

We have also used PCXI in conjunction with computed tomography (PC-CT) [11,12] to provide three-dimensional (3D) data with greatly enhanced soft tissue contrast of the highly complex mouse nasal airways. This is the primary site for gene therapy assessment (using electrophysiological recording) in transgenic CF mouse models, since the lungs in mice do not display the pathophysiology of CF. We demonstrate that PC-CT can reveal these soft tissue structures with great clarity, to enhance our knowledge of mouse nasal anatomy and permit targeting of the correct epithelial tissue.

## 2. Materials and methods

All animal imaging was conducted at the Biomedical Imaging Centre of the SPring-8 synchrotron in Hyogo, Japan, using propagation based PCXI, under approvals from the SPring-8 Animal

Ethics Committee and the Women’s and Children’s Hospital Adelaide Animal Ethics Committee, and the supervision of the facility Chief Bioscientist (NY).

For live imaging of the airways (nasal passages and trachea), Nembutal-anaesthetised C57Bl/6 mice ( $\sim 20$  gm) were imaged at beamline 20XU using a monochromatic beam of 25 keV ( $\lambda = 0.5 \text{ \AA}$ ) and a propagation distance of 100 cm. Mice were anaesthetised using Pentobarbital i.p. (45 mg/kg) and fur was removed over the imaging regions using commercial depilatory cream, to prevent the hair interfering with the image clarity. Mice were secured, head high, using a stereotactic frame; the dorsal incisors were hooked onto a stainless-steel wire loop and metal bars were positioned in the ear canals to hold the head still during respiratory movements. Horizontal rotation of the stereotactic frame permitted both ventro-dorsal and lateral views. Depth of anaesthesia was monitored, and was maintained by additional anaesthetic injections via a syringe driver when necessary. Mice remained anaesthetised and were humanely killed by overdose after imaging was completed.

Images were acquired using a Hamamatsu phosphor coupled to a CCD camera (0.45  $\mu\text{m}$  pixels, 1.8(H) mm  $\times$  1.2(V) mm field of view) at 10–30 s intervals (100 ms exposure). Baseline images were acquired for 5 min duration, prior to 5 min of nebulisation treatment with hypertonic saline (HS) (7%) delivered by an AeroLab nebuliser (3.32  $\mu\text{m}$  MMD) known to increase the ASL depth [13], followed by  $\sim 35$  min of continued imaging. Captured images were conventionally corrected for dark current offset and flat field non-uniformity.

For mouse CT images, data was acquired at beamline 20B2 using a monochromatic beam of 17 keV ( $\lambda = 0.7 \text{ \AA}$ ) and a propagation distance of 65 cm. Mice were humanely killed by Pentobarbital overdose, and a dummy  $\sim 350 \mu\text{m}$  diameter polyethylene recording cannula was inserted at specified depths into one nostril. Mice were firmly restrained in plastic tubes during data acquisition. A CCD camera with an effective pixel size of 12  $\mu\text{m}$  ( $2 \times 2$  binning) was used to acquire projection images with a maximum field of view of  $\sim 23$ (H) mm  $\times$  15(V) mm, necessitating CT acquisition in several vertical sections to acquire data for the entire mouse head. CT reconstruction was performed using a filtered backprojection algorithm with a Haning filter.

## 3. Results and discussion

Nasal or tracheal imaging clearly revealed the airway surfaces, enhanced by phase contrast effects. Fig. 1(a) indicates the nasal area of interest for assessment of gene transfer effects. This region was well suited to imaging at these high resolutions since movement artefacts were minimal. As is typical of PCXI, the soft tissue interfaces are rendered particularly conspicuous, with the nostrils, sinuses and nasopharynx easily discernible. Viewing the sequence of images from the total  $\sim 45$  min acquisition period as a time-lapse reconstruction clearly revealed the dynamic nature of airway surfaces, and material was noted transiting the airway surface. Fig. 1(b–e) is a small subset from one of these image sequences, in which the transport of surface-bound objects along the airway surface was detected at speeds

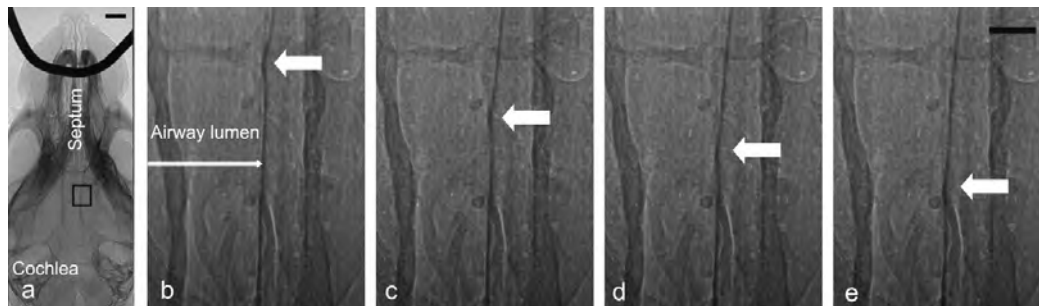


Fig. 1. (a) Area of interest for CF gene therapy, indicated with black square (scale bar = 1 mm) and (b–e) a high resolution image sequence of this area indicating the MCC of surface debris (arrows, scale bar = 100  $\mu\text{m}$ ). The interval between each frame is 30 s.

consistent with MCC rates likely to be present under deep Pentobarbital anaesthesia. Such sensitivity towards airway surface activity suggests a potential role in non-invasively detecting the early small alterations in mucus presence thought to accompany the beginnings of CF airway disease in the small airways of young children. Since MCC should also be improved if the CF gene defect is corrected, detection of mucus presence and movement may also provide an alternate or complementary method to assess the success of gene delivery if our attempts to directly measure ASL depth are not successful. The potential for similar approaches to assess other airspace diseases characterised by compromised MCC are also apparent.

To determine the effectiveness of treatment with HS, expected to increase the ASL depth, and thus decrease the overall airway width, image sequences were analysed by determining the airway width as a function of time. These studies were restricted to nasal imaging sequences because tracheal image sequences often suffered from unacceptable movement artefacts or overlapping anatomy obscuring the airway edges. Since the edge enhancement produced by PCXI produces a characteristic bright/dark fringe at the airway surface interface, the minima in the first derivative of a smoothed horizontal intensity profile were used to consistently identify the airway edges. The distance between these airway-wall fringes was calculated over the entire image height and the resulting median width measurement from each image was recorded as a function of time post-treatment, relative to the initial airway width. Three of seven mice treated with HS showed decreases in airway width of 0.5–1% (S.D. = 0.2%). This would be equivalent to an increase in ASL depth of the order of approximately 2–5  $\mu\text{m}$ ; a 2  $\mu\text{m}$  change is similar to the difference in ASL depth that has been reported between normal and null transgenic CF [5].

The results of airway width measurements were not consistent. The remaining four mice given nasal HS treatment underwent unexpectedly large variations over short periods (5–10 min), both increasing and decreasing in magnitude. In some cases, increases in apparent airway width were as much as 5–15% (S.D. = 2%) above the initial width; changes of this magnitude are highly unlikely to be from changes in the ASL alone. Active airway contraction is an effect sometimes apparent in humans given nebulised HS [14]. In addition, it was

apparent though unexpected that gross fluid bubbles/foam could form in the airways as a result of HS nebulisation, and these bubble edges will confound our automated measurement system.

Despite these uncertainties, it is apparent that PCXI has both the temporal and spatial resolution for direct, *in vivo* detection of MCC and ASL changes. It is likely that the simple measure of airway width change described here is not sufficiently sensitive to be a reliable measure of ASL changes. Although the edge-enhancement offered by PCXI vastly increases visibility of the airway surface, there are in fact two interfaces involved in this analysis: the airway lumen-ASL interface, and the ASL-tissue interface. Simulated data indicate that the fringes arising from these two interfaces can be distinguished, albeit with some difficulty since the ASL is a very thin layer of liquid with very similar composition to the soft tissues, which offers the possibility of deriving a quantitative measure of the ASL depth from the fringe characteristics (Fig. 2).

High resolution PCXI can also be combined with computed tomography (CT) to provide high resolution 3D rendering of the airways. Fig. 3 displays an example of the exquisite soft-

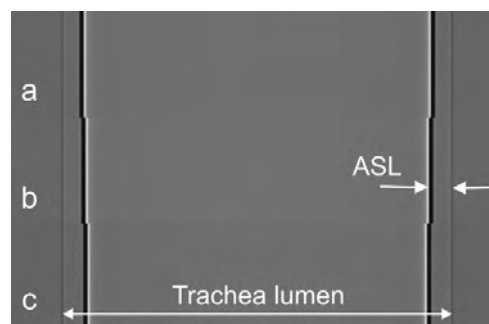


Fig. 2. Simulation of phase contrast images from a simple model of the trachea assuming a cylindrical airway (1 mm diameter) surrounded by homogeneous tissue, with an airway surface liquid layer of (a) 45  $\mu\text{m}$  depth, (b) 50  $\mu\text{m}$  depth, and (c) 55  $\mu\text{m}$  depth. Data was simulated using an X-ray energy of 25 keV, propagation distance of 100 cm, at 245 m from the finite source size (1100(H)  $\mu\text{m}$   $\times$  25(V)  $\mu\text{m}$  FWHM), additive Poisson noise, and a detector pixel size of 0.45  $\mu\text{m}$ .



Fig. 3. Volume rendering of a mouse head from PC-CT data. The top quadrant of the mouse head has been “cut away” digitally to reveal the small nasal passages, the clinical target area for CF therapies in transgenic mouse models of airway disease.

tissue delineation possible using high resolution PCXI coupled with tomographic reconstruction techniques (volume rendering prepared using VolView 2.0, Kitware Inc.). In this example the top quadrant of the mouse head has been “cut away” digitally to reveal the small nasal passages, the therapeutic target area for testing potential therapies in the transgenic CF mouse. Tomographic reconstruction was applied to PCXI images as for conventional absorption contrast CT, using a filtered backprojection algorithm. Since each interface, particularly air-tissue boundaries are enhanced in PCXI, the resulting volume rendering permits striking visualisation of both high-density bones and soft tissues, simultaneously. Other anatomical features, such as the skin, whiskers and fur hair are also highlighted with clarity and detail.

Measurement of mouse airway gene transfer is performed electrophysiologically using a fine fluid-perfused cannula inserted into the mouse nostril, so we inserted dummy cannulas to specified depths to mimic the critical depth-placement required. With this approach we wished to determine which regions (and therefore cell types) a cannula would reach [6]. Although data capture took approximately 1 h, this was a considerable improvement over the many months needed for anatomical characterisation using standard histological sectioning. The location of the cannula tip could be examined *in situ*, and the underlying cell types examined using the known distribution of cell types [15] and by correlated histological staining if required. Improved cannula placement can then be arranged. The PCXI-CT data also revealed that cannula insertion to 2.5 mm avoided damage to the deeper fragile nasal turbinates, and the tip remained in the medio-dorsal regions of the airway where the target respiratory epithelium is found.

#### 4. Conclusion

These pilot experiments have demonstrated that PCXI offers a non-invasive, rapid and readily repeatable (within radiation dose limitations) means of assessing the efficacy and longevity therapies for respiratory diseases. With further development and attention to radiation dose this approach could eventually be applied for use in human diagnostics and therapeutic monitoring. Airway surfaces were rendered with sufficient contrast and spatial and temporal resolution to observe MCC activity, and the airway width changes noted after aerosol treatment indicates the technique could provide quantitative assessment of ASL depth change. Phase contrast enhanced CT data also shows great promise in characterising soft tissue nasal structures at high resolution, and can be used to improve electrophysiological monitoring of potential CF airway gene therapies.

#### Acknowledgements

The authors gratefully acknowledge the support of the National Health and Medical Research Council (Australia), the Access to Major Research Facilities Program (Australia), and the Cystic Fibrosis Foundation (USA). The rapid and generous support of corporate and individual sponsors to the Adelaide CF Gene Therapy Group allowed these studies to begin. We are also grateful to M. Donnelley for comments on the manuscript.

#### Conflict of interest

All authors declare that they have no conflicts of interest.

#### References

- [1] Roomans GM, Kozlova I, Nilsson H, et al. Measurements of airway surface liquid height and mucus transport by fluorescence microscopy, and of ion composition by X-ray microanalysis. *J Cyst Fibros* 2004;3(Suppl 2):135–9.
- [2] Koldej R, Cmielewski P, Stocker A, et al. Optimisation of a multipartite human immunodeficiency virus based vector system; control of virus infectivity and large-scale production. *J Gene Med* 2005;7:1390–9.
- [3] Limberis M, Anson DS, Fuller M, et al. Recovery of airway cystic fibrosis transmembrane conductance regulator function in mice with cystic fibrosis after single-dose lentivirus-mediated gene transfer. *Hum Gene Ther* 2002;13:1961–70.
- [4] Song Y, Thiagarajah J, Verkman AS. Sodium and chloride concentrations, pH, and depth of airway surface liquid in distal airways. *J Gen Physiol* 2003;122:511–9.
- [5] Tarran R, Grubb BR, Parsons D, et al. The CF salt controversy: in vivo observations and therapeutic approaches. *Mol Cell* 2001;8:149–58.
- [6] Parsons DW, Hopkins PJ, Bourne AJ, et al. Airway gene transfer in mouse nasal-airways: importance of identification of epithelial type for assessment of gene transfer. *Gene Ther* 2000;7:1810–5.
- [7] Lewis RA. Medical phase contrast X-ray imaging: current status and future prospects. *Phys Med Biol* 2004;49:3573–83.
- [8] Wilkins SW, Gureyev TE, Gao D, et al. Phase-contrast imaging using polychromatic hard X-rays. *Nature* 1996;384:338–1338.
- [9] Suzuki Y, Yagi N, Uesugi K. X-ray refraction-enhanced imaging and a method for phase retrieval for a simple object. *J Synchrotron Radiat* 2002;9:160–5.
- [10] Snigirev A, Snigireva I, Kohn V, et al. On the possibilities of X-ray phase contrast microimaging by coherent high-energy synchrotron radiation. *Rev Sci Instrum* 1995;66:5486–92.

- [11] Cloetens P, Ludwig W, Baruchel J, et al. Holotomography: quantitative phase tomography with micrometer resolution using hard synchrotron radiation X-rays. *Appl Phys Lett* 1999;75:2912–4.
- [12] Gureyev TE, Paganin DM, Myers GR, et al. Phase-and-amplitude computer tomography. *Appl Phys Lett* 2006;89:034101–2.
- [13] Daviskas E, Anderson SD. Hyperosmolar agents and clearance of mucus in the diseased airway. *J Aerosol Med* 2006;19:100–9.
- [14] Rodwell LT, Anderson SD. Airway responsiveness to hyperosmolar saline challenge in cystic fibrosis: a pilot study. *Pediatr Pulmonol* 1996;21:282–9.
- [15] Mery S, Gross EA, Joyner DR, et al. Nasal diagrams: a tool for recording the distribution of nasal lesions in rats and mice. *Toxicol Pathol* 1994;22:353–72.



---

## Appendix C

*High-resolution visualization of airspace structures in intact mice via synchrotron phase-contrast x-ray imaging (PCXI).*

by David W. Parsons, Kaye Morgan, Martin Donnelley, Andreas Fouras, Jeffrey Crosbie, Ivan Williams, Richard C. Boucher, Kentaro Uesugi, Naoto Yagi and Karen K. W. Siu.

Published in the Journal of Anatomy **213**, pp. 217-227, 2008.

---

This paper was published in the Journal of Anatomy and is made available as an electronic reprint with the permission of Blackwell Publishing. The paper can be found at the following URL on the Wiley website: <http://onlinelibrary.wiley.com/doi/10.1111/j.1469-7580.2008.00950.x/abstract>. Systematic or multiple reproduction or distribution to multiple locations via electronic or other means is prohibited and is subject to penalties under law.

---

### Declaration for Appendix C, work supplementary to Thesis Chapter 6

In the case of Appendix C, contributions to the work involved the following:

Name	% contribution	Nature of contribution
David Parsons		Provided the context for the imaging problem, contributed to the planning and original CT and live imaging experiments, data analysis and wrote up the paper
Kaye Morgan	10%	Contributed to the planning and original CT and live imaging experiments, image processing and 3D render movie visualisation and proofreading
Martin Donnelley		Contributed to the planning and original live imaging experiments, data analysis and the write-up
Andreas Fouras		Contributed to the original CT and live imaging experiments
Jeffrey Crosbie		Contributed to the original CT and live imaging experiments
Ivan Williams		Contributed to the original CT and live imaging experiments
Richard Boucher		Contributed to the context of the imaging problem and planning
Kentaro Uesugi		Contributed to the original experiments
Naoto Yagi		Contributed to the original experiments
Karen Siu		Contributed to the planning and original CT and live imaging experiments, image processing and 3D render still image visualisation and the write-up

#### Declaration by co-authors

The undersigned hereby certify that:

1. the above declaration correctly reflects the nature and extent of the candidate's contribution to this work, and the nature of the contribution of each of the co-authors.
2. they meet the criteria for authorship in that they have participated in the conception, execution, or interpretation, of at least that part of the publication in their field of expertise;
3. they take public responsibility for their part of the publication, except for the responsible author who accepts overall responsibility for the publication;
4. there are no other authors of the publication according to these criteria;
5. potential conflicts of interest have been disclosed to (a) granting bodies, (b) the editor or publisher of journals or other publications, and (c) the head of the responsible academic unit; and
6. the original data are stored at the following location(s) and will be held for at least five years from the date indicated below: School of Physics and Monash Centre for Synchrotron Science, Clayton Campus, Monash University, Australia.

#### Signatures:

David Parsons:		Date: 15-10-10
Kaye Morgan:		Date: 18/10/10
Martin Donnelley:		Date: 18-10-10
Andreas Fouras:		Date: 19/10/10
Jeff Crosbie:		Date: 20/10/10
Ivan Williams:		Date: 19-10-2010
Richard Boucher:		Date: 15-10-10
Kentaro Uesugi:		Date: 19-10-2010
Naoto Yagi:		Date: 19-10-2010
Karen Siu:		Date: 19.10.2010



## METHODS

## High-resolution visualization of airspace structures in intact mice via synchrotron phase-contrast X-ray imaging (PCXI)

David W. Parsons,<sup>1,2,3</sup> Kaye Morgan,<sup>4</sup> Martin Donnelley,<sup>1</sup> Andreas Fouras,<sup>5</sup> Jeffrey Crosbie,<sup>4,6</sup> Ivan Williams,<sup>4</sup> Richard C. Boucher,<sup>7</sup> Kentaro Uesugi,<sup>8</sup> Naoto Yagi<sup>8</sup> and Karen K. W. Siu<sup>4,6</sup>

<sup>1</sup>Department of Pulmonary Medicine, Women's and Children's Hospital

<sup>2</sup>Department of Paediatrics, University of Adelaide

<sup>3</sup>Women's & Children's Child Health Research Institute, Adelaide

<sup>4</sup>School of Physics; <sup>5</sup>Division of Biological Engineering; and <sup>6</sup>Monash Centre for Synchrotron Science, Monash University, Victoria, Australia

<sup>7</sup>CF Research and Treatment Center, University of North Carolina at Chapel Hill, NC, USA

<sup>8</sup>Spring-8/JASRI, Hyogo, Japan

### Abstract

Anatomical visualization of airspace-containing organs in intact small animals has been limited by the resolution and contrast available from current imaging methods such as X-ray, micro-computed tomography and magnetic resonance imaging. Determining structural relationships and detailed anatomy has therefore relied on suitable fixation, sectioning and histological processing. More complex and informative analyses such as orthogonal views of an organ and three-dimensional structure visualizations have required different animals and image sets, laboriously processed to gather this complementary structural information. Precise three-dimensional anatomical views have always been difficult to achieve in small animals. Here we report the ability of phase-contrast synchrotron X-ray imaging to provide detailed two- and three-dimensional visualization of airspace organ structures in intact animals. Using sub-micrometre square pixel charge-coupled device array detectors, the structure and anatomy of hard and soft tissues, and of airspaces, is readily available using phase-contrast synchrotron X-ray imaging. Moreover, software-controlled volume-reconstructions of tomographic images not only provide unsurpassed image clarity and detail, but also selectable anatomical views that cannot be obtained with established histological techniques. The morphology and structure of nasal and lung airways and the middle ear are illustrated in intact mice, using two- and three-dimensional representations. The utility of phase-contrast synchrotron X-ray imaging for non-invasively localizing objects implanted within airspaces, and the detection of gas bubbles transiting live airways, are other novel features of this visualization methodology. The coupling of phase-contrast synchrotron X-ray imaging technology with software-based reconstruction techniques holds promise for novel and high-resolution non-invasive examination of airspace anatomy in small animal models.

**Key words** airspaces micro CT; airway surface; imaging; mice; non-invasive; phase-contrast; synchrotron; X-ray.

### Introduction

In developing airway gene transfer procedures for the treatment of cystic fibrosis airway disease, we seek new approaches to non-invasive detection of airway health and disease in live mouse models.

#### Correspondence

Dr D. W. Parsons, Department of Pulmonary Medicine, Women's and Children's Hospital, 72 King William Road, North Adelaide, South Australia.  
E: david.parsons@cywhs.sa.gov.au

Accepted for publication 8 April 2008

Although traditional light and electron microscopy histological methods are used to produce high-resolution images and measurements of airway structure in animal models, they require invasive tissue sampling and are usually terminal procedures. In humans, similar levels of histological analysis are possible via invasive biopsy, but often require anaesthesia and are not suited to repeat assessment to track, for example, the durability of a therapeutic treatment. The non-invasive options for intact imaging in humans, such as ultrasound, diagnostic X-ray, high-resolution spiral CT, and standard or hyperpolarized-helium MRI provide an extraordinary range of complementary

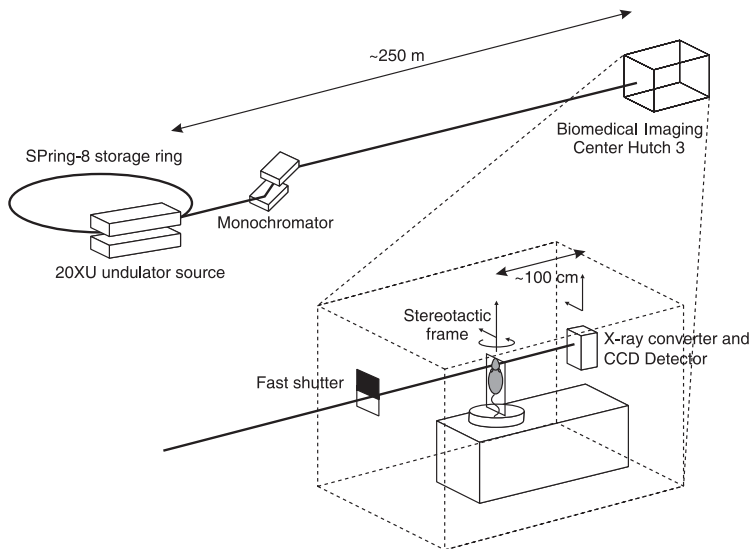


**Fig. 1** Arrangement for synchrotron imaging of mouse airway *in vivo*, or post-mortem (for CT slices). Mice were held vertically and the beam directed through the mouse as required for 2D or CT imaging. Rotation of the stereotactic frame was provided remotely via the baseplate. For CT slice imaging mice were constrained in a plastic tube.

information. However, when directed towards small animal model systems, these methods lack adequate contrast and they have poor spatial and temporal resolution. Laboratory X-ray imaging systems designed for small animals provide improved resolution, but airspace structures are poorly detected, contrast remains low, and high resolution scans can involve lengthy image capture and processing times.

Phase-contrast imaging utilizes X-ray refraction effects, in addition to conventional absorption, to create image contrast. It is particularly useful for soft tissue contrast, where the absorption differences are small, and tissue boundaries are enhanced by phase effects due to variations in refractive indices. Propagation-based phase contrast X-ray imaging (PCXI) is the simplest method, rendering phase effects visible as intensity changes by utilizing an increased distance between the sample and the detector (Fig. 1). The technique demands a source with high coherence (i.e. the source size is sufficiently small or, equivalently, the incident X-rays may be considered parallel). This requirement is easily realized using a synchrotron X-ray source, particularly at long beamlines such as those at the Biomedical Imaging Centre at the SPring-8 synchrotron in Japan (Gotto et al. 2001).

PCXI can provide the substantially increased resolution and contrast needed for non-invasive imaging in small animals. Soft tissues and airspaces such as airways and lungs can now be imaged and processed to give clarity of images that is similar to that provided by bone. Here we reveal the capability of this method for use in anatomical study via two- and three-dimensional imaging in selected mouse airspace organs.

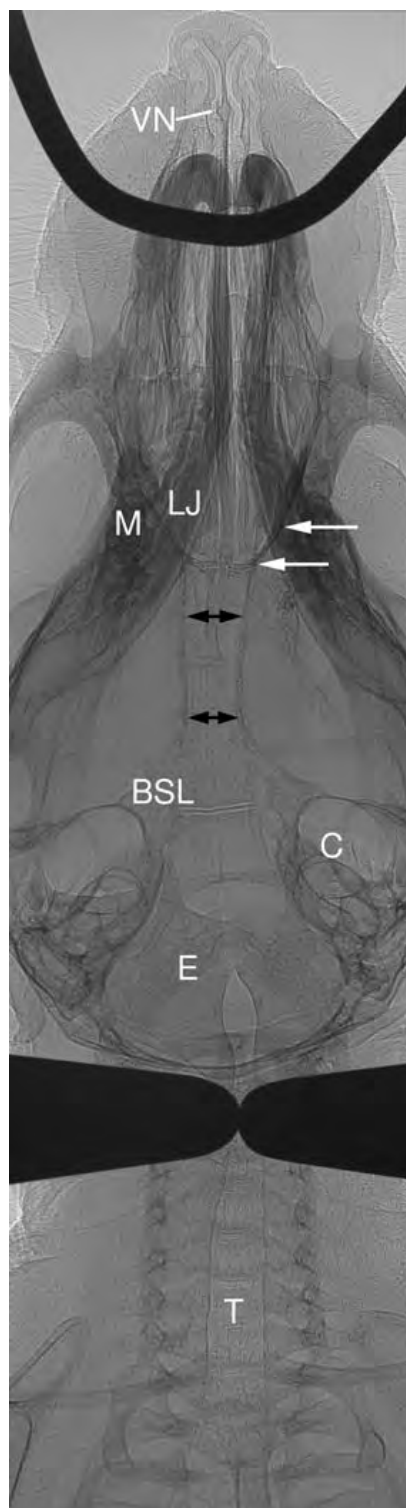
## Materials and methods

Adult C57Bl/6 mice weighing 18–20 g were imaged under approvals from the Animal Ethics Committee of SPring-8, and of the Women's and Children's Hospital, CYWHS, Adelaide. All PCXI images were collected at the Biomedical Imaging Centre, SPring-8 Synchrotron facility, Hyogo, Japan. Live mice were anaesthetized with nembutal (45 mg kg<sup>-1</sup>, i.p.). Post-mortem mice were imaged fresh (Figs 2, 3) or at room temperature after having been kept chilled for up to 2 days (4 °C, and passive rewarming over several hours – Figures and supplementary material numbered 5, 6, and 7). Fur produced very strong phase-contrast effects, but removal with depilatory cream prior to imaging improved the clarity of the two-dimensional images.

### Two-dimensional airway studies in live and post-mortem mice

Figure 1 shows the Biomedical Imaging Beamline layout at SPring-8. Post-mortem, or anaesthetized, mice (Fig. 4) were secured head-high in a stereotaxic frame. The dorsal incisors were hooked over a stainless-steel wire loop and metal bars were positioned at the rear of the skull or in the external ear canal to minimize respiratory movements during live imaging. The torso was supported from below with foam blocks placed under the hindquarters. The depth of anaesthesia was monitored by foot pinch and changes in respiration, and when required, top-up injections were given at half the starting dose of nembutal. Mice remained anaesthetized until humanely killed by nembutal overdose (approximately 500 mg kg<sup>-1</sup> i.p.) at the end of each imaging study.

Two dimensional studies were conducted on the undulator Beamline BL20XU where the imaging hutch is located 245 m from the storage ring. Monochromatic X-rays of 25 keV ( $\lambda = 0.5\text{\AA}$ ) were selected using a standard double-crystal monochromator. At the imaging station, the beam size was approximately 10 (H)  $\times$  6 (V) mm. The restraint frame was mounted on the imaging baseplate, which permitted translations perpendicular to the beam direction



and rotation in the horizontal plane. The beam was directed dorso-ventrally through the mouse to image the nasal airways and lower airways, using a propagation (sample to detector) distance of 100–150 cm. Images were captured using a high-resolution X-ray converter (10 mm diameter field of view: AA50 and AA40P Hamamatsu Photonics) with a charge-coupled device (CCD) detector. The converter used a scintillator ( $\text{Lu}_2\text{SiO}_5:\text{Ce}$ ) to convert X-rays to visible light, which was then directed to the CCD using a microscope objective lens. Two detectors were used: C4742-98-24ER ( $1344 \times 1024$  with  $6.6 \mu\text{m}$  native pixel size, Hamamatsu Photonics), and a pco. 4000 ( $4000 \times 2672$  with  $9 \mu\text{m}$  native pixel size, PCO Imaging). By changing a combination of the X-ray converter, its objective lens and the CCD used, effective pixel sizes between  $6.6 \mu\text{m}$  (objective lens magnification,  $\times 1$ , AA40P, C4742-98-24ER) and  $0.45 \mu\text{m}$  ( $\times 20$ , AA50, pco4000) square were available. Exposure times between 100 ms and 300 ms were used; with the shorter time it was possible to minimize movement artefact whilst maintaining an adequate signal to noise ratio for the smaller pixel size detector.

In addition, as some regions of interest (ROI) were larger than the CCD field of view the (post-mortem) mice were translated through the beam in a grid pattern to form a raster-scan of multiple images (e.g. Figs 2, 3). All captured images were conventionally corrected for dark-current offset and flat-field non-uniformity before being digitally tiled to form a composite image. A raster scan of  $2 \text{ (H)} \times 6 \text{ (V)}$  images using the  $6.6 \mu\text{m}$  pixel detector allowed viewing of the entire length of the adult mouse head and trachea, whilst similar sized rasters with an effective pixel of  $0.45 \mu\text{m}$  (i.e.  $\times 20$  magnification, AA50 X-ray converter and pco4000 CCD) were used to view the airways in detail.

### Three-dimensional studies – ultra high-resolution CT slices, and volume reconstructions

Mice were humanely killed using nembutal overdose, then drawn into a securely fitting (30 mL) plastic syringe barrel by a loop of thread secured around their upper incisors. This imaging system limited slow body and organ shifting during the longer imaging periods required for these CT studies (between 30 and 90 min). Data were acquired with mice held upright at the bending magnet Beamline 20B2 using a monochromatic beam of 17 keV ( $\lambda = 0.7 \text{ \AA}$ ) and a propagation distance of 65 cm. In some mice a small diameter polyethylene recording cannula was inserted to a depth of 2.5 mm or 5 mm into one nostril, to test the ability to direct the cannula tip to specific regions of airway epithelium. Projection images were acquired using the AA60 X-ray Converter

**Fig. 2** Low resolution ( $6 \times 6 \mu\text{m}$  pixel detector) image of adult mouse post-mortem showing the oral and nasal airways of the head. Nostrils, septum and the ventral septum expansion housing the vomeronasal organ (VN) associated with pheromone detection are clear. The loop of 500  $\mu\text{m}$  diameter stainless steel wire suspends the mouse via its upper incisors within the restraint frame. The lower jaw (LJ) and molar teeth (M) are shown. One side of the lateral/posterior edge of the olfactory turbinate region is indicated by white open arrows. Double-ended black arrows indicate the nasopharyngeal airway below the brain. BSL is a ventral bone suture line containing cartilage (see Discussion; a smaller similar suture is present more anteriorly, between the two pairs of black arrows, and is the BSL shown in Fig. 4). Bilateral globular structures are the cochlea (C). In this mouse the trachea (T) is deviated, and its diameter reduced, by the positioning of the two metal fingers used for rear head restraint. E is the epiglottis at the anterior end of the trachea.

220 Non-invasive visualization of airspaces, D. W. Parsons et al.

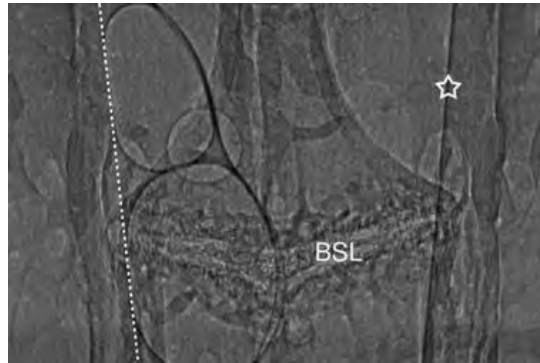
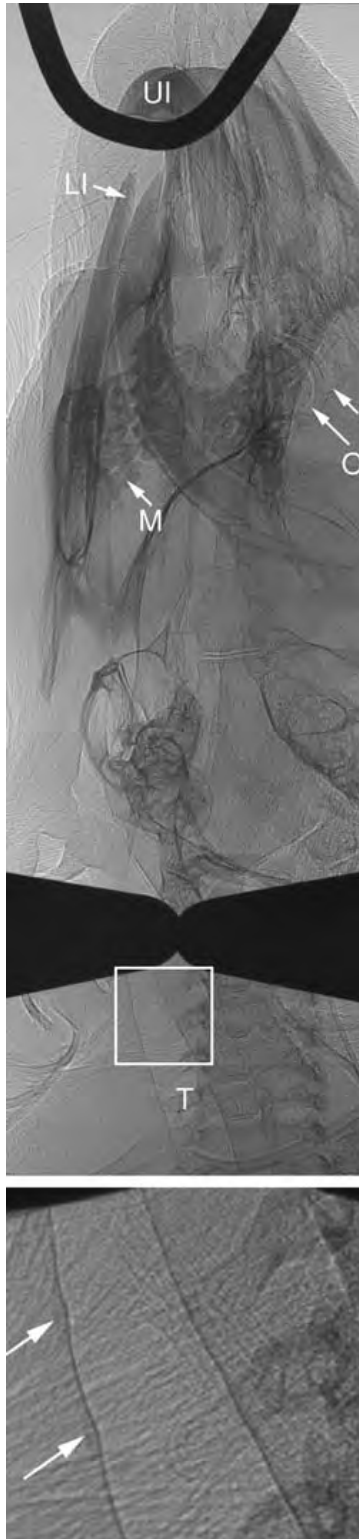


**Fig. 4** Live airway: detection of gas bubbles. At 17 min after a 20  $\mu$ L bolus of saline was introduced into the right nostril this image was captured from the nasopharyngeal airway. A distinctive bone suture-line (BSL) with an associated anterior central bilateral curvature provides a landmark for positioning of the imaging beam. Before fluid was instilled, the lumen edge on the left appeared similar to that shown on the right side (star); the original position of the airway surface is shown by the dotted line. At least three bubbles (of many 100s that appeared and transited posteriorly during the live imaging period) are associated on the left wall of the lumen. Two large flattened bubbles are situated adjacent dorso-ventrally to each other, and we propose the one small circular bubble is present separately either in front of or behind the large bubble pair, overlapping the larger bubbles and providing a 'lensing' effect that increases the image intensity inside the bubble area. See Supplementary material Fig. 4.avi for additional information.

(35 mm field of view; see [http://jp.hamamatsu.com/products/x-ray/pd450/xrayimag/index\\_en.html](http://jp.hamamatsu.com/products/x-ray/pd450/xrayimag/index_en.html) for specifications for this and for the AA50 converter noted earlier) and C4880-415 CCD (Hamamatsu Photonics) in  $2 \times 2$  binning mode. This gave a maximum field of view of 2000 (H)  $\times$  1312 (V)  $\times$  12  $\mu$ m pixels, i.e. 24 (H)  $\times$  15 (V) mm, necessitating CT acquisition in several vertical sections to collect data for the entire mouse head. CT reconstructions were performed using a Hanning filter and conventional filtered backprojection algorithm without any phase reconstruction techniques, producing a volume with an effective isotropic voxel size of 12  $\mu$ m. The intrinsic edge enhancement in the phase contrast projection images means that the reconstructed volumes also demonstrate this characteristic emphasis of boundaries, rendering airway surfaces particularly well without the necessity for further processing. In volume renderings (Software: VolVIEW 2.0, Kitware Inc. USA; and Amira, Mercury Systems) we applied a linear gradient to the greyscale palette for optimal display of these surfaces in the volume rendering.

**Fig. 3** Oblique image of the mouse shown in Fig. 2 provides improved image clarity for the trachea (T, arrows) due to elimination of bone from the projection. The lack of interference from the teeth allowed the olfactory turbinates (O, arrows) to be more clearly seen. The presence and structure of the molar teeth (M) and the upper (UI) and lower (LI) incisors are also revealed with greater clarity in this oblique profile. Inset at three-fold magnification shows the tracheal wall, with slight indentations and density increases (two arrows) associated with the tracheal cartilage rings. The presence of these rings is most obvious on the left hand edge of the trachea, and they can also be seen clearly in the rendering shown in Fig. 5B.

## Results

### Two-dimensional imaging – live and post-mortem mice

Because of our interest in airways, we primarily examined the nose, trachea, and lung. The murine nasal airways are of special interest because of their routine use as a model site for assessing the success of reporter gene and CFTR (cystic fibrosis transmembrane conductance regulator) gene transfer in pre-clinical studies of gene transfer and expression (Grubb & Boucher, 1999). Nasal airways were well suited to live imaging because they displayed little movement during respiration. In contrast, tracheal imaging could suffer from movement artefact in live animal studies.

Synchrotron PCXI revealed unprecedented detail of the mouse body, and the organs associated with airspaces. Figure 2 (typical of the four mice in that series) shows nasal, tracheal and middle ear airspaces at low resolution in a dorsal-ventral view. The anatomical relationships between the bony structures of the head and the airspaces are readily apparent. The olfactory regions are difficult to see in this view due to the overlap of the jaw, teeth and skull. In these X-ray images, the airway interface was well-delineated in the trachea where surrounding structures did not interfere with the image. Figure 3 is an oblique view of the same mouse, and the trachea is now clearly visible (see inset).

This method is able to resolve individual hairs (see nose tip, Fig. 2) in high contrast. The anatomical relationship of the airspace, the cartilage rings, the soft tissues of the neck, and the bone of the vertebrae demonstrates the power of PCXI to simultaneously visualize a range of tissue types.

### Gas bubbles: detection in live airways

PCXI can detect hitherto unobservable features on and in airways. Bubble presence during normal respiration was produced when a bolus of saline was instilled into the nasal airway of an anaesthetized mouse. A short time later, gas bubbles appeared in the airway, and these continued to transit the field of view for much of the imaging period (Fig. 4, and Fig. 4.avi in Supplementary material). Of interest is that individual and conjoined bubbles, as well as bubble interstices, were all readily apparent. The non-invasive detection of airway surface bubbles within a living animal non-invasively is a unique feature of PCXI that extends the possibilities of the method for high resolution studies and the novel detection of *in vivo* airway activity.

### High resolution CT – two-dimensional and three-dimensional anatomical imaging

Upper body and head CT studies were performed on 17 mice. The results show that high-resolution CT imaging via

PCXI produces striking illustrative images of small animals and animal organs. Histology-like thin slices, as well as three-dimensional volume reconstructions with arbitrary viewpoints chosen as desired, are both available.

Figure 5 shows a short series of CT slices through the lung of one mouse, revealing details of bifurcations of airways down to approximately 85  $\mu\text{m}$  diameter with slice reconstruction; a representative volume-rendered view of the upper body of another animal is displayed in Fig. 5B. The three-dimensional relationships of the airways, airway cartilage (for trachea), bone, fur, and other anatomical structures are displayed in striking detail and contrast. The image was taken from an animation (see Fig. 5B.avi in Supplementary material for 360° rotation animation) constructed using VolVIEW software and clearly shows the spatial relationships between these anatomical structures. To enable volume rendering of this large volume, the dataset size was reduced by  $2 \times 2 \times 2$  binning, giving an effective voxel size of 24  $\mu\text{m}^3$ . The azimuth and elevation of the volume can be changed interactively, and quantitative measurements (such as airway width/diameter, and organ size) can be made on screen if desired. Note again the simultaneous presentation of skin, bone, and cartilage, each with clarity and in high detail.

In 10 of the 17 mice we completed CT slice acquisition and volume reconstructions with dummy polyethylene cannulae inserted into the nostril. This was done to simulate the cannula placement used during electrical recording of nasal airway transepithelial potential difference for gene transfer assessment (Fig. 6). Both the CT slices and three-dimensional reconstructions were used to localize the position of the cannula tip after placement at the same insertion depths used in our mouse gene-transfer studies in mice. We found the small diameter (~300  $\mu\text{m}$ ) heat-thinned cannula tips rested in either the upper or medial nasal airway regions, close to the midline. In contrast to the thinner cannulae, when an unmodified (610  $\mu\text{m}$  diameter) PE10 size cannula was inserted either 5 mm or 2.5 mm into the nose, these cannulae (Fig. 6C) were large enough to displace the nasal septum or turbinates physically. When these high resolution CT slices were volume-rendered for one animal (Fig. 6.avi in Supplementary material) the three-dimensional relationship between the cannula and the nostril airways was clearly demonstrated.

### Lung airways and gas-exchange regions

The detailed morphology of the alveolar and conducting airspaces of a mouse lung is shown in the reconstructed CT slices (Fig. 7A). These images provide similar information to that obtainable from human lung CT slice images, though at a much higher resolution (12  $\mu\text{m}$  isotropic voxels compared to the current best possible CT resolution of approximately 350  $\mu\text{m}$  isotropic voxels). Conducting airways, alveolar spaces, and the edges of lung lobes in the

222 Non-invasive visualization of airspaces, D. W. Parsons et al.



**Fig. 5** A) Four consecutive mouse lung CT slices ( $2.06 \times 2.06$  cm image with  $12\text{-}\mu\text{m}$ -square pixels and a slice spacing of  $12\text{ }\mu\text{m}$ ) show a small part of a branching progression (e.g. at arrow) of airways in the lung. The heart (H), forearm bones and musculature (FA), vertebra (V) and the space between the mouse body and the plastic imaging tube are clear. B) Lateral view of the volume-reconstructed mouse ( $12\text{ }\mu\text{m}$  isotropic voxels), with software-selected removal of the right upper quarter of the head to reveal detail of the left jaw, molars, and exposed olfactory turbinate region (black arrow). Skull bone sutures lines are also apparent. In the chest region the trachea and associated cartilage rings, sternum, ribcage, spine and shoulder structures are shown. In this instance, the method of restraint in the tube induced hyperextension of the neck. An animation of this dataset is provided in Supplementary material Fig. 5B.avi.

chest cavity can be seen. The muscle bundles that surround the chest are also apparent.

Volume-rendering of CT slices from the lung provided a unique three-dimensional view of selected portions of the lung. The clarity of the airway wall and lumen suggests that airway obstructions produced by mucous accumulation, or disorders of airway wall structure, may be detected non-invasively in rodent models.

The unique visualization abilities of synchrotron PCXI in anatomical studies are further demonstrated in Fig. 7. Starting with CT slices like those shown in Fig. 5A, different volume-rendered portions of mouse chest, lung, airway, and alveolar regions were produced from the same data. Different representations of the enclosed lung airway and alveolar regions were created using the dataset that produced Fig. 7A (see Fig. 7A-1, 7A-2.avi in Supplementary material). A rendering of the details of lung structure in another orientation provides supporting understandings of the lung structure (Fig. 7B, and Fig. 7B.avi in supplementary material). The relative importance of the types of

tissue to be displayed, based on their radiographic intensity, was adjusted using the volume-rendering software.

A CT slice through a mouse middle ear and the corresponding tissue below that slice are shown in Fig. 7C,D. Note that the cross-section in Fig. 7C was of a single CT slice, and the uncovering of the three-dimensional organ detail below that slice (in Fig. 7D) was performed by manipulating the volume-rendering software. The mouse remained intact, no dissection or tissue removal was required, and a wide range of other user-selected positions and views can be readily obtained by altering settings in the image-manipulation software. In Supplementary material Fig. 7D.avi extends the appreciation of the normally hidden ear structures via a three-dimensional animation.

The traditional visualization of airspace structure in organisms has relied on destructive cross-sectioning and staining, and this has limited the viewpoints available in each sample. Virtual journeys through these airspaces can now greatly improve the understanding of the organ and its spatial relationships within the body. In Fig. 8.mpg

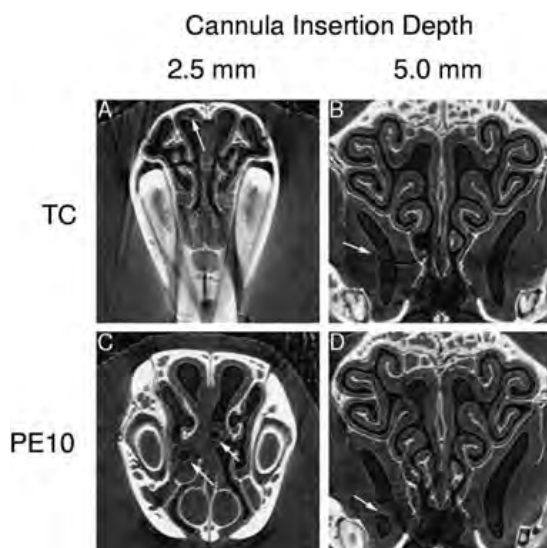


**Fig. 6** CT sections of mouse airway showing the position of PE cannulae inserted to specified depths, based on ink markings on the cannula at 2.5 mm and 5.0 mm from the tip. Arrows show the cannula location in the nose. For clarity, images are taken approximately four CT slices prior to the tip, but note the cannula tip may appear indistinct (compare Left cannula with Right cannula in C) because of deformation by the cutting blade during tip preparation, and the presence of fluid bridges between the cannula and the airway walls. The ring-like structures in the images are artefacts of the reconstruction algorithm, and derive from a non-uniform response of the detector in certain pixels. Although standard correction procedures are employed to reduce these effects (see Materials and methods) they sometimes cannot correct all artefacts. In five of the 10 animals an inserted cannula (TC) lay in the upper nasal airway (e.g. in A), the remaining five lay in the medial airway adjacent to the septum (similar to that shown for the left-side PE10 size cannula in C). Both the thinned (B) and PE10 cannula (D) could enter the boomerang-shaped maxillary sinus when inserted to the nominal 5 mm depth; in D the cannula is filled with fluid and neither the lumen nor the cannula walls can be seen within the fluid bridge produced. TC, heat-pulped thinned cannula; PE10, standard diameter PE10 polyethylene cannula. A volume-rendered animation of a thinned-cannula placement in the mouse nose is provided in supplementary material (Supplementary material Fig. 6.avi file).

(Supplementary material) an example 'virtual journey' through the mouse nose and lung has been constructed using suitable software (Amira; see Materials and methods) and is able to provide user-definable virtual travel into and through the airspaces.

## Discussion

The inherent high coherence and intensity of synchrotron X-ray sources allows the exploitation of phase-contrast effects to enhance airway edge visibility well above that possible from conventional X-ray imaging and can do so at a potentially lower dose of radiation (Lewis, 2004), at least

for two-dimensional imaging. The intrinsic high brightness of X-rays from a synchrotron source – typically many orders of magnitude greater than conventional sources – coupled with fast, high resolution detectors, provides a method of imaging that has shown considerable potential for high resolution imaging of airways and lungs. Furthermore, no contrast agents or other invasive procedures are required.

With the improvements in digital image-capture technology and storage, and technical advances in the control and use of synchrotron X-rays for biological and medical imaging, PCXI imaging studies of animals and organs have begun to appear. The first demonstration of the phase-contrast methodology by Snigirev (Snigirev et al. 1995) and Wilkins, and the subsequent use by other groups (Wilkins et al. 1996; Yagi et al. 1999; Suzuki et al. 2002; Westneat et al. 2003; Sera et al. 2005) has demonstrated its technical simplicity, with only a separation between sample and the detector needed to provide substantial contrast improvement. The ability to detect tissue types that could not be easily revealed with conventional X-rays is reviewed by Lewis (2004). Of some interest to respiratory biologists is the ability to detect airway cartilage (see Fig. 5B), a tissue that is largely invisible using conventional X-rays. Figure 2 demonstrates cartilage well, as it reveals a ventral skull suture that can otherwise only be detected histologically. This suture separates the basi-sphenoid and basi-occipital bones; it is formed from the somatic mesoderm, which produces a sandwich of cartilage in the suture line. In contrast, the flat bones of the skull are formed from neural-crest derived neuroectoderm, which produces purely bony sutures that are separated by the types of sutures easily seen on the skull surface (Fig. 5B).

One of the early significant applications of PCXI to the biological anatomy and physiology of small airspaces was that reported by the Westneat group (Westneat et al. 2003; Socha et al. 2007). Their study superbly revealed the detailed anatomy of the tracheal system of a 1.5-cm carabid beetle, *in situ*, and their *in vivo* studies provided the first evidence of tracheal pumping in this species. In small insects and organisms less than 1 mm<sup>3</sup>, a recent European study has comprehensively described the basis and specific techniques for PCXI imaging of muscle groups and tissues in preserved samples (Betz et al. 2007).

Since the studies of lung airway using synchrotron phase contrast have appeared (Yagi et al. 1999; Suzuki et al. 2002; Sera et al. 2003), these techniques have been adopted by others interested in lung anatomy and physiology. More recently, the short exposure times and the high contrast between airspace and tissue have been used to capture extraordinary images in rabbit pups, showing the first *in-vivo* demonstration of lung aeration and lung liquid clearance at birth (Hooper et al. 2007).

The combination of imaging with histological techniques has similarly progressed, and this combination offers unique opportunities for anatomical studies. Co-registration of

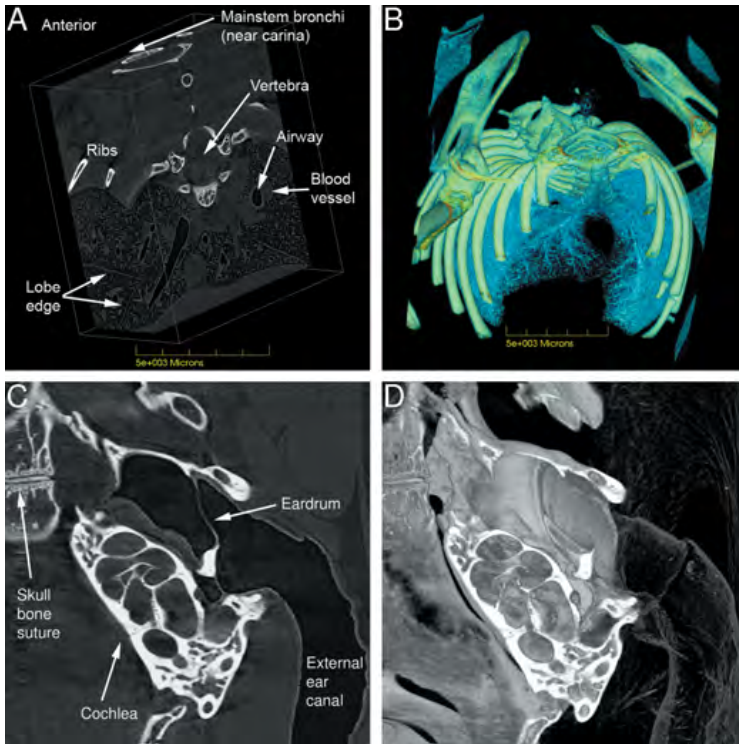


**Fig. 7** Chest and lung images; middle ear. A) Volume reconstruction of a block of lung tissue, derived from cropped CT slices. In this representation, bone, airway, blood (including heart), interstitial tissues and gas exchange regions are all visible. See Supplementary material Fig. 7A.avi and Fig. 7B.avi for the associated animations using different software settings able to reveal other anatomical features and relationships that cannot be represented using static images. B) Mouse chest cavity, rendered to optimize visualization of bone and lung airways. The associated animation in Supplementary material (Fig. 7B.avi) dynamically illustrates the organization of the airway branching pattern amongst the lightly rendered lung lobes and alveolar tissues. C) The middle ear spaces and the cochlea are shown in one 12- $\mu\text{m}$ -thick CT slice. D) Volume reconstruction of the middle-ear region on one side of the section shown in Fig. 7C enhances appreciation of the anatomy of the organ and the external ear canal. In Supplementary material (Fig. 7D.avi) a 360° animation of this reconstructed region provides an even higher level of understanding of the complexity and interrelatedness of the structures of the external and middle ear. The width of the imaged area is 7.2 mm.

sample coordinates across X-ray and histological methods has produced the 'Digimouse' atlas (Dogdas et al. 2007). Although conventional X-ray images were used in the Dogdas study, resulting in far lower resolution and contrast than is available with synchrotron PCXI, the resulting system for identification and viewing of the intact spatial relationships of organs and tissues provides a novel tool that could be applied to visualization and understanding of airspace organs.

Small-animal laboratory micro-CT systems are approaching the resolution levels suitable for preclinical study in small animals like mice, and might be considered for imaging similar to that described here. However, laboratory X-ray radiation is polychromatic and cannot provide the direct quantification that is possible with monochromatic synchrotron X-ray sources. Furthermore, polychromatic light gives lower effective resolution when used in conjunction with phase contrast imaging.

#### Resolution of airspace edges – bubble wall detection

Based on the Nyquist sampling theorem, in these studies the maximum resolution achievable using a 0.45- $\mu\text{m}$ -square pixel detector array (Fig. 4) in these studies is theoretically  $\sim 1 \mu\text{m}$ . However, scattering in the phosphor scintillator and (objective lens) optics that convert the X-rays to visible light for recording by the CCD produce a practical limit of  $\sim 2 \mu\text{m}$  here. Accordingly, at least four adjacent pixels are

needed reliably to detect the smallest difference in contrast created by a real anatomical structure.

Figure 4 shows the ability of PCXI to resolve gas bubbles *in situ*. Based on interferometry analyses of soap-bubble films in visible light, a bubble wall thickness is likely to be less than several 100 nm, and thus is well below the direct resolution of the detector system here. However, PCXI is able to detect bubble walls due to the phase contrast effects that the latter produce. Effectively, PCXI 'inflates' the width of the bubble wall because the wall offers extreme differences in refractive index and thus phase contrast: between the air inside the bubble, across the nanometre-thin fluid of the bubble wall, and then to the airspace outside the bubble wall. The resulting image is a wider representation of the real bubble wall with high contrast that is consequently highly visible. These airway bubble images were captured in live anaesthetized mice, and appear to be the first report of non-invasive detection of airway-surface bubbles *in vivo*.

By comparison with the unaffected right side of the airway, the gas bubbles detected on the live airway surface (Fig. 4, and see also Supplementary material Fig. 4.avi) show novel features of surface-bound bubble behaviour in live airway. The flattened bases of the two larger-diameter bubbles indicate their dynamic distensibility when embedded within a smoothly enveloping fluid mass on the airway surface. The darkening of image intensity in the interstitial

fluid-filled space between the large bubbles (where the small circular bubble overlaps them, see Fig. 4) indicated the excellent sensitivity of PCXI to the additional fluid present there.

### Imaging airspace surfaces

The ability to reveal airway surfaces and bubbles lodged along the airway surface is unique to PCXI. The strong contrast between the air, fluid and tissue layers permits non-invasive detection of airway diameter, and thus airway narrowing or obstruction could be detected in animal-disease models. These two-dimensional and three-dimensional techniques provide complementary information about airspaces in these small animals. Our two-dimensional studies in live airways have been able to reveal the dynamic activity in major airways, such as bubbles transiting airways after fluid instillations.

Three-dimensional CT studies in post-mortem animals can reveal striking anatomical detail that is very difficult to achieve in any other way. In deep lung airways the resolution was sufficient to display small conducting airways to approximately 80  $\mu\text{m}$  in diameter. With such resolution, changes in diameter due to a disease-based mucus accumulation, physical object obstruction, or an inherited disorder, could be easily identified. The clarity of the mouse cochlea (Fig. 7C,D) exceeded that reported recently using the diffraction enhanced imaging (DEI) method of phase contrast in much larger preserved guinea-pig cochlea specimens (Gao et al. 2006). There are several reasons for the improved visualization here. The detector uses pixels of 10-fold better resolution; the X-rays are detected under phase-contrast conditions that boost edge detection and detail; and the cochlea remains *in situ*, thus preserving spatial relationships within the mouse ear. Furthermore, DEI is reliant on using a perfect crystal analyser to render the phase differences visible as intensity differences. Although DEI is a more sensitive method than propagation-based phase contrast in theory, in practice the crystal is prone to stability problems and has a limited field of view compared to propagation-based methods.

Our results show that three-dimensional PCXI imaging can reveal considerable detail about the spatial relationships of organ structures, and should provide useful supplementary information to support and sometimes surpass the capabilities of traditional dissection and histological cross-sectioning to obtain structural information from small animals.

### An application of PCXI: localization of recording electrode position in airways

Physiological recordings of airway electrical potential difference from airways and airspaces in small animals are complicated by the inability to know exactly where a

recording electrode is placed. When recording airway potential difference, researchers can only rely on cannula placement according to the depth of insertion into the nose. It is not possible to know where the recording tip rests within this complex structure, and thus whether recorded signals come from the desired regions of ciliated airway epithelium. In a previous study we noted that correct depth placement of the cannula tip in the nasal airway was important (Parsons et al. 2000). These new images, however, provide evidence of the variability inherent in this recording method. Because cannula tips were localized to the respiratory epithelium of either the upper (Fig. 6A) or the medial (Fig. 6C) nasal airway equally often in our studies, and as the deeper upper regions of epithelium are exclusively olfactory, this finding confirms our earlier data, using electrochemical marking of tip position (Parsons et al. 2000), that a shallow (2.5 mm) recording depth is more likely, but not certain, to access nasal respiratory epithelium. We also noted cannulae inserted to 5 mm could enter the maxillary sinus (Fig. 6B,D) where the entire surface is known to be ciliated respiratory epithelium. These PCXI studies have thus identified the possibility for cannulations of mouse sinuses. Given the complex topography of the mouse nose this possibility could not have been predicted before, nor readily tested using invasive dissection techniques. If this type of sinus access is confirmed in further studies, the maxillary sinus may have utility for the creation, study and manipulation of sinus disorders and disease in mouse models.

### New options for visualizing animal airspaces

The imaging potential offered by the combination of PCXI and current image manipulation software is apparent in Figs 7 and 8. The images in Fig. 7 were taken from one animal, with the different organs, views, colouring, detail, and ability to return to the dataset for new visualizations all controlled by the user.

Supplemental material Fig. 8.mpg suggests one of the novel directions now available for representation of anatomical and morphological analyses in small animals, echoing the developing virtual bronchoscopy techniques within human CT analyses (Finkelstein et al. 2004; Bauer & Steiner, 2007). Exploration of normally inaccessible or hidden airspaces such as sinuses, nasal airways, and the airways of the lung is possible at resolutions already sufficiently high to detect obstructions and congenital defects non-invasively in intact small animals such as mice. With appropriate beamline and detector technology in place, larger organisms and animals could also be studied in this way.

### Concluding remarks

Our findings show that synchrotron PCXI can provide several complementary visualization approaches able to

improve anatomical, biological, and physiological studies in small animals. High resolution two-dimensional images of airspace structures in living or deceased animals (such as those shown in Figs 2–4) can be readily produced. Animations and 'virtual tours' based on the three-dimensional reconstructions (Fig. 8) strengthen the understanding of the spatial relationships within and around the organs studied. Given the high resolution and clarity achievable now, the expected improvements in detectors, data capture and image processing, advances in these techniques for use in small animal models and live non-invasive imaging of airspace biology can be expected.

The unprecedented structural contrast and resolution available from PCXI CT slicing offers researchers near histological-quality sections and resolutions of complex organs such as lung (Figs 4, 5A). With volume-reconstructions the overall structure of organs can be interactively viewed intact or cut away from any angle (Figs 5B, 6B, 7A,B). Tailoring the parameters of the reconstruction software allows specified regions of interest to be rendered with emphasis on different components of the tissue (e.g. conducting airway vs. gas-exchange regions) if tissue absorption or phase-contrast properties permit. Although these studies were developed in mice we speculate that with technical advances and tailoring of radiation dose, PCXI may eventually have a role in specialized diagnostic imaging studies at very high resolution in larger animals, and potentially in humans. With a recent report providing the basis for development of a compact laser-based synchrotron X-ray source (Schlenvoigt et al. 2008) the utility of PCXI in biology and medicine for imaging investigations at the tissue, organ and organism level may become substantial.

### Acknowledgements

Studies supported by NH&MRC Australia, USA CF Foundation, & philanthropic donors. SPring-8 experiments completed under proposals J05A20XU-0533N, 2006A1066, & 2007A1287. Prof. Ian Gibbins, Flinders University, advised on the identity and embryology of the cartilaginous skull-bone sutures. Dr Peter Self, Adelaide Microscopy, provided advice and datasets concerning non-synchrotron X-ray imaging. D.W.P., K.K.W.S., J.C., and I.W. acknowledge the support of the Access to Major Research Facilities Program, Commonwealth of Australia.

### References

- Bauer TL, Steiner KV (2007) Virtual bronchoscopy: clinical applications and limitations. *Surg Oncol Clin N Am* **16**, 323–328.
- Betz O, Wegst U, Weide D, et al. (2007) Imaging applications of synchrotron X-ray phase-contrast microtomography in biological morphology and biomaterials science. I. General aspects of the technique and its advantages in the analysis of millimetre-sized arthropod structure. *J Microsc* **227**, 51–71.
- Dogdas B, Stout D, Chatziioannou AF, Leahy RM (2007) Digimouse: a 3D whole body mouse atlas from CT and cryosection data. *Phys Med Biol* **52**, 577–587.
- Finkelstein SE, Summers RM, Nguyen DM, Schrupp DS (2004)

Virtual bronchoscopy for evaluation of airway disease. *Thorac Surg Clin* **14**, 79–86.

- Gao X, Luo S, Yin H, et al. (2006) A micro-tomography method based on X-ray diffraction enhanced imaging for the visualization of micro-organs and soft tissues. *Comput Med Imaging Graph* **30**, 339–347.
- Gotto K, Takeshita K, Suzuki Y, et al. (2001) Construction and commissioning of a 215-m-long beamline at SPring-8. In *7th International Conference on Synchrotron Radiation Instrumentation, Nuclear Instruments & Methods in Physics Research, Section A (Accelerators, Spectrometers, Detectors and Associated Equipment)*, pp. 682–685.
- Grubb BR, Boucher RC (1999) Pathophysiology of gene-targeted mouse models for cystic fibrosis. *Physiol Rev* **79**, S193–S214.
- Hooper SB, Kitchen MJ, Wallace MJ, et al. (2007) Imaging lung aeration and lung liquid clearance at birth. *FASEB J* **21**, 3329–3337.
- Lewis RA (2004) Medical phase contrast x-ray imaging: current status and future prospects. *Phys Med Biol* **49**, 3573–3583.
- Parsons DW, Hopkins PJ, Bourne AJ, Boucher RC, Martin AJ (2000) Airway gene transfer in mouse nasal-airways: Importance of identification of epithelial type for assessment of gene transfer. *Gene Therapy* **7**, 1810–1815.
- Schlenvoigt H-P, Haupt K, Debus A, et al. (2008) A compact synchrotron radiation source driven by a laser-plasma wakefield accelerator. *Nature Physics* **4**, 103–133.
- Sera T, Fujioka H, Yokota H, et al. (2003) Three-dimensional visualization and morphometry of small airways from microfocal X-ray computed tomography. *J Biomech* **36**, 1587–1594.
- Sera T, Uesugi K, Yagi N (2005) Refraction-enhanced tomography of mouse and rabbit lungs. *Med Phys* **32**, 2787–2792.
- Snigirev A, Snigireva I, Kohn V, Kuznetsov S, Schelokov I (1995) On the possibilities of X-ray phase contrast microimaging by coherent high-energy synchrotron radiation. *Rev Sci Instrum* **66**, 5486–5492.
- Socha JJ, Westneat MW, Harrison JF, Waters JS, Lee WK (2007) Real-time phase-contrast x-ray imaging: a new technique for the study of animal form and function. *BMC Biol* **March**, 6–21.
- Suzuki Y, Yagi N, Uesugi K (2002) X-ray refraction-enhanced imaging and a method for phase retrieval for a simple object. *J Synchrotron Radiat* **9**, 160–165.
- Westneat MW, Betz O, Blob RW, Fezzaa K, Cooper J, Lee W (2003) Tracheal respiration in insects visualized with synchrotron X-ray imaging. *Science* **299**, 558–560.
- Wilkins SW, Gureyev TE, Gao D, Pogany A, Stevenson AW (1996) Phase-contrast imaging using polychromatic hard X-rays. *Nature* **384**, 335–338.
- Yagi N, Suzuki Y, Umetani K, Kohmura Y, Yamasaki K (1999) Refraction-enhanced x-ray imaging of mouse lung using synchrotron radiation source. *Med Phys* **26**, 2190–2193.

### Supplementary material

The following supplemental material is available for this article:

**Fig. 4.avi** Example of gas bubbles detected non-invasively whilst transiting intact live airway. The first six frames (all frames were taken 10 s apart) show 1 min of baseline images prior to fluid instillation. After four separating black frames, the 19 following frames reveal a range of bubble sizes and groups moving down the airway from the

overlying nostril region towards the pharyngeal area, over a 3-min period. Individual and linked bubbles as well as the rapidly changing fluid level associated with the bubbles is apparent. Frame 18 and the scale are the same as Fig. 4.

**Fig. 5. avi** Animated view of rendered head and chest. Views of the skull, neck and chest from all horizontal directions show with greater clarity the features noted in Fig. 5B. This particular digital sectioning and rotation permits viewers to simultaneously appreciate the detail of skull-bone suture lines, the detail within the cutaway section exposing the olfactory turbinate region, and the soft tissues of the outer ears and neck.

**Fig. 6. avi** Non-invasive localization of cannula in upper nasal airway. The cannula is visible entering the nasal orifice (in frame 1 the cannula has been overlaid in red), and can be tracked through the nostril to its termination in the nasal airway. The white nasal-bone can be seen dorsally, where it terminates before reaching the nose tip. Similarly, the (white) anterior portion of the dorsal incisor is present ventrally. Note also the resolution of hair of the fur on the nose outer surface.

**Fig. 7A-1. avi** This animation was produced from the same dataset that provided the image of Fig. 7A, but here is shown with a different orientation and with progressive magnification. It was rendered to be similar to the view of a block of fixed lung tissue produced by simple right-angled cuts with a blade. At the top of the first frame the base of the trachea and the carina with the two mainstem bronchi are shown; note the regular bilateral whitened regions of airway cartilage on the airway wall. With rotation past the side of the lung some medium-size airways, and the edges of two lung lobes can be seen (see Fig. 7A for labeling). With further rotation the left and right sides of the lung, the continuation of the lobe edge, and the large airways that connect back to the carina become apparent. The last frame shows three smaller airways, mostly in cross-section, with their accompanying blood vessels.

**Fig. 7A-2. avi** This animation is the same dataset, orientation, rotation and magnification as in animation 7A-1. avi, but with rendering and coloration designed to separate out airways and bone. The dorso-posterior sweep of the mainstem bronchi is apparent as they connect into the lung lobes, and the digital removal of blood from the lung can be seen in the empty blood vessel adjacent to the large airway right of centre in the last frame. This rendering has also removed the heart and associated thoracic tissues, leaving the lung tissue largely intact. Note that some lung lobe edges are fragmented due to the effect of digital region cropping when digitally producing this block of chest tissue for viewing.

**Fig. 7B. avi** An anterior to posterior rotation animation, again using the same dataset and with rendering settings assigned as for 7A-2. avi, but starting from an anterior viewpoint. However, the degree of cropping has been relaxed, to include more of the ribs and the full posterior extent of the lungs. At Frame 50 a small structure below the lungs appears, and was found to be in the position of the stomach in other renderings (data not shown). The structure here represents the top of the stomach, containing an air bubble and food material (follow to the last frame for more clarity). By Frame 130 the medio-ventral edge of a right lobe is silhouetted against the background.

**Fig. 7D. avi** Slow 360° rotation (2° increments) of the ear dataset rendered in image Fig. 7D. The relationships amongst the outer ear, ear canal, eardrum region, middle-ear bony structures and the cochlea are seen in fine detail. Scale as in Fig. 7D.

**Fig. 8. mpg** Virtual tour of mouse nose and lung reconstructed from CT slices. This is the same mouse as that used for Fig. 6C. Beginning with a view of the posterior edge of the CT slice series, sections through the ribs, forearms, and the anterior end of the stomach (containing food material) can be seen. Rotation to the nose tip displays the mounting tube, the animal with its outer ears laid flat, and the skull, teeth, and whiskers. The two polyethylene cannulae (see Fig. 6C) can be seen in the nostrils, and once the view has progressed inside the nose, two views of the upper nasal turbinates are seen (frames 380–480). The viewpoint progresses posteriorly along the left nasal airway until (frame 670) the scene scans to ventral airspaces before crossing to the right airway region at this same depth. From the right nasal airway (frame 960) the view moves posteriorly with the septum on the right, until centralizing in the nasopharynx (frame 1200). The larynx and trachea come into view (frame 1220) with the viewer taken down into the trachea, past the carina (frame 1510), and into the right bronchus and deeper airway branches. At frame 1820 the view passes through the airway wall, exits the base of the lung, and rotates to reveal the stomach, ribs and forearms of the first frame (permitting continuous loop animation).

This material is available as part of the online article from: <http://www.blackwell-synergy.com/doi/abs/10.1111/j.1469-7580.2008.00950.x> (This link will take you to the article abstract).

Please note: Blackwell Publishing is not responsible for the content or functionality of any supplementary materials supplied by the authors. Any queries (other than missing material) should be directed to the corresponding author for the article.



---

## Appendix D

*Real-time non-invasive detection of inhalable particulates delivered into live mouse airways.*

by Martin Donnelley, Kaye S. Morgan, Andreas Fouras, William Skinner, Kentaro Uesugi, Naoto Yagi, Karen K. W. Siu and David W. Parsons.

Published in the Journal of Synchrotron Radiation **16**, pp. 553-561, 2009.

---

This paper was published in the Journal of Synchrotron Radiation and is made available as an electronic reprint with the permission of the IUCr. The paper can be found at the following URL on the Wiley website: <http://onlinelibrary.wiley.com/doi/10.1107/S0909049509012618/abstract>. Systematic or multiple reproduction or distribution to multiple locations via electronic or other means is prohibited and is subject to penalties under law.

---

### Declaration for Appendix D, work supplementary to Thesis Chapter 6

In the case of Appendix D, contributions to the work involved the following:

Name	% contribution	Nature of contribution
Martin Donnelley		Contributed to the planning and original live imaging experiments, data analysis and the wrote up the paper
Kaye Morgan	10%	Contributed to the planning and original live imaging experiments, image processing and proofreading
Andreas Fouras		Contributed to the original live imaging experiments
William Skinner		Contributed to the planning and provided some pollutants for use in the experiments
Kentaro Uesugi		Contributed to the original experiments
Naoto Yagi		Contributed to the original experiments
Karen Siu		Contributed to the planning and original experiments, data analysis and proofreading
David Parsons		Provided the context for the imaging problem, contributed to the planning and original experiments, data analysis and proofreading

#### Declaration by co-authors

The undersigned hereby certify that:

1. the above declaration correctly reflects the nature and extent of the candidate's contribution to this work, and the nature of the contribution of each of the co-authors.
2. they meet the criteria for authorship in that they have participated in the conception, execution, or interpretation, of at least that part of the publication in their field of expertise;
3. they take public responsibility for their part of the publication, except for the responsible author who accepts overall responsibility for the publication;
4. there are no other authors of the publication according to these criteria;
5. potential conflicts of interest have been disclosed to (a) granting bodies, (b) the editor or publisher of journals or other publications, and (c) the head of the responsible academic unit; and
6. the original data are stored at the following location(s) and will be held for at least five years from the date indicated below: School of Physics and Monash Centre for Synchrotron Science, Clayton Campus, Monash University, Australia.

#### Signatures:

Martin Donnelley:		Date: 16.10.10
Kaye Morgan:		Date: 18/10/10
William Skinner:		Date: 15.10.10
Kentaro Uesugi:		Date: 17.10.2010
Naoto Yagi:		Date: 19.10.2010
Karen Siu:		Date: 15.10.10
David Parsons:		Date: 15.10.10

## Real-time non-invasive detection of inhalable particulates delivered into live mouse airways

Martin Donnelley,<sup>a,\*</sup> Kaye S. Morgan,<sup>b</sup> Andreas Fouras,<sup>c</sup> William Skinner,<sup>d</sup> Kentaro Uesugi,<sup>e</sup> Naoto Yagi,<sup>e</sup> Karen K. W. Siu<sup>b,f</sup> and David W. Parsons<sup>a,g,h</sup>

<sup>a</sup>Respiratory and Sleep Medicine, Women's and Children's Hospital, Adelaide, Australia, <sup>b</sup>School of Physics, Monash University, Victoria, Australia, <sup>c</sup>Division of Biological Engineering, Monash University, Victoria, Australia, <sup>d</sup>Materials and Environmental Surface Science, University of South Australia, Australia, <sup>e</sup>Spring-8/JASRI, Hyogo, Japan, <sup>f</sup>Monash Centre for Synchrotron Science, Monash University, Victoria, Australia, <sup>g</sup>Department of Paediatrics, University of Adelaide, Australia, and <sup>h</sup>Women's and Children's Health Research Institute, Adelaide, Australia.  
E-mail: martin.donnelley@adelaide.edu.au

Fine non-biological particles small enough to be suspended in the air are continually inhaled as we breathe. These particles deposit on airway surfaces where they are either cleared by airway defences or can remain and affect lung health. Pollutant particles from vehicles, building processes and mineral and industrial dusts have the potential to cause both immediate and delayed health problems. Because of their small size, it has not been possible to non-invasively examine how individual particles deposit on live airways, or to consider how they behave on the airway surface after deposition. In this study, synchrotron phase-contrast X-ray imaging (PCXI) has been utilized to detect and monitor individual particle deposition. The *in vitro* detectability of a range of potentially respirable particulates was first determined. Of the particulates tested, only asbestos, quarry dust, fibreglass and galena (lead sulfate) were visible *in vitro*. These particulates were then examined after delivery into the nasal airway of live anaesthetized mice; all were detectable *in vivo* but each exhibited different surface appearances and behaviour along the airway surface. The two fibrous particulates appeared as agglomerations enveloped by fluid, while the non-fibrous particulates were present as individual particles. Synchrotron PCXI provides the unique ability to non-invasively detect and track deposition of individual particulates in live mouse airways. With further refinement of particulate sizing and delivery techniques, PCXI should provide a novel approach for live animal monitoring of airway particulates relevant to lung health.

### 1. Background

Inhalation of pollutant particles starts immediately after birth, and the type of particles inhaled depends on the surrounding environment. Children can be unknowingly exposed to a wide range of potentially harmful particles of varied toxicity, ranging from established toxins such as asbestos and fibreglass fibres, lead fumes from smelters and (previously) motor vehicles, coal and mineral dusts from mines and quarries, to everyday dusts in the air. The lung size, airway physiology, breathing patterns and rapid development of young children significantly increases their risk over that of adults experiencing the same pollutant particle exposure (Wildhaber, 2006). Although the eventual effects on lung health from inhaling

some of these particles are well known, particularly for asbestos (Addison & McConnell, 2008), no studies have examined the manner in which such particles deposit on airways, nor their physical behaviour and immediate fate after contacting the airway surface. Knowledge of particle deposition behaviour may help reveal factors that influence retention and thus the later pathophysiology in the lungs.

The ability of airways to clear inhaled particles *via* mucociliary transit is a clear diagnostic indicator of airway health. We are developing methods to monitor mucociliary transit in mice *in vivo* to assist in determining the effectiveness of genetic (Limberis *et al.*, 2002) and other potential therapeutics in cystic fibrosis airway disease. Although reliable methods for bulk detection of the clearance of particles in airways exist

## research papers

(Grubb *et al.*, 2004; Donaldson *et al.*, 2007; Livraghi & Randell, 2007), respiratory science currently lacks a non-invasive method of detecting these individual particulates, or tracking their motion in real time. Knowledge of the behaviour of deposited particles in animal models may provide clues to the initiation of animal and human pathophysiology, and thus suggest potential preventative measures for use in young children as well as in adults. We therefore utilized novel synchrotron phase-contrast X-ray imaging (PCXI) to detect and monitor the deposition and comparative transit behaviour of representative pollutant particles in live mouse airways.

PCXI utilizes X-ray refraction in addition to conventional absorption to improve image contrast, and it is particularly useful for achieving soft tissue contrast where the absorption differences are small. Tissue boundaries are enhanced by the phase changes induced by differences in their X-ray refractive indices, provided the incident beam has sufficient spatial coherence and the sample-to-detector distance is sufficiently long (Snigirev *et al.*, 1995; Cloetens *et al.*, 1996; Wilkins *et al.*, 1996). We have already shown the ability of PCXI for non-invasive airspace imaging in small animals (Parsons *et al.*, 2008). The aim of this study was to test the capability of PCXI for non-invasive particulate detection in live mouse airways.

### 2. Methods

The experiment first utilized an *in vitro* study to determine which of a range of biologically relevant particulates were detectable using synchrotron PCXI. For those particles that were adequately detectable, we then examined their *in vivo* behaviour when deposited on live mouse airways.

The experiment was performed on the undulator beamline BL20XU at the SPring-8 Synchrotron Radiation Facility, Hyogo, Japan. The imaging hutch was located 245 m from the storage ring in the Biomedical Imaging Centre, and the imaging layout was as shown previously (Parsons *et al.*, 2008). Monochromatic X-rays of 25 keV ( $\lambda = 0.5 \text{ \AA}$ ) were selected using a standard double-crystal monochromator (Yabashi *et al.*, 1999). At the imaging station the beam size was approximately 10 mm (H)  $\times$  6 mm (V) and the incident photon flux was approximately  $4.37 \times 10^9$  photons  $\text{s}^{-1}$ , producing an estimated dose rate of 0.61 Gy  $\text{s}^{-1}$ . The propagation (sample to detector) distance was 135 cm, chosen to produce a sufficiently strong bright/dark fringe from each particle, so that they could be identified amid intensity variations introduced by overlying tissue and skin. Images were captured using a high-resolution X-ray converter (10 mm maximum diameter field of view; AA50 Hamamatsu Photonics) with a charge-coupled device (CCD) detector. The converter used a 10  $\mu\text{m}$ -thick scintillator ( $\text{Lu}_2\text{SiO}_5\text{:Ce}$ ) to convert X-rays to visible light, which was then directed to the CCD using a  $\times 20$  X-ray converter microscope objective lens with a numerical aperture of 0.4. The detector was a pco.4000 (PCO Imaging) with an array size of 4008  $\times$  2672 pixels and a 9  $\mu\text{m}$  native pixel size. This set-up resulted in an effective isotropic pixel size of 0.45  $\mu\text{m}$  and a field of view of 1.8 mm  $\times$  1.2 mm. The FWHM of the point spread function, as determined from a horizontal

edge image, was measured at 3.6  $\mu\text{m}$ . Exposure times between 90 ms and 300 ms were used for the *in vitro* studies, and 300 ms for the *in vivo* studies.

#### 2.1. *In vitro* studies

A range of potentially respirable pollutant particles were examined dry or suspended in a carrier fluid (distilled water) to determine their visibility using PCXI. Chrysotile (white asbestos), provided by the South Australian Museum, and fibreglass from a commercial pipe insulation were separately ground under water to produce fibres suited for examination. Galena, the natural mineral form of lead sulfide (PbS), was also obtained from the South Australian Museum, and dolomite quarry dust was provided courtesy of the Boral Resources (SA) Limited Linwood Quarry, Adelaide, South Australia. Other relevant compounds, tested to confirm, in part, theoretical limitations in the application of PCXI imaging, included combusted diesel particles and standard roadside PM10 filtered particulate matter (provided by Dr I. Gilmour, USA EPA, Research Triangle, NC, USA), and laser printer toner (Epson).

All particle samples (except asbestos, see *Results*) were sieved using a 25  $\mu\text{m}$   $\times$  25  $\mu\text{m}$  orifice stainless-steel mesh; a small sample was then tapped, puffed or dropped onto the exposed adhesive surface of short lengths of Kapton tape, a polyimide film highly transparent to X-rays (PC500 1  $\mu\text{m}$ -thick with 1.5  $\mu\text{m}$ -thick silicon adhesive; Argon Masking Inc.). The particles were then sealed in place using a second piece of tape. The samples were mounted on a controllable XY stage in the hutch for imaging. Comparative images taken under light microscopy at  $\times 400$  magnification were also used to ensure the regions imaged using PCXI included the particles of interest.

#### 2.2. *In vivo* studies

For the *in vivo* experiments, ten hairless mice (CrJ:CD1-Foxn1<sup>tm</sup>) weighing  $\sim 18$ –26 g were imaged under approval from the Animal Ethics Committee of SPring-8 and of the Children, Youth and Women's Health Service, Adelaide. Mice were anaesthetized with Nembutal (45 mg  $\text{kg}^{-1}$ , i.p.) and were humanely killed *via* Nembutal overdose (500 mg  $\text{kg}^{-1}$ , i.p.) at the end of each study without awakening. The anaesthetized mice were secured on a polyethylene imaging board containing an open slot to allow the passage of the X-ray beam directed anterior to posterior along the centre line of the mouse. The dorsal incisors were hooked over a stainless-steel wire loop, and the limbs and shoulders, and above and below the imaging area in the head, were taped to minimize body movements owing to respiration during imaging. The level of anaesthesia was monitored by foot pinch and changes in respiration. Nembutal was continuously infused by a syringe pump *via* an indwelling i.p. needle (typically at a rate of 0.9  $\mu\text{l min}^{-1}$ ), with additional top-up Nembutal injections given as required.

A small-diameter polyethylene recording cannula, made from heat-pulled and thinned polyethylene PE10 tubing (Tyco

Electronics), was placed to a depth of 10 mm in the right nostril, to provide a route for direct delivery of test particulate agents suspended in water to the nasal airway. The position of the cannula tip in the nose was recorded at the end of several deposition studies by inserting a fine wire, previously aligned to reach to the end of the cannula tip. The distinctive bone suture line in the nasopharyngeal airway posterior to the olfactory region provided an easily locatable landmark near which the airway imaging was performed (Fig. 2). Nasal airways in laboratory mice were utilized here since they are commonly used as a model site for pre-clinical testing of airway function after gene transfer procedures by our group (Limberis *et al.*, 2002) and others (Grubb & Boucher, 1999). The mouse nasal airway is lined with the ciliated respiratory epithelium which mimics that present in human lung conducting airways. This region is also well suited to these first live PCXI particulate imaging procedures because the airway is stable within the head and shows little movement during breathing; in contrast, lung airways are in almost continuous motion during breathing.

Images were captured at a rate of 0.2 Hz. After 1 min of baseline collection, samples of particulates suspended in distilled water were delivered *via* the nasal cannula either manually or using a syringe pump, at volumes between 15  $\mu\text{l}$  and 50  $\mu\text{l}$ , in one bolus over 10 to 60 s (see *Results*). Image collection was continued at 0.2 Hz for a further 19 min, creating a dataset consisting of 240 images, close to the maximum number of images (260) the pco.4000 camera's onboard memory buffer could record.

The anatomy of the mouse head at the imaging location introduced confounding detail (from other head structures in the path of the X-ray beam) into the PCXI images, which could obscure individual small particles in single images. To facilitate rapid and accurate location of relevant particles, each image sequence was analysed with simple motion-detection software (*VirtualDub*, Version 1.8.6, Avery Lee, using the MSU Motion Estimation plug-in, Graphics and Media Lab, Moscow State University) to reveal where motion was occurring by applying digital image subtraction and filtering algorithms that identify regions of the image that change between frames. The output of this motion-detection software was sequential frames that were neutral grey where there was no motion detected, and lighter or darker grey where motion was detected. The dark outlines corresponded to the most recent position of the moving object, and the light outlines corresponded to the position of the object in the previous frame. For high-quality motion detection the background must remain still compared with the moving objects to be detected, hence the special efforts we made to minimize the movement of the mouse during imaging.

### 3. Results

#### 3.1. *In vitro* studies

We first tested the range of potential pollutant or toxic particles encapsulated between adhesive Kapton tape and

examined their detectability under PCXI, prior to use in live mice. At a propagation distance of 135 cm, many particles were visible both from phase contrast or absorption, or a combination of both. For example, galena absorption dominated the image contrast, and thus produced shadows with no fringes. In contrast, the glass beads refracted the X-rays and introduced variations in the phase of the X-ray wave across the width of the object. The interference of the phase-shifted waves produced light and dark fringes, *i.e.* phase contrast, but not a dark shadow where the glass was, since it did not absorb strongly. Some particles, such as quarry dust, showed both phase and absorption contrast, appearing darker where the object attenuated the beam, as well as having some bright/dark fringes around the edges. The 300 ms exposure length produced the optimum images, capturing sufficient incident photons to fill the potential dynamic range ( $2^{14}$  grey levels), thus providing the maximal signal-to-noise ratio without inducing detector saturation. Fig. 1 shows results of these *in vitro* studies, and clearly demonstrates the differences in detectability between particle types.

Small individual asbestos fibre bundles, ranging in width from 4  $\mu\text{m}$  to 15  $\mu\text{m}$  and in length from near 25  $\mu\text{m}$  through to several millimetres, could be seen in the PCXI images (Fig. 1*a*). Additionally, many large fibre bundles were also present, some with widths up to 200  $\mu\text{m}$ , as observed under light microscopy. Despite extensive manual wet-grinding, asbestos particles could not be ground and separated into uniform size fractions. In addition, asbestos ground under water formed an enmeshed fibrous meshwork that resisted centrifugation (6500 r.p.m. up to 5 min) or extended ultrasonification (up to 10 min) that should have assisted in its preparation into finer diameter fractions. For safety reasons, in this study we did not attempt to employ dry grinding to produce smaller dry asbestos fibres. As a result, the delivery of asbestos was technically difficult because large fibres could clog the cannula tip when the fluid dose was drawn into, or ejected from, the dosing cannula. Thus we relied on settling in water in an attempt to obtain finer size fractions. Nevertheless, clumps of fine fibres could still be observed when samples were ejected onto a clean surface, suggesting that asbestos fibre clumps could still occur when delivered *via* a cannula.

Like asbestos, quarry dust was also readily detectable (phase and absorption contrast) but appeared as compact irregularly shaped particles primarily between 7  $\mu\text{m}$  and 30  $\mu\text{m}$ . Although particles (apart from asbestos) were sieved through a 25  $\mu\text{m}$  square stainless-steel mesh, occasional larger particles (up to 90  $\mu\text{m}$ ) were also present (*e.g.* Fig. 1*b*) possibly owing to clumping effects. The quarry dust produced more image contrast than the asbestos (but significantly less than galena, see below).

Fibreglass was substantially less visible than either asbestos or quarry dust (phase contrast and absorption). Under PCXI the fibreglass particles had the same individual fibre/rod morphology present in light microscopy (Fig. 1*c*). Most fibres were between 12  $\mu\text{m}$  and 25  $\mu\text{m}$  in length, but again there were a small number of fibres with lengths up to 100  $\mu\text{m}$ . Unlike asbestos fibres there was little variation in fibre width, with all

## research papers

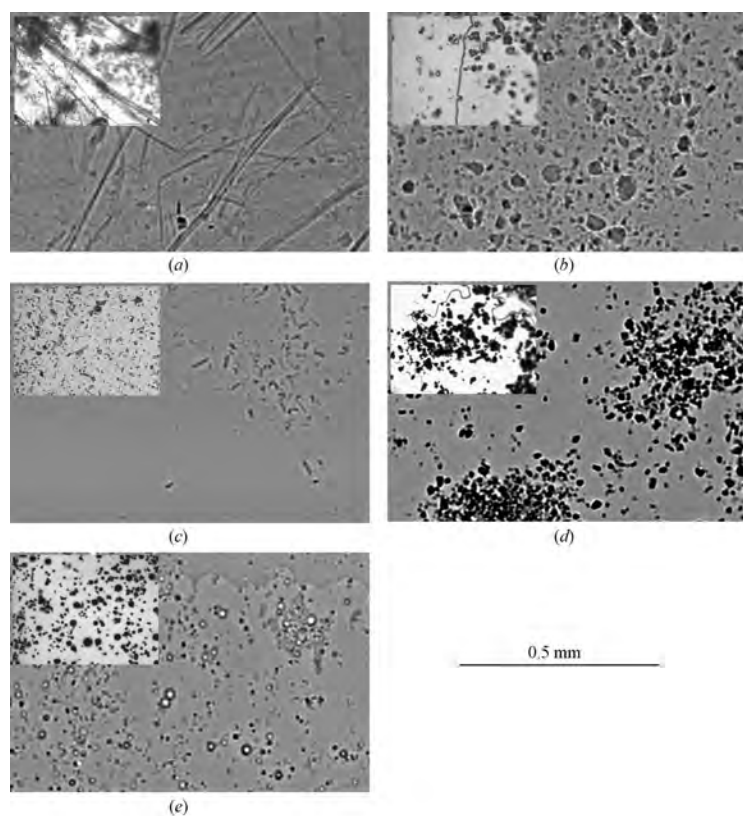


**Figure 1**  
*In vitro* dry particulate testing revealed the particulates that were visible using PCXI. Samples were examined under PCXI (main pictures) and light microscope (insets): (a) asbestos, (b) quarry dust, (c) fibreglass, (d) galena and (e) silver-coated hollow glass beads. The morphology of each of the particulates is clearly very different. For layout and presentation purposes, and so they are at the same level of magnification, the PCXI images are cropped to 0.90 mm  $\times$  0.60 mm, and the light microscope images are 0.365 mm  $\times$  0.27 mm.

visible fibres approximately 8  $\mu\text{m}$  wide. Similar to asbestos, fibreglass fibres used here were normally longer than 100  $\mu\text{m}$ , but unlike asbestos the grinding process was effective for reducing the length of the fibres. We did not observe an enmeshed network when examining the fibreglass samples and there was no difficulty drawing or expelling the fibreglass samples in solution *via* the thin cannula.

Samples containing lead were obtained by grinding galena (PbS). Not surprisingly, these particles were easily detected under PCXI, primarily *via* absorption, and appeared similar to images obtained under light microscopy (Fig. 1*d*). The galena particles ranged in size from 10  $\mu\text{m}$  up to 30  $\mu\text{m}$ , and in comparison with the quarry dust they were denser, more uniform in shape, and were less varied in size. Since all samples were prepared as a percentage *w/v*, the galena samples contained fewer particles per volume owing to the higher density of the mineral; nevertheless, there were sufficient particles present for *in vitro* detection.

We have routinely employed silver-coated hollow glass beads as PCXI markers (Fig. 1*e*) because the air within the bead provides good visibility under PCXI. This is due to the enhanced phase-contrast effect from the high-refractive-index gradient across the glass–air boundary, despite the material producing little absorption. In both the PCXI and light microscopy images the beads were easily detected, with diameters varying between 12  $\mu\text{m}$  and 25  $\mu\text{m}$  despite the stated nominal diameter being 14  $\mu\text{m}$ . Under light microscopy all the beads appeared solid, because the silver coating makes them opaque to visible light. However, under PCXI most beads appeared hollow because the air within them refracted the X-ray beam so that they showed up more clearly with phase contrast. Some of the smaller beads present were not hollow, and so produced little phase contrast.

At the completion of the *in vitro* testing, five particle types were considered sufficiently visible to warrant study *in vivo*. Not all particles detected *in vitro* were suitable because the mouse head structures surrounding the airway being imaged would obscure particulates that were poorly visible *in vitro*. For *in vivo* study we selected the fibrous particulates asbestos and fibreglass, and the non-fibrous quarry dust and galena. We also used silver-coated hollow glass beads as reference particles. The largely carbon-based particulates, combusted diesel, PM10 and laser printer toner, were not sufficiently visible to warrant *in vivo* testing.

### 3.2. *In vivo* studies

**3.2.1. Site of particulate delivery in mouse airway.** The 10 mm delivery depth of the nasal airway cannula placed the tip just anterior to the origin of the nasopharyngeal airway (Fig. 2). This location was approximately 5.5 mm anterior to our standard nasopharyngeal imaging region near the skull-bone suture line (Parsons *et al.*, 2008) that is readily located in each animal.

**3.2.2. Determination of dosing protocol.** Based on the *in vitro* studies, an initial testing protocol for use in live mice was created to achieve maximal use of each mouse and the limited beam time available. After a brief baseline imaging period (no treatment), each animal received one of the fibrous particle instillations (either asbestos or fibreglass), along with the reference hollow glass beads. The instillation was

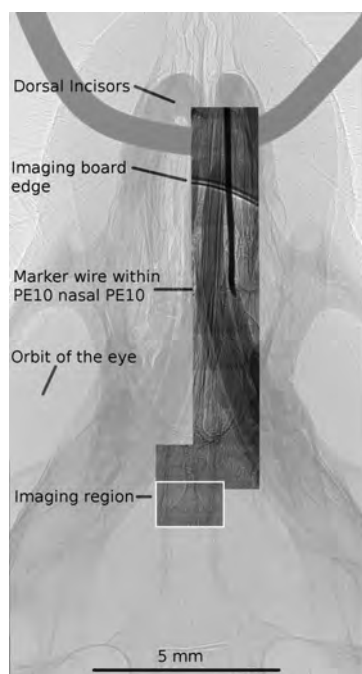


**Figure 2**  
A montage of 13 individual adjacent and offset PCXI images showing the cannula position and the imaging location (white square), overlaid on a larger general PCXI image of the whole mouse skull (taken from Parsons *et al.*, 2008). The fine-gauge wire reaching to the cannula tip is apparent (the cannula itself cannot be discerned at this magnification). As shown here, the tip is located at the rear of the olfactory region. The plastic restraint board used in these latter studies included a cut-out region; the curved edge of this opening is noted. For additional anatomical landmarks, see Parsons *et al.* (2008).

performed remotely over 60 s using a syringe pump (dose volumes as determined below). Approximately 25 min later one of the non-fibrous particulates (either galena or quarry dust) was delivered manually over 10 s; manual solution changes required opening of the imaging hutch for physical access to the instillation syringe by the experimenter. This protocol ensured that all particulates could be tested using a small number of mice, while the simultaneous delivery of the control particles (glass beads) was used to confirm that successful instillation had occurred.

**3.2.3. Effect of particulate delivery volume, rate and concentration.** Based on the overall particulate density seen in the *in vitro* PCXI images, concentrations of 0.5% *w/v* for fibreglass and asbestos (mixed with 0.5% *w/v* reference glass beads) and 0.1% for galena and quarry dust were chosen, to provide a sufficient quantity of particulates to be visible *in vivo*, but to limit the possibility of cannula or airway blockage during deposition.

Initially the volume was set at 50  $\mu\text{l}$  delivered over 10 s, replicating the tolerable dose volume typically used when dosing the mouse lung *via* the nasal airway. This combination

was tested in one mouse. Fluid and particles were detected immediately after dose delivery began. However, the 50  $\mu\text{l}$  volume produced a period of cough-like respiratory excursions that, while small and transient, caused sufficient body movement to produce blurring of some captured images. These factors suggested that smaller doses delivered over a longer period should be trialled to minimize movements caused by the dosing protocol, while retaining the ability to detect particles in the nasal airway.

Accordingly, the dose volume was progressively reduced in two subsequent mice. We found that a 15  $\mu\text{l}$  dose volume provided sufficient visible fluid and particulates to be monitored in the nasal airway, but induced only a brief increase ( $< 1$  min) in respiratory effort. Importantly, subsequent dosing in the same animal was also well tolerated with this dose volume. For the fibrous particulates the 15  $\mu\text{l}$  dose was delivered by syringe pump over a period of 60 s, commencing after the initial 60 s of baseline imaging. As the galena and quarry dust particles settled more rapidly, these were manually instilled over a period of approximately 10 s. This protocol was used for the seven remaining animals.

**3.2.4. Particulate detection.** Using the motion-detection software all five particulates could be detected *in vivo*, although with different degrees of visibility and with varying levels of difficulty. On the airway surface the fibrous particulates were surrounded with fluid; since this was of similar refractive index to these particles it resulted in a reduction in phase contrast and a loss of particle visibility within the fluid envelope. Thus *in vivo* detection of all particles (other than the hollow glass beads) was more reliant on absorption contrast than phase contrast.

For both fibrous particles an initial bulk liquid dose moved past the imaging site within approximately 90 s after the start of dose delivery. The rapid movement coupled with relatively long exposure times meant that we could not determine whether particulates were contained within the moving liquid. Because the heavier non-fibrous particulates (galena and quarry dust) were delivered manually and there was a delay (typically 1 min) between particulate delivery and imaging, during which the beamline hutch was closed and the X-ray shutter was opened, we were unable to determine whether an initial bulk movement of the dose liquid was present immediately after delivery.

Compared with the number and size of the particulates detected *in vitro* (Fig. 1), very few large particulates were seen *in vivo* (Figs. 3–7). Large particles that were detected took longer to appear at the imaging site than the small particulates. Additionally, in some animals asbestos fibres took 4 to 5 min to appear. In comparison, all other particulates appeared within 1 min of commencing instillation (or as soon as imaging could be started in the case of the galena and quarry dust).

The rate at which the different particulate types moved along the airway varied widely, between 0.1  $\text{mm min}^{-1}$  and 4.4  $\text{mm min}^{-1}$ . When examining the non-fibrous particulates, a small number of fibrous particulates from the first part of the dosing protocol 30 min beforehand continued to move past the imaging site. However, the different appearance of each

## research papers

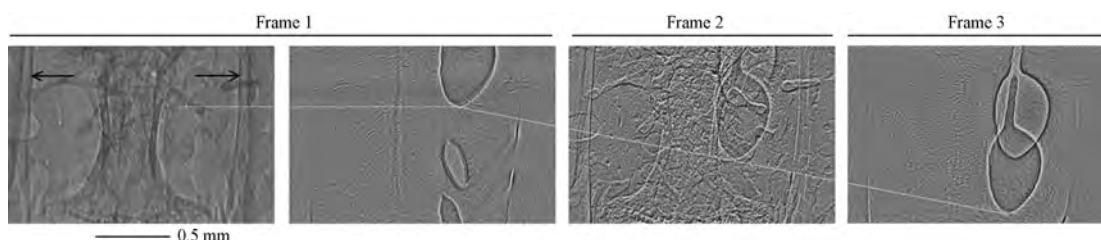


**Figure 3** Asbestos particulate detection. The two panes on the left show the original PCXI image and its corresponding motion-detected frame that revealed the moving object on the airway. The panes on the right are the next two motion-detected frames in the sequence. The black arrows mark the nasal airway edge running vertically through the image, and the white lines follow the same object across the three sequential frames each separated by 5 s. The last frame shows an enveloped clump of fibres with an elongated tail. These enveloped structures moved along the airway faster than all other particles studied, here at a rate of  $4.4 \text{ mm min}^{-1}$ .

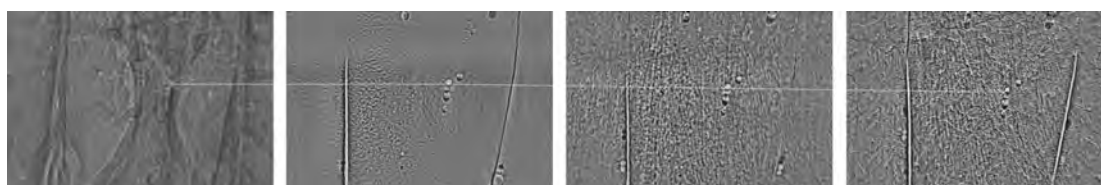


**Figure 4** Four particles of quarry dust are visible at the centre of the motion-detected frames. Particles did not aggregate or have the appearance of trapping liquid around them on the airway surface. In this sequence the quarry dust particles are moving at a rate of  $0.41 \text{ mm min}^{-1}$ .

particle type in the airway ensured that they could still be differentiated.

### 3.2.5. Appearance of particulates in live mouse airway.

**Asbestos.** Fig. 3 shows the appearance of asbestos fibres as revealed using the motion-detection software (see *Methods*). In this and all other *in vivo* images presented here, the first frame is the raw PCXI image and the second is its corresponding motion-detected frame. On the right are the next two motion-detected frames captured 5 s and 10 s, respectively, after the original frame. Interestingly, the third pane in Fig. 3 shows more background detail because a slight movement of the mouse head was picked up by the motion detection. Unlike in the *in vitro* study, individual asbestos fibres were not detected, but appeared as agglomerations of enmeshed fibres trapped in liquid. The enveloped structure could be seen moving along the airway. We noted that there were few of these agglomerations present, but where detected they were large compared with the sizes of the individual fibres, in some cases up to 1 mm in length. These structures moved more rapidly *in vivo* than the other particulates. The sequence in Fig. 3 shows the unusual shape of these airway surface structures which often possessed a 'tail' that trailed behind the fluid envelope.

**Quarry dust.** The quarry dust was also readily detectable *in vivo* (Fig. 4) where it appeared as compact and irregularly shaped particles. The smallest detectable dust particles were approximately  $10 \mu\text{m}$ , but, unlike in the *in vitro* study where large particles up to  $90 \mu\text{m}$  diameter were present, most *in vivo* particles were smaller, less than  $\sim 50 \mu\text{m}$ . While the quarry dust particles produced a greater image contrast than that

seen with asbestos, there was no appearance of aggregation; the dust was only present as individual particles and did not show a fluid envelope when detected on the airway surface.

**Fibreglass.** Although fibreglass was substantially less visible than either asbestos or quarry dust *in vitro*, it was readily detectable *in vivo* (see Fig. 5). Fibreglass fibres displayed the smooth, enveloped, but irregularly shaped form similar to that seen with asbestos. Individual fibres were generally not visible, thus we could not determine a minimum detection size. These enveloped fibreglass shapes moved at approximately one tenth of the rate of the larger asbestos objects.

**Galena (PbS).** Despite its high density, galena was difficult to detect *in vivo*. The particles were smaller than quarry dust and did not provide strong phase contrast (*i.e.* detection appeared to be *via* absorption only) (Fig. 6).

**Hollow glass beads.** As noted above, the air contained within these small beads enhanced their visibility owing to phase contrast. When delivered concurrently with the fibrous particulates they were visible (albeit sometimes in low numbers) in many images (Fig. 7). Like galena and quarry dust, the hollow glass beads appeared as individual particles and their appearance did not indicate that a liquid envelope was present whilst moving along the airway surface.

## 4. Discussion

The primary goal of this study was to determine whether the refractive (phase) and absorption characteristics of common pollutant particles permitted their detection in live mouse airways using synchrotron PCXI. The *in vitro* results showed



**Figure 5**

Fibreglass appears similar to asbestos, but the objects were smaller and had shorter tails. Like asbestos, the fibres appeared to smoothly trap liquid around them so that individual fibreglass fibres could not be seen. Fibreglass moved at the same speed as the quarry dust, at  $0.41 \text{ mm min}^{-1}$ .

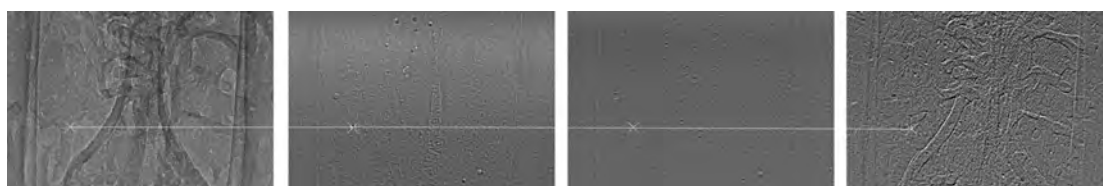


**Figure 6**

Galena particles were the most difficult to locate in the *in vivo* PCXI images, and also moved the slowest, at  $0.1 \text{ mm min}^{-1}$ .

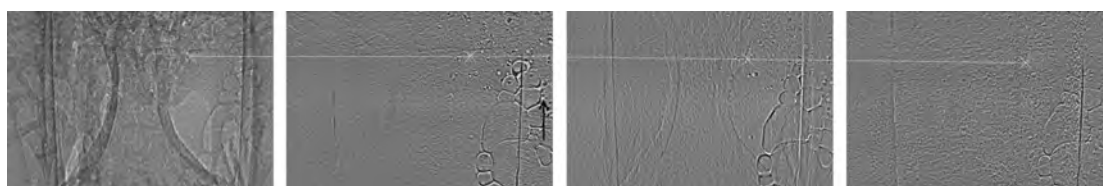


**Figure 7**

Reference hollow glass beads. In this animal, beads are located in the nasal airway, but also in the mouth (black arrow to the right of the right-hand-side airway edge). The glass beads moved in the nasal airway at  $0.3 \text{ mm min}^{-1}$ .

that the PCXI technology was well suited to the detection of asbestos, quarry dust, fibreglass and galena as raw particulates.

To our knowledge this is the first report of the ability to detect and monitor the surface behaviour of these pollutant particles, non-invasively, in live airways. This capability is significant because PCXI has the unique ability to image the initial deposition, airway surface appearance, and the movement characteristics of individual particulates on an intact live airway surface. Furthermore, this approach has provided new information about the behaviour of individual particles of potential significance in studying respiratory disease from the earliest points of interaction in the airway, at times far earlier than previously possible.

Our ability to use *in vivo* PCXI imaging during the actual instillations of particulates, *via* a remote-controlled syringe pump, demonstrated that a volume of  $15 \mu\text{l}$  was sufficient to produce detectable particulates in the nasal airway, and that this dose setting ensured there were minimal respiratory side effects able to cause movements that blurred subsequent image captures. These side effects may have been greater than normal because mice were imaged in a vertical orientation, whereas mice are normally studied supine or prone when anaesthetized in biomedical studies. Gravity may also have

impeded clearance of instilled fluid that reached the lung, causing higher than normal cough and respiratory excursions.

In general, there were smaller numbers of particulates detected than expected, given the concentration and volume delivered. Some of the delivered volume may have been trapped in the tortuous olfactory passages present in mice, and it is not possible to know the exact location of the cannula tip in this complex organ [see Mery *et al.* (1994) for anatomical details] when introduced *via* the nose (Parsons *et al.*, 2008). More frequent detection of particulates could occur if the particle concentration was higher, especially for galena and quarry dust. However,  $0.1\% \text{ w/v}$  is the common standard dose concentration for fluid-based instillations in mouse models, when testing the effects of atmospheric particulates on airway and lung health (I. Gilmour, personal communication). Accordingly, use of higher particle concentrations [as a percentage (*w/v*)] would not align with accepted practice. We believe that better targeting of cannula tip, confirmed by placement *via* orthogonal imaging at the commencement of PCXI studies, will improve nasal as well as lung delivery when using small dose volumes.

Although individual asbestos and fibreglass fibres were not visible *in vivo*, both fibres appeared to attract a liquid

## research papers

---

envelope around them when observed on the airway surface. In contrast, galena and quarry dust remained visible as individual particles. The fibreglass particle agglomerates were smaller than for asbestos, presumably owing to the much shorter particle lengths created by the grinding process. Asbestos fibres naturally aggregate through hydrogen bonding, depending on the relative exposure of their hydroxylated surfaces, either in the natural mineral or after extended exposure to water (Healey & Young, 1954; Pundsack, 1955). Our inability to grind the asbestos under water (Papirer & Roland, 1981) to produce uniform suspensions of smaller fibres supports this interpretation. In this setting we interpret the objects found transiting the airway surface after dosing as enmeshed asbestos fibre clumps enveloped with fluid, and this interpretation is supported by the similar structures present after fibreglass fibre delivery. Furthermore, both types of fibres clumped such that in many cases an enclosed 'tail' followed behind the direction of movement of the object. Although we could not detect individual fibres within these objects, it seems likely that these tails contained fibres that extended behind the core meshed clump of fibres as it moved along the airway surface.

Since we never observed individual asbestos fibres on the airway we could not determine the size of the delivered fibres or the minimum size of asbestos fibres that were detectable *in vivo* via PCXI. The high rate of movement of these objects, much larger than both the similar fibreglass-based objects and the other individual particles, raises the possibility that airways deal with the deposition and transport of fibre-based particles on live airway surfaces *via* a fundamentally different mechanism to that underlying deposition of non-fibrous particles like dust and galena. Inhalation of asbestos can have devastating health consequences on lung health, and further study of the way that airways handle such fibres when they are first encountered may provide new insights into the earliest pathophysiological components of asbestos lung disease.

Galena was difficult to detect *in vivo* despite its high density because it was the smallest of all the particles, and there were fewer particles present (on a *w/v* basis). We also noted that galena particulates rapidly settled out of the delivery fluid, reducing the delivery effectiveness from the dosing cannula. In addition, because of the imaging delay after manual instillation and the upright orientation of the mouse, some of the heavier particulates may have already passed the imaging site by the time imaging commenced, especially if carried within a large initial bolus that would likely have been produced by delivery over the shorter instillation time of 10 s. Smaller galena particles could also be mistaken for the small dark spots present in baseline images and probably caused by individual or overlaid phase-contrast edge-enhancement effects derived from the various skull-bone fine structure encountered by the X-ray beam as it transits the head. Accordingly, we propose that it is essential to analyse these image sequences using motion-detection routines so that only moving particles were detected. Galena also produced little phase contrast and it did not trap an envelope of liquid around it. We speculate that the absence of a liquid layer around the

galena, quarry dust and glass beads could also in part be due to the interaction between their shape and the local surface tension environment on the airway surface.

To our knowledge this is the first study to examine PCXI detection of individual particles *in vivo*, and there are a number of limitations inherent in the techniques and the interpretation of the results we have provided. While our findings are novel, use particles relevant to respiratory health (excluding the reference hollow glass beads) and show the potential of PCXI for studying live mouse airways, the nature and controllability of the particulate doses is not yet optimal, and the normal exposure and uptake of those particulates is quite different.

Firstly, the effective (aerodynamic) diameter of inhaled particulates must be less than approximately 10  $\mu\text{m}$  to be capable of inhalation past the oropharynx, into the lung of humans. Fibres and particles below approximately 1–2  $\mu\text{m}$  in diameter can be inhaled into the deepest parts of the lungs (Miserocchi *et al.*, 2008) while larger sizes such as the >7  $\mu\text{m}$  fibres we examined *in vitro* would contact the conducting-airway walls and be removed by mucociliary clearance and coughing. An improvement in the minimum size detectable under PCXI will be important for ensuring biological relevance in future instillation or inhalation studies, especially with the growing awareness of the importance of ultrafine (<2.5  $\mu\text{m}$  diameter) particles. Secondly, the lead-containing particles were ground galena which is a form of lead different to that inhaled as lead fumes (*e.g.* lead sulfates or oxides) from a lead smelter or in leaded petrol. Finally, for fibreglass there are many forms and uses of this fibre, and the type of fibreglass we used (from pipe lagging) may not be representative of that producing exposure at health-affecting levels in industrial or residential settings.

Although convenient experimentally, delivering particles into mouse airways within a distilled water bolus is not usual in life; inhalation as an aerosol or a dry powder is more physiologically relevant, and planned studies will examine this particle delivery approach. The methodology we used, though effective, also warrants improvement if PCXI is to become a useful technique in respiratory research. While the skull-bone suture line is easy to locate in the mouse nasal airway and produces a repeatable and stable imaging location under PCXI, we are now examining effects in lung airways since this is the relevant target organ.

Despite some difficulty detecting and tracking particles in the raw image sequences, moving particulates could be readily revealed using motion-detection processing. Unfortunately motion-detection analysis is not suited to detecting stationary particles. However, from our experience we propose that such analysis will be essential when performing such *in vivo* non-invasive studies of airway particulate deposition.

In these first studies little effort was made to limit radiation dose, which was too intense to consider animal recovery and repeated imaging. The current rapid development of synchrotron and imaging technology suggests there will continue to be improvements in CCD sensor technology, and analytical techniques such as motion detection and particle

tracking. Combined, they should lead to improved image resolution and higher light sensitivity, allowing smaller, and therefore more physiologically relevant, particulates to be detected and tracked. Minimizing tissue motion *via* combined respiratory and cardiac gating (Sera *et al.*, 2008) will reduce blurring and motion artefacts and result in more usable images. These gradual improvements should result in better particulate visualization to permit deposition and detection of smaller particulates, as well as shorter exposure times that both minimize motion artefact and produce essential reductions in radiation dose. However, despite these needs for improvement there are no imaging alternatives that can non-invasively detect and track such small and individual particles or fibre clusters *in vivo*, and these PCXI techniques should provide a novel addition to the imaging tools available for use in live airways.

Studies supported in part by the NH&MRC Australia, USA CF Foundation and philanthropic donors *via* Cure4CF (<http://www.cure4cf.org/>). SPring-8 experiments were conducted under proposal 2008B1985. Mr Paul Whiffen, Environment Manager, Boral Resources (SA) Limited, provided access to the dolomite quarry dust samples. Dr Ian Gilmour, USA EPA, supplied the combusted diesel and PM10 particulates. KSM was supported by an Australian Postgraduate Award, a Monash University J. L. William Scholarship and a Cystic Fibrosis Australia Studentship.

## References

- Addison, J. & McConnell, E. E. (2008). *Regul. Toxicol. Pharmacol.* **52**, S187–S199.
- Cloetens, P., Barrett, R., Baruchel, J., Guigay, J. P. & Schlenker, M. (1996). *J. Phys. D*, **29**, 133–146.
- Donaldson, S. H., Corcoran, T. E., Laube, B. L. & Bennett, W. D. (2007). *Proc. Am. Thorac. Soc.* **4**, 399–405.
- Grubb, B. R. & Boucher, R. C. (1999). *Physiol. Rev.* **79**, S193–S214.
- Grubb, B. R., Jones, J. H. & Boucher, R. C. (2004). *Am. J. Physiol. Lung Cell Mol. Physiol.* **286**, L588–L595.
- Healey, F. H. & Young, G. J. (1954). *J. Phys. Chem.* **58**, 885–886.
- Limberis, M., Anson, D. S., Fuller, M. & Parsons, D. W. (2002). *Human Gene Ther.* **13**, 2112.
- Livraghi, A. & Randell, S. H. (2007). *Toxicol. Pathol.* **35**, 116–129.
- Mery, S., Gross, E. A., Joyner, D. R., Godo, M. & Morgan, K. T. (1994). *Toxicol. Pathol.* **22**, 353–372.
- Miserocchi, G., Sancini, G., Mantegazza, F. & Chiappino, G. (2008). *Environ. Health*, **7**, doi:10.1186/1476-069X-7-4.
- Papirer, E. & Roland, P. (1981). *Clays Clay Miner.* **29**, 161–170.
- Parsons, D. W., Morgan, K., Donnelley, M., Fouras, A., Crosbie, J., Williams, I., Boucher, R. C., Uesugi, K., Yagi, N. & Siu, K. K. W. (2008). *J. Anat.* **213**, 217–227.
- Pundsack, A. L. (1955). *J. Phys. Chem.* **59**, 892–895.
- Sera, T., Yokota, H., Fujisaki, K., Fukasaku, K., Tachibana, H., Uesugi, K., Yagi, N. & Himeno, R. (2008). *Phys. Med. Biol.* **53**, 4285–4301.
- Snigirev, A., Snigireva, I., Kohn, V., Kuznetsov, S. & Schelokov, I. (1995). *Rev. Sci. Instrum.* **66**, 5486–5492.
- Wildhaber, J. H. (2006). *Paediatr. Respir. Rev.* **7**(Suppl. 1), S86–S87.
- Wilkins, S. W., Gureyev, T. E., Gao, D., Pogany, A. & Stevenson, A. W. (1996). *Nature (London)*, **384**, 335–338.
- Yabashi, M., Yamazaki, H., Tamasaku, K., Goto, S., Takeshita, K., Mochizuki, T., Yoneda, Y., Furukawa, Y. & Ishikawa, T. (1999). *Proc. SPIE*, **3773**, 2–13.



---

## Appendix E

*A new technique to examine individual pollutant particles and fibre deposition and transit behaviour in live mouse trachea.*

by Martin Donnelley, Karen K. W. Siu, Kaye S. Morgan, William Skinner, Yoshio Suzuki, Akihisa Takeuchi, Kentaro Uesugi, Naoto Yagi and David W. Parsons.

Published in the Journal of Synchrotron Radiation **17**, pp. 719-729, 2010.

---

This paper was published in the Journal of Synchrotron Radiation and is made available as an electronic reprint with the permission of the IUCr. The paper can be found at the following URL on the IUCr website: <http://scripts.iucr.org/cgi-bin/paper?S0909049510028451> Systematic or multiple reproduction or distribution to multiple locations via electronic or other means is prohibited and is subject to penalties under law.

---

### Declaration for Appendix E, work supplementary to Thesis Chapter 6

In the case of Appendix E, contributions to the work involved the following:

Name	% contribution	Nature of contribution
Martin Donnelley		Contributed to the planning and original live imaging experiments, data analysis and the wrote up the paper
Karen Siu		Contributed to the planning and original experiments, data analysis and proofreading
Kaye Morgan	10%	Contributed to the planning and original live imaging experiments, image processing and proofreading
Andreas Fouras		Contributed to the original live imaging experiments
William Skinner		Contributed to the planning and provided some pollutants for use in the experiments
Yoshio Suzuki		Contributed to the original experiments
Akihisa Takeuchi		Contributed to the original experiments
Kentaro Uesugi		Contributed to the original experiments
Naoto Yagi		Contributed to the original experiments
David Parsons		Provided the context for the imaging problem, contributed to the planning and original experiments, data analysis and proofreading

#### Declaration by co-authors

The undersigned hereby certify that:

1. the above declaration correctly reflects the nature and extent of the candidate's contribution to this work, and the nature of the contribution of each of the co-authors.
2. they meet the criteria for authorship in that they have participated in the conception, execution, or interpretation, of at least that part of the publication in their field of expertise;
3. they take public responsibility for their part of the publication, except for the responsible author who accepts overall responsibility for the publication;
4. there are no other authors of the publication according to these criteria;
5. potential conflicts of interest have been disclosed to (a) granting bodies, (b) the editor or publisher of journals or other publications, and (c) the head of the responsible academic unit; and
6. the original data are stored at the following location(s) and will be held for at least five years from the date indicated below: School of Physics and Monash Centre for Synchrotron Science, Clayton Campus, Monash University, Australia.

#### Signatures:

Martin Donnelley:		Date: 18.10.10
Karen Siu:		Date: 17.10.2010
Kaye Morgan:		Date: 18/10/10
William Skinner:		Date: 15-10-10
Yoshio Suzuki:		Date: }
Akihisa Takeuchi:		Date: 19.10.2010
Kentaro Uesugi:		Date: }
Naoto Yagi:		Date: }
David Parsons:		Date: 15-10-10

## A new technique to examine individual pollutant particle and fibre deposition and transit behaviour in live mouse trachea

Martin Donnelley,<sup>a\*</sup> Karen K. W. Siu,<sup>b,c</sup> Kaye S. Morgan,<sup>c</sup> William Skinner,<sup>d</sup> Yoshio Suzuki,<sup>e</sup> Akihisa Takeuchi,<sup>e</sup> Kentaro Uesugi,<sup>e</sup> Naoto Yagi<sup>e</sup> and David W. Parsons<sup>a,f,g,h</sup>

<sup>a</sup>Respiratory and Sleep Medicine, Women's and Children's Hospital, Adelaide, Australia, <sup>b</sup>Monash Centre for Synchrotron Science, Monash University, Victoria, Australia, <sup>c</sup>School of Physics, Monash University, Victoria, Australia, <sup>d</sup>Ian Wark Research Institute, ARC Special Research Centre for Particle and Material Interfaces, University of South Australia, Australia, <sup>e</sup>Spring-8/JASRI, Hyogo, Japan, <sup>f</sup>Centre for Stem Cell Research, University of Adelaide, Australia, <sup>g</sup>Department of Paediatrics and Reproductive Health, University of Adelaide, Australia, and <sup>h</sup>Women's and Children's Health Research Institute, Adelaide, Australia. E-mail: martin.donnelley@adelaide.edu.au

During respiration, particles suspended in the air are inhaled and unless cleared by airway defences they can remain and affect lung health. Their size precludes the use of standard imaging modalities so we have developed synchrotron phase-contrast X-ray imaging (PCXI) methods to non-invasively monitor the behaviour of individual particles in live mouse airways. In this study we used these techniques to examine post-deposition particle behaviour in the trachea. PCXI was used to monitor the deposition and subsequent behaviour of particles of quarry dust and lead ore; fibres of asbestos and fibreglass; and hollow glass micro-spheres. Visibility was examined *in vitro* and *ex vivo* to avoid the complicating effects of surrounding tissue and respiratory or cardiac motion. Particle behaviour was then examined after deposition onto the tracheal airway surfaces of live mice. Each particle and fibre looked and behaved differently on the airway surface. Particles lodged on the airway shortly after deposition, and the rate at which this occurred was dependent on the particle type and size. After the live-imaging experiments, excised airway samples were examined using light and electron microscopy. Evidence of particle capture into the airway surface fluids and the epithelial cell layer was found. PCXI is a valuable tool for examining post-deposition particulate behaviour in the tracheal airway. These first indications that the interaction between airways and individual particles may depend on the particle type and size should provide a novel approach to studying the early effects of respired particles on airway health.

### 1. Introduction and objectives

Air pollution is a significant environmental and health concern. Man-made airborne pollutants from a wide variety of sources are suspended in the air in liquid, gaseous or solid forms. We have previously described a new technique to image solid particulates and fibres such as quarry dust, fibreglass, asbestos and lead in mouse nasal airways (Donnelley *et al.*, 2009). These pollutants have the potential to produce deleterious acute or delayed health effects, and can impact on asthma, cystic fibrosis (CF), bronchitis, emphysema, respiratory allergies and heart disease (O'Connor *et al.*, 2008). For example, CF patients living in regions with high particulate

matter air pollution, such as in metropolitan areas, have decreased lung function as well as an increased risk of pulmonary exacerbations (Goss *et al.*, 2004). Particulate pollution can affect young children more severely than adults, owing to their different lung size and physiology, breathing patterns and rapid development (Wildhaber, 2006). The manner in which particulates deposit onto the airway surface and their behaviour after deposition are poorly understood but are likely to influence or predict key aspects of their subsequent pathophysiology.

Mucociliary transit (MCT) function is one measure of the likely effectiveness by which the airways clear inhaled pollutant particles and is a diagnostic indicator of airway health. To

## research papers

help determine the effectiveness of genetic (Stocker *et al.*, 2009; Limberis *et al.*, 2002) and other potential therapeutics for CF airway disease we have developed novel MCT monitoring methods, based on measuring the transit rate of individual deposited particles, that can be used *in vivo* in mice. Existing methods for quantifying bulk particle clearance in airways (Grubb *et al.*, 2004; Donaldson *et al.*, 2007; Livraghi & Randell, 2007) are unable to non-invasively detect and track the motion of individual pollutant particles in real time and with high resolution. Direct non-invasive visualization of the behaviour of deposited particles in animal-model airways is expected to improve our understanding of airway surface function and suggest novel methods for prevention or treatment of respiratory disease in both young children and adults.

This study utilized synchrotron phase-contrast X-ray imaging (PCXI) to detect, monitor and compare the deposition and transit behaviour of selected pollutant particles in the tracheal airway in live mice. PCXI provides enhanced image contrast by utilizing X-ray refraction in addition to conventional absorption and is particularly useful for achieving soft tissue contrast where the absorption differences are small. Tissue boundaries are enhanced by the phase changes induced by differences in their X-ray refractive indices, provided the X-ray beam has sufficient spatial coherence and the sample-to-detector distance is sufficiently long (Snigirev *et al.*, 1995; Cloetens *et al.*, 1996; Wilkins *et al.*, 1996), characteristics that are achievable using a synchrotron source. We have demonstrated the use of PCXI for novel non-invasive airspace imaging in small animals (Parsons *et al.*, 2008), and for non-invasive particulate detection in live mouse *nasal* airways (Donnelley *et al.*, 2009; Siu *et al.*, 2008). Since deleterious respiratory health effects are predominantly lung-based, the objective of the current study was to establish PCXI techniques to examine particulate deposition and transit behaviour in live mouse trachea. Using commonly inhaled pollutants delivered within a saline carrier we sought to document particle and fibre visibility, post-deposition behaviour on the *tracheal* airway surface, transit rates, differences between particle and fibre types, histological effects and radiation dose. We also aimed to determine whether the anatomical and physiological differences between the *nasal* and *tracheal* airways resulted in different post-deposition behaviour to that which we previously recorded in the mouse nose.

## 2. Methods

Experiments were performed on the BL20XU undulator beamline at the SPring-8 synchrotron radiation facility in Japan, under approvals from the Animal Ethics Committee of SPring-8, and of the Children, Youth and Women's Health Service, Adelaide. The imaging hutch was located in the Biomedical Imaging Centre, 245 m from the storage ring, and the imaging layout (see Fig. 1) was as shown previously (Parsons *et al.*, 2008). Monochromatic 25 keV ( $\lambda = 0.5 \text{ \AA}$ ) X-rays were selected using a standard double-crystal monochromator (Yabashi *et al.*, 1999). At the imaging station the beam size was approximately 4 mm (H)  $\times$  2 mm (V). A



**Figure 1**

The *in vivo* imaging set-up in the BL20XU imaging hutch with the approximate path of the X-ray beam shown in yellow. A diagram of the set-up was shown previously by Parsons *et al.* (2008). The X-ray beam passed through a shutter, ion chamber and the mouse trachea before reaching the X-ray converter and camera. The propagation distance between the mouse and X-ray converter was 135 cm. The hand of a researcher is visible on the right, preparing to deliver a particulate sample to the mouse trachea.

propagation (sample-to-detector) distance of 135 cm was chosen to produce a sufficiently strong bright/dark fringe from the boundary of each particle, so that they could be identified amid intensity variations introduced by overlying tissue and skin. Images were captured using a high-resolution X-ray converter (AA50 Hamamatsu Photonics) with a charge-coupled device (CCD) detector. The converter used a 10  $\mu\text{m}$ -thick scintillator ( $\text{Lu}_2\text{SiO}_5:\text{Ce}$ ) to convert X-rays to visible light, which was then directed to the CCD using a  $\times 20$  microscope objective lens with a numerical aperture of 0.4. The CCD detector was a pco.4000 (PCO Imaging) with an array size of  $4008 \times 2672$  pixels and a  $9 \mu\text{m} \times 9 \mu\text{m}$  native pixel size. This set-up resulted in an effective isotropic pixel size of  $0.45 \mu\text{m}$  and a field of view of  $1.8 \text{ mm} \times 1.2 \text{ mm}$ . The beam was limited to approximately this size using slits where the beam enters the experimental hutch to reduce the radiation dose to the animals. The FWHM of the point spread function, as determined from a horizontal edge image, was measured at  $3.6 \mu\text{m}$ . A fast shutter (Uniblitz XRS6 with VMM-T1 timer unit) received triggers from the ventilator (refer to the *in vivo* study description below) to control image capture to minimize the dose between exposures. Exposure times of 100 ms, 180 ms and 280 ms were used for the *in vitro*, *ex vivo* and *in vivo* studies, respectively. These exposure lengths produced the optimum images, capturing sufficient incident photons to fill the potential dynamic range ( $2^{14}$  grey

levels) of the detector, providing the maximal signal-to-noise ratio without inducing detector saturation.

### 2.1. *In vitro* studies

In this experiment the same five raw pollutant samples previously tested in the mouse *nasal* airway (Donnelley *et al.*, 2009) were examined *in vitro* to verify the particle visibility under PCXI, the particle size distribution, and to determine a suitable concentration for *in vivo* testing in the *trachea*. Chrysotile (white asbestos), provided by the South Australian Museum, was manually ground under water and allowed to settle to produce fibre fractions suitable for examination. Fibreglass from a commercial pipe insulation, and galena, the natural mineral form of lead sulfide (PbS) in lead ore, from the South Australian Museum, were both finely ground using a mortar and pestle. Dolomite quarry dust that settled out of airborne suspension was provided courtesy of the Boral Resources (SA) Limited Linwood Quarry (Adelaide, South Australia). Hollow silver-coated glass beads with a median diameter of 14  $\mu\text{m}$  were obtained from Potter Industries (Melbourne, Australia) for use as reference particles of known composition, shape and size.

For the *in vitro* study raw samples were prepared in physiological saline at concentrations of 0.1% *w/v* and 1% *w/v*, and 15  $\mu\text{l}$  samples were pipetted inside small steel washers (7/32" inside diameter) pressed onto the adhesive surface of Kapton tape, a polyimide film highly transparent to X-rays (Argon Masking, PC500,  $\sim 25 \mu\text{m}$  thick with  $\sim 38 \mu\text{m}$ -thick silicon adhesive). The washers containing the samples were then sealed using a second piece of tape (test samples are shown in Fig. 2f) and mounted for imaging within the imaging hutch on a motorized sample stage with *x* and *y* translation (in a plane perpendicular to the beam direction).

The *in vivo* PCXI images of the pollutants were analysed using *Matlab* (version 7.9.0 R2009b, The MathWorks) to determine their size distribution. Images were automatically adjusted using adaptive histogram equalization, a threshold applied to binarize the image, and a connectivity analysis performed to identify unique objects. The effective diameter of the particles as well as the length and width of the fibres were then calculated using the known effective pixel resolution of the image to produce a distribution histogram. Only objects with a size greater than 4  $\mu\text{m}$  were included because smaller fragments could not be accurately separated by this analysis.

### 2.2. *Ex vivo* studies

A pilot *ex vivo* experiment was performed using one HOS:HR-1 mouse humanely killed by Nembutal overdose ( $\sim 325 \text{ mg kg}^{-1}$  i.p.). The trachea was excised and placed into a sealed and humidified study chamber with Kapton film windows to minimize specimen dehydration during the experiment. The chamber held the excised trachea vertically with each end cannulated with 20 Ga i.v. catheters (Insite, Becton Dickinson, Utah, USA). The chamber was mounted on the sample stage in the imaging hutch such that the X-ray

beam passed laterally through the excised trachea in the same orientation used in subsequent *in vivo* studies. Images were captured at baseline and after delivery of 15  $\mu\text{l}$  bolus samples of the particulates suspended in 0.9% saline. After treatment the sample chamber was also translated vertically to allow the full length of the excised trachea to be imaged using a number of exposures (see Fig. 4a).

### 2.3. *In vivo* studies

*In vivo* experiments were performed using 15 hairless HOS:HR-1 mice weighing  $\sim 18\text{--}26 \text{ g}$ . This hairless strain, commonly used for dermatological experiments in Japan, was chosen to eliminate interference from fur in the high-resolution PCXI images. Mice were anaesthetized with Nembutal ( $\sim 72 \text{ mg kg}^{-1}$ , i.p.) and the imaging area around the trachea was cleared of residual fur using depilatory cream (Nair, Church & Dwight, Australia). The mice were then intubated using an arterial guide wire and a 20 Ga i.v. catheter as an endotracheal (ET) tube (Hamacher *et al.*, 2008). The ET tube was inserted into the trachea to a fixed depth of 22.5 mm from the nose tip to avoid physical perturbation of the more distal imaging region. The catheter needle-hub was immediately cut off to minimize respiratory dead-space, and so that the ET tube was ready for connection to the ventilator circuit. Mice were secured to a polyethylene imaging board with their dorsal incisors hooked over a stainless-steel wire loop and the limbs, shoulders and torso taped to the board to minimize body movements that interfere with high-resolution imaging.

The imaging board was mounted on the hutch sample stage such that the X-ray beam passed laterally through the mouse trachea, at approximately three cartilage rings below the tip of the ET tube (see Figs. 1 and 4b). The ET tube was connected to a flexiVent small animal ventilator (Scireq, Canada), and anaesthesia was maintained using a passively humidified isoflurane  $\text{O}_2$  mixture [Fisher and Paykel HC100 respiratory humidifier and Univentor U400 (Zejtun, Malta) isoflurane vaporiser]. Ventilation was set at 80 breaths per minute, a tidal volume of 20  $\text{ml kg}^{-1}$  (minute ventilation of approximately 1.6  $\text{ml g}^{-1}$ ), and  $\sim 3 \text{ cm H}_2\text{O}$  of PEEP. The almost continuous motion present during normal breathing provides a technically challenging experimental setting so the ventilatory profile was configured with  $T_{\text{inspiration}} = 0.1875 \text{ s}$ ,  $T_{\text{pause}} = 0.3125 \text{ s}$  and  $T_{\text{expiration}} = 0.25 \text{ s}$ , providing a sufficient end-inspiratory pause to allow relatively motion-artefact-free image capture.

Groups of three mice were exposed to each of the five particulates. Image capture was triggered by the ventilator once every 14 breaths (10.5 s). After 3.5 min of baseline collection (20 images) a 15  $\mu\text{l}$  sample of the particulate suspended in saline was manually delivered in a single bolus over 10 s *via* the ET tube using a 25  $\mu\text{l}$  glass syringe. This involved opening the hutch door, manually disconnecting and reconnecting the ET tube from the ventilator and closing the hutch door, producing a delay of typically 1 min between particulate delivery and imaging. Image acquisition was resumed at the same rate for a further 42 min ( $\sim 240$  images), creating a dataset consisting of 260 images per mouse. Since

## research papers

these mice were not allowed to recover after completion of the experiment we did not attempt to minimize the delivered radiation dose (beyond using slits to reduce the beam size and a fast shutter to minimize exposure to the beam); rather, we maximized both the number and quality of the images acquired to ensure the best possible experimental results.

### 2.4. Post-experimental analyses

Mice were humanely killed *via* Nembutal overdose without loss of anaesthesia. In some animals the trachea was excised and fixed for at least 1 h in a non-aqueous fixative (perfluorocarbon FC-72, 3M Corporation, containing 1% osmium tetroxide, OsO<sub>4</sub>) to preserve surface fluid, secretions and mucous *in situ* for subsequent light and electron microscopy to determine where particulates lodged after deposition (Sims *et al.*, 1991). The fixed samples were transferred to 70% ethanol, embedded in acrylic resin and sectioned for light microscopy (post-stained with toluidine-blue) and transmission electron microscopy (post-stained with a saturated solution of ~4% uranyl acetate followed by lead citrate). The elemental composition of the particulates in the fixed tracheal sections was also verified under transmission electron microscopy (TEM) using energy-dispersive X-ray spectroscopy (EDS) microanalysis (Philips CM-200) of unstained sections. Control samples of the raw test particulates were also embedded in resin to provide EDS reference spectra with which the results were compared.

The mouse anatomy at the imaging location introduced confusing detail into the PCXI images since other structures in the path of the X-ray beam, such as rings of tracheal cartilage, skin, bone and other tissues, could obscure individual small particles in single images. To facilitate rapid and accurate location of relevant particles, each image sequence was flat/dark-corrected and contrast enhanced (*Matlab*), and analysed with simple motion-detection software (VirtualDub, version 1.8.6, Avery Lee, using the MSU Motion Estimation plug-in, Graphics and Media Lab, Moscow State University) to reveal where motion was occurring by applying digital image subtraction and filtering algorithms that identify regions of the image that change between frames (Donnelley *et al.*, 2009). For high-quality motion detection the background must remain still compared with the moving objects to be detected, hence special efforts were made to minimize the movement of the mouse during imaging, including the use of restraining boards and respiratory-gating as described above. Particle transit rates were calculated by manually tracking the motion of an individual particle through the image sequence, measuring the distance it travelled using the known effective pixel resolution of the image and then dividing by the elapsed time between the frames.

## 3. Results

### 3.1. *In vitro* studies

The *in vitro* PCXI visibility of the pollutant particles in saline was similar to that previously reported for samples

mixed in distilled water (Donnelley *et al.*, 2009). Owing to the relatively long propagation distance many particles were visible owing to phase or absorption contrast, or a combination of both. Fig. 2 shows the results from these *in vitro* studies, and clearly demonstrates the differences in appearance between particle types. The samples were visible both dry and within saline, indicating that saline had little effect on the overall contrast. For example, absorption dominated the image contrast for galena, and produced shadows with few fringes (Fig. 2*d*). By comparison, hollow glass beads strongly refracted the X-rays and produced phase contrast visible as light and dark fringes; however, no dark shadows were produced since the beads are very thin walled and hollow (Fig. 2*e*). Other particles, such as quarry dust, showed both phase and absorption contrast, appearing darker where the object attenuated the beam, as well as displaying bright/dark fringes around the particle edges (Fig. 2*b*).

Based on our *in vitro* observations a concentration of 1% *w/v* was selected for the *ex vivo* and *in vivo* studies to ensure sufficient particulates were present in a 15  $\mu$ l sample to potentially be visible when deposited into the mouse trachea. The manual grinding employed during the particulate preparation was clearly effective as few large particulates were present, excluding some long asbestos and fibreglass fibres. As

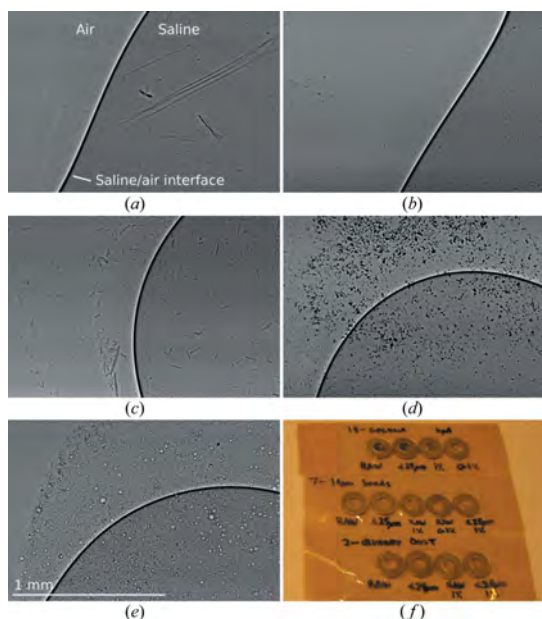


**Figure 2**

PCXI images (1.8 mm  $\times$  1.2 mm) of 15  $\mu$ l samples of 1% *w/v* particulates suspended in saline used for the *in vivo* study are shown for (a) asbestos, (b) quarry dust, (c) fibreglass, (d) galena and (e) silver-coated hollow glass beads. All images are arranged so that the particulates can be seen wet and dry. The dry particles are on the top/left, and the particles in saline are present in the bottom/right. The test sample set-up is shown in (f); samples were placed in the centre of small washers that were encapsulated in Kapton tape.

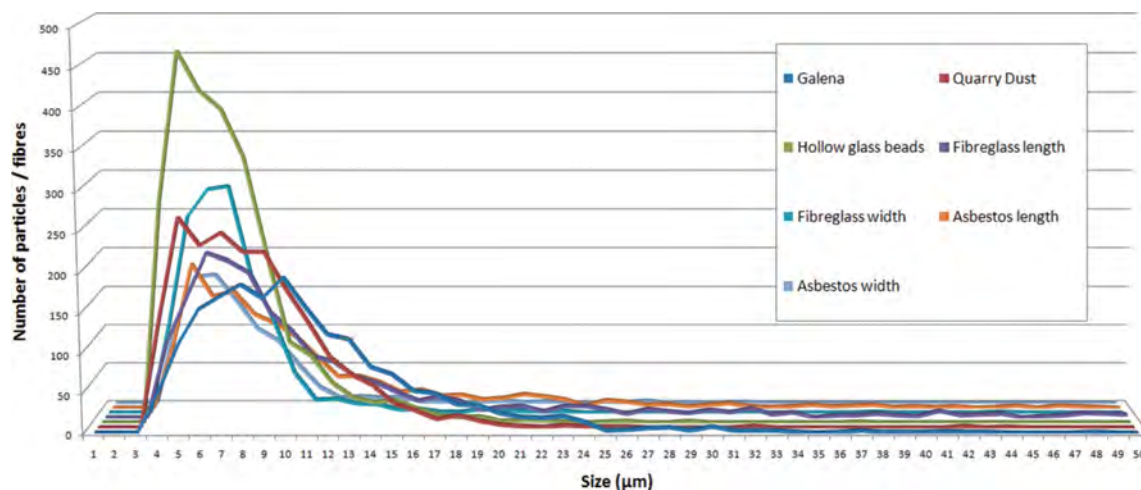


**Figure 3**  
Particle and fibre size distribution measured from the *in vivo* images in Fig. 2.

previously reported (Donnelley *et al.*, 2009), the asbestos could not be finely ground so we relied on differential settling in water to obtain finer size fractions. The size distribution of the particles and fibres is shown in Fig. 3, and verifies that particles typically ranged in diameter from 5 µm up to 12 µm with a small number of larger particles present. The width of the fibres was also within this range, but the lengths were significantly greater. Fibreglass fibres of length  $\geq 40$  µm were not uncommon, but only the asbestos fibres were longer than 50 µm. Despite a stated manufacturers nominal diameter of 14 µm, the majority of the glass beads were smaller.

### 3.2. *Ex-vivo* studies

Prior to use in live mice, particle visibility was verified in a segment of excised mouse trachea. All particulates were easily detected and had similar appearances to those observed in the *in vitro* study [all particulates are visible in Fig. 4(a)]. Although all particulates were detectable, the quarry dust particles were more difficult to detect than the fibreglass, galena and the hollow glass beads. In addition, only one bundle of asbestos fibres was visible in the trachea in contrast to the other particulates, of which many individual particles could be detected. Despite using an enclosed chamber we did find that the excised trachea tended to rapidly and visibly dehydrate resulting in noticeable shrinkage even over a 10 min imaging period. Since the airway tissue was grossly affected by this process we did not attempt to use this system to analyse post-deposition behaviour.

### 3.3. *In vivo* studies

**3.3.1. Site of particulate delivery in mouse airway.** We found that inserting the ET tube to a depth of 22.5 mm placed the ET catheter tip two to three cartilage rings below the top of the trachea (Fig. 4b). In most cases the imaging region was

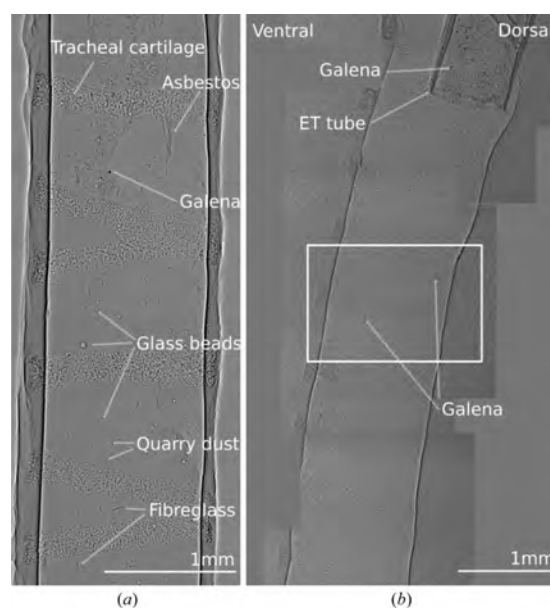


**Figure 4**  
(a) A montage of nine individual PCXI images from the pilot *ex vivo* experiment that examined an excised mouse trachea. The images were taken after all five particulates had been delivered within individual 15 µl boluses. All five particle types are clearly visible and marked. (b) An *in vivo* montage of 15 individual PCXI images with the ET tube uppermost in the trachea. The ET tube opening is approximately two cartilage rings from the top, and the standard imaging location, usually three rings below the bottom of the ET tube, is marked with a white rectangle. Dark particles of galena are apparent within the ET tube as well as at the imaging site in the trachea. Image alignment is poor at some montage frame edges owing to respiratory movements that occurred between image captures.

## research papers

three cartilage rings (~1.5–2 mm) below the end of the ET tube, but in some mice this was adjusted slightly to ensure a clear and less obstructed view of the trachea.

### 3.3.2. Imaging set-up and particulate delivery effects.

The 15  $\mu\text{l}$  dose provided sufficient visible fluid and particulates to be monitored in the trachea and induced no noticeable change in respiratory effort or frequency, as measured by monitoring the airway pressure recorded by the flexiVent. In earlier pilot studies higher doses induced transient coughing that produced blurred images. We noted that for the first 30 min of the experiment image quality was excellent, due largely to the respiratory-gating. It is important to note that the gating only minimized intra-frame motion. Some inter-frame motion still made isolating particle-motion difficult, although securely taping the body to the restraint board minimized this effect. After approximately 30 min most mice displayed large irregular respiratory excursions initially every ~10 breaths, increasing in frequency and magnitude as the experiment continued. Mice remained deeply anaesthetized as assessed by foot pinch, but these movements eventually degraded the quality of the images because the end-inspiratory breath holds became ineffective. Independently increasing the level of anaesthesia (e.g. isoflurane to 3.5%) as well as the tidal volume (to 25 ml  $\text{kg}^{-1}$ ), or using a single total lung capacity manoeuvre once every 5 min to ensure complete lung filling did not alter these complicating respiratory effects.

One mouse was imaged in a supine position and this almost eliminated the irregular respiratory movements, suggesting that the head-high mounting was a likely cause of the respiratory instability we observed. Consistent with this was the observation that the tracheal diameter of some mice reduced over the extended imaging periods, in one case by up to ~0.2 mm. The abdominal contents in some mice also slumped substantially by the end of the imaging period, and cartilage rings moved down slowly relative to the X-ray beam, in some cases by up to ~0.2 mm, such that the imaging position appeared to change over time.

During these experiments the incident photon flux was approximately  $7.47 \times 10^9$  photons  $\text{s}^{-1}$ , producing an estimated dose of approximately 0.13 Gy per exposure delivered to the 1.8 mm  $\times$  1.2 mm imaging area for each of the 280 ms exposures used *in vivo*.

**3.3.3. Appearance and behaviour of particulates in live mouse trachea.** The presence and behaviour of fibreglass, galena, quarry dust and the hollow silver-coated glass beads could be detected *in vivo*, with visibility improved by using motion-detection software during post-experimental processing. Of the pollutants that we could detect with PCXI, galena was the most visible and quarry dust the least visible. Fibreglass and the hollow silver-coated glass beads provided inter-

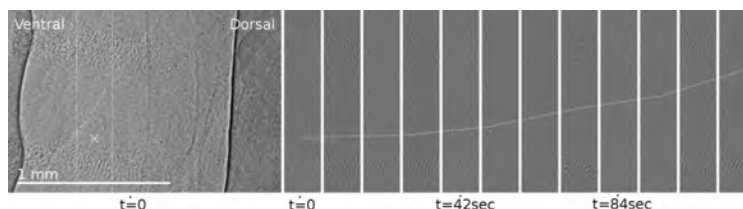


**Figure 5**

*In vivo* imaging of quarry dust in a live mouse trachea. The image on the left was captured approximately 1.75 min after imaging was started, and the location of a quarry dust particle is marked with an X. The sequence of image strips to the right (10.5 s apart) were created by cropping complete image frames as marked, to show the same region in subsequent motion-detected frames. The motion of the dust particle is tracked by the grey line, and demonstrates variability in the rate of particle transit for even a single particle. Other particles were also visible when viewed dynamically, but cannot be seen on these static images. Movie S1 in the online supporting information (QuarryDust.avi) contains a time-lapse movie of the *in vivo* behaviour of quarry dust particles.

mediate visibility. Despite analysing both the raw and motion-detected images we did not positively identify asbestos fibres in any of the image sequences.

Independent of the particle type and size, most particle deposition and particle motion occurred on the dorsal region of the trachea. Compared with the number of particulates detected in the 15  $\mu\text{l}$  *in vitro* samples (for example galena in Fig. 2*d*), few particulates were detected *in vivo*. Interestingly, Fig. 4(*b*) shows that galena particulates remained in the ET tube after delivery to the trachea. As we did not normally image at the ET tube site, it is unclear whether this 'trapping' of galena particles in the ET tube was a consistent phenomena.

When particulates were detected they remained visible throughout the entire imaging period. However, most particle motion in the trachea occurred within the first few minutes of imaging, with almost all particles lodging by the end of the imaging period. Small and/or low-density particles continued their motion for longer than large and/or dense particles; the latter were observed to lodge quickly on the airway surface. Almost all galena particulates appeared to be motionless from the initiation of imaging (~1 min after dose delivery), but in comparison some glass beads continued moving for almost the entire imaging period. The motion and lodging of quarry dust and fibreglass were between these two extremes. Quarry dust appeared as compact and irregularly shaped particles. The smallest detectable dust particles were approximately 5  $\mu\text{m}$  in their largest dimension with larger particles up to 20  $\mu\text{m}$ -diameter present. Most dust particles were approximately 10  $\mu\text{m}$  in diameter. Fig. 5 shows a quarry dust particle moving along the airway over a period of 2.1 min.<sup>1</sup> The transit rate of this particle (and many others) was not uniform, and varied between zero and ~0.5 mm  $\text{min}^{-1}$ . Dust particles were particularly difficult to detect when stationary as they were easily confused with speckled areas of the images, for example regions of bone, cartilage, connective tissue and skin, although motion made these particles more easily detectable.

<sup>1</sup>Supplementary data for this paper are available from the IUCr electronic archives (Reference: MS5027). Services for accessing these data are described at the back of the journal.

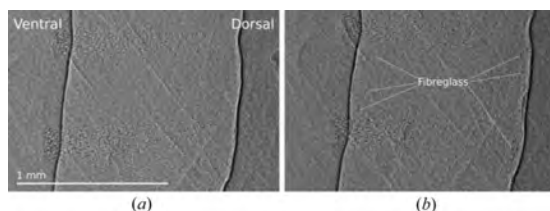


**Figure 6**  
*In vivo* imaging of fibreglass in a live mouse trachea. (a) The trachea immediately prior to fibreglass delivery, and (b) the first image captured after imaging began. Although the fibres were visible in the trachea, they did not move throughout the imaging period. Most fibres were located on the dorsal tracheal surface but in this animal a small number were also visible on the ventral surface. Movie S2 in the online supporting information (Fibreglass.avi) contains a time-lapse movie of the *in vivo* behaviour of fibreglass fibres.

Most fibreglass fibres were 10  $\mu\text{m}$  to 15  $\mu\text{m}$  in width, and ranged in length from 30  $\mu\text{m}$  to 80  $\mu\text{m}$ . The relatively long fibre lengths made fibreglass easier to detect *in vivo* than the quarry dust because they were conspicuous against the tissue background. Small approximately spherical fibreglass particles  $\sim 10$   $\mu\text{m}$  in diameter were also sometimes visible. Fig. 6 shows one example of stationary fibreglass fibres in the trachea. Fibres collected predominantly along the dorsal surface of the trachea, although in this animal a small number of fibres were also present on the ventral surface.

Galena particles did not move substantially over the imaging period, but were easily detected *in vivo* owing to their strong absorption contrast. Particles generally ranged in size from 10  $\mu\text{m}$  up to 25  $\mu\text{m}$ , but clusters of galena approximately 60  $\mu\text{m}$  in diameter were present in two mice. Clusters of this size were not seen in the *in vitro* study (where galena particles were typically less than 25  $\mu\text{m}$  in diameter), suggesting that clustering may have occurred at or after deposition onto the airway surface. In one animal the galena cluster looped between two points in the airway rather than staying stationary; however, this was in contrast to the behaviour of most large galena particles which tended to lodge quickly on the airway surface. Fig. 7 shows the behaviour of this large cluster, with both the transit motion of the galena cluster and the changes in cluster orientation owing to rotation also displayed.

The air contained within the hollow glass beads enhanced their visibility by improving phase contrast, with their spherical shape producing a lensing effect making them visible as relatively bright circles. In the airway the beads were readily visible and varied in size from 10  $\mu\text{m}$  up to  $\geq 20$   $\mu\text{m}$  (despite a stated manufacturer's nominal diameter of 14  $\mu\text{m}$ ). Fig. 8 shows the motion of multiple glass beads along the dorsal tracheal surface and, like galena, their particle motion was not uniform; beads could move in different directions and at different rates. The transit rate of the marked particles varied between  $\sim 0.02$   $\text{mm min}^{-1}$  distally (toward the lung)

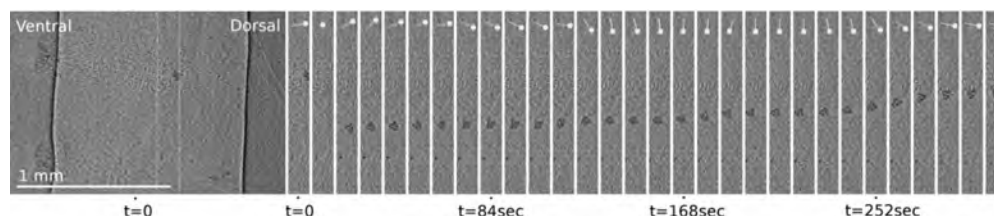


**Figure 7**  
*In vivo* imaging of galena in a live mouse trachea. The image on the left is the first image captured after imaging began, and shows a large cluster of lead particles, as well as smaller individual particles spread throughout the trachea. The strips on the right (10.5 s apart) show the motion of the lead cluster. The indicator at the top of each strip shows the relative rotation of the cluster. Note that between the first and third strips the cluster movement was briefly retrograde. The majority of the other individual galena particles are located toward the dorsal tracheal wall. Movie S3 in the online supporting information (Galena.avi) contains a time-lapse movie of the *in vivo* behaviour of galena particles.

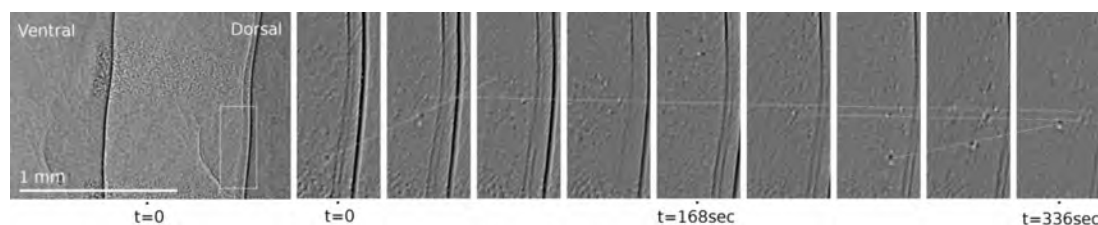


**Figure 8**  
*In vivo* imaging of silver-coated hollow glass beads in a live mouse trachea. The image on the left was captured approximately 2 min after imaging was started. The strips on the right are motion-detected frames 42 s apart from within the marked white rectangle. The motion of four separate particles is marked: two are moving up the trachea at different speeds, and two are moving more slowly down the trachea. A large number of smaller particles moved faster than these, but are not clear on these static images. The majority of the glass bead particle transit was located toward the dorsal tracheal wall. Movie S4 in the online supporting information (GlassBeads.avi) contains a time-lapse movie of the *in vivo* behaviour of hollow glass beads.

## research papers

and  $\sim 0.37 \text{ mm min}^{-1}$  proximally (toward the larynx). In the same animal (data not shown) we also measured smaller glass beads moving proximally at more than twice this rate.

**3.3.4. Histological analyses.** Histological examination using light microscopy revealed that all the particulate types except asbestos were located on or in the airway epithelium. Samples from mice exposed to quarry dust were inadvertently incorrectly processed and could not be examined. Fig. 9 shows the appearance of the particulates in the trachea under light microscopy. Galena appeared as dense black particles, fibreglass as short green and yellow fibres, and the silver-coated hollow glass beads had a distinctive round shape with a dark edge. We did not identify any asbestos fibres in cross sections from asbestos-treated animals. Particles were located above the airway surface captured in fine mucus strings (visible only in TEM images), embedded within the mucus layer adhering to and overlying the epithelium; and enveloped within the

epithelial cells or the epithelial cell ciliary layer. Galena particles were often found more deeply in the epithelial layer than the fibreglass fibres which were typically found at the epithelial cell/air interface, while the glass beads appeared to lodge within and partly displace the cilia and surface liquid of the airway. The spherical glass beads had different apparent diameters and surface detail depending on the level at which they were cut, and small fragments of glass and the silver coating (as verified by EDS analysis) surrounded all of these beads.

EDS analysis was used to confirm the elemental composition of particles present on or in the airway epithelium. Galena produced spectral peaks that corresponded to elements including lead and sulfur; fibreglass to sodium, magnesium, aluminium, silicon and calcium; and the silver-coated glass beads to silicon and silver. The spectra of the particulates present in the trachea sections matched those in the control spectra, confirming the identity of the particles.

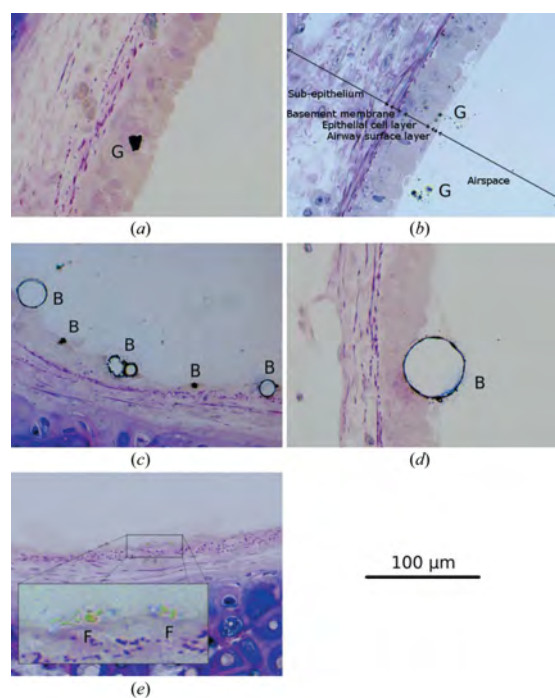


**Figure 9**

Examples of galena (G), fibreglass (F) and hollow silver-coated glass beads (B), captured on the mouse tracheal airway surface. Tissues were fixed using perfluorocarbon  $\text{OsO}_4$ , and semi-thin resin sections cut and stained with toluidine blue. Panel (b) labels the relevant airway epithelium structures in a typical cross section; note that not all features are present on all panels. (a) Galena captured on the surface of the epithelial cell layer, and (b) smaller particles within the cell cilia (in the airway surface layer) and embedded in fine mucus strings (not visible here) above the epithelial cells. (c) The distinctive glass beads are captured on the airway surface, and (d) one large bead of approximately  $55 \mu\text{m}$  diameter appears displaced into the airway epithelium. (e) Small fibreglass fibres embedded in the overlying mucus layer.

## 4. Discussion

The primary goal of this study was to establish methods to deposit a range of common pollutant particles and fibres into live mouse lung airways to enable monitoring of their post-deposition behaviour using synchrotron PCXI. Using histological methods we also sought confirmation of the specific location, and elemental identity, of these particles on or within the cell and surface fluid layers of the airway.

Our *in vivo* results show the suitability of PCXI technology for the detection of particles as diverse as quarry dust, fibreglass, galena and the reference hollow silver-coated glass beads in an intact animal. To our knowledge this is the first report detailing the non-invasive detection and monitoring of the airway surface behaviour of these pollutant particles in live lung airways. This capability is significant because PCXI has the unique ability to image the initial deposition, appearance and movement characteristics of individual pollutant and reference particulates on a live and intact airway surface. The varieties of individual particle behaviour (encompassing consistent speed and direction; stop and start; retrograde movement; changing direction; and rotation behaviour) reveal the diversity in how the airways can handle the deposition and transport of particles. However, the sample size was insufficient to determine whether the different particle types produced distinct patterns of airway surface behaviour. Nevertheless, this new information about the behaviour of individual particles of potential significance in respiratory disease can now supplement well established methods and data derived from monitoring bulk transit rates in airways (Grubb *et al.*, 2004) and can help focus new research into the consequences of particle deposition from the earliest points of their interaction within the airway.

The *ex vivo* pilot study demonstrated that the particulates could easily be detected in an excised trachea with little loss of the identifying characteristics present in our *in vitro* studies.

We suspect that the visible tissue dehydration was caused by the dry air within the imaging hutch, and was further exacerbated by repeated exposures to the intense X-ray beam. With fluid bathing, reliable and precise temperature control, heat dissipation and physiological support we expect that tissue viability would be maintained and dehydration would be eliminated. Since this pilot was only intended to examine the visibility of the tissue and particulates and to demonstrate the feasibility of performing an *ex vivo* study, we did not use it to examine the deposition and clearance behaviour of the test particulates. Comparison with the *in vivo* images confirmed that the tissue surrounding the trachea was the source of background detail that could obscure some particles in captured images. The absence of surrounding tissues, as well as respiratory and cardiac movements, substantially improved particulate visualization in the *ex vivo* system, particularly for those particulates that lodged on the airway surface. We propose that trials in a functional *ex vivo* system may provide a rapid and accurate method to estimate baseline transit rates prior to testing *in vivo*, although the absence of reciprocating airflows may alter airway surface clearance behaviour, as flows are known to affect epithelial cell physiology (Tarran *et al.*, 2005).

In earlier studies of mouse nasal airways (Donnelley *et al.*, 2009) we determined that a 15  $\mu\text{l}$  delivered dose was sufficient, but a particle/fibre concentration of 0.1% *w/v* used there did not provide an adequate number of particles to detect and analyse transit behaviour. Not surprisingly, compared with that nasal study the ten-fold higher particle concentration (1% *w/v*) used here resulted in many more deposited particulates, although still less than expected based on the *in vitro* results. This difference could be explained by the different delivery set-ups: a pipette for the *in vitro* study and a long cannula and glass syringe for the *in vivo* study. Interestingly, we noted there were many particulates visible in the ET tube (*e.g.* Fig. 4b) suggesting that the effectiveness of the delivery system was not optimal. The cannula material may have adherent properties for these particles, so delivery may be improved by using different cannula materials or surface coatings, altering the particulate delivery rate, or adjusting the volume and rate of ET airflow. In addition, unlike in the nasal study we did not detect asbestos fibres *in vivo* using PCXI, nor in sections examined under light microscopy or TEM. In bench studies we have noted that asbestos fibres are prone to clustering and blockage of fine delivery cannulae, so we speculate that asbestos was not successfully delivered to the trachea. In future studies we will refine our techniques and set-up to ensure correct asbestos delivery.

The behaviour of fibreglass fibres in the trachea differed from that noted in earlier nasal airway studies (Donnelley *et al.*, 2009). In the trachea, individual fibreglass fibres were observed, whilst in the nasal airway study fibres were only present within a liquid envelope and individual fibres were not visible. This finding indicates that particle behaviour may be determined by the deposition location within the respiratory system. This may not be surprising, since the nose has evolved to trap particles after inhalation to prevent their inhalation

into the conducting airways and lungs. We also noted that particle behaviour in the trachea was determined by both the type and size of the particles. Smaller and/or low-density particles tended to move faster and for longer periods, and we speculate this was because these particles take longer to be captured on the epithelial surface or in mucus on and above the surface. Regardless of the type or size of the particles, individual particle behaviour was often extremely variable. Thus, while it was possible to visualize individual particle behaviour, this technique does not measure bulk particle transit rates. Despite the vertical orientation of the animal the transit of all particles was consistently localized to the dorsal tracheal wall.

Histological analysis showed that galena particles and glass beads could displace cilia and surface liquid and lodge within the surface of the airway epithelium. Such a behaviour has been predicted for small particles elsewhere (Gehr & Schurch, 1992) and may be related to the surface tension forces acting on the particles. This effect may also be independent of the presence of airway surface mucus. Such a non-specific process might help explain why we observed that so many particles ceased moving soon after delivery.

There were several limitations in this study. Although our PCXI set-up can resolve particles down to less than 4  $\mu\text{m}$ , the visual complexity produced by the anatomical structures surrounding a moving trachea in a live animal means that particles of approximately 5  $\mu\text{m}$  diameter are currently the smallest particles we can accurately detect and track. This is close to the upper size limit for particles that can reach and deposit in the human trachea after inhalation (Oberdorster *et al.*, 2005). Despite this limitation, PCXI was demonstrated to be suitable for examining particulate deposition and post-deposition behaviour, and with improvements in technology the visualization of smaller particles will be possible in the near future.

Both Nembutal (King *et al.*, 1979) and isoflurane (Robertson *et al.*, 2004) have been reported to alter mucociliary transit by affecting mucus rheology and ciliary beat frequency. Therefore it is likely that the true rate of transit is faster than the results suggest. However, the ciliary beat pattern has been shown to be unaffected by isoflurane anaesthesia (Robertson *et al.*, 2004). We are limited by Japanese Government regulation in the choice of anaesthetics available for experiments at the SPring-8 synchrotron, but it is apparent that across the different particle and fibre types, all delivered under the same anaesthetic regime, there are clear differences in post-deposition transit behaviour.

This study was also constrained by the inability to enter the synchrotron imaging hutch during imaging. In these first experiments the ventilator was integrated into the imaging set-up in a manner that required manual particulate instillations to be performed. This necessarily introduced a delay while the beamline hutch door was closed and the X-ray shutter was opened to begin imaging, so it was not possible to visualize the actual instillation of the particulates into the mouse airway. Accordingly, we could not observe the presence and clearance of the initial bulk-liquid dose, and our first live images (albeit

## research papers

performed within 1 min of instillation) sometimes revealed that particles had already lodged on the airway surface. Owing to this delay it was also impossible to assess whether any particles in the initial 15 µl bolus were carried directly down toward the lungs. However, the absence of bulk dose fluid on the airway surfaces immediately after dosing (when imaging began) suggests there was a very rapid loss of the dose vehicle, leaving the pollutants deposited on the airway surface. It also suggests that delivering the pollutants within a liquid carrier rather than as dry particles or fibres may have little persistent effect on the airway environment or the deposition behaviour. The experimental complexity and the occupational hazards to researchers when delivering dry or aerosolized pollutant particles are difficult to handle; however, these studies have provided encouraging data to support the efforts needed to safely and effectively test these more physiologically normal delivery methods in the future.

Owing to image complexity from the mouse anatomy and motion from respiratory movements we limited the analysis to the trachea rather than examining the intrapulmonary airways. In future studies we plan to modify the delivery and imaging set-up to enable particulate delivery during imaging to capture the first interactions of the pollutants with the airways and to examine the deeper lung airways where particulate deposition is also important.

Although we limited the radiation dose by reducing the size of the imaging area and minimizing the exposure times, at present the dose delivered using this experimental set-up is too large to consider animal recovery or repeat-imaging experimental designs. However, in other experiments we have found that the exposure times and dose can be reduced by at least a factor of three by increasing the thickness of the scintillator and using a higher quality objective lens. In addition, depending on the experimental aims the number of exposures can be substantially reduced and image quality may be traded for further reductions in exposure length and dose. In addition, the rapid development of imaging and synchrotron technologies should also produce improvements in light sensitivity and image resolution that could allow shorter exposure times to minimize motion artefact and produce desired reductions in radiation dose. With these improvements we expect the dose could realistically be reduced by a factor of ten compared with that delivered in this experiment. Our goal remains to progressively improve our maximum resolution, allowing smaller and therefore more physiologically relevant particulates to be detected and tracked.

Despite these limitations and challenges there are currently no alternative *in vivo* imaging modalities able to non-invasively detect and track such small individual particles or fibre clusters in the mouse *trachea*. Thus we propose that PCXI is a valuable technique for studying the deposition and behaviour of pollutant particles and fibres in the airways of live animal models. We also expect that these experimental techniques will be useful for other synchrotron experiments imaging the upper lung airways of small animals, and are a practical addition to the range of related techniques we have established for use in mouse *nasal* airways.

### 5. Supplementary files

The four supplementary files contain movie sequences showing particulate and fibre behaviour on the tracheal airway surface, and are the source of the images shown in Figs. 5–8. Each 10 s time-lapse video shows 3.5 min of baseline image collection (20 images, 10.5 s apart), followed by 14 min of post-deposition imaging (80 images, 10.5 s apart), and are presented at 105× normal speed. Between the acquisition of these two sequences the particulates were manually delivered into the trachea. All videos are avi files, were encoded using the *DivX* codec and can be played using the free VLC Media Player (available at <http://www.videolan.org/vlc/>).

These studies were supported by the WCH Foundation, NH&MRC Australia, USA CF Foundation and philanthropic donors *via* the CURE4CF Foundation (<http://www.cure4cf.org/>). The synchrotron radiation experiments were performed on the BL20XU beamline at SPring-8, with the approval of the Japan Synchrotron Radiation Institute (JASRI) under proposal number 2009A1878. Dr Andreas Fouras, Monash University Division of Biological Engineering, provided imaging advice and supplied essential experimental equipment including the CCD detector. Mr Paul Whiffen, Environment Manager, Boral Resources (SA) Limited, provided dolomite quarry dust samples. Ruth-Ellen Williams performed the histological preparation and assisted with TEM and EDS at Adelaide Microscopy, and Richard Bright performed the light microscopy and sample preparation at the Women's and Children's Hospital. KSM was supported by an Australian Postgraduate Award, a Monash University J. L. William Scholarship and a Cystic Fibrosis Australia Studentship. MD, KSM, KKWS and DWP were supported by the AMRF Program, Commonwealth of Australia.

### References

- Cloetens, P., Barrett, R., Baruchel, J., Guigay, J. P. & Schlenker, M. (1996). *J. Phys. D*, **29**, 133–146.
- Donaldson, S. H., Corcoran, T. E., Laube, B. L. & Bennett, W. D. (2007). *Proc. Am. Thorac. Soc.* **4**, 399–405.
- Donnelley, M., Morgan, K. S., Fouras, A., Skinner, W., Uesugi, K., Yagi, N., Siu, K. K. W. & Parsons, D. W. (2009). *J. Synchrotron Rad.* **16**, 553–561.
- Gehr, P. & Schurch, S. (1992). *News Physiol. Sci.* **7**, 1–5.
- Goss, C. H., Newsom, S. A., Schilderout, J. S., Sheppard, L. & Kaufman, J. D. (2004). *Am. J. Respir. Crit. Care Med.* **169**, 816–821.
- Grubb, B. R., Jones, J. H. & Boucher, R. C. (2004). *Am. J. Physiol. Lung Cell Mol. Physiol.* **286**, L588–L595.
- Hamacher, J., Arras, M., Bootz, F., Weiss, M., Schramm, R. & Moehrlen, U. (2008). *Lab. Animals*, **42**, 222–230.
- King, M., Engel, L. A. & Macklem, P. T. (1979). *J. Appl. Physiol.* **46**, 504–509.
- Limberis, M., Anson, D. S., Fuller, M. & Parsons, D. W. (2002). *Human Gene Therap.* **13**, 2112.
- Livraghi, A. & Randell, S. H. (2007). *Toxicol. Pathol.* **35**, 116–129.
- Oberdorster, G., Oberdorster, E. & Oberdorster, J. (2005). *Environ. Health Perspect.* **113**, 823–839.
- O'Connor, G. T., Neas, L., Vaughn, B., Kattan, M., Mitchell, H., Crain, E. F., Evans, R., Gruchalla, R., Morgan, W., Stout, J., Adams, G. K.

## research papers

- & Lippmann, M. (2008). *J. Allergy Clin. Immunol.* **121**, 1133–1139.
- Parsons, D. W., Morgan, K., Donnelley, M., Fouras, A., Crosbie, J., Williams, I., Boucher, R. C., Uesugi, K., Yagi, N. & Siu, K. K. W. (2008). *J. Anat.* **213**, 217–227.
- Robertson, A., Stannard, W., Passant, C., O'Callaghan, C. & Banerjee, A. (2004). *Clin. Otolaryngol.* **29**, 157–160.
- Sims, D. E., Westfall, J. A., Kiorpes, A. L. & Horne, M. M. (1991). *Biotech. Histochem.* **66**, 173–180.
- Siu, K. K. W., Morgan, K. S., Paganin, D. M., Boucher, R., Uesugi, K., Yagi, N. & Parsons, D. W. (2008). *Eur. J. Radiol.* **68**, S22–S26.
- Snigirev, A., Snigireva, I., Kohn, V., Kuznetsov, S. & Schelokov, I. (1995). *Rev. Sci. Instrum.* **66**, 5486–5492.
- Stocker, A., Kremer, K., Koldej, R., Miller, D., Anson, D. & Parsons, D. (2009). *J. Gene Med.* **11**, 861–867.
- Tarran, R., Button, B., Picher, M., Paradiso, A. M., Ribeiro, C. M., Lazarowski, E. R., Zhang, L. Q., Collins, P. L., Pickles, R. J., Fredberg, J. J. & Boucher, R. C. (2005). *J. Biol. Chem.* **280**, 35751–35759.
- Wildhaber, J. H. (2006). *Paediatr. Respir. Rev.* **7**(Suppl. 1), S86–S87.
- Wilkins, S. W., Gureyev, T. E., Gao, D., Pogany, A. & Stevenson, A. W. (1996). *Nature (London)*, **384**, 335–338.
- Yabashi, M., Yamazaki, H., Tamasaku, K., Goto, S., Takeshita, K., Mochizuki, T., Yoneda, Y., Furukawa, Y. & Ishikawa, T. (1999). *Proc. SPIE*, **3773**, 2–13.



---

## Appendix F

*Animals in synchrotrons: Overcoming challenges for high-resolution, live, small-animal imaging.*

by Martin Donnelley, David Parsons, Kaye Morgan and Karen Siu.

Published in the AIP Conference Proceedings **1266**, pp. 30-34, 2010.

---

This paper was published in AIP Proceedings and is made available as an electronic reprint with the permission of AIP. The paper can be found at the following URL on the AIP website:

<http://link.aip.org/link/?APCPCS/1266/30/1>.

Reprinted with permission from the AIP. Copyright 2010, American Institute of Physics.

Systematic or multiple reproduction or distribution to multiple locations via electronic or other means is prohibited and is subject to penalties under law.

---

### Declaration for Appendix F, work supplementary to Thesis Chapter 6

In the case of Appendix F, contributions to the work involved the following:

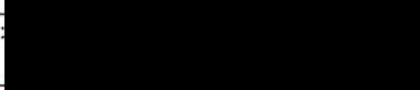
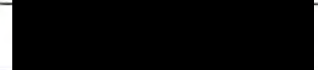
Name	% contribution	Nature of contribution
Martin Donnelley		Contributed to the planning, original experiments and wrote up the paper
David Parsons		Contributed to the planning, original experiments and proof-reading
Kaye Morgan	10%	Contributed to the planning, original experiments and proof-reading
Karen Siu		Contributed to the planning, original experiments and proof-reading

#### Declaration by co-authors

The undersigned hereby certify that:

1. the above declaration correctly reflects the nature and extent of the candidate's contribution to this work, and the nature of the contribution of each of the co-authors.
2. they meet the criteria for authorship in that they have participated in the conception, execution, or interpretation, of at least that part of the publication in their field of expertise;
3. they take public responsibility for their part of the publication, except for the responsible author who accepts overall responsibility for the publication;
4. there are no other authors of the publication according to these criteria;
5. potential conflicts of interest have been disclosed to (a) granting bodies, (b) the editor or publisher of journals or other publications, and (c) the head of the responsible academic unit; and
6. the original data are stored at the following location(s) and will be held for at least five years from the date indicated below: School of Physics and Monash Centre for Synchrotron Science, Clayton Campus, Monash University, Australia.

#### Signatures:

Martin Donnelley:		Date: 15.10.10
David Parsons:		Date: 15.10.10
Kaye Morgan:		Date: 18/10/10
Karen Siu:		Date: 19.10.2010

# Animals In Synchrotrons: Overcoming Challenges For High-Resolution, Live, Small- Animal Imaging

Martin Donnelley<sup>1</sup>, David Parsons<sup>1,2,3,4</sup>, Kaye Morgan<sup>5</sup>, Karen Siu<sup>5,6</sup>

<sup>1</sup>*Respiratory and Sleep Medicine, Women's and Children's Hospital, Adelaide, South Australia.*

<sup>2</sup>*Women's and Children's Health Research Institute, Adelaide, South Australia.*

<sup>3</sup>*Department of Paediatrics and Reproductive Health and* <sup>4</sup>*Centre for Stem Cell Research, University of Adelaide, South Australia.*

<sup>5</sup>*School of Physics and* <sup>6</sup>*Monash Centre for Synchrotron Science, Monash University, Melbourne, Victoria.*

**Abstract.** Physiological studies in small animals can be complicated, but the complexity is increased dramatically when performing live-animal synchrotron X-ray imaging studies. Our group has extensive experience in high-resolution live-animal imaging at the Japanese SPring-8 synchrotron, primarily examining airways in two-dimensions. These experiments normally image an area of 1.8mm x 1.2mm at a pixel resolution of 0.45 $\mu$ m and are performed with live, intact, anaesthetized mice.

There are unique challenges in this experimental setting. Importantly, experiments must be performed in an isolated imaging hutch not specifically designed for small-animal imaging. This requires equipment adapted to remotely monitor animals, maintain their anesthesia, and deliver test substances while collecting images. The horizontal synchrotron X-ray beam has a fixed location and orientation that limits experimental flexibility. The extremely high resolution makes locating anatomical regions-of-interest slow and can result in a high radiation dose, and at this level of magnification small animal movements produce motion-artifacts that can render acquired images unusable. Here we describe our experimental techniques and how we have overcome several challenges involved in performing live mouse synchrotron imaging.

Experiments have tested different mouse strains, with hairless strains minimizing overlying skin and hair artifacts. Different anesthetics have also been trialed due to the limited choices available at SPring-8. Tracheal-intubation methods have been refined and controlled-ventilation is now possible using a specialized small-animal ventilator. With appropriate animal restraint and respiratory-gating, motion-artifacts have been minimized. The animal orientation (supine vs. head-high) also appears to affect animal physiology, and can alter image quality. Our techniques and image quality at SPring-8 have dramatically improved and in the near future we plan to translate this experience to the Imaging and Medical Beamline at the Australian Synchrotron.

Overcoming these challenges has permitted increasingly sophisticated imaging of animals with synchrotron X-rays, and we expect a bright future for these techniques.

**Keywords:** Synchrotron, X-ray, phase contrast imaging, mouse, lung, airway.

**PACS:** 87.85.Pq

## INTRODUCTION

There is little scientific literature available about how to perform live animal imaging using synchrotron radiation. Our group has extensive experience in animal model studies at the Women's and Children's Hospital in Adelaide, where we are researching gene therapy treatments for cystic fibrosis airway disease<sup>1,2</sup>. We have transferred and adapted these animal handling techniques to high-resolution live-animal imaging at the Japanese SPring-8 synchrotron. We

typically perform 2D longitudinal imaging studies of airways or air containing structures using a field of view of 1.8mm x 1.2mm at a pixel resolution of 0.45 $\mu$ m. In this paper we describe our experimental techniques, identify areas that limit or alter standard experimental approaches, and describe some of the ways we have overcome the challenges involved in imaging the airways of live mice using a synchrotron.

There are many advantages to using synchrotron X-rays, including the ability to acquire very high-resolution images, as well as to utilize techniques such

as phase contrast imaging<sup>3, 4</sup>. However there are also a number of challenges involved in utilizing this unique imaging modality. Firstly, imaging is confined to a specialized imaging hutch, a lead-lined experimental room attached to the end of a synchrotron beamline. The hutch is essential for containing the intense radiation produced by the high flux source. This means that when performing live-animal imaging it is necessary to perform remote animal monitoring, maintain stable anesthesia and remotely deliver any test substances or pharmaceuticals. Secondly, the fixed beam location and orientation limits experimental flexibility in terms of animal restraint and positioning. Finally, the high imaging magnification produces its own set of challenges including the significant time and radiation dose required to locate a small region of interest within complex anatomy, minimizing motion artifacts produced by respiratory, cardiac and skeletal muscle movements, and eliminating the image artifacts produced by the animals fur.

### SYNCHROTRON IMAGING SETUP

Experiments are typically performed on the BL20XU undulator beamline at the SPring-8 synchrotron radiation facility in Japan. Here a 25keV monochromatic beam is used for synchrotron phase contrast X-ray imaging (PCXI). PCXI provides enhanced image contrast by utilizing X-ray refraction in addition to conventional absorption and is particularly useful for achieving soft tissue contrast where the absorption differences are small. Tissue boundaries are enhanced by the phase changes induced by differences in their X-ray refractive indices, provided the X-ray beam has sufficient spatial coherence and the sample to detector distance is sufficiently long<sup>5, 6</sup>, characteristics that are achievable using a synchrotron source. We have demonstrated the use of PCXI for novel non-invasive airspace imaging in small animals<sup>4, 7</sup>, and for non-invasive particulate detection in live mouse nasal airways<sup>3</sup>. Throughout these experiments we have been able to improve image quality in a number of ways.

### Ethical Treatment Of Animals

All studies were approved by the Animal Ethics Committees of the Women's and Children's Hospital and SPring-8 Synchrotron. Protocols are designed to ensure that experimental animals do not suffer pain, discomfort or distress, and that they remain sufficiently anesthetized throughout the experiments. While the animals are isolated in the closed imaging hutch they are closely monitored using video surveillance via two PTZ IP cameras (Panasonic BB-

HCM580). These real-time video feeds allow the level of anesthesia to be visually verified to be adequate at all times, from any computer on the local network. Visual impression are always supplemented with monitoring of physiological parameters such as the ventilator respiratory pressures, ECG and body temperature (SCIREQ flexiVent). Although it would be valuable to measure oxygen saturation, mouse-specific equipment reliable enough for primary use has not yet been located.

### Animal Strain

When performing high-resolution PCXI the mouse fur can cause image artifacts as it produces strong phase effects. Two strategies have been used to eliminate these effects. Firstly, using nude strains such as Crl:CD1-Foxn1<sup>tm</sup>, an athymic and T-cell deficient immunodeficient mouse, or HOS:HR-1 a commercial hairless mouse available in Japan, was found to be an apparently simple solution. While this allowed us to easily acquire images without fur artifacts, we are unsure whether these strains exhibit other physiological differences compared to normal mice that may affect our respiratory studies. In addition, using only hairless strains precludes the imaging of other useful strains such as the transgenic cystic fibrosis mice that are the focus of much of our non-synchrotron research efforts. The second strategy is removing fur from the imaging area (e.g. the trachea) of normal C57BL/6 mice using depilatory cream (e.g. Nair, Church & Dwight, Australia). Provided the area to be imaged is small and the cream is not vigorously rubbed into the skin there appears to be little adverse reaction, and the images are free from fur artifacts.

### Airway Access

For some imaging studies there are advantages to having airway access via tracheotomy or intubation, including the ability to perform mechanical ventilation, pulmonary function testing and pharmaceutical delivery. In early experiments tracheotomies were performed to gain airway access, but this was a relatively slow and invasive procedure and could significantly alter airway biology (including potentially allowing blood to enter the trachea). In considering our future need for repeat-imaging studies, tracheal intubations are now performed via the mouth, since these can be rapid, minimally invasive and readily repeatable.

We have adapted an intubation method described by MacDonald<sup>8</sup>, in which we use a 0.5mm plastic fiber optic guide as an introducer, and a 20Ga i.v. catheter (Insyte, Becton Dickinson, Utah, USA) as the

endotracheal (ET) tube (See Figure 1). The end of the fiber is attached to a bright fiber-light source so that the tip, which extends ~5mm past the end of the ET tube, provides good direct illumination to visualize the vocal cords and trachea for ET tube placement.

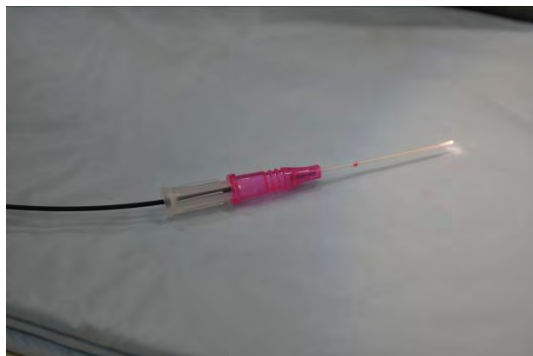


**FIGURE 1.** The 20Ga. Insyte intubation cannula and plastic fiber optic introducer.

The ET tube is inserted into the trachea to a fixed depth of 22.5mm from the nose tip (as marked in Figure 1) to avoid physical perturbation of the more distal imaging region in the trachea. For lung imaging studies this depth may not be so critical and the ET tube could be inserted deeper. The catheter needle-hub is immediately cut off to minimize respiratory dead-space, and so that the ET tube is ready for connection to the ventilator circuit.

### Anesthesia

Due to Japanese government regulations only two anesthetics are available at the SPring-8 synchrotron. We use pentobarbital (~72 mg/kg, i.p.) for anesthetic induction as well as for maintenance of anesthesia in non-ventilated animals. The limitations of pentobarbital include the need for continuous injection to maintain anesthesia, the induction of unpredictable leg “kick” movements in some mice despite deep anesthesia, and the potential for overdose. Thus, wherever possible we use the inhalable anesthetic isoflurane (2% in oxygen) delivered by an isoflurane vaporizer (Univentor U400, Malta). Advantages of isoflurane are that the concentration can be easily set and adjusted from outside the hutch, it does not produce leg movements as with pentobarbital, and its wide therapeutic index means there is a far lower potential for overdose. Thus, for all free-breathing experiments we use pentobarbital with maintenance doses delivered by syringe pump (World Precision Instruments, UMP2) to a 30Ga needle placed i.p. For all experiments requiring mechanical ventilation we

induce anesthesia with pentobarbital and then switch to isoflurane for maintenance. In a typical lung airway imaging study the isoflurane and oxygen mix is passively humidified by bubbling it through 10cm of water prior to delivery to the ventilator inspiratory circuit.

### Mechanical Ventilation

Wherever possible mice are mechanically ventilated using a flexiVent small animal ventilator (SCIREQ, Canada) when performing synchrotron imaging studies. This type of system has three significant advantages. Firstly, it allows respiratory system mechanics to be measured throughout an experiment to determine the physiological effects of a treatment while also simultaneously acquiring images. Secondly, it allows for the coordinated delivery of aerosols for pharmaceutical or test substance delivery. Thirdly, it enables respiratory-gated image acquisition so that images can be captured at corresponding points within the respiratory cycle and within a breath hold to minimize respiratory movements.

Ventilation is normally set at 80 breaths/min with a tidal volume of 20 ml/kg (minute ventilation of approximately 1.6 ml/g), and ~3 cmH<sub>2</sub>O of PEEP. The almost continuous chest motion present during normal breathing provides a technically challenging experimental setting, especially at the high image magnifications we use. With a requirement for a 75ms exposure length the ventilatory profile is configured with  $T_{\text{inspiration}} = 0.25$  sec,  $T_{\text{pause}} = 0.1$  sec and  $T_{\text{expiration}} = 0.4$  sec, providing a sufficient end-inspiratory pause to allow relatively motion-artifact-free image capture.

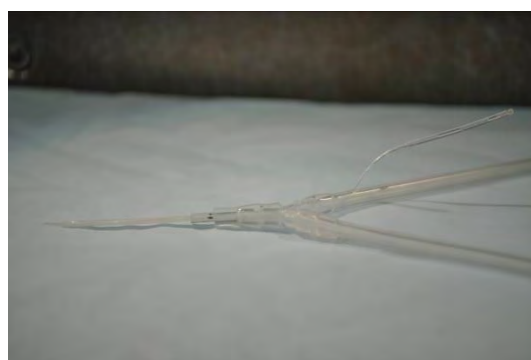


**FIGURE 2.** The ET tube (left), Y-connector, inspiratory and expiratory tubes (right) that connection to the ventilator, and the fine delivery cannula.

The i.v. catheter ET tube is easily connected to the ventilator circuit as shown in Figure 2. The diameter of the tubing between the tip of the ET tube and the Y-

piece is small so that the respiratory dead-space is minimized. The diameter and composition of the inspiratory and expiratory tubes does not appear to be critical, but nonetheless the shortest possible lengths are used. In addition, for some studies a length of heat-thinned PE10 tubing is fed through the wall of the inspiratory tube to the tip of the ET tube to allow test substances or pharmaceuticals to be delivered to the trachea or lung airways. The diameter of this tube is sufficient for liquid delivery, but not so large that it perturbs airflow through the ET tube. Liquid delivery is typically performed using a remote control syringe pump (World Precision Instruments, UMP2) connected to the PE10 cannula via a 30Ga needle.

One important limitation of the flexiVent software is its inability to perform data logging. Although it can display the cylinder displacement, pressure, ECG and temperature onscreen, those signals cannot be recorded for later analysis. Thus, for applications where these signals are required a separate data logger and sensors must be used.

### Animal Positioning

The fixed location and orientation of the X-ray beam limits experimental flexibility in terms of animal restraint and positioning. For anterior-posterior (AP) imaging it is necessary to mount the animals in a head-high orientation, but for lateral imaging they can be mounted head-high or supine (although the non-uniform shape of the X-ray beam can limit setup choices).

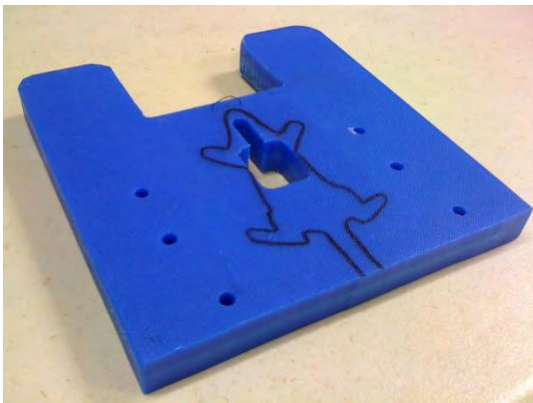


**FIGURE 3.** The mouse imaging board including a wire loop for the teeth, 6 holes for mounting to the X-Y-rotation stage in the hutch, and a slot and cutout for AP imaging.

In early experiments a stereotactic frame that attached at the incisors and ears was used to hold the mice securely in the beam in a head-high position. The

frame was difficult to set up and did not adequately prevent movement. This was a severe limitation because at the high magnifications at which we image, even small amounts of movement can severely degrade the images. This setup has since been redesigned to use a flat imaging board cut from an 18mm thick polyethylene kitchen cutting-board. The board contains a wire loop to support the teeth, and the mouse body is tethered using surgical tape (Micropore, 3M Corporation) onto the skin. The board (See Figure 3) contains a cutout to allow AP imaging of the nasal airways and lung, and mounting holes to directly attach it to the X-Y-rotation stage in the hutch. In practice this setup was substantially more effective at minimizing small body movements during imaging.

For technical simplicity our previous lung studies have oriented the imaging board and mouse in a head-high orientation. Despite being well anesthetized, after approximately 25-30 minutes of imaging some mice appeared unsettled and displayed uncontrollable and unpredictable respiratory excursions that degraded image quality, limiting usable imaging time to less than 30 minutes. Changing to a supine imaging position prevented these movements from occurring, and we speculate that loading on the diaphragm in the head-high position was causing muscle fiber shortening, ventilatory loading and potential hypoxemia and hypercapnia. In addition, venous return problems when vertical may have also reduced cardiac output and potentially metabolism, further exacerbating the problem.

When possible we now utilize a supine imaging position to minimize respiratory movements and image artifacts due to movement.

### Dose Minimisation

Several strategies have been implemented to minimize the radiation dose delivered during imaging. A fast imaging shutter that is only opened during the image exposure is used so that at all other times the mouse does not receive any radiation. The delivered dose is measured using an ion chamber located downstream of this shutter. During recent experiments the dose rate was calculated to be 0.44Gy/sec. The exposure times are also reduced wherever possible, thus trading image quality for dose. Finally, laser alignment is used in the hutch prior to beam activation, so that the anatomical region of interest can be rapidly located and the amount of radiation delivered prior to an experiment actually commencing can be reduced.

Although we attempted to limit the radiation dose by reducing the size of the imaging area and limiting the exposure times, at present it remains too intense to

consider animal recovery, or repeat-imaging experimental designs.

## CONCLUSIONS

We propose that PCXI is a valuable technique for studying the airways of live mouse models, and that despite its limitations there are currently no other imaging modalities with these capabilities. The rapid development of imaging and synchrotron technologies has and will continue to produce improvements in light sensitivity and image resolution that could allow shorter exposure times to minimize motion artifact and produce desired reductions in radiation dose.

Imaging live mice using synchrotron X-rays has many challenges, but overcoming these challenges has permitted increasingly sophisticated imaging of animals with synchrotron X-rays. We expect a bright future for these techniques.

## ACKNOWLEDGMENTS

Studies supported by the WCH Foundation, NH&MRC Australia, USA CF Foundation and philanthropic donors via the CURE4CF Foundation Limited ([www.cure4cf.org](http://www.cure4cf.org)). The synchrotron radiation experiments were performed on the BL20XU beamline at SPring-8, with the approval of the Japan Synchrotron Radiation Institute (JASRI) under proposal number 2009A1878 and 2009B1922. We thank Naoto Yagi, Kentaro Uesugi, Yoshio Suzuki and Akihisa Takeuchi for their assistance at the BL20XU beamline. Dr Andreas Fouras, Monash University Division of Biological Engineering, provided imaging advice and supplied essential experimental equipment including the CCD detector. Don Wanasinghe from AFW Technologies Pty Ltd provided the plastic optic fiber for performing the intubations. KM was supported by an Australian Postgraduate Award, a Monash University JL William Scholarship and a Cystic Fibrosis Australia Studentship. We acknowledge travel funding provided by the ANSTO Access to Major Research Facilities Program (AMRFP), and the International Synchrotron Access Program (ISAP) managed by the Australian Synchrotron. The ISAP is an initiative of the Australian Government being conducted as part of the National Collaborative Research Infrastructure Strategy.

## REFERENCES

1. M. Limberis, D. S. Anson, M. Fuller and D. W. Parsons, *Human Gene Therapy* **13** (17), 2112-2112 (2002).
2. A. Stocker, K. Kremer, R. Koldej, D. Miller, D. Anson and D. Parsons, *The Journal of Gene Medicine* (2009).
3. M. Donnelley, K. Morgan, A. Fouras, W. Skinner, K. Uesugi, N. Yagi, K. Siu and D. Parsons, *Journal of Synchrotron Radiation* **16** (4), 553-561 (2009).
4. D. W. Parsons, K. Morgan, M. Donnelley, A. Fouras, J. Crosbie, I. Williams, R. C. Boucher, K. Uesugi, N. Yagi and K. K. W. Siu, *Journal of Anatomy* **213** (2), 217-227 (2008).
5. P. Cloetens, R. Barrett, J. Baruchel, J. P. Guigay and M. Schlenker, *Journal of Physics D (Applied Physics)* **29** (1), 133-146 (1996).
6. A. Snigirev, I. Snigireva, V. Kohn, S. Kuznetsov and I. Schelokov, *Review of Scientific Instruments* **66** (12), 5486-5492 (1995).
7. K. K. W. Siu, K. S. Morgan, D. M. Paganin, R. Boucher, K. Uesugi, N. Yagi and D. W. Parsons, *European journal of radiology* **68** (3), S22-S26 (2008).
8. K. D. MacDonald, H. Y. S. Chang and W. Mitzner, *J Appl Physiol* **106** (3), 984-987 (2009).



---

# Supplementary Media

The cd inserted at the back of this thesis contains an electronic copy of the thesis and supplementary movies as below.

- Pdf of the thesis
- Chapter 5 supplementary
  - *Figure 1 supplementary media, Media 1:* Consecutive frames of the flat field at BL20XU, SPring-8, shown in false colour for each of no diffuser, a stationary diffuser and a spinning diffuser.
- Chapter 6 supplementary
  - *Figure 6.5 supplementary media:* A render of the CT set taken of the upper half of a mouse, following a path in through the nose and down through the airways to the lungs.
  - *Figure 6.29 a) supplementary media:* Time-lapse images of the transit of introduced hollow glass beads up away from the lungs, along the trachea surface.
  - *Figure 6.29 b) supplementary media:* The difference between consecutive frames for the time-lapse of the particulate motion given as Figure 6.28 a) supplementary. Taking the difference between frames makes the motion of the beads more easily visible.
- Appendix C supplementary
  - *Figure 4 supplementary media:* Example of gas bubbles detected non-invasively whilst transiting intact live airway. The first six frames (all frames were taken 10 s apart) show 1 min of baseline images prior to fluid instillation. After four separating black frames, the 19 following frames reveal a range of bubble sizes and groups moving down the airway from the overlying nostril region towards the pharyngeal area, over a 3-min period. Individual and linked bubbles as well as the rapidly changing fluid level associated with the bubbles is apparent. Frame 18 and the scale are the same as Fig. 4.
  - *Figure 5 supplementary media:* Animated view of rendered head and chest. Views of the skull, neck and chest from all horizontal directions show with greater clarity the features noted in Fig. 5B. This particular digital sectioning and rotation permits viewers to simultaneously appreciate the detail of skull-bone suture lines, the detail within the cutaway section exposing the olfactory turbinate region, and the soft tissues of the outer ears and neck.
  - *Figure 6 supplementary media:* Non-invasive localization of cannula in upper nasal airway. The cannula is visible entering the nasal orifice (in frame 1 the cannula has been overlaid in red), and can be tracked though the nostril to its termination in the

- nasal airway. The white nasal-bone can be seen dorsally, where it terminates before reaching the nose tip. Similarly, the (white) anterior portion of the dorsal incisor is present ventrally. Note also the resolution of hair of the fur on the nose outer surface.
- *Figure 7A-1 supplementary media:* This animation was produced from the same dataset that provided the image of Fig. 7A, but here is shown with a different orientation and with progressive magnification. It was rendered to be similar to the view of a block of fixed lung tissue produced by simple right-angled cuts with a blade. At the top of the first frame the base of the trachea and the carina with the two mainstem bronchi are shown; note the regular bilateral whitened regions of airway cartilage on the airway wall. With rotation past the side of the lung some medium-size airways, and the edges of two lung lobes can be seen (see Fig. 7A for labeling). With further rotation the left and right sides of the lung, the continuation of the lobe edge, and the large airways that connect back to the carina become apparent. The last frame shows three smaller airways, mostly in cross-section, with their accompanying blood vessels.
  - *Figure 7A-2 supplementary media:* This animation is the same dataset, orientation, rotation and magnification as in animation 7A-1.avi, but with rendering and coloration designed to separate out airways and bone. The dorso-posterior sweep of the mainstem bronchi is apparent as they connect into the lung lobes, and the digital removal of blood from the lung can be seen in the empty blood vessel adjacent to the large airway right of centre in the last frame. This rendering has also removed the heart and associated thoracic tissues, leaving the lung tissue largely intact. Note that some lung lobe edges are fragmented due to the effect of digital region cropping when digitally producing this block of chest tissue for viewing.
  - *Figure 7B supplementary media:* An anterior to posterior rotation animation, again using the same dataset and with rendering settings assigned as for 7A-2.avi, but starting from an anterior viewpoint. However, the degree of cropping has been relaxed, to include more of the ribs and the full posterior extent of the lungs. At Frame 50 a small structure below the lungs appears, and was found to be in the position of the stomach in other renderings (data not shown). The structure here represents the top of the stomach, containing an air bubble and food material (follow to the last frame for more clarity). By Frame 130 the medio-ventral edge of a right lobe is silhouetted against the background.
  - *Figure 7D supplementary media:* Slow 360° rotation (2° increments) of the ear dataset rendered in image Fig. 7D. The relationships amongst the outer ear, ear canal, eardrum region, middle-ear bony structures and the cochlea are seen in fine detail. Scale as in Fig. 7D.
  - *Figure 8 supplementary media:* Virtual tour of mouse nose and lung reconstructed from CT slices. This is the same mouse as that used for Fig. 6C. Beginning with a view of the posterior edge of the CT slice series, sections through the ribs, forearms, and the anterior end of the stomach (containing food material) can be seen. Rotation to the nose tip displays the mounting tube, the animal with its outer ears laid flat, and the skull, teeth, and whiskers. The two polyethylene cannulae (see Fig. 6C) can be seen in the nostrils, and once the view has progressed inside the nose, two views of the

upper nasal turbinates are seen (frames 380×480). The viewpoint progresses posteriorly along the left nasal airway until (frame 670) the scene scans to ventral airspaces before crossing to the right airway region at this same depth. From the right nasal airway (frame 960) the view moves posteriorly with the septum on the right, until centralizing in the nasopharynx (frame 1200). The larynx and trachea come into view (frame 1220) with the viewer taken down into the trachea, past the carina (frame 1510), and into the right bronchus and deeper airway branches. At frame 1820 the view passes through the airway wall, exits the base of the lung, and rotates to reveal the stomach, ribs and forearms of the first frame (permitting continuous loop animation).

- Appendix E Supplementary

- *Figure 5 supplementary media, S1:* A time-lapse movie of the *in vivo* behaviour of quarry dust particles on the trachea surface.
- *Figure 6 supplementary media, S2:* A time-lapse movie of the *in vivo* behaviour of fibreglass fibres on the trachea surface.
- *Figure 7 supplementary media:* A time-lapse movie of the *in vivo* behaviour of galena particles on the trachea surface.
- *Figure 8 supplementary media:* A time-lapse movie of the *in vivo* behaviour of hollow glass beads on the trachea surface.